



Universität Hamburg

DER FORSCHUNG | DER LEHRE | DER BILDUNG

Elucidating signal transduction in multi-domain BLUF photoreceptors by studying the Photoactivated Adenylate Cyclase OaPAC

Responsible Professor: Prof. Dr. Arwen Pearson

Responsible Professor: Prof. Dr. Chris Meier

Responsible Tutor: Dr. Robin Schubert

Responsible Tutor: Dr. Kristina Lorenzen

Dissertation submitted to

University of Hamburg, Hamburg, Germany

Faculty of Mathematics, Informatics and Natural Sciences

Department of Chemistry

Doctoral dissertation written by:

Anaïs Chretien

2024

First Reviewer: Prof. Dr. Arwen Pearson

Second Reviewer: Prof. Dr. Christian Betzel

Oral defense committee:

Chair: Prof. Dr. Daniel Wilson

Deputy Chair: Prof. Dr. Arwen Pearson

Member: Prof. Dr. Andrew Torda

Member: Dr. Robin Schubert

Member: Dr. Christopher Milne

Date of disputation:

September 13th 2024

Monograph following the
Doctoral Degree Regulations MIN Faculty (2018)

For the degree of
Doctor rerum naturalium (Dr. rer. nat.)

Doctorate in cooperation with a non-university research institute
European X-ray Free Electron Laser GmbH, Schenefeld, Germany

Doctorate following a graduate school program
PIER Helmholtz Graduate School, Hamburg, Germany

The doctorate took place
between Winter Semester 2020 and Summer Semester 2024
at European X-ray Free Electron Laser GmbH, Schenefeld, Germany



Partnership of
Universität Hamburg and DESY

Publications

- **Anaïs Chretien**, Marius F. Nagel, Sabine Botha, Raphaël de Wijn, Lea Brings, Katerina Dörner, Huijong Han, Jayanath C. P. Koliyadu, Romain Letrun, Adam Round, Tokushi Sato, Christina Schmidt, Radu-Costin Secareanu, David von Stetten, Mohammad Vakili, Agnieszka Wrona, Richard Bean, Adrian Mancuso, Joachim Schulz, Arwen R. Pearson, Tilman Kottke, Kristina Lorenzen, Robin Schubert, Light-induced Trp_{in}/Met_{out} switching during BLUF domain activation in ATP-bound photoactivatable adenylate cyclase OaPAC, *Journal of Molecular Biology*, Volume 436, Issue 5, 2024, 168439, ISSN 0022-2836, <https://doi.org/10.1016/j.jmb.2024.168439>.
- Patrick Y. A. Reinke, Robin Schubert, Dominik Oberthür, Marina Galchenkova, Aida Rahmani Mashhour, Sebastian Günther, **Anaïs Chretien**, Adam Round, Brandon Charles Seychell, Brenna Norton-Baker, Chan Kim, Christina Schmidt, Faisal H. M. Koua, Alexandra Tolstikova, Wiebke Ewert, Gisel Esperanza Peña Murillo, Grant Mills, Henry Kirkwood, Hévila Brognaro, Huijong Han, Jayanath Koliyadu, Joachim Schulz, Johan Bielecki, Julia Lieske, Julia Maracke, Juraj Knoska, Kristina Lorenzen, Lea Brings, Marcin Sikorski, Marco Kloos, Mohammad Vakili, Patrik Vagovic, Philipp Middendorf, Raphael de Wijn, Richard Bean, Romain Letrun, Seonghyun Han, Sven Falke, Tian Geng, Tokushi Sato, Vasundara Srinivasan, Yoonhee Kim, Oleksandr M. Yefanov, Luca Gelisio, Tobias Beck, Andrew S. Doré, Adrian Mancuso, Christian Betzel, Saša Bajt, Lars Redecke, Henry N. Chapman, Alke Meents, Dušan Turk, Winfried Hinrichs & Thomas J. Lane, SARS-CoV-2 M^{pro} responds to oxidation by forming disulfide and NOS/SONOS bonds, *Nature Communications*, 15, 3827, 2024, <https://doi.org/10.1038/s41467-024-48109-3>.

Contents

Publications	IV
List of Figures	VIII
List of Tables	XI
List of Appendices	XIII
List of Abbreviations	XV
Zusammenfassung	XVII
Abstract	XIX
1. Introduction	1
1.1. Introduction to Photosensory Receptors	1
1.2. BLUF Photoreceptors: Overview and Structures	6
1.3. Signalling State and Signal Transduction in BLUF Photoreceptors	15
1.4. Photoactivated Adenylate Cyclase: A Case Study	18
1.5. Perspectives for BLUF Photoreceptors in Optogenetics	22
1.6. Experimental Techniques for the Study of Photosensory Proteins	26
1.7. Aim of this Project	31
2. Materials and Methods	33
2.1. Materials	33
2.1.1. Chemicals, Consumables and Reagents	33
2.1.2. Buffers and Growth Media	35
2.2. Methods	37
2.2.1. Cloning Strategy for OaPAC	37
2.2.2. Cloning Procedures	40
2.2.3. Gene Expression	43

2.2.4.	Protein Purification	44
2.2.5.	Basic Methods for Biochemical Characterization.....	47
2.2.6.	Oligomeric State and Stability	48
2.2.7.	<i>In vitro</i> Adenylate Cyclase Activity Assay	50
2.2.8.	Spectroscopic Analysis in Solution	50
2.2.9.	<i>In crystallo</i> Optical Spectroscopy	52
2.2.10.	Crystallization and Structure Determination.....	54
3.	Results and Discussion	66
3.1.	Background	66
3.2.	Biophysical and Structural Characterization of OaPAC	67
3.2.1.	Gene Expression and Protein Purification Optimization	67
3.2.2.	Protein Stability.....	73
3.2.3.	Spectroscopic and Enzymatic Properties of OaPAC ₁₋₃₅₀	76
3.2.4.	Crystallization	81
3.2.5.	Dark State Structural Model of OaPAC ₁₋₃₅₀	87
3.3.	Characterization of OaPAC Photoactivation and Signal Transduction Mechanisms	96
3.3.1.	Early Photoactivation Mechanism of OaPAC	96
3.3.2.	Laser Power Titration	109
3.3.3.	Slow Conformational Changes in OaPAC ₁₋₃₅₀ Crystals Revealed by Time-Resolved Optical Spectroscopy	112
3.3.4.	Signal Transduction on the Millisecond Time Scale.....	115
3.3.5.	Steady State of OaPAC ₁₋₃₅₀ Light-Activated State in C222 ₁ Crystal	121
3.3.6.	FTIR Study to Understand the Absence of ATP to cAMP Turnover in OaPAC ₁₋₃₅₀ Crystals	132
3.4.	Enzymatic Domain, Allosteric Communication & Relaxation	137

3.4.1.	Binding Configuration of ATP in the Active Site	137
3.4.2.	SAXS Analysis of OaPAC ₁₋₃₅₀ in the Presence and Absence of ATP.....	147
3.4.3.	FTIR Study on Signal Transduction in the Presence or Absence of ATP	159
3.4.4.	Allosteric Regulation and Relaxation in OaPAC	162
4.	Conclusion	167
4.1.	Early Photoactivation Events in BLUF Photoreceptors	167
4.2.	Importance of the Semi-Conserved Tryptophan Residue in Signal Transduction in BLUF Photoreceptors	168
4.3.	Signal Transduction to the AC Domain in PAC Photoreceptors	170
	References	174
A.	Appendices	208
A.1.	Appendix Figures.....	208
A.2.	Appendix Tables.....	225
A.3.	List of Hazardous Substances According to GHS	229
	Acknowledgements	236
	Declaration on Oath.....	238

List of Figures

Figure 1: Diversity of photosensory receptors represented by seven photoreceptors families.	5
Figure 2: Structure of the BLUF sensor domain and insight into photoactivation.	8
Figure 3: Diversity of BLUF photoreceptors represented by multi-domain and short proteins. ...	14
Figure 4: Structural models of PAC photoreceptor.	20
Figure 5: pColdI vector used for the expression of the genes of interest.	37
Figure 6: OaPAC crystals used at TR-icOS for UV-Vis absorption spectroscopy.	54
Figure 7: SDS-PAGE analysis of His-tag_OaPAC ₁₋₃₅₀ expression and solubility for different growth conditions.	68
Figure 8: Comparison of IMAC purification of His-tag_OaPAC ₁₋₃₅₀ after gene expression for 16 h at 30 °C with three different E. coli strains.	69
Figure 9: Comparison of cell lysis methods for the production of OaPAC proteins.	70
Figure 10: Optimized final purification step and SDS-PAGE analysis for His-tag_OaPAC ₁₋₃₅₀	71
Figure 11: Purification strategy for OaPAC ₁₋₃₅₀ and OaPAC ₁₋₃₆₆ consists of a combination of anion-exchange, cation-exchange and size exclusion chromatography.	72
Figure 12: Protein stability analysis of three OaPAC variants after purification, flash-freezing and thawing, based on DLS-measurements.	75
Figure 13: Spectral properties of OaPAC ₁₋₃₅₀ in solution.	78
Figure 14: ATP turnover analysis in OaPAC ₁₋₃₅₀ in solution using activity assay and FTIR spectroscopy.	80
Figure 15: OaPAC ₁₋₃₅₀ crystallization trial at 4 °C.	82
Figure 16: Spectral properties of OaPAC ₁₋₃₅₀ crystals.	84
Figure 17: OaPAC ₁₋₃₅₀ crystal images recorded before and after 355 nm-laser exposure.	85
Figure 18: Microcrystal slurry suitable for TR-SSX and TR-SFX experiments.	86
Figure 19: Structural models of OaPAC and bPAC.	89

Figure 20: Temperature factors analysis of OaPAC ₁₋₃₅₀ structural models derived from X-ray crystallography data collection at cryogenic temperature and at room-temperature, with and without ATP.	90
Figure 21: Close-up of the flexible region in the BLUF domain of OaPAC ₁₋₃₅₀	91
Figure 22: Structural details of the BLUF domain in ATP-bound OaPAC ₁₋₃₅₀ at cryogenic temperature.	93
Figure 23: Structural details of the AC domain in ATP-bound OaPAC ₁₋₃₅₀ at cryogenic temperature.	95
Figure 24: Oscilloscope trace of the TR-SFX experiment illustrating the applied pump-probe pulse pattern in LIGHT-DARK1-DARK2 succession.	98
Figure 25: BLUF activation via blue light excitation of flavin chromophore in OaPAC revealed by TR-SFX and extrapolation process.	104
Figure 26: BLUF activation via blue light excitation of flavin chromophore in OaPAC revealed by TR-SFX and multi-copy refinement.	109
Figure 27: Laser power titration analysis of C222 ₁ OaPAC ₁₋₃₅₀ crystals.	111
Figure 28: Time-resolved analysis of OaPAC ₁₋₃₅₀ C222 ₁ crystal UV-Vis absorption recorded at the TR-icOS platform.	113
Figure 29: Signal transmission in the BLUF domain of OaPAC revealed at 50 ms pump-probe delay by TR-SSX.	117
Figure 30: Signal transmission in the BLUF domain of OaPAC ₁₋₃₅₀ revealed at 480 and 960 ms pump-probe delays by TR-SSX.	119
Figure 31: Signal transmission in OaPAC ₁₋₃₅₀ revealed at 50, 480 and 960 ms pump-probe delays by TR-SSX.	120
Figure 32: Transition from Trp _{out} to Trp _{in} in OaPAC revealed by cryo-trapped data after 5 s of continuous light excitation.	124
Figure 33: OaPAC shows a restructuring of β -sheet 5 and both loops preceding and succeeding it together with the Met _{out} /Trp _{in} transition upon light excitation.	127

Figure 34: Overlay of OaPAC ₁₋₃₅₀ structural model from the cryo-trapping experiment with the TR-SSX data.....	129
Figure 35: Analysis of changes in the linker region and AC domain upon light exposure in the C222 ₁ crystals.....	132
Figure 36: FTIR and crystal packing analysis of OaPAC C222 ₁ crystals.	134
Figure 37: Crystal packing and FTIR analysis of P2 ₁ 2 ₁ 2 ₁ crystals.	136
Figure 38: Details of ATP binding coordination in OaPAC active site.	139
Figure 39: Representation of hydrogen bond and magnesium coordination bond network coordinating ATP in the active site of OaPAC.	140
Figure 40: Details of active site rearrangement upon ATP binding in OaPAC.	143
Figure 41: Analysis of ATP-free OaPAC closed conformation and open conformation.	146
Figure 42: SAXS data from OaPAC ₁₋₃₅₀	148
Figure 43: SAXS data analysis of the first measurement of OaPAC ₁₋₃₅₀ at 4 mg/mL without ATP.	149
Figure 44: SAXS data analysis of the first measurement of OaPAC ₁₋₃₅₀ at 4 mg/mL with ATP.	150
Figure 45: Analysis of the fit between the X-ray scattering data of OaPAC ₁₋₃₅₀ in solution and the crystallography models of OaPAC ₁₋₃₅₀	156
Figure 46: Ab initio modelling obtained from the SAXS data of OaPAC ₁₋₃₅₀ in the absence of substrate.....	158
Figure 47: Light-minus-dark FTIR difference spectra of OaPAC in solution in the presence or absence of ATP and analogues.	162
Figure 48: Relaxation kinetics of structural changes after photoexcitation of OaPAC observed with TR-FTIR.....	164
Figure 49: Difference map revealing changes in the active site and the tongue region between holo and ATP-free OaPAC.....	166
Figure 50: Proposed signal transmission pathway of OaPAC photoreceptor.....	173

List of Tables

Table 1: List of chemicals and broths used in this project.	33
Table 2: List of consumables used in the project.	34
Table 3: List of enzymes, reagents and competent cells used in this project.	35
Table 4: List of DNA and activity assay kits used in this project.	35
Table 5: List of bacterial growth media and buffers used in this project.	36
Table 6: Variants of pColdI_OaPAC plasmids required for this project.	39
Table 7: Cloning strategies to obtain the vectors and genes for 3 out of 4 plasmids.	39
Table 8: List of primers necessary to obtain the 3 different plasmids of interest.....	39
Table 9: PCR steps for the amplification of OaPAC DNA fragments and pColdI_no-tag vector.	41
Table 10: PCR steps for the colony PCR tests	42
Table 11: Extinction coefficients for OaPAC protein variants.	47
Table 12: Equation parameters and values from data analysis of OaPAC variants stability performed by the Origin software version 2024 using a linear fit as shown in Figure 12.....	76
Table 13: Values from data analysis of OaPAC ₁₋₃₅₀ activation and relaxation kinetics performed by the Origin software version 2024 using a one-phase exponential fit as shown in Figure 13.....	79
Table 14: Description of the crystallization conditions used to obtain the crystals shown in Figure 15.	83
Table 15: Description of data collection setup and results during TR-SFX beamtime at the SPX/SFX instrument of EuXFEL with proposal 2829.	98
Table 16: Description of hit rate and indexed lattices during the data processing of four data sets (5, 50, 500 ns and 4.58 μ s delay) and corresponding light (LIGHT), light-contaminated (DARK1) and dark (DARK2) sub-data sets.....	100
Table 17: Power titration experiment for C222 ₁ crystals of OaPAC ₁₋₃₅₀	110

Table 18: Description of data collection setup and data processing results during TR-SSX beamtimes at the T-REXX instrument of PETRA III P14.EH2 beamline with proposal MX947.	116
Table 19: SAXS parameters and statistics of OaPAC ₁₋₃₅₀ study obtained with Guinier and distance distribution analysis.....	154
Table 20: P-values from the pairwise similarity tests between OaPAC SAXS data in solution without or with ATP and OaPAC crystallographic model fit depending on the AC domain conformation obtained with CRY SOL as shown in Figure 45.....	157
Table 21: P-values from the pairwise similarity tests between OaPAC SAXS data in solution without ATP and OaPAC most representative ab initio model fit obtained with DAMMIF as shown in Figure 46.	159

List of Appendices

Appendix Figure 1: Mass spectrometry analysis of Tag-free OaPAC ₁₋₃₅₀ in solution.	208
Appendix Figure 2: BLUF photoexcitation after 1,823 ns delay revealed by TR-SFX.....	209
Appendix Figure 3: Occupancy determination of the light-activated states during TR-SFX experiment using the difference map method.	209
Appendix Figure 4: Bleaching analysis of C222 ₁ OaPAC ₁₋₃₅₀ crystals.....	210
Appendix Figure 5: Dark spectra of C222 ₁ OaPAC ₁₋₃₅₀ crystals recorded before each subsequent photoexcitation during the time series analysis shown in Figure 28.....	210
Appendix Figure 6: Difference electron density map between holo OaPAC dark state at cryogenic temperature and OaPAC 5 s light illuminated cryo-trapped state.	211
Appendix Figure 7: Light-minus-dark FTIR difference spectra of OaPAC ₁₋₃₅₀ and OaPAC ₁₋₁₃₇ and their double difference spectrum isolating contributions of the AC domain.	211
Appendix Figure 8: ATP binding conformations in OaPAC active site at room-temperature.	212
Appendix Figure 9: Difference electron density map revealing differences in the active site between holo and ATP-free OaPAC.....	212
Appendix Figure 10: X-ray scattering pattern from OaPAC ₁₋₃₅₀ SAXS data.....	213
Appendix Figure 11: SAXS data analysis of the first measurement of OaPAC ₁₋₃₅₀ at 2 mg/mL without ATP.	214
Appendix Figure 12: SAXS data analysis of the second measurement of OaPAC ₁₋₃₅₀ at 2 mg/mL without ATP.	215
Appendix Figure 13: SAXS data analysis of the third measurement of OaPAC ₁₋₃₅₀ at 2 mg/mL without ATP.	216
Appendix Figure 14: SAXS data analysis of the first measurement of OaPAC ₁₋₃₅₀ at 2 mg/mL with ATP.	217
Appendix Figure 15: SAXS data analysis of the second measurement of OaPAC ₁₋₃₅₀ at 2 mg/mL with ATP.	218

Appendix Figure 16: SAXS data analysis of the third measurement of OaPAC ₁₋₃₅₀ at 2 mg/mL with ATP.	219
Appendix Figure 17: SAXS data analysis of the second measurement of OaPAC ₁₋₃₅₀ at 4 mg/mL without ATP.	220
Appendix Figure 18: SAXS data analysis of the third measurement of OaPAC ₁₋₃₅₀ at 4 mg/mL without ATP.	221
Appendix Figure 19: SAXS data analysis of the second measurement of OaPAC ₁₋₃₅₀ at 4 mg/mL with ATP.	222
Appendix Figure 20: SAXS data analysis of the third measurement of OaPAC ₁₋₃₅₀ at 4 mg/mL with ATP.	223
Appendix Figure 21: <i>Ab initio</i> model from the SAXS data of OaPAC ₁₋₃₅₀ in the presence of ATP.	224
Appendix Table 1: Synchrotron data collection and processing statistics.	225
Appendix Table 2: Data collection and refinement statistics of TR-SFX data.	226
Appendix Table 3: Data collection and refinement statistics of TR-SSX data.	227

List of Abbreviations

AC domain	adenylate cyclase domain
ApC _{pp}	adenosine-5'-[(a-b)-methylene]triphosphate
ATP	adenosine-5'-triphosphate
BLUF	blue light sensor using FAD
cAMP	cyclic adenosine-3',5'-monophosphate
CHT	ceramic hydroxyapatite type
FAD	flavin adenine dinucleotide
FMN	flavin mononucleotide
FPLC	fast protein liquid chromatography
FTIR	Fourier-transform infrared spectroscopy
HEPES	2-[4-(2-hydroxyethyl)piperazin-1-yl]ethanesulfonic acid
IMAC	immobilised metal ion affinity chromatography
IPTG	isopropyl-β-d-1-thiogalactopyranoside
kb	kilobase
LB	Luria-Bertani (broth)
MS	mass spectrometry
OD _{600nm}	optical density measured at 600 nm
PAC	photoactivated adenylyl cyclase
PBS	phosphate-buffered saline
PCR	polymerase chain reaction
QHP	quaternary amino group high performance
RMSD	root-mean-square deviation

SDS	sodium dodecyl sulphate
SDS-PAGE	sodium dodecyl sulphate polyacrylamide gel electrophoresis
SEC	size exclusion chromatography
SPG	sucrose, phosphate, glutamate
TEA	tris, acetate, EDTA
TRIS	tris(hydroxymethyl)-aminomethane
TR-SFX	time-resolved serial femtosecond crystallography
TR-SSX	time-resolved serial synchrotron crystallography
TRX	time-resolved crystallography

Zusammenfassung

Photosensorische Rezeptoren sind wichtige molekulare Einheiten in allen Lebensbereichen. Sie ermöglichen es Organismen, Lichtreize zu erkennen und darauf zu reagieren. Dies unterstreicht ihre essentielle Rolle bei der Regulierung biologischer Prozesse wie Phototropismus, circadianer Rhythmen, Photomorphogenese und Photosynthese. Unter den unzähligen Arten photosensorischer Rezeptoren zeichnen sich blaues Licht wahrnehmende Proteine, wie die *Blue Light Using Flavin* (BLUF)-Photorezeptoren, durch ihre Fähigkeit aus, blaues Licht zur Signalgebung zu nutzen. BLUF-Photorezeptoren zeichnen sich durch die konservierte Struktur ihrer BLUF Sensordomäne aus und kommen in einer Vielzahl von Organismen vor, von Bakterien und Algen bis hin zu Pflanzen und bestimmten Pilzen. Sie sind für ihre Fähigkeit bekannt, Flavin-Chromophore – typischerweise Flavin-Adenin-Dinukleotid (FAD) – zu binden. Bei der Absorption blauer Photonen verändern sie ihre Konformation, was zu nachfolgenden Signalereignissen führt und ihre zentrale Rolle bei der adaptiven Reaktion verschiedener Organismen auf Licht unterstreicht. Diese Dissertation bietet eine umfassende Untersuchung der BLUF-Photorezeptoren, wobei der Schwerpunkt insbesondere auf dem Photoaktivierten Adenylatcyclase-Protein von *Oscillatoria acuminata* (OaPAC) liegt, das aus einer BLUF-Sensordomäne besteht, die mit einer Adenylatcyclase-(AC)-Effektordomäne verknüpft ist und die Umwandlung von ATP in cAMP katalysiert. Ziel dieser Studie ist es, den Photoaktivierungsmechanismus von OaPAC und den daraus folgenden Signalübertragungsweg aufzuklären. Dabei wird ein integrativer Ansatz verwendet, der zeitaufgelöste Kristallographie, Kleinwinkelstreuung, Spektroskopie und biochemische Charakterisierungstechniken nutzt. Besonderes Augenmerk wird auf die Tyr-Gln-Met-Triade in der BLUF-Domäne gelegt, die eine entscheidende Rolle bei den anfänglichen lichtinduzierten Konformationsänderungen spielt. Darüber hinaus liegt ein Hauptaugenmerk auf den bislang weniger verstandenen Aspekten der BLUF-Photorezeptoren, insbesondere der Übertragung des anfänglichen Lichtsignals auf weiter entfernte Teile des Proteins, welche letztlich zur biologischen Aktivität führen. Diese Forschung identifiziert einen Met_{außen}/Trp_{innen}-Übergang als entscheidendes Element bei der Signalübermittlung an die α -Helix-Linkerregion. Schließlich liefern Strukturmodelle von OaPAC mit im aktiven Zentrum gebundenem ATP zusammen mit ergänzenden FTIR-Untersuchungen ein umfassendes Verständnis der ATP-Bindung und der allosterischen Kommunikation. Infolgedessen erweitert die in dieser Dissertation vorgestellte

Forschung nicht nur das grundlegende Verständnis der BLUF-Photorezeptorbiologie, sondern bietet auch einen Rahmen für zukünftige Studien zur Entschlüsselung vollständiger Signalübertragungswege in Multi-Domänen BLUF-Photorezeptoren und zur Entwicklung optogenetischer Werkzeuge.

Abstract

Photosensory receptors, essential molecular entities across all domains of life, enable organisms to detect and respond to light stimuli, underpinning their critical involvement in regulating biological processes such as phototropism, circadian rhythms, photomorphogenesis, and photosynthesis. Among the myriad types of photosensory receptors, blue light sensing proteins such as Blue Light Using Flavin (BLUF) photoreceptors distinguish themselves through their ability to utilize blue light for signalling. Characterized by the conserved structure of their sensor domain, BLUF photoreceptors are found in a wide array of organisms, from bacteria and algae to plants and certain fungi. Known for their capacity to bind flavin chromophores, typically flavin adenine dinucleotide (FAD), they undergo conformational changes upon blue photon absorption, leading to downstream signalling events, highlighting their pivotal role in the adaptive responses of various organisms to light. This dissertation provides a comprehensive exploration of the BLUF photoreceptors, particularly focusing on the Photoactivated Adenylate Cyclase protein from *Oscillatoria acuminata* (OaPAC), which comprises a BLUF sensor domain linked to an Adenylate Cyclase (AC) effector domain, catalysing the conversion of ATP into cAMP. This study aims to elucidate the photoactivation mechanism of OaPAC and the ensuing signal transduction pathway, employing an integrative approach that leverages time-resolved crystallography, small angle X-ray scattering, spectroscopy, and biochemical characterization techniques. Special emphasis is placed on the Tyr-Gln-Met triad in the BLUF domain, which plays a crucial role in the initial light-induced rearrangements. Additionally, significant attention is given to the less understood aspects of BLUF photoreceptors, particularly the transduction of the initial light signal to more distal parts of the protein, which ultimately leads to biological activity. This research identifies a Met_{out}/Trp_{in} transition as a crucial element in conveying the signal to the α -helix linker region. Finally, structural models of OaPAC with ATP bound in the active site, along with complementary FTIR investigations, provide a thorough understanding of ATP binding and allosteric communication. As a result, the research presented in this dissertation not only expands the fundamental understanding of BLUF photoreceptor biology, but also provides a framework for future studies aimed at deciphering complete signal transduction pathways in multi-domain BLUF photoreceptors and towards the development of optogenetic tools.

1. Introduction

1.1. Introduction to Photosensory Receptors

Photosensory receptors play critical roles in enabling organisms to perceive and respond to light, underpinning essential processes such as photosynthesis, vision, circadian rhythms, photoavoidance and phototropism (van der Horst and Hellingwerf, 2004). These photoreceptors are represented by seven main families, which include rhodopsins, xanthopsins, phytochromes, cryptochromes, ultraviolet-resistance locus 8 family proteins, Light, Oxygen, or Voltage (LOV) domain, and Blue Light Using FAD (BLUF) domain containing proteins (Masuda, 2013). They interact with light through chromophores, molecular structures capable of absorbing specific wavelengths, for which the absorbed wavelength can vary widely from ultraviolet to infrared. The initial interaction with light triggers ultrafast events, often in less than 1 ns, leading to a cascade of molecular transformations critical for the organism's survival and adaptation to its environment. These cascades of events span a broad time range, making photoreceptors an interesting target to study and understand functional protein dynamics. Indeed, light energy is converted into distinct protein structural alterations through diverse mechanisms to perform all sort of functions, of which many underlying structural dynamics are still poorly understood.

Every photoreceptor family has quite distinctive characteristics, although some share common functions or common early photoactivation mechanisms. For rhodopsins, xanthopsins and phytochromes, for instance, a *trans* to *cis* isomerization of the chromophore is observed upon photo absorption, while their response to light will lead to different signalling pathways (van der Horst and Hellingwerf, 2004).

Rhodopsins are a key type of light-sensitive receptors found across all forms of life, and the only family of transmembrane photoreceptors (Nagata and Inoue, 2021). Their functions are diverse and rhodopsins are usually divided into two main groups. Type I rhodopsins can be light ion-gated channels, or sense light for signal transduction as in phototaxis (Nagel *et al.*, 2003). Visual or type II rhodopsins are found in animals and are involved in the complex phenomenon of vision. Type II rhodopsins undergo a conformational change upon light absorption between 355 and 600 nm,

activating a G protein-coupled receptor pathway and initiating the visual transduction process (Palczewski, 2006; Nagata and Inoue, 2021). Both types have a similar structure with seven membrane-spanning helices and contain a retinal chromophore, capable of absorbing light over nearly the full visible light spectrum (Figure 1A) (Palczewski *et al.*, 2000; Borshchevskiy *et al.*, 2017). A new kind of rhodopsin has recently been found with a more complex structure and different functions, linking light detection directly to enzymatic function. These enzyme-rhodopsins include guanylyl and adenylyl cyclases, catalysing the formation of 3',5'-cyclic adenosine monophosphate (cAMP) and guanosine monophosphate (cGMP), essential signalling molecules affecting a wide range of cellular activities (Fischer *et al.*, 2024).

Phytochromes are photoreceptors that absorb red and far-red light via a bilin chromophore, and are primarily found in plants, bacteria, and fungi (Rockwell and Lagarias, 2010). They regulate various physiological processes, including development, reproduction and photosynthesis (Do *et al.*, 2024). Phytochromes are composed of a Per-Arnt-Sim (PAS) N-terminal domain and a chromophore binding domain, adopting a figure-of-eight knot like structure, to which the functional PHY domain is bound, necessary to achieve the active state after red-photon absorption (Figure 1B) (Essen *et al.*, 2008). Phytochromes switch between active and inactive forms depending on the ambient light (red light or far-red light), making them essential in light-dependent developmental processes as they possess the ability to differentiate between direct sunlight and shaded conditions (Davis *et al.*, 1999). Cyanobacteriochromes are distant homologs of phytochromes, covering the full range of the visible spectrum (Rockwell and Lagarias, 2010).

Ultraviolet-resistance locus 8 family proteins initiate alterations in gene expression regulation in response to ultraviolet-B light (280–315 nm) (Christie *et al.*, 2012a). UVR8 is the only photoreceptor family to respond to light without a co-factor as chromophore, instead using endogenous amino acids where tryptophan is one of the main candidates (Jenkins, 2009). UVR8 is postulated to form a symmetric homodimer of seven subunits containing β -sheets (Figure 1C), that dissociates into monomers following exposure to UV-B, enabling gene expression in response to DNA damage (Christie *et al.*, 2012a). Although its mechanism remains elusive, UVR8 is known to enhance plant development and ensure survival in sunlight.

Xanthopsins are blue light photoreceptors using a unique thiol ester linked *p*-coumaric acid as chromophore (Kort *et al.*, 1996). In the xanthopsins family, Photoactive Yellow Protein (PYP)

stands out as the most extensively researched member. PYP has evolved from the PAS superfamily, and hence also adopts a PAS domain, showing an α/β fold with 6 antiparallel β -sheets adjoined on both sides by helices and loops (Figure 1D) (Borgstahl *et al.*, 1995; Getzoff *et al.*, 2003). Xanthopsins can absorb a blue photon, with an absorption maximum at 446 nm for PYP, which induces a chain of reactions that can be involved in gene expression, biofilm formation, and motility after *trans* to *cis* isomerization of the chromophore (Pande *et al.*, 2016; Xing *et al.*, 2022). The three other main photoreceptor families, cryptochromes, LOV and BLUF photoreceptors all bind to a flavin chromophore, either flavin adenine dinucleotide (FAD) or flavin mononucleotide (FMN). Although they share the same chromophore and thereby all absorb in the blue light region, these three families have distinct photoactivation mechanisms (van der Horst and Hellingwerf, 2004; Zoltowski and Gardner, 2011).

For instance, in cryptochromes, blue light exposure induces FAD photoreduction via an electron transfer from a tryptophan triad (Fraikin and Belenikina, 2023). Cryptochromes have similar sequences to photolyase DNA repair enzymes and use the same FAD cofactor, although they lack the DNA repair ability (Brudler *et al.*, 2003). The structure of cryptochromes is arranged into two domains, an α/β domain and a FAD binding helical domain containing only α -helices, linked by an extended loop (Figure 1E) (Czarna *et al.*, 2013). Cryptochromes can be found in plants and animals. In plants, they contribute to growth, development, and circadian rhythm regulation. In animals, cryptochromes are involved in circadian rhythms and possibly in sensing magnetic fields for navigation, although the latter is controversial (Kattinig *et al.*, 2016; Kyriacou and Rosato, 2022). Recently, one type of cryptochrome photoreceptor called DASH photoreceptors was discovered to also affect many metabolic pathways in algae, including chlorophyll and carotenoid biosynthesis, glycolysis, dark fermentation and the oxidative pentose phosphate pathway (Rredhi *et al.*, 2024).

LOV (Light, Oxygen, or Voltage) photoreceptors, also called phototropins, are another class of blue light photoreceptors found across all kingdoms of life. They use FMN as chromophore, show a PAS domain-like structure for the sensor domain, like phytochromes and PYP, and are linked to effector domains via a long coiled-coil α -helix linker (Figure 1F) (Harper *et al.*, 2003; Diensthuber *et al.*, 2013). Upon light absorption, LOV domains undergo major conformational changes that affect their interaction with the linked effector domains via the coiled-coil α -helix, modulating various physiological responses (Harper *et al.*, 2004). LOV have been found to bind many

enzymatic domains, such as diguanylate cyclases, which control the process of differentiation, movement, or growth of cells through a switch-like mechanism (Vide *et al.*, 2023). The enzyme has a two-step activation method where its function is blocked in the dark because of the confined structure which traps the enzymatic domain, but is activated by light through the extension of the coiled-coil linker. Studies on LOV domains have also explored the early photoactivation process, and discovered a unique mechanism in which the FMN chromophore forms a reversible covalent bond with a highly conserved neighbouring cysteine residue, through a process that involves triplet states (Crosson and Moffat, 2002; Möglich and Moffat, 2007; Konold *et al.*, 2016; Iuliano *et al.*, 2018).

BLUF photoreceptors share some similarities with LOV photoreceptors, but the photoactivation and signal transductions mechanisms are radically different. The first photoactivation event of BLUF photoreceptors involves a proton and electron transfer from a nearby tyrosine to the flavin chromophore, inducing a cascade of rather small conformational changes, which subsequently permits transmission of the lit-state signal to linked effector domains (Barends *et al.*, 2009; Masuda, 2013; Ohki *et al.*, 2016). BLUF photoreceptors are found to bind various effector domains, involved in photoavoidance, gene expression and biofilm formation. The sensor domain in BLUF photoreceptors adopts an α/β structure in a ferredoxin $\beta\alpha\beta\beta\alpha\beta\beta$ topology, where the flavin chromophore sits on top of the β -sheet and is flanked by the two α -helices (Figure 1G) (Jung *et al.*, 2006; Hendriks *et al.*, 2009). BLUF photoreceptors, which are in the focus of this study, will be reviewed in more detail in the following section.

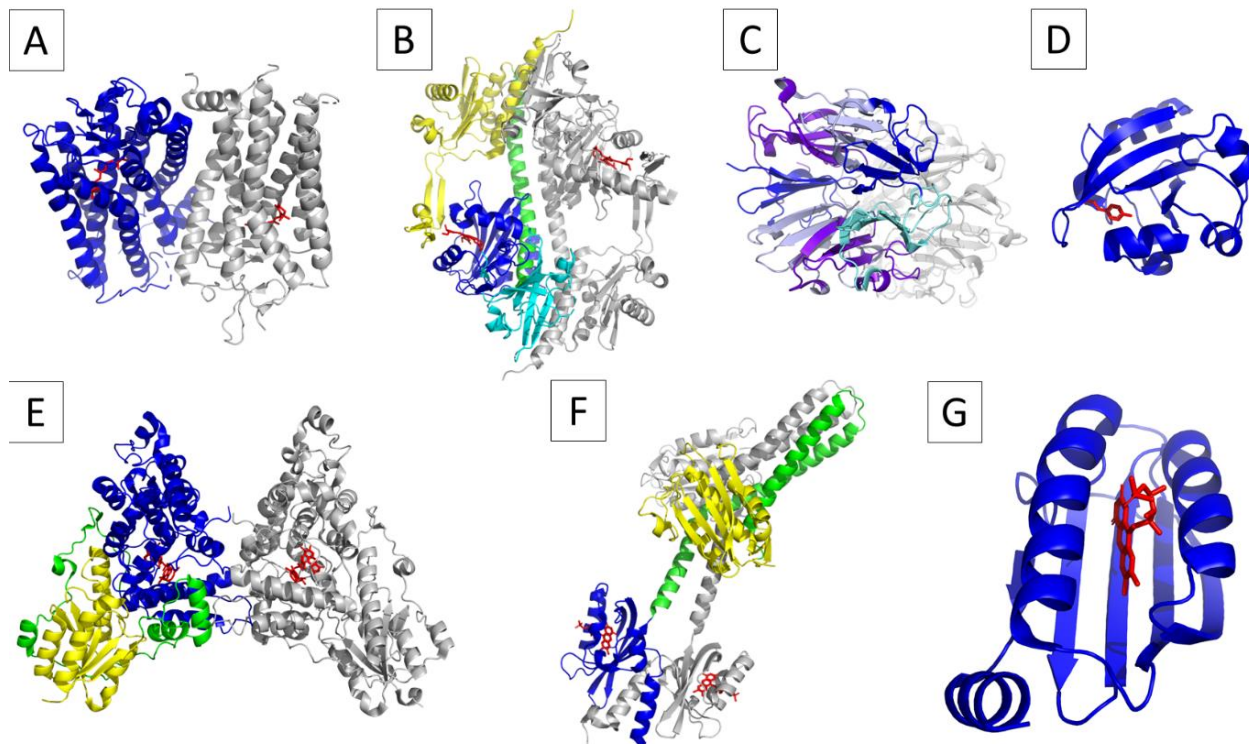


Figure 1: Diversity of photosensory receptors represented by seven photoreceptors families.

(A) Crystal structure of a bovine rhodopsin, PDB 1F88 (Palczewski et al., 2000). The chromophore binding domain (blue) comprises seven α -helices embedded in the cellular membrane. The retinal chromophore is highlighted in red. The second protomer is represented in grey. (B) Crystal structure of the sensory module of the cyanobacterial phytochrome Cph1, PDB 2VEA (Essen et al., 2008). Each protomer contains a PAS domain (cyan), a chromophore binding domain adopting a figure-of-eight knot like structure (blue). The phycobilin chromophore is highlighted in red. The PHY domain (yellow) is linked to the chromophore binding domain via an extended α -helix (green). The second protomer is represented in grey. (C) Crystal structure of UVR8, PDB 4D9S (Christie et al., 2012a). The structure is a symmetric homodimer with one protomer in blue shades, purple or cyan and the other in grey. Each protomer contains seven β -stranded subunits (blue shades). UVR8 is the only photoreceptor which does not use a chromophore for light sensing. (D) Crystal structure of a bacterial PYP, PDB 1NWZ (Getzoff et al., 2003). The sensor domain is a PAS domain (blue) covalently bound to a unique thiol ester linked p-coumaric acid as chromophore (red). (E) Crystal structures of the *Drosophila* cryptochrome, PDB 4JZY (Czarna et al., 2013). The structure has two domains per protomer, linked by an extended linker (green) composed of loops and α -helices. The N-terminal domain (yellow) shows an α/β structure, whereas the C-terminal domain (blue) only contains α -helices and binds a FAD chromophore (red). The second protomer is represented in grey. (F) Crystal structure of a sensor histidine kinase containing a LOV sensor domain, PDB 4GCZ (Diensthuber et al., 2013). The LOV domain (blue) has a PAS domain-like structure binding FMN as chromophore (red). The sensor domain is linked to the histidine kinase effector domain (yellow) via a long helical structure (green). The dimer interface is formed by the linker establishing a long coiled-coil with the second protomer. The second protomer is shown in grey. (G) Crystal structure of the BLUF sensor domain of AppA BLUF photoreceptor; PDV 2YIG (Jung et al., 2006). The structure has a $\beta\alpha\beta\beta\alpha\beta$ -fold topology for the sensor domain (blue), with the flavin chromophore (red) lying on the β -sheet bed, flanked by the two α -helices.

Figures prepared by the PyMOL Molecular Graphics System, Version 2.5.4 Schrödinger, LLC (Schrödinger and DeLano, 2020).

Recent investigations into their structure, photochemistry and signal transduction have provided unprecedented understanding of the mechanisms of operation within each photoreceptor family. Typically, the photoexcitation of the chromophore induces alterations through isomerization, changes in redox or protonation states, or hydrogen bond networks, which is followed by conformational changes in the protein. These changes can lead to product formation, opening of ion channels or interaction with binding partners (van der Horst and Hellingwerf, 2004; Hendriks *et al.*, 2009; Masuda, 2013; Conrad *et al.*, 2014; Nagata and Inoue, 2021). The diversity among photoreceptors and within each family has increased the interest in these captivating proteins. Specifically, their contribution in optogenetics has been of great interest. Optogenetics is a technique that involves using light to control cells within living tissue, typically neurons, that have been genetically modified to express light-sensitive ion channels or other light-responsive proteins. In the last decades, photosensory proteins have revolutionized optogenetics as reversible, non-invasive tools with precise spatiotemporal control of cellular activities. These photoreceptors have expanded optogenetics beyond neuroscience, unlocking new applications. The successful engineering of novel photoreceptors continues to grow, promising exciting future advances. This study aimed to contribute additional information to the photoreceptor and optogenetics fields, by elucidating more of the unknowns behind the activation mechanism of BLUF photoreceptors.

1.2. BLUF Photoreceptors: Overview and Structures

The first protein containing a BLUF domain was identified in 1995 by Gomelsky and Kaplan with the discovery of AppA (activation of photopigment and *puc* expression) in *Rhodobacter sphaeroides* (Gomelsky and Kaplan, 1995), although the terminology BLUF was not introduced at that time. Following their first publication, extensive work to unravel the role of AppA was performed, leading to the discovery of a novel FAD binding domain family (Gomelsky and Kaplan, 1997, 1998). It was only in 2002 that the nomenclature BLUF was introduced (Gomelsky and Klug, 2002). The same year, two other groups worked on the BLUF photoreceptor AppA analysing the mechanisms of control of photosynthesis gene expression in the same purple bacteria *R. sphaeroides* and investigating its binding partner, PpsR repressor (Braatsch *et al.*, 2002; Masuda

and Bauer, 2002). Following the discovery of AppA, sequence homology with the BLUF sensor domain enabled the identification of many more BLUF photoreceptors, including PAC, BlrP1, YcgF, BlrB, BlsA, PapB, PixD/Slr1694 and TePixD/Tll0078 (Masuda, 2013).

BLUF sensors domains are small water soluble domains consisting of approximately 100 amino acids (11 kDa) and harbour a flavin chromophore, which serves as the primary light-absorbing moiety (Figure 2) (Gomelsky and Klug, 2002). BLUF photoreceptors are a diverse group primarily found in prokaryotes, but also in single-cellular eukaryotes (Kennis and Mathes, 2013). They are predominantly observed in two branches of bacteria: cyanobacteria and proteo- or purple bacteria (Hendriks *et al.*, 2009).

Like LOV domains, BLUF sensor domains are organized in an α/β fold, but the arrangement of β -sheets and α -helices differs. BLUF domains present 5 antiparallel β -sheets and 2 α -helices forming a ferredoxin like typology (Figure 2) (Hendriks *et al.*, 2009; Park and Tame, 2017). The core of the flavin cofactor is firmly secured between these two helices within an hydrophobic pocket formed by residues exhibiting high conservation across all identified BLUF domains (Kennis and Mathes, 2013). Side chains of neighbouring residues in the chromophore binding pocket contact the riboflavin. The adenosine and the phosphates are less tightly bound and are exposed to the solvent (Jung *et al.*, 2005). BLUF photoreceptors were proven to bind FAD non-covalently *in vivo*, although FMN was also found in heterologous expression in *Escherichia coli* (Hendriks *et al.*, 2009). Of note, several studies showed that the adenosine diphosphate (ADP) moiety of the FAD was not necessary for the photoactivation of BLUF photoreceptors (Ito *et al.*, 2005; Masuda *et al.*, 2005a; Schroeder *et al.*, 2008).

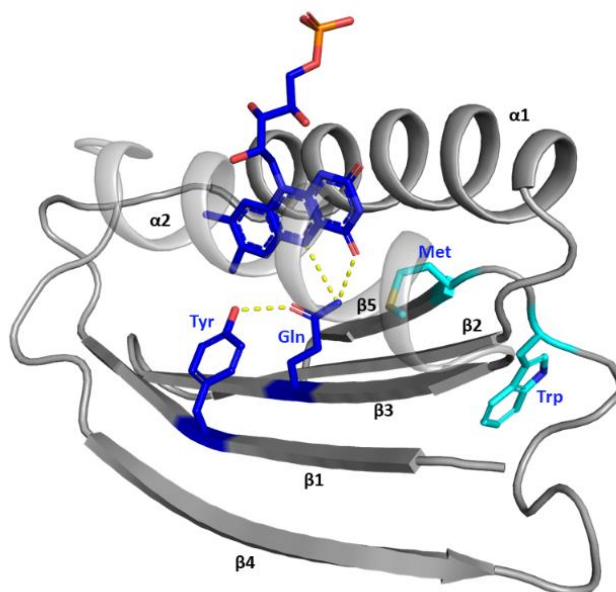


Figure 2: Structure of the BLUF sensor domain and insight into photoactivation.

BLUF domain shows a $\beta\alpha\beta\beta\alpha\beta$ topology with the flavin chromophore, here an FMN (blue), sitting on top of the five β -sheets between both α -helices. The amino acids Tyr and Gln involved in the first photoactivation steps are highlighted in blue. Trp is assigned as solvent exposed whereas Met is buried in the chromophore pocket in the dark state (cyan). Hydrogen bonds changing due to blue photon absorption are highlighted in yellow.

Figure prepared by the PyMOL Molecular Graphics System, Version 2.5.4 Schrödinger, LLC (Schrödinger and DeLano, 2020).

BLUF photoreceptors can be divided into 2 groups: multi-domain proteins where the BLUF domain is linked to an effector domain, and short BLUF proteins constituted of a few tens extra amino acids in addition to the BLUF domain (Hendriks *et al.*, 2009). The latter mainly possess short helical extensions, and usually transmit the light signalling state via interaction with binding partners (Kennis and Mathes, 2013). Examples of short BLUF proteins are BlrB (Jung *et al.*, 2005), BlsA (Chitrakar *et al.*, 2020), PixD/Slr1694 (Yuan *et al.*, 2006) and TePixD/Tll0078 (Kita *et al.*, 2005). In multi-domain BLUF photoreceptors, photon absorption produces a cascade of rearrangements to transmit the lit-state signal to an effector domain in order to activate it. The latter can be an adenylate cyclase, as in photoactivated adenylate cyclases (PAC) (Iseki *et al.*, 2002), an cyclic diguanylate-specific phosphodiesterase (EAL domain) as in BlrP1 (Barends *et al.*, 2009), and domains involved in the regulation of photosynthesis gene expression, as in AppA (Gomelsky and Kaplan, 1997).

BLUF photochemistry has been studied for a long time, and the understanding of the overall mechanism seems to have come to a consensus, although some details remain controversial. Especially, rearrangement of the hydrogen bond network in the chromophore binding pocket after photon absorption is still under debate. BLUF domains sense blue light through an oxidized flavin, and unlike other photoreceptors, undergo a photoactivation mechanism that only involves minor structural changes in the region immediately surrounding the chromophore (Masuda, 2013). The chromophore binding pocket contains three important conserved amino acids, namely a tyrosine, a glutamine and a methionine (Figure 2). Hasegawa and co-workers suggested in their study of PixD/Slr1694, that a proton transfer to the flavin is involved in the photocycle (Hasegawa *et al.*, 2005). Following this study, an electron transfer from the conserved tyrosine to the flavin and a proton transfer first from tyrosine to glutamine and then from glutamine to flavin was proposed by Gauden *et al.* (Gauden *et al.*, 2006b). They studied PixD with femtosecond transient absorption spectroscopy and observed the disruption of hydrogen bonds between tyrosine and glutamine and a protonation at flavin N5. The photoexcitation of the flavin induces this proton-coupled electron transfer (PCET) to the flavin, forming a neutral flavin semiquinone radical FADH[•] and a tyrosyl radical Tyr[•] (Gauden *et al.*, 2007; Bonetti *et al.*, 2008; Bonetti *et al.*, 2009; Hendriks *et al.*, 2009; Udvarhelyi and Domratcheva, 2011; Goings *et al.*, 2020; Collado *et al.*, 2022).

In the first crystal structure of AppA BLUF domain from Anderson *et al.* the conserved methionine (Met102 for AppA) was assigned in a Met_{out} or solvent exposed conformation, while the semi-conserved tryptophan (Trp104 for AppA) was found in the chromophore pocket in a Trp_{in} conformation (Anderson *et al.*, 2005). This assignment raised questions about the potential involvement of the tryptophan in electron transfer to the flavin (Gauden *et al.*, 2007). However, the involvement of the tryptophan in the PCET was quickly disproved by several studies (Gauden *et al.*, 2007; Bonetti *et al.*, 2009; Goyal and Hammes-Schiffer, 2017). For instance, time-resolved (TR) fluorescence and absorbance spectroscopy analysis on AppA by Gauden *et al.* and free-energy simulations on PixD by Goyal and Hammes-Schiffer showed that the tryptophan could only be involved in a non-productive electron transfer pathway, while the tyrosine was the only amino acid that could lead to a productive signalling state formation. With site-directed mutagenesis, Bonetti *et al.* could also show that Trp91Phe and Ser28Ala mutants in PixD/Slr1694 retained the formation of the signalling state, while a Tyr8Trp mutant did not, suggesting that Tyr was the only essential amino acid in the electron transfer pathway among the three tested candidates (Bonetti *et al.*, 2009).

The proposed role of tryptophan in the PCET was finally completely refuted when the tryptophan was found to be incorrectly assigned in the dark structure of AppA by further crystallographic studies (Jung *et al.*, 2005; Kita *et al.*, 2005; Jung *et al.*, 2006; Winkler *et al.*, 2013), by structure-based simulations (Collette *et al.*, 2014) and by fluorescence spectroscopy (Karadi *et al.*, 2020), which indicated Met102 should be in a Met_{in} conformation and Trp104 solvent exposed (Trp_{out}).

Therefore, after twenty years of research on the BLUF photocycle, most studies are converging toward an electron transfer from tyrosine to flavin and a double proton transfer from tyrosine to glutamine and glutamine to flavin after several tens of ps. Yet, questions remain as to whether the activation process is based on a PCET or rather a concerted proton electron transfer (CPET), as proposed recently by Collado *et al.* for OaPAC (Collado *et al.*, 2022; Tolentino Collado *et al.*, 2024). They suggested that the electron and proton donation from the tyrosine to the flavin happen simultaneously as a forward CPET to form the neutral semiquinone flavin FADH[•] / Tyr[•] radical pair, followed by a reversed PCET to reach the signalling state of the flavin. This hypothesis was also proposed by Zhou *et al.* with their study of OaPAC using transient absorption spectroscopy, where they proposed a CPET for the forward reaction, and an ultrafast PCET or CPET for the reverse proton and electron transfer, both on the ps time scale, forming the signalling or lit state (Zhou *et al.*, 2022). According to these studies, OaPAC seems to take a different path than PixD photoreceptors, for which the forward reaction clearly shows an intermediate FMN^{•-} state, showing that the electron and double proton transfer in PixD is sequential (Gauden *et al.*, 2006b; Bonetti *et al.*, 2008; Goings and Hammes-Schiffer, 2019).

The forward PCET/CPET and reverse PCET reaction in BLUF photoreceptors lead to a different hydrogen bond network in the chromophore pocket and the formation of an uncommon glutamine tautomer, which forms the signalling state in BLUF photoreceptors, and is remarkably stable for a long time (from several s to min) (Lukacs *et al.*, 2014). Yet, the role and changes in the glutamine upon photoactivation are also under debate. In the lit state, BLUF photoreceptors show a characteristic and unique red shift of their absorption maximum around 450 nm of approximately 10 nm (Hendriks *et al.*, 2009). This absorption shift is known to result from the change in the hydrogen bond network between the highly conserved tyrosine and glutamine and the flavin chromophore (Figure 2) (Unno *et al.*, 2005; Stelling *et al.*, 2007; Domratcheva *et al.*, 2008). Particularly, the downshift of the C4=O and C=N stretches of the flavin, accompanied with changes in glutamine C=N and tyrosine C-OH stretches were observed with FTIR spectroscopy, indicating

a stronger hydrogen bonding interaction with flavin C4=O and N5 in the light state (Hasegawa *et al.*, 2005; Bonetti *et al.*, 2008; Iwata *et al.*, 2011). Following these observations, several studies converged on the presence of a keto–enol tautomerisation of the glutamine resulting in an imidic acid, establishing hydrogen bonds with flavin C4=O and N5 (Domratcheva *et al.*, 2008; Sadeghian *et al.*, 2008; Iwata *et al.*, 2011; Khrenova *et al.*, 2013; Udvarhelyi and Domratcheva, 2013; Collette *et al.*, 2014; Domratcheva *et al.*, 2016; Goings *et al.*, 2020; Hontani *et al.*, 2023). For instance, Collette 2014 *et al.* used structure-based simulation of electrochromic shifts of the flavin chromophore combined with site-directed mutagenesis to show that the light-activated state of BLUF photoreceptors presents a keto–enol tautomerization of the glutamine.

Suggestions of a rotation of the glutamine started in 2005 after the release of the AppA crystal structure by Anderson *et al.*, where they hypothesized that a rotation of the side chain would change the hydrogen bond with the flavin C4=O in the light state, but this assumption was made on a wrongly assigned methionine and tryptophan as well as glutamine side chain positions in the dark (Met_{out}/Trp_{in} instead of Met_{in}/Trp_{out}) (Anderson *et al.*, 2005). Following this suggestion, femtosecond transient absorption spectroscopy (Gauden *et al.*, 2006b), ultrafast spectroscopy (Kennis and Groot, 2007), fluorescence decay on H/D exchange (Bonetti *et al.*, 2008), a spectroscopy and quantum chemical calculations approach combined with mutagenesis (Unno *et al.*, 2006), and NMR studies (Grinstead *et al.*, 2006) on BLUF photoreceptors all confirmed the plausibility of the glutamine rotation.

Ultimately, questions were raised as to whether the glutamine tautomerization could be accompanied by the aforementioned 180° rotation of the glutamine side chain. Domratcheva and co-workers were the first to propose this idea in 2008, after discovering that molecular models developed from crystal structures and quantum mechanical simulations suggested a possible pathway of tautomerization of the glutamine associated with its rotation, allowing a radical pair recombination (reverse PCET) and ultimately favourable interactions with the isoalloxazine ring (Domratcheva *et al.*, 2008). These findings were later supported by computational calculations from Khrenova *et al.*, where a minimum-energy pathway displayed the rotation of the glutamine side chain followed by the formation of a Z-E imidic acid tautomer, and finally reverse PCET allowing the formation of a Z-Z imidic acid tautomer (Khrenova *et al.*, 2013). Hybrid quantum mechanical/molecular mechanical (QM/MM) molecular dynamics simulations also supported the formation of a rotated glutamine side chain in an imidic acid tautomer form (Goings *et al.*, 2020).

Spectroscopic experiments from Hontani *et al.* further supported this pathway (Hontani *et al.*, 2023). With a combination of femtosecond stimulated Raman spectroscopy, computational chemistry and site-selective isotope labelling FTIR spectroscopy, they came to the same conclusion that formation of an imidic acid tautomer is accompanied by rotation of the glutamine.

Consequently, several studies seemed to converge toward a glutamine rotation along its C γ -C δ axis, and Z-Z imidic acid tautomerisation of the glutamine side chain (Salvadori *et al.*, 2024). Combining these findings with the electron and proton transfer to the flavin, a potential pathway would be a forward PCET/CPET, followed by glutamine rotation and concluded by the reverse PCET for radical pair recombination to retrieve the original oxidation and protonation states of the Tyr-Gln-flavin triad and to form the imidic acid tautomer. This process would lock the glutamine in an unusual rotated imidic acid tautomer form and create a new hydrogen-bonding environment, representing the long lit/signalling state of BLUF photoreceptors. It is a unique feature of BLUF photoreceptors that the chromophore itself is not transformed during the photoactivation, but rather only the surrounding environment.

Although several attempts were made to observe these changes with structural characterization methods such as X-ray crystallography, the rotation (and even less the tautomerization) of the glutamine has not yet been observed. Jung *et al.* crystallized AppA in a dark and in an intermediate light-activated state and compared the data, but could not confirm the glutamine rotation due to the limitations of the resolution achieved (2.95 Å) (Jung *et al.*, 2006). Nonetheless, a clear change in the conformation of the neighbouring methionine was observed, and this change would necessitate a rotation of the glutamine to restore favourable interactions between the two residues. They therefore stated that the data support the hypothesis of a glutamine side chain rotation after photoexcitation of AppA. Ohki *et al.* tested the same approach with OaPAC crystals, and were able to observe a 40° rotation of the side chain along the C γ -C δ axis in the light-activated state (Ohki *et al.*, 2017). They suggested that only a small rotation of the side chain, potentially accompanied with its tautomerisation, led to the hydrogen bond changes in the chromophore pocket and represented the signalling state of OaPAC, instead of the suggested 180° rotation. The lack of structural evidence for the glutamine rotation during the early events after photoexcitation in BLUF photoreceptors explains why, 20 years after the first structural and spectroscopy studies, the pathway leading to the signalling state is still under debate in the photoreceptor community.

During the first decade of BLUF photoreceptors research, studies focused on the BLUF domain photocycle and early steps of signal transduction, and only short BLUF proteins or truncated versions of multi-domain BLUF photoreceptors containing only the BLUF sensor domain were studied. Only in 2009 was the first structure of the full length multi-domain BLUF photoreceptor BlrP1 solved (Figure 3A) (Barends *et al.*, 2009). BlrP1 is a BLUF photoreceptor with a linked C-terminal phosphodiesterase EAL domain, and is known to possess a cyclic dimeric guanine monophosphate (c-di-GMP) phosphodiesterase activity (Hasegawa *et al.*, 2006; Barends *et al.*, 2009). Following BlrP1, the full length structure of one of the most studied BLUF photoreceptors AppA was released in 2013, in complex with its binding partner the transcriptional repressor PpsR (Figure 3B) (Winkler *et al.*, 2013). AppA regulates photosynthesis gene expression and has a dual control, as it reacts to light with its BLUF sensor domain and to redox signals via a sensor domain containing heme instead of cobalamin (SCHIC) domain, sensing oxygen (Gomelsky and Klug, 2002; Gauden *et al.*, 2005; Grinstead *et al.*, 2006; Gil *et al.*, 2016).

PAC was the last of the so far known multi-domain BLUF photoreceptors to see its structure solved (Figure 3C) (Ohki *et al.*, 2016). The BLUF domain in PAC is linked to an adenylate cyclase domain, catalysing the conversion of adenosine triphosphate (ATP) into cAMP, another essential second messenger, which induces a photophobic response when PAC is exposed to blue light (Iseki *et al.*, 2002). The crystal structure of PAC exhibits a different organization in the linker region between sensor and effector domain than BlrP1 or AppA (Ohki *et al.*, 2016; Lindner *et al.*, 2017). The BLUF photoreceptor PAC, which is of interest in this study, will be reviewed in more detail in the next section.

Beside multi-domain proteins, several short BLUF photoreceptors have also been extensively studied, including PixD (Slr1694 and Tll0078) (Figure 3D) (Kita *et al.*, 2005; Yuan *et al.*, 2006; Gil *et al.*, 2017; Hall *et al.*, 2019), BlrB and BlsA (Figure 3E-F) (Jung *et al.*, 2005; Zirak *et al.*, 2006; Golic *et al.*, 2019; Chitrakar *et al.*, 2020; Yang *et al.*, 2023).

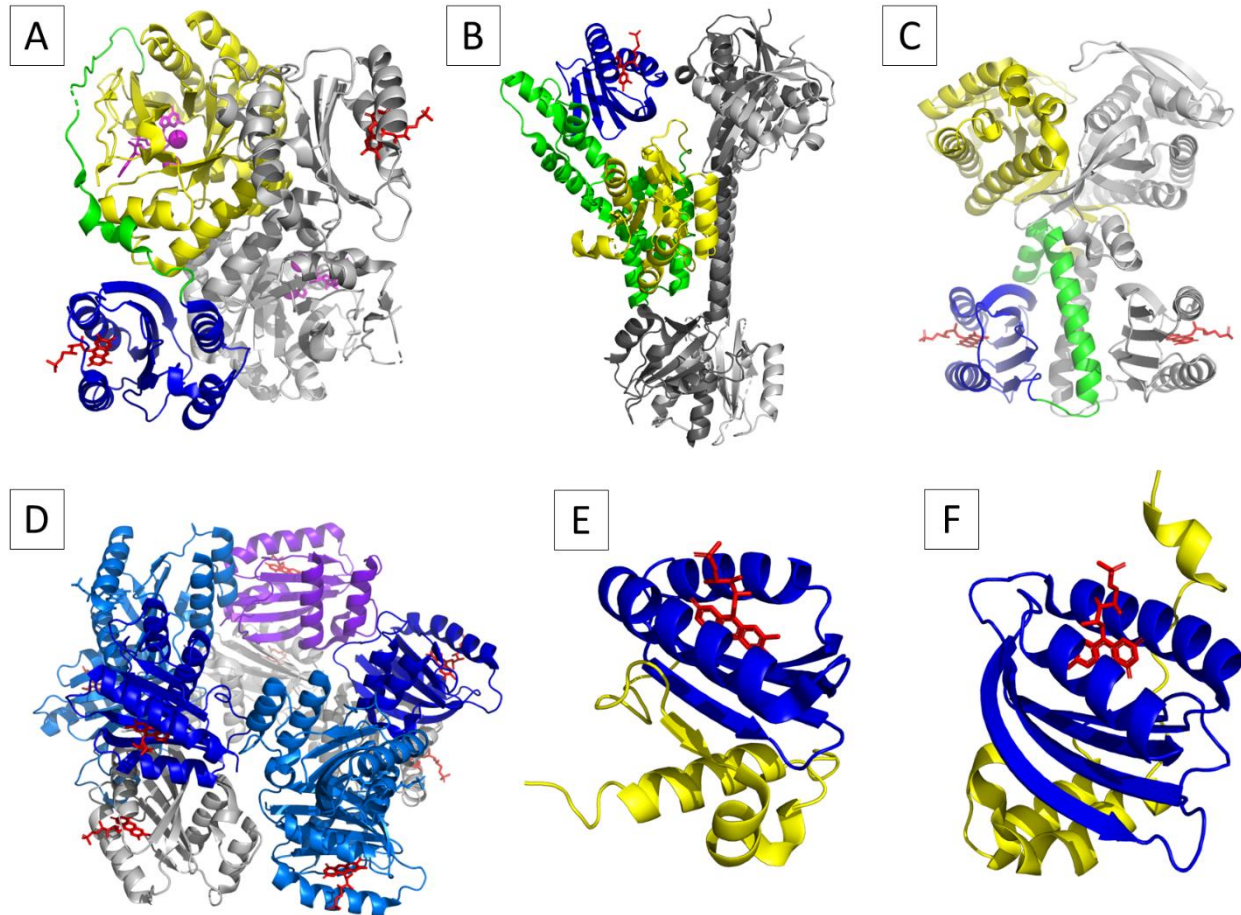


Figure 3: Diversity of BLUF photoreceptors represented by multi-domain and short proteins.

(A) Crystal structure of BlrP1, PDB 3GG1 (Barends et al., 2009). The BLUF sensor domain (blue) is linked to the effector domain (yellow) via a 50 Å long linker (green). The effector domain binds *c*-di-GMP (magenta) and possesses a *c*-di-GMP phosphodiesterase activity. The second protomer is represented in grey. (B) Crystal structure of AppA in complex with its binding partner PpsR, PDB 4HH1 and 4HH3 (Winkler et al., 2013). The BLUF sensor domain of AppA (blue) is linked to the SCHIC domain (yellow) via a four-helix bundle followed by a linker region (green). AppA binds to the PpsR transcriptional repressor dimer (grey) in the dark. (C) Crystal structure of OaPAC, PDB 4YUS (Ohki et al., 2016). The BLUF sensor domain (blue) is linked to the effector domain (yellow) via a linker composed of two α -helices (green). The effector domain is an adenylate cyclase which catalyses the conversion of ATP into cAMP. (D) Crystal structure of PixD/Slr1694, PDB 2HFN (Yuan et al., 2006). PixD/Slr1694 contains five short BLUF proteins per protomer revealing a pentamer ring structure (shades of blue). It forms a large complex involving a second pentameric ring (grey) facing the first pentamer. (E) Crystal structure of BlrB, PDB 2BYC (Jung et al., 2005). BlrB is a short BLUF protein containing a BLUF sensor domain (blue) extended by a short helical structure at the C-terminus (yellow). (F) Crystal structure of BlsA, PDB 6W6Z (Chitrakar et al., 2020). BlsA is a short BLUF protein, very similar to BlrB, with a slightly different and longer C-terminal extension (yellow) to the BLUF domain (blue).

All the BLUF photoreceptors bind a flavin chromophore represented in red.

Figures prepared by the PyMOL Molecular Graphics System, Version 2.5.4 Schrödinger, LLC (Schrödinger and DeLano, 2020).

In summary, BLUF photoreceptors exhibit a diverse range of effector domains and binding partners, as well as differences in their photoactivation mechanisms. The latter is particularly astonishing given the high conservation within BLUF sensor domain structure and the involved amino acids in the chromophore binding pocket (Tyr-Gln-Met).

Although some structural characterization of full length BLUF photoreceptors have been performed, many studies have focused on the early photoactivation events of BLUF photoreceptors, leaving out the more distant conformational changes essential for signal transduction and activation of linked effector domains or binding partners. Hendrik *et al.* stated in 2009 “The mechanism by which the initial local structural changes in the vicinity of FAD are transferred to the molecular surface is poorly understood.” (Hendriks *et al.*, 2009), and this statement is still correct nowadays.

1.3. Signalling State and Signal Transduction in BLUF Photoreceptors

Novel research studies should focus on full-length multi-domain BLUF photoreceptors, as this is essential to understand signal transduction, especially how structural alterations after light activation propagate to effector domains and trigger downstream signalling events. Structural information in truncated mutants could be incorrect or lacking crucial knowledge, especially for the C-terminal region of BLUF domains, which might adopt a different conformation when the effector domain is present. Besides, comparison of BLUF photoreceptors with and without binding partners, if any, should also be a standard.

Hasegawa *et al.* studied both the BLUF domain alone of YcgF and full length YcgF with its EAL effector domain (Hasegawa *et al.*, 2006). They realised that although UV-Visible (UV-Vis) absorbance showed similar red-shifted spectra and relaxation kinetics, most of the FTIR bands representing changes in the protein during signal transmission were suppressed in the truncated protein, including structural changes that happen in the BLUF domain. This suggests that red shift in the absorbance spectrum is not a sufficient indication to confirm photosignalling, and that

changes induced by photon absorption in the chromophore pocket are decoupled from the signalling state formation. It also confirms that studies on lone BLUF domains of multi-domain BLUF photoreceptors are not representative of a fully active protein and of the native changes during signal transmission.

Studies have tried to characterize the structural changes associated with signal transduction. Jung *et al.* were the first to show the importance of the highly conserved methionine in signal transmission from the chromophore binding pocket to the protein backbone (Jung *et al.*, 2006). The rotation of the glutamine during the early photoactivation events generates an unfavourable interaction with the methionine at its initial position, necessitating the movement of the methionine away from the chromophore pocket to restore favourable geometry. Masuda *et al.* also observed that the Met93Ala mutant in PixD was not active, although the red-shifted absorption spectrum was observed upon photoexcitation (Masuda *et al.*, 2008). They showed that conformational rearrangements during signal transmission corresponding to changes in the FTIR amide-II region were missing in the mutant, demonstrating the importance of the methionine in transmitting the light-induced signal. Similarly, Yuan *et al.* observed that a mutation of Met93 in PixD did not eliminate the red-shift, but rendered the protein incapable of interacting with its binding partner PixE (Yuan *et al.*, 2011).

In addition to the importance of the methionine in signal transduction, the role of the semi-conserved tryptophan has also been debated. Masuda *et al.* revealed the absence of key conformational changes when tryptophan was mutated into an alanine in AppA, based on changes in the FTIR amide-I region (Masuda *et al.*, 2005c). Brust *et al.* also suggested the tryptophan to be essential in signal transduction, based on FTIR data on a Trp104Ala mutant of AppA showing clear differences compared to the wild type, including a drastic acceleration of the relaxation kinetics (Brust *et al.*, 2013). A potential switch of the tryptophan residue from a solvent exposed or “out” conformation to an “in” conformation buried in the chromophore binding pocket during signal transmission was speculated early on, but has never been shown by crystallographic studies (Jung *et al.*, 2006; Sadeghian *et al.*, 2008; Barends *et al.*, 2009). More recently, with fluorescence anisotropy decay and lifetime measurements, a dynamic behaviour of the semi-conserved tryptophan upon photon absorption was shown, where the prevalent population of tryptophan conformation changes from “out” to “in” conformation (Karadi *et al.*, 2020). This switch in the tryptophan conformation, replacing the methionine near the flavin chromophore, could be the

pathway of signal transmission, with induced changes in the protein backbone due to the displacement of residues on the β -sheet 5 in the BLUF sensor domain (Figure 4B) (Sadeghian *et al.*, 2008; Lukacs *et al.*, 2022). Changes in β -sheet structure after light activation were indeed shown by FTIR studies, and disappeared in the inactive Trp103Ala mutant in AppA, confirming that Trp103 is involved in communicating the signal through β -sheet alteration (Masuda *et al.*, 2005c). Jung *et al.* hypothesized that changes from a kinked to a straight β -strand in β -sheet 5 was the potential pathway from dark to lit state (Jung *et al.*, 2006). Additionally, mutations on the β -sheet 5 also demonstrated an altered signalling mechanism (Stierl *et al.*, 2014). Some other studies contradict this hypothesis, as they did not observe any relevant change in the tryptophan position during signal transmission (Toh *et al.*, 2008; Dragnea *et al.*, 2010; Unno *et al.*, 2010). Nevertheless, all these studies were performed on truncated version of AppA containing the BLUF domain only and may therefore be misleading.

Although changes in BLUF photoreceptors were thought to be subtle, studies of the multi-domain photoreceptors YcgF and BlrP1 in solution with nuclear magnetic resonance (NMR) demonstrated large structural rearrangements (Schroeder *et al.*, 2008; Wu and Gardner, 2009), suggesting that a tryptophan conformation switch combined with a drastic restructuring of β -sheet 5 is plausible. Schroeder *et al.* found the α -helix 3 linker to be affected during signal transmission, and Wu *et al.* observed changes in the β -sheet 5 and preceding loop, as well as the loop between α -helices 3 and 4, indicating a pathway for signal transmission from the β -sheet 5 to the α -helix 3 linker and beyond (Figure 4B).

The time scale of signal transmission covers a broad range, from ps to s or even min depending on the protein. The changes localized around the chromophore occur on the ps to ns time scale, including forward PCET/CPET, hydrogen bond rearrangements with glutamine tautomerization and potential rotation and reverse PCET (Brust *et al.*, 2013; Gil *et al.*, 2016). Structural rearrangements related to signal transduction following photoexcitation start on the μ s time scale (Majerus *et al.*, 2007; Brust *et al.*, 2013; Lukacs *et al.*, 2022). Interestingly, relaxation kinetics are really diverse in BLUF photoreceptors, with a half-life of less than 20 s for PixD and PAC being the fastest, 9 min for BlsA and up to 30 min for AppA (Lukacs *et al.*, 2014; Ohki *et al.*, 2016). Questions remain on the mechanism by which BLUF photoreceptors stay in a signalling state for such a long time, although they reach the lit state remarkably fast.

Several studies have also revealed an allosteric communication in the signal transmission pathway of multi-domain BLUF photoreceptors, as hypothesized by Barends *et al.* (Barends *et al.*, 2009). Different time scales were observed during relaxation with transient vibrational spectroscopy, showing that the involved residues around the chromophore were returning to their dark state position more slowly than more distant residues (Brust *et al.*, 2013). Similarly, ultrafast time-resolved infrared spectroscopy measurements demonstrated a multi-exponential relaxation pathway (Lukacs *et al.*, 2022). Notably, activation and relaxation kinetics were found to vary widely among BLUF proteins, demonstrating again the diversity within the BLUF family, although sharing a conserved BLUF sensor domain structure (Lukacs *et al.*, 2022; Tokonami *et al.*, 2022).

1.4. Photoactivated Adenylate Cyclase: A Case Study

PAC or photoactivated adenylate cyclase is a prominent member of the BLUF photoreceptor family, found in various bacterial species or unicellular eukaryotes, including *Euglena gracilis*, *Beggiatoa sp.* and *Oscillatoria acuminata* (Penzkofer *et al.*, 2016). PAC represents a multi-domain photoreceptor that couples the light-sensing capabilities of the BLUF sensor domain with the enzymatic activity of an adenylate cyclase (AC) domain. Upon blue light illumination, the photoexcited BLUF domain undergoes structural changes that activate the adjacent AC effector domain, leading to the synthesis of cAMP from ATP, and initiating downstream signalling cascades. cAMP generated by AC enzymes is an important second messenger and plays a crucial role in diverse signalling pathways (Penzkofer *et al.*, 2011). It mediates various responses by interacting with cAMP binding-mediated proteins such as protein kinase A (PKA) for metabolism processes, or cAMP response-element binding protein (CREB) involved in transcription (Kimata *et al.*, 1997; Gold *et al.*, 2013).

PAC was first discovered in 2002 when analysing the photoavoidance response of the unicellular algae *Euglena gracilis* (EuPAC) (Iseki *et al.*, 2002). They discovered sudden deviations of the algae's direction during an intensification of blue light, demonstrating a step-up photophobic response. EuPAC is a heterotetramer consisting of two subunits α and β arranged in an $\alpha_2\beta_2$ stoichiometry (Ito *et al.*, 2005; Ito *et al.*, 2010). Each subunit is able to bind two flavin

chromophores, meaning that eight BLUF domains are found in total in EuPAC. Later, other PAC photoreceptors were found in the unicellular flagellate eukaryotes *Naegleria gruberi* (NgPAC) (Penzkofer *et al.*, 2011) and *Naegleria australiensis* (NaPAC) (Yasukawa *et al.*, 2013), the bacteria *Leptonema Illini* (LiPAC) (Penzkofer *et al.*, 2014) and *Turneriella parve* (TpPAC) (Penzkofer *et al.*, 2015), the sulphur bacterium *Beggiatoa sp.* (bPAC) (Ryu *et al.*, 2010; Stierl *et al.*, 2011) and the cyanobacterium *Oscillatoria acuminata* (OaPAC) (Ohki *et al.*, 2016). Due to the small size of bPAC (350 aa) and OaPAC (366 aa), their low dark activity and a high activity increase upon blue light exposure, both proteins were directly identified as promising tools for optogenetics applications (Ryu *et al.*, 2010; Stierl *et al.*, 2011; Ohki *et al.*, 2016).

Following their discovery, bPAC and OaPAC have been well studied, and structural models of both proteins were determined by X-ray crystallography (PDB 4YUS and 4YUT for OaPAC and PDB 5M2A for bPAC) (Ohki *et al.*, 2016; Lindner *et al.*, 2017). The three homodimeric crystal structures share a similar secondary structure (Figure 4A), with a sequence identity between OaPAC and bPAC of approximately 58 %. The conserved BLUF sensor domain is linked to the AC effector domain via a long α -helix linker (helix-3), forming a coiled coil between both sensor domains (Figure 4B). The following α -helix 4, sometimes called the handle, communicates with the enzymatic domain via the tongue region between β -sheet 9 and 10. The AC domain follows the structure of the class III cyclases family, the most common type of enzymes catalysing cAMP production (Penzkofer *et al.*, 2011). The homodimeric structure of bPAC and OaPAC yield two active sites at the interface of the dimer, with both protomers being involved in ATP binding in both active sites. Yet, none of the crystallographic studies could observe ATP bound in the active site of a wild type PAC protein. Ohki *et al.* tried to crystallize OaPAC in the presence of non-hydrolysable ApCpp but could not observe it in the electron density map (Ohki *et al.*, 2016). Lindner *et al.* only observed ATP in a constitutively active mutant of bPAC, mutated at the highly conserved tyrosine (Tyr7Phe) (Lindner *et al.*, 2017). Small angle X-ray scattering (SAXS) measurements of OaPAC in solution confirmed the dimeric structure and described a stretching and increased flexibility of the protein upon ATP binding (Ujfalusi-Pozsonyi *et al.*, 2024). The data also suggested the protein structure described by crystallography to be more compact than the actual structure in solution, with a higher distance distribution function in solution (90 Å versus 83.5 Å calculated for the crystal structure PDB 4YUT).

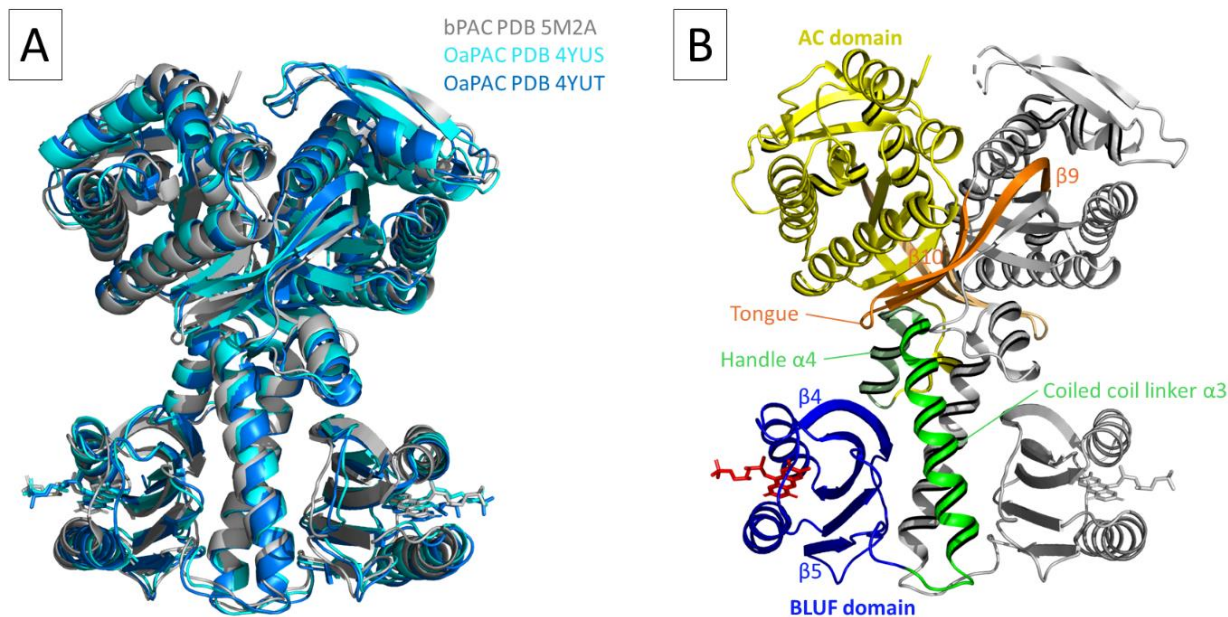


Figure 4: Structural models of PAC photoreceptor.

(A) Overlay of structural models of bPAC and OaPAC. Model representing bPAC crystal structure from Lindner *et al.* (PDB 5M2A) (grey) (Lindner *et al.*, 2017), and OaPAC crystal structures from Ohki *et al.* with hexagonal space group (PDB 4YUS) (cyan) and orthorhombic space group (PDB 4YUT) (blue) (Ohki *et al.*, 2016). The secondary structure is well conserved between bPAC and OaPAC. (B) Crystal structure of bPAC with annotation of secondary structure elements, PDB 5M2A (Lindner *et al.*, 2017). BLUF domain in dark blue, bound to FMN in red, and AC domain in yellow colour. The linker region in green is composed of the α -helix 4 named the handle, and of the α -helix 3 coiled coil representing the dimerization interface. The tongue region highlighted in orange is located between β -sheet 9 and 10 in the AC domain and interacts with the handle. The tongue region of bPAC in this structure reveals an asymmetry between both protomers (light orange and orange), with one tongue in an upper position. The second protomer is shown in grey.

Figure prepared by the PyMOL Molecular Graphics System, Version 2.5.4 Schrödinger, LLC (Schrödinger and DeLano, 2020).

Early on during research on adenylate cyclases, studies demonstrated that two catalytic ions were needed for catalysis (Tesmer *et al.*, 1999; Steegborn *et al.*, 2005). Later, the physiologically relevant metal ions for ATP conversion were shown to be magnesium ions (Hahn *et al.*, 2015; Grigorenko *et al.*, 2020). Grigorenko *et al.* also used molecular dynamics (MD) and QM/MM simulations to propose the most energetically favourable ATP binding in the active site of the mammalian type V adenylyl cyclase (Grigorenko *et al.*, 2020). Interestingly, this conformation is not the one observed by Lindner *et al.* in the constitutively active mutant of bPAC (Lindner *et al.*, 2017). The most favourable conformation derived from simulation shows an ATP stabilized by two magnesium ions, which are coordinated by two adjacent aspartates and an isoleucine (Grigorenko *et al.*, 2020). The ribose is positioned with its O3' facing the magnesium and the aspartates, 3 Å away from the phosphate P α . This permits an in-line nucleophilic attack and facilitates proton translocation to one

of the aspartates through an adjacent water molecule. However, in the crystal structure of the bPAC mutant, the ribose is rotated 180° with the O3' atom facing the opposite direction (Lindner *et al.*, 2017). This ATP conformation in the active site could be an artefact of the crystallization, locking the ATP in a non-native conformation, but can also suggest that the native ATP conformation in PAC active site does not follow the conformation with the lowest energy barrier, necessitating additional energy for the conversion to cAMP to happen.

As they are multi-domain BLUF photoreceptors with the possibility to follow the activity easily by quantifying cAMP production, bPAC and OaPAC have become a model system for studying BLUF receptor domain-mediated signal transduction (Stierl *et al.*, 2014). Recent studies have converged toward the proton and electron transfer in PAC after photoexcitation being concerted (CPET) (Collado *et al.*, 2022; Zhou *et al.*, 2022). The rest of the photocycle is as described for other BLUF photoreceptors, with changes in the hydrogen bond network and reverse PCET. The photoactivation of PAC is fully reversible, and the relaxation follows a single-exponential with a half-life below 20 s, but this varies widely depending on the protein origin (Penzkofer *et al.*, 2016; Lindner *et al.*, 2017; Ohki *et al.*, 2017). Specifically, UV-Vis absorption measurements revealed that OaPAC relaxation kinetics fluctuate with a time constant between 4 and 5 s (Collado *et al.*, 2022).

bPAC and OaPAC share a lot of similarities, but OaPAC only shows a 20-fold activity increase upon light exposure compared to its dark activity (Ohki *et al.*, 2016) against 300-fold for bPAC (Stierl *et al.*, 2011). The main difference between both proteins is the C-terminal region, being 16 amino acids longer for OaPAC. Consequently, Hirano *et al.* studied the influence of the C-terminal region on OaPAC photoreceptors, and discovered an increase in photoactivity associated with C-terminal truncation, with a truncation between 9 to 18 amino acids resulting in the highest activity (Hirano *et al.*, 2019). The truncation led to a cAMP-dependent luminescence of up to 60-fold higher compared to the wild type, demonstrating that the C-terminal region is able to reduce OaPAC activity. However, OaPAC activity after truncation and upon illumination was still lower than bPAC, suggesting other regions are involved in the lower activity of OaPAC.

Studies of the signal transduction with crystallography resulted in several hypotheses. Lindner *et al.* observed an asymmetry in the tongue region of bPAC between β -sheet 9 and 10 (Figure 4B), with one tongue of one protomer in an upper position and the other in a down position (Lindner *et*

al., 2017). They suggested the role of the tongue is as a lever to open up the AC domain of both protomers and hence the active sites, enabling ATP turnover. Involvement of the kink in β -sheet 4 during signal transmission to the C-terminal of the nearby α -helix 3 was also proposed (Lindner *et al.*, 2017). Ohki *et al.* did not observe any asymmetry in OaPAC, nor an opening of AC domain after 20 s illumination of the crystals (Ohki *et al.*, 2017). Nonetheless, they confirmed the involvement of the α -helix 3 linker in transmitting the signal by showing a loss of AC activity upon mutating specific residues on the linker region (Ohki *et al.*, 2016).

Consequently, despite several crystallographic studies on PAC signal transduction, the mechanism remains elusive (Ohki *et al.*, 2016; Lindner *et al.*, 2017; Ohki *et al.*, 2017; Lindner, 2018). This thesis aims to expand the understanding of PAC photoreceptors and signal transduction in multi-domain BLUF photoreceptors by characterizing the BLUF photoreceptors OaPAC, using a combination of biochemical and biophysical techniques.

1.5. Perspectives for BLUF Photoreceptors in Optogenetics

Light is an important external stimulus that controls various biological processes in nature in a temporally and spatially resolved manner. Following this, artificial light-regulation of protein function has become a growing research field. Besides photoswitchable ligands used in photopharmacology (Hüll *et al.*, 2018; Wranik *et al.*, 2023), incorporation of light sensitive unnatural amino acids (Kneuttinger *et al.*, 2019) and more generally photocaged molecules for time-resolved structural studies (Monteiro *et al.*, 2021), photosensory domains used in optogenetics have emerged as powerful techniques to establish non-invasive photocontrol in biological systems in various research fields (Deisseroth, 2011; Losi *et al.*, 2018).

Optogenetics offers a refined method for the precise manipulation and observation of biological functions at the level of cells, tissues, or organs. This approach achieves high temporal and spatial precision through the integration of optical lasers and genetic engineering techniques. Optogenetics

using photosensory domains has already demonstrated a great impact in medicine with, for instance, the use of opsins to restore vision (Deisseroth, 2015; Lindner *et al.*, 2022).

BLUF photoreceptors have a strong impact on the level of second messengers, making them extremely attractive for use in optogenetics. To this end, many studies have demonstrated the potential of using PAC photoreceptors for an unprecedented precise and reversible spatiotemporal control of cAMP production (Nagahama *et al.*, 2007; Schröder-Lang *et al.*, 2007; Ryu *et al.*, 2010; Weissenberger *et al.*, 2011; Efetova *et al.*, 2013; Losi *et al.*, 2018). PAC proteins are particularly valuable in neurology, or more generally cell biology, to increase cAMP concentration at specific location and to study specific cAMP-related physiological responses.

Notably, a few years after the discovery of PAC proteins, the functional expression of EuPAC in various systems, including HEK293 cells, *Xenopus laevis* oocytes and *Drosophila melanogaster*, demonstrated its versatility and effectiveness (Schröder-Lang *et al.*, 2007). In *Drosophila*, for instance, neuronal expression of EuPAC and study of subsequent light-induced behavioural changes related to learning and memory underscored the profound impact of precise cAMP modulation in living organisms. EuPAC was also used in *Caenorhabditis elegans* to demonstrate the role of cAMP in initiating acetylcholine release at the neuromuscular junction for pre-synaptic activation (Weissenberger *et al.*, 2011). However, due to its large size and complex structure, EuPAC has shown limitations in potential optogenetics applications. Since then, with their smaller size, low dark activity and functionality over a wide pH and temperature range, bPAC and OaPAC have proven highly suitable for optogenetics applications (Ryu *et al.*, 2010). For instance, bPAC was used to investigate second messenger sensing in cAMP-dependent pathway in *Drosophila*, via exchange proteins activated by cAMP (EPAC) and PKA pathways (Efetova *et al.*, 2013). PAC proteins have also been successfully mutated to photoactivated guanylyl cyclases (PGC) for the precise synthesis of cGMP instead of cAMP, rendering natural PAC and engineered PGC highly attractive for second messengers control using optogenetics (Ryu *et al.*, 2010; Tanwar *et al.*, 2018).

Besides using natural PAC photoreceptors, BLUF photoreceptors can also be utilised as building blocks to expand the optogenetics toolbox (Christie *et al.*, 2012b). As only few biological processes are inherently sensitive to light, allowing them to be activated by a short optical laser pulse, most of the interesting biological processes cannot be easily studied with light activation. It is nevertheless theoretically possible to render many light-inert reactions sensitive to light by using

optogenetics. Indeed, thanks to their modular architecture, BLUF domains have the potential to be functionally fused to effectors that are light insensitive in nature, similar to what has been done with modular LOV photoreceptors (Möglich *et al.*, 2009; Wu *et al.*, 2009; Strickland *et al.*, 2010; Christie *et al.*, 2012b; Grusch *et al.*, 2014; Moffat, 2014; Pudasaini *et al.*, 2015; Losi *et al.*, 2018; Farahani *et al.*, 2021). By fusing LOV domains to various effector domains, researchers have already successfully engineered a new class of optogenetic tools that respond to light, enabling the remote control of biological activities. Möglich *et al.* exchanged the oxygen sensitive but light-insensitive sensor domain of a histidine kinase with the blue light sensor domain LOV, successfully reducing kinase activity with blue light and revealing a thousand-fold difference in activity between dark and blue light exposure (Möglich *et al.*, 2009). Similarly, combining a BLUF domain from multi-domain photoreceptors with various enzymes or transcription factors could allow the artificial precise control of these fused proteins with light (Christie *et al.*, 2012b). Han *et al.* tested the modularity of multi-domain BLUF photoreceptors by fusing the BLUF domain of EuPAC to the C-terminal SCHIC domain of AppA. Blue light signal could be successfully transmitted, and gene expression was regulated by the engineered protein, although the BLUF domains of AppA and EuPAC only share a 30 % sequence identity. This study demonstrates the potential of BLUF domain modularity.

In addition to the previously described applications in cell biology and neurology to control enzymatic or gene expression processes, this technique also has potential in time-resolved crystallography (Moffat, 2014). Since the development of XFEL sources, TR-SFX experiments can be conducted to visualize structural rearrangements in proteins down to ps or even fs time scales (Pandey *et al.*, 2020). However, TR-SFX, and TRX in general, requires the rapid, ideally instantaneous, initiation of the reaction of interest, to ensure that fine structural changes of short-lived intermediates are not “blurred out” by the different molecules in the crystal reacting in a non-synchronized manner. For this, biological reactions initiated with a fs laser pulse in pump-probe experiments are extremely well suited, as the molecules can be efficiently and uniformly activated in the crystals, although the total number of molecules activated in the crystal will depend on the quantum yield and extinction coefficient of each protein. In comparison, reaction initiation inside crystals by mixing with substrates depends on the diffusion speed of the substrate into the crystals and does not provide a time resolution greater than sub-ms time scale (Schmidt, 2020). By this, it reduces the temporal synchronization of the reaction initiation. Unfortunately, TRX pump-probe

experiments initiated with an optical laser in the visible wavelength range can theoretically only be applied to light-sensitive targets, which highly limits the range of biological questions that can be addressed on the fs to μ s time scale if only naturally light sensitive proteins are suitable. Nonetheless, optogenetics offers a promising avenue to broaden the scope of time-resolved crystallography, as it has the potential to convert light-inert reactions into light-sensitive ones. By fusing a light-sensitive domain such as a BLUF sensor domain to light-inert proteins, the range of biological questions that can be studied with TRX on the ultrafast time scale and with homogeneous reaction initiation can be greatly expanded (Moffat, 2014). This exploitation of optogenetics in structural biology is an innovative approach to unlock the full potential of TRX experiments at XFEL sources, extending its applicability beyond a limited set of naturally light-sensitive biological targets.

The development of BLUF domain-based optogenetic tools, nevertheless, faces challenges, including ensuring the functional integrity of the fusion protein and maintaining its light sensitivity. Screening of constructs with different light sensing domains, as well as various linker regions between sensor and effector domains, is the most promising strategy for now, but achieving rational design of artificially light sensitive proteins is more efficient and should become the standard. To fully leverage the diverse toolbox provided by nature, including modular BLUF sensor domains, it is essential to gain a deeper insight into allosteric control within multi-domain proteins. In particular, it is important to understand how regulatory signals are produced and conveyed to an effector domain in the context of photosensory proteins. For this, this study on PAC photoreceptors intends to expand the understanding of signal transduction in the complete BLUF sensor–effector system, helping the rational design of BLUF-based light sensitive proteins. It will help the optogenetics field to advance, allowing promising applications to continue to come to light.

1.6. Experimental Techniques for the Study of Photosensory Proteins

Crystallography allows the determination of the three-dimensional (3D) structure of a molecule, such as proteins. Yet, under cryogenic conditions it only provides information about the average structure, while proteins have a dynamic behaviour. Time-resolved crystallography (TRX) is a powerful tool to understand the dynamic processes in proteins, and especially photosensory receptors, and has received increased attention since the nineteen eighties (Moffat *et al.*, 1984). The possibility of visualizing dynamic aspects of structural changes during critical biological processes, including small molecule binding, enzyme catalysis or photocycle-mediated changes, has given an additional dimension to crystallographic studies.

Moffat described both time resolved and chemical/physical trapping approaches to study dynamics in proteins and visualize structures of reaction intermediates (Moffat, 2001). Chemical and physical trapping are powerful and simpler techniques to study reactions in macromolecules. Yet, these techniques often lead to inhomogeneous samples with several intermediates present within a crystal, rendering the study of small and transient intermediates at fast time scale impossible to achieve. This technique is suitable for the study of slower and more stable intermediates or for the identification of steady states. Time resolved serial crystallography (TRX) at room-temperature is experimentally more complex and demanding than trapping (Caramello and Royant, 2024). It requires an extensive sample preparation, as often several thousands of crystals are required for collecting a complete diffraction data set, and the data analysis is usually laborious. Nevertheless, TRX can reach significantly higher time-resolution, down to the ps time scale at X-ray Free Electron Laser (XFEL) sources and μ s time scales at synchrotrons.

Advances in X-ray sources, either at XFELs (Pandey *et al.*, 2020) or advanced synchrotron infrastructures (Pearson and Mehrabi, 2020), have opened unprecedented opportunities to capture biochemical reactions at very short time intervals and over broad time scales (from ps to s or even min), thus matching the kinetics of many biochemical reactions. For instance, TRX has been successfully applied to capture reaction states in enzymatic catalysis using synchrotron radiation (Mehrabi *et al.*, 2019), to watch the release of a photo-pharmacological drug, by using both

synchrotron and XFEL sources (Wranik *et al.*, 2023), or to study photolyase during DNA repair using XFELs (Christou *et al.*, 2023). TRX has also emerged as a powerful tool for investigating the structural dynamics of photosensory proteins, such as PYP (Pande *et al.*, 2016), the LOV2 domain of phototropin-2 (Aumonier *et al.*, 2020), retinal proteins (Panneels *et al.*, 2015), proton pump bacteriorhodopsins (Weinert *et al.*, 2019) and chloride pump microbial rhodopsins (Mous *et al.*, 2022), among others. By capturing snapshots of protein conformations at various time points following light stimulation, TRX provides invaluable insights into the photoactivation mechanism, including the identification of intermediate states and elucidation of signal transduction.

Yet, so far, capturing light-activated intermediate states of BLUF photoreceptors using TRX has not been achieved. Most studies have used cryo-trapping to capture steady-state or reaction intermediates during signal transmission, but this has remained challenging. Jung *et al.* tried to unravel an intermediate state of AppA with cryo-trapping. However, they only observed subtle changes in the protein structure after 5 s illumination (Jung *et al.*, 2006). A less red-shifted UV-Vis absorption spectrum was also noted in the crystal, suggesting that the protein could not undergo the structural changes necessary for the signalling state in the crystalline form. Ohki *et al.* also observed almost no features in the chromophore binding pocket after 20 s illumination before cryo-trapping, describing only minor changes during signal transmission in OaPAC (Ohki *et al.*, 2017). No major change was noticeable in the AC domain or around the active site, although full functionality of the protein in the crystal was claimed in this study. Lindner *et al.* also only reported minor structural changes after photoexcitation, with a C α RMSD of 0.88. Nonetheless, a change from an up to a down position of the tongue region in bPAC was observed, which was described as an opening process of the AC domains to initiate ATP conversion (Lindner *et al.*, 2017). Interestingly, 30 s illumination before cryo-trapping of BlsA crystals revealed large structural rearrangements of the two helices at the C-terminal of the BLUF domain, but did not show any relevant changes for the flavin and neighbouring residues (Chitrakar *et al.*, 2020). As a result, although several studies suggested the presence of large structural rearrangements during signal transduction in multi-domain BLUF photoreceptors in solution using FTIR (Masuda *et al.*, 2005b), NMR (Schroeder *et al.*, 2008; Wu and Gardner, 2009) and transient grating (Nakasone *et al.*, 2023), cryo-trapped intermediates obtained with crystallography have not revealed major structural rearrangements, or only displayed confusing changes, and no study using TRX at room-temperature on BLUF photoreceptors has yet been reported.

Many limitations to a successful time-resolved crystallography or trapping experiment come from the technique itself being extremely demanding. Several attempts have been made to lower the barriers for conducting TRX experiments. First, detailed explanations for a thorough preparation of the sample and experimental conditions before data collection have been made available (Schulz *et al.*, 2022). Advice on necessary preliminary data, complementary techniques, microcrystal preparation and decision on sample environment help to increase the success rate of TRX studies. Advances in beamline automation with preinstalled laser optics or mixing devices, as well as automated data processing, for instance at the T-REXX instrument at the P14 end-station of PETRA III synchrotron (Horrell *et al.*, 2019), considerably lower the expertise needed from users to perform time-resolved serial synchrotron crystallography (TR-SSX) experiments. Upgrades of synchrotron beamlines, such as ID29 at the European Synchrotron Radiation Facility (ESRF) for TR-SSX experiments, also provide additional resources to collect data at a time-resolution down to 10 μ s (Pearson and Mehrabi, 2020). Development of segmented flow generators to obtain microdroplets of crystal slurry “on demand” reduce the required amount of sample during time-resolved serial femtosecond crystallography (TR-SFX) experiments at XFELs substantially, and especially at European XFEL (EuXFEL) with its unusual bunch pattern (Echelmeier *et al.*, 2020). Likewise, several developments of fixed target chips enable the efficient use of sample and reduce the volume of crystal slurry required for TRX significantly (Mueller *et al.*, 2015; Mehrabi *et al.*, 2020; Horrell *et al.*, 2021; Galchenkova *et al.*, 2023; Owen *et al.*, 2023). Advances in data processing software such as CrystFEL (White *et al.*, 2012; White, 2019) and data analysis software including Xtrapol8 (de Zitter *et al.*, 2022) play a large role in facilitating TRX experiments. Finally, automation for cryo-trapping experiments such as the *spitrobot* also enables experiments to be conducted faster and reproducibly, with better time-precision and resolution (Mehrabi *et al.*, 2023). Hopefully, thanks to this progress, studying dynamics with cryo-trapping and TRX will become more accessible in the coming years.

Besides TRX, complementary biochemical and biophysical characterization of BLUF photoreceptors is necessary to fully understand the photoactivation process and signal transmission. UV-Vis absorption is known to be an interesting tool to study proteins with a flavin-based chromophore (Macheroux, 1999). Yet, it provides only limited information about signal transmission. The absorption spectrum of BLUF photoreceptors shows a red shift on the ps to ns

time scale, even if the protein is not fully active, meaning it does not interact with its partner protein, or the effector domain does not catalyse the enzymatic reaction at the same time scale when the red shift is established (Masuda *et al.*, 2005c; Hasegawa *et al.*, 2006; Brust *et al.*, 2013). Additionally, the red shift is then stable for s or min until relaxation, although many structural changes are ongoing in the protein, showing that UV-Vis absorption alone is not sufficient to study flavoproteins (Gauden *et al.*, 2005). UV-Vis absorption spectroscopy should always be combined with other spectroscopic methods to obtain the full picture during signal transduction.

To this end, FTIR spectroscopy is a powerful complementary tool. Studies of AppA showed that UV-Vis spectrum was unchanged between hundreds of ps and 100 s (Gauden *et al.*, 2005), but TR-FTIR measurements confirmed that several intermediate states were visible in the ms and s time range (Majerus *et al.*, 2007). FTIR spectroscopy offers significant mechanistic understanding of photoreceptors. First, the O-H stretch of tyrosine, C=N stretch of glutamine and C4=O and C=N stretches of flavin provide important information on hydrogen bond network in the flavin binding pocket (Hasegawa *et al.*, 2005; Bonetti *et al.*, 2008; Iwata *et al.*, 2011; Yamada and Kandori, 2014). Changes in specific β -sheet and α -helix structures are relevant for signal transmission via the protein backbone and can also be revealed by TR-FTIR and provide information on the time-scale where intermediates are present (Masuda *et al.*, 2005c; Majerus *et al.*, 2007; Stierl *et al.*, 2014; Collado *et al.*, 2022). Additionally, FTIR is particularly well suited for the study of PAC photoreceptors, as conversion of ATP to cAMP can be observed in the spectral range of 900–1300 cm^{-1} (Barth and Mäntele, 1998). Furthermore, thanks to improvements in time-resolved step-scan FTIR spectroscopy, it has become feasible to track changes well beyond the ms timescale, rendering this method particularly appealing for studying multi-domain BLUF photoreceptors and their late reaction rearrangements (Majerus *et al.*, 2007).

Other spectroscopic methods, such as fluorescence spectroscopy (Bonetti *et al.*, 2008; Karadi *et al.*, 2020) or resonance Raman spectroscopy (Unno *et al.*, 2005; Unno *et al.*, 2010) have also been used to study BLUF photoreceptors. SAXS and NMR studies have also provided structural information on BLUF photoreceptors in solution (Schroeder *et al.*, 2008; Wu and Gardner, 2009; Ujfalusi-Pozsonyi *et al.*, 2024). Hydrogen/deuterium exchange mass spectrometry (HDX-MS) is a complementary method to time-resolved structural studies for the understanding of dynamics (Lindner *et al.*, 2017). Computational methods, such as MD simulation, are also interesting for the study of the photochemical process and early photoactivation events (Domratcheva *et al.*, 2008;

Udvarhelyi and Domratcheva, 2011; Khrenova *et al.*, 2013; Udvarhelyi and Domratcheva, 2013; Domratcheva *et al.*, 2016; Goyal and Hammes-Schiffer, 2017; Goings and Hammes-Schiffer, 2019; Goings *et al.*, 2020; Salvadori *et al.*, 2024). Furthermore, mutagenesis experiments on BLUF photoreceptors help to further expand the understanding of photoactivation and signal transduction mechanisms. For instance, site-directed mutagenesis of OaPAC helped to identify key amino acids involved in mediating signal transmission between BLUF and AC domains (Ohki *et al.*, 2016). By selectively perturbing specific residues and assessing their impact on cAMP production, it was possible to elucidate some of the molecular determinants of signal transduction specificity and efficiency. Consequently, a combination of different biophysical, biochemical, molecular biology and computational techniques is necessary to obtain complementary information and decipher the characteristics of BLUF photoreceptors.

Spectroscopic analysis is not only essential to obtain information on the protein in solution, but can also be used to characterize the protein when crystallized. *In crystallo* optical spectroscopy enables the examination of kinetics in crystals and unravelling of potential differences with kinetics in solution or any signalling pathway limitations or blockages caused by steric hindrance or by the crystallization solution (von Stetten *et al.*, 2015; Konold *et al.*, 2020; Schulz *et al.*, 2022). To this end, specific platforms such as the time-resolved *in crystallo* optical spectroscopy (TR-icOS) at ESRF enables the recording of pump-probe UV-Vis absorption spectra from μs to several s (Engilberge *et al.*, 2024). A titration of laser intensities on crystals of photosensory proteins is crucial to avoid artefacts due to high laser intensities resulting in multi-photon absorption. Indeed, a growing concern in the time-resolved crystallography community has been the use of extremely high laser intensities to activate photosensory proteins and maximize observed differences in difference electron density maps, creating multi-photon absorption pathways that deviate from the natural physiological pathway upon single photon absorption in photoreceptors (Grünbein *et al.*, 2020; Barends *et al.*, 2024; Do *et al.*, 2024). Verifying spectroscopic properties of protein crystals and comparing them to protein in solution is therefore essential to authenticate the results obtained with time-resolved crystallography. FTIR spectra can also be recorded for protein crystals, which is once again complementary to *in crystallo* UV-Vis absorption measurements to verify the correctness of the signalling pathway in BLUF photoreceptors crystallography studies (Hadden *et al.*, 1995).

1.7. Aim of this Project

Despite significant progress in elucidating the photoactivation of BLUF photoreceptors over the last years, several challenges prevent the full potential of this photoreceptor family for optogenetic applications being unlocked. In particular, the proposed rotation of the highly conserved glutamine in the vicinity of the FAD chromophore during the early photoactivation needs additional structural evidence to be confirmed. Furthermore, the structural rearrangements involved in signal transmission from the BLUF sensor domain to the effector domain in multi-domain photoreceptors are still poorly understood. Future research endeavours should focus on integrating multi-disciplinary approaches, such as structural biology, spectroscopy, and computational modelling, to fully unravel the intricacies of BLUF-mediated signalling pathways.

Although multi-domain BLUF photoreceptors control a wide variety of effector functions, ranging from transcription factors to enzymes, the structure of their sensor domain is well conserved. This suggests the presence of a common mechanism for signal transmission to the interface of sensor and effector domain. Consequently, the study of one particular BLUF photoreceptor provides information which can be transferred to other BLUF photoreceptors. Additionally, understanding key elements in signal transmission in BLUF multi-domain photoreceptors will greatly help the rational design of new, engineered light sensitive proteins fused to BLUF sensor domains. The development of novel optogenetic tools based on BLUF sensor domains holds promise for precise spatiotemporal control of cellular processes, with potential applications in synthetic biology and biotechnology.

To unravel signal transduction in BLUF multidomain photoreceptors, the photoactivatable adenylate cyclase OaPAC will be used as case study. For this, OaPAC will be recombinantly produced, purified and biochemically and biophysically characterized, verifying stability and proper functionality of both domains. An enzymatic activity assay will be established to confirm ATP conversion in solution. It is aimed to obtain structural models of OaPAC in its dark state with ATP bound in the active site by X-ray crystallography from data recorded at cryogenic temperature and room-temperature.

Further, time-resolved crystallography (TRX) experiments will be performed, as the photoreaction cycle ranges from ps to several s, hence making OaPAC an ideal target for TRX studies both at synchrotrons and XFELs. Key open questions as to the presence or absence of the glutamine rotation, as well as the subsequent early structural changes upon photoexcitation will be explored by the TR-SFX studies. Later rearrangements during signal transduction will be investigated with TR-SSX and cryo-trapping studies. Based on these results, the pathway for signal transmission between the BLUF sensor domain to the adenylate cyclase effector domain will be explored. Emphasis will be placed on the investigation of the α -helix linker region, which is of crucial interest for the use of BLUF sensor domains as modular blocks for optogenetics applications. TRX will be combined with TR-UV-Vis and FTIR spectroscopic analysis of OaPAC in solution and *in crystallo* to corroborate and complement the crystallographic results.

Finally, the study of AC activity and allosteric regulation will potentially decipher common allosteric mechanisms with other multi-domain proteins or multi-enzyme complexes. To this end, TR-FTIR data combined with crystallography and SAXS analysis will help elucidate the enzymatic mechanism of AC enzymes and the dynamic interplay between BLUF and AC domains.

In summary, the insights gained from this study on OaPAC will have broad implications for both basic research and biotechnological applications. Understanding the molecular mechanisms underlying light-induced signal transduction will not only enhance our knowledge of fundamental biological processes and deepen our understanding of how organisms perceive and respond to light signals, but will also enable the rational design of optogenetic tools for controlling cellular behaviour with high spatiotemporal precision.

2. Materials and Methods

2.1. Materials

2.1.1. Chemicals, Consumables and Reagents

Chemicals, buffers and broths required during laboratory work for this project are listed in Table 1, and consumables and columns are listed in Table 2.

Chemicals, buffers and Broth	Manufacturer
2-mercaptoethanol, ammonium acetate (MS grade), disodium succinate	Sigma-Aldrich (St. Louis, MO, USA)
2x YT broth, agar, agarose, ammonium sulphate, ampicillin sodium salt, ATP sodium salt, di-potassium hydrogen phosphate, di-sodium hydrogen phosphate heptahydrate, ethidium bromide solution (0.025% w/v), glycerol, guanidine hydrochloride, HEPES, imidazole, IPTG, LB broth, magnesium chloride hexahydrate, potassium dihydrogen phosphate, SDS, sodium chloride, sodium hydroxide solution (20% w/v), TRIS, TRIS hydrochloride, tryptone, nuclease-free water, yeast extract	Carl Roth (Karlsruhe, Germany)
cOmplete™ Mini EDTA-free Protease Inhibitor	Roche (Basel, Switzerland)
SOC broth	New England Biolabs (Ipswich, MA, USA)
Hydrochloric acid solution (37% w/v), Flavin adenine dinucleotide disodium salt hydrate	Merck (Darmstadt, Germany)
Adenosine-5'-triphosphate disodium salt	Alfa Aesar (Haverhill, MA, USA)
1M SPG buffer pH 4, 1M SPG buffer pH 10	Molecular Dimension (Rotherham, UK)

Table 1: List of chemicals and broths used in this project.

Consumables and columns	Manufacturer
1.5 mL black Rotilabo® eppendorfs	Carl Roth (Karlsruhe, Germany)
500 µL to 20 mL Vivaspin® Ultrafiltration Units	Satorius (Göttingen, Germany)
Filtropur syringe filters 0.45 and 0.2 µm, Filtropur 500 ml vacuum filtration unit 0.45 µm, Quality tips 0.5 µL to 1 mL	Starstedt (Nümbrecht, Germany)
Spectra/Por® dialysis membranes (MWCO 12-14 kDa)	Spectrum Labs (San Francisco, CA, USA)
50 to 10 µm CellTrics® gravity flow filters	Sysmex Partec (Goerlitz, Germany)
0.5 mL to 2 mL DNA LoBind Tubes	Eppendorf (Hamburg, Germany)
1 to 50 mL Luer lock HENKE-JECT® syringes	HenkeSassWolf (Tuttlinger, Germany)
PD10 desalting column, Superdex 75 Increase 10/300 GL column, Superdex 200 Increase 10/300 GL column, HiLoad 26/600 Superdex 200 pg, HiTrap Q HP 16/100, 1 mL & 5 mL HisTrap HP column, 5 mL HiTrap Q HP	Cytiva (Marlborough, MA, USA)
Bio-Scale CHT20-I column, 4–15% (w/v) Mini-PROTEAN® TGX Stain-Free™ protein gels	BioRad (Hercules, CA, USA)
Unstained Protein Standard, Prestained Protein Standard	New England Biolabs (Ipswich, MA, USA)
6x Laemmli SDS sample buffer	Thermo Fisher Scientific (Waltham, MA, USA)
384-well microplate with flat bottom white polystyrene	Corning (New-York, NY, USA)
96-well MRC-2 crystallization plates	SWISSCI (High Wycombe, United Kingdom)
Mounted Round LithoLoops™, Mounted Mesh LithoLoops™	Molecular Dimensions (Holland, OH, USA)

Table 2: List of consumables used in the project.

Enzymes, reagents and competent cells used during laboratory work for this project are listed in Table 3 and DNA kits or activity assays kits are listed in Table 4.

Enzymes, Reagents and Competent Cells	Manufacturer
XhoI, NdeI, CutSmart® buffer, Q5 High-fidelity DNA polymerase, Q5 reaction buffer, dNTPs (deoxynucleotide solution mix 10mM), 6x purple DNA loading dye, 1 kb DNA ladder, Gibson Assembly Master Mix	New England Biolabs (Ipswich, MA, USA)
DreamTaq polymerase, DreamTaq buffer, DH5 α , BL21 Star™ (DE3), Rosetta (DE3)	Thermo Fisher Scientific (Waltham, MA, USA)
ArcticExpress (DE3)	Agilent (Santa Clara, CA, USA)

Table 3: List of enzymes, reagents and competent cells used in this project.

Kits	Manufacturer
Monarch® DNA Gel Extraction Kit, Monarch® PCR & DNA cleanup kit, Monarch® Plasmid Miniprep Kit	New England Biolabs (Ipswich, MA, USA)
cAMP-Glo™ Assay	Promega (Madison, WI, USA)

Table 4: List of DNA and activity assay kits used in this project.

2.1.2. Buffers and Growth Media

Bacterial growth media which were not bought premade by the supplier and buffers used during laboratory work for this project are listed in Table 5. Buffers were prepared with MilliQ water from an integrated water purification system Barnstead GenPure™ (Thermo Fisher Scientific Waltham, MA, USA). Buffers were composed using the buffer calculator tool (Centre from Proteome Research) to estimate the pH. pH of the final solutions was verified using a SevenCompact pH meter (Mettler Toledo, Gießen, Germany) and adjusted with NaOH or HCl if needed.

Name	Composition
LB-Agar growth media	10 g/L tryptone 5 g/L yeast extract 10 g/L NaCl 15 g/L agar
TAE buffer	40 mM TRIS 20 mM acetic acid 1 mM EDTA pH 8.3
OaPAC QHP BINDING buffer	20 mM TRIS/TRIS-HCl 20 mM NaCl pH 7.5
OaPAC QHP ELUTION buffer	20 mM TRIS/TRIS-HCl 1 M NaCl pH 7.5
OaPAC CHT BINDING buffer	5 mM KH ₂ PO ₄ /K ₂ HPO ₄ 50 mM NaCl pH 6.8
OaPAC CHT ELUTION buffer	500 mM KH ₂ PO ₄ / K ₂ HPO ₄ 50 mM NaCl pH 6.8
OaPAC SEC buffer	50 mM TRIS-HCl 50 mM NaCl pH 8.5
OaPAC MS buffer	50 mM ammonium acetate pH 8.0
His-tag_OaPAC IMAC BINDING buffer	10 mM HEPES 150 mM NaCl 20 mM imidazole pH 7.5
His-tag_OaPAC IMAC ELUTION buffer	10 mM HEPES 150 mM NaCl 500 mM Imidazole pH 7.5
His-tag_OaPAC SEC buffer	10 mM HEPES 150 mM NaCl pH 7.5
10x PBS buffer	100 mM Na ₂ HPO ₄ 18 mM KH ₂ PO ₄ 1.37M NaCl 27mM KCl
SDS-PAGE running buffer	25 mM TRIS 192 mM glycine 0.1 % (w/v) SDS
OaPAC vapor diffusion crystallization buffer	100 mM SPG buffer pH 7.0 1.2 M disodium succinate 100 mM guanidine hydrochloride 5 mM MgCl
OaPAC batch crystallization buffer	100 mM SPG buffer pH 7.0 1.4 M disodium succinate 100 mM guanidine hydrochloride 5 mM MgCl

Table 5: List of bacterial growth media and buffers used in this project.

2.2. Methods

Sample preparation was performed in the XBI (XFEL Biology Infrastructure) laboratories at the European XFEL GmbH campus in Schenefeld, Germany (Han *et al.*, 2021).

2.2.1. Cloning Strategy for OaPAC

Vectors were used for the expression of the different genes necessary for this project. The vector pColdI (Qing *et al.*, 2004) (TakaraBio, Saint-Germain-en-Laye, France) shown in Figure 5 was used to express the genes coding for OaPAC₁₋₃₅₀, OaPAC₁₋₃₆₆ and OaPAC₁₋₁₃₇.

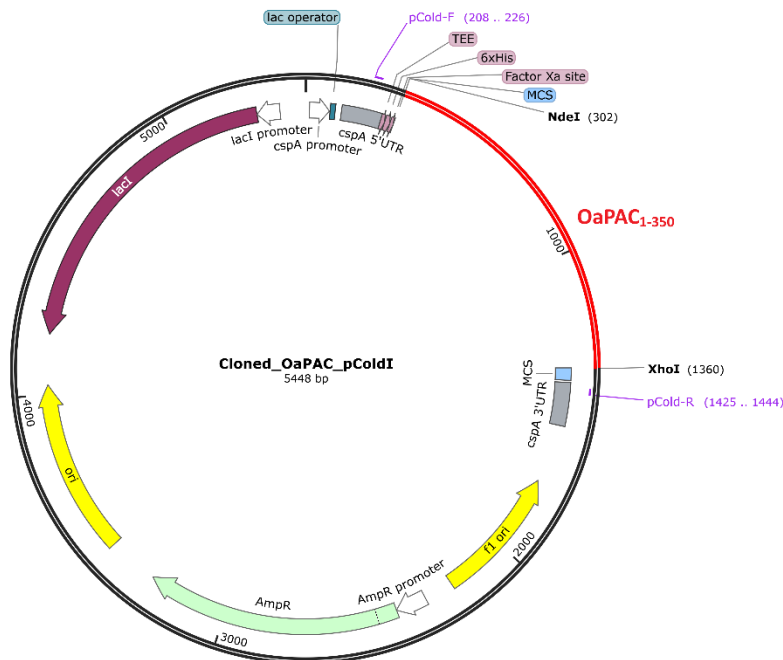


Figure 5: pColdI vector used for the expression of the genes of interest.

This vector contains one multiple cloning site preceded by a translation enhancing element, a poly-histidine tag and a factor Xa cleavage site. It possesses an ampicillin resistance gene. The vector encodes a cold-shock Protein A (*cspA*) promoter combined with a *lac* operator: The dual use of IPTG and cold shock is required to induce protein expression. OaPAC₁₋₃₅₀ DNA sequence was inserted between *NdeI* and *XhoI* cleavage site to obtain his-tag_{OaPAC₁₋₃₅₀}. Figure created with SnapGene software (www.snapgene.com).

The protein sequence from the UniProt ID K9TLZ5 (OaPAC₁₋₃₆₆) was used for generating the coding sequence of OaPAC₁₋₃₅₀, corresponding to the full-length OaPAC with C-terminal truncation of 16 amino acids. The codons were optimized according to the codon usage frequency table of *Escherichia coli*. The gene was synthesized by Eurofins Genomics and provided in a pEX cloning vector.

Four different plasmids were prepared with different gene lengths inserted and the presence or absence of a poly-histidine tag at the N-terminus. The four pColdI_OaPAC plasmid variants are described in Table 6. The strategies used and primers required to obtain 3 out of 4 of the plasmids of interest are presented in Table 7 and Table 8, respectively. The primers were designed using the NEBuilder Assembly Tool version 2.2.7 (New England Biolabs).

The coding sequence for OaPAC₁₋₃₅₀ was cloned into the pColdI expression vector. The expression vector was digested using XhoI and NdeI restriction enzymes and the gene containing overlapping sequences with the expression vector was generated with PCR. This resulted in the pColdI_his-tag_OaPAC₁₋₃₅₀ plasmid, encoding for OaPAC₁₋₃₅₀ carrying a translation enhancing element (TEE) (Qing *et al.*, 2004), an N-terminal poly-histidine tag, a Factor Xa cleavage site and one additional amino acid.

For the second plasmid, both expression vector and gene were prepared with PCR and the primer sequences were selected in order to eliminate the poly-histidine tag and the Factor Xa cleavage site from the final construct. This resulted in the pColdI_no-tag_OaPAC₁₋₃₅₀ plasmid, encoding for OaPAC₁₋₃₅₀ in its native form without tag.

The third plasmid containing the gene coding for the full length OaPAC₁₋₃₆₆ without C-terminal truncation was prepared the same way as pColdI_no-tag_OaPAC₁₋₃₅₀. Only the primer sequence of No_Tag_OaPAC₁₋₃₆₆_Fwd_primer was modified with 54 nucleotides added as a spacer (48 nucleotides from the gene sequence and two stop codons) in order to extend the gene length inserted in the expression vector. This resulted in the pColdI_no-tag_OaPAC₁₋₃₆₆ plasmid, encoding for OaPAC₁₋₃₆₆ in its native form without tag.

Vector	Poly-histidine tag	Inserted gene coding for	Plasmid name
pColdI	Yes	OaPAC ₁₋₃₅₀	pColdI_his-tag_OaPAC ₁₋₃₅₀
pColdI	No	OaPAC ₁₋₃₅₀	pColdI_no-tag_OaPAC ₁₋₃₅₀
pColdI	No	OaPAC ₁₋₃₆₆	pColdI_no-tag_OaPAC ₁₋₃₆₆
pColdI	Yes	OaPAC ₁₋₁₃₇	pColdI_his-tag_OaPAC ₁₋₁₃₇

Table 6: Variants of pColdI_OaPAC plasmids required for this project.

Component name	Produced by	5' End	3' End
pColdI_his-tag vector	Restriction Digest	XhoI (position 319)	NdeI (position 302)
His-tag_OaPAC₁₋₃₅₀ gene	PCR	His-tag_OaPAC ₁₋₃₅₀ _Fwd_primer	His-tag_OaPAC ₁₋₃₅₀ _Rev_primer
pColdI_no-tag vector	PCR	pColdI_Fwd_primer	pColdI_Rev_primer
No-tag_OaPAC₁₋₃₅₀ gene	PCR	No-tag_OaPAC ₁₋₃₅₀ _Fwd_primer	No-tag_OaPAC ₁₋₃₅₀ _Rev_primer
No-tag_OaPAC₁₋₃₆₆ gene	PCR	No-Tag_OaPAC ₁₋₃₆₆ _Fwd_primer	No-Tag_OaPAC ₁₋₃₆₆ _Rev_primer

Table 7: Cloning strategies to obtain the vectors and genes for 3 out of 4 plasmids.

Primers name	Primer sequence 5' (overlap/spacer/ANNEAL)	Annealing temp (°C)
His-tag_OaPAC₁₋₃₅₀_Fwd_primer	catcatatcgaaggtaggcaTATGAAACGCTTGACGTATATTTTC	61
His-tag_OaPAC₁₋₁₅₀_Rev_primer	caagcttgaattcggatcccTTACTACACACGCTCCAG	61
No-tag_OaPAC₁₋₃₅₀_Fwd_primer	ttattaagaggtataacaccATGAAACGCTTGACGTATATTTTC	61.5
No-Tag_OaPAC₁₋₃₅₀_Rev_primer	tgctttaagcagagattacTTACTACACACGCTCCAG	61.5
No-Tag_OaPAC₁₋₃₆₆_Fwd_primer	ttattaagaggtataacaccATGAAACGCTTGACGTATATTTTC	61.5
No-Tag_OaPAC₁₋₃₆₆_Rev_primer	tgctttaagcagagattacctattacaggggcaagcttttcacgcaaaaaatctggctcggttgacgatcgccCACACGCTCCAGATAGTG	61.5
pColdI_no-tag_Fwd_primer	GTAATCTCTGCTTAAAAGCAC	56.5
pColdI_no-tag_Rev_primer	GGTGTATTACCTCTTAATAATTAAG	56.5

Table 8: List of primers necessary to obtain the 3 different plasmids of interest.

In order to produce the last pColdI_his-tag_OaPAC₁₋₁₃₇ plasmid containing the gene coding for OaPAC₁₋₁₃₇, the pColdI_his-tag_OaPAC₁₋₃₅₀ reference plasmid was used and modified. This

reference plasmid was sent to BioCat (Heidelberg, Germany) and a mutation of 6 nucleotides was performed to modify the codon numbers 138 and 139 (corresponding to the nucleotides 412 to 417) into two stop codons. The mutation changed the codons ACG and AAT into TAA and TAG, which provides a shorter gene sequence coding for only the first 137 amino acids of OaPAC. The resulting pColdI_his-tag_OaPAC₁₋₁₃₇ plasmid encoded for OaPAC₁₋₁₃₇ carrying a translation enhancing element, an N-terminal poly-histidine tag, a Factor Xa cleavage site and one additional amino acid. OaPAC₁₋₁₃₇ corresponds to the full-length OaPAC with C-terminal truncation of 229 amino acids.

2.2.2. Cloning Procedures

2.2.2.1. Agarose Gel Electrophoresis

1 % (w/v) agarose was dissolved in TAE buffer by warming it up in the microwave. Two drops of ethidium bromide were added to the solution before pouring a gel into the agarose gel system (neoLab, Heidelberg, Germany). After solidification of the gel, TAE buffer was added to fill the system. Digested DNA was mixed with 6x purple DNA loading dye and loaded into the gel, next to a 1 kb DNA ladder. 100 V was applied for 1 h to enable separation between the linearized vector and the small fragment of cut DNA. Gel was observed on the UVP transilluminator tray (Analytik Jena, Jena, Germany) with 302 nm for a brief moment. In order to recover DNA if needed, bands of interest were extracted from the gel and DNA was purified using the Monarch® DNA Gel Extraction Kit according to the manufacturer's instructions.

2.2.2.2. Restriction Digest

The pColdI_his-tag vector ready to insert the His-tag_OaPAC₁₋₃₅₀ gene was prepared with restriction digest. 2 µg of pColdI vector was digested with XhoI and NdeI for 3 h at 37 °C in CutSmart buffer, followed by 20 min heat inactivation at 65 °C.

2.2.2.3. Polymerase Chain Reaction (PCR)

All the OaPAC DNA fragments and the pColdI_no-tag vector were prepared with PCR. PCR tubes were filled with a PCR mix containing 2 ng of template DNA, 1x Q5 reaction buffer, 10 mM dNTPs, 10 μ M of forward primer and 10 μ M of reverse primer according to Table 8, 1 U of Q5 High-Fidelity DNA polymerase and filled to 50 μ L with nuclease-free water. The PCR amplifications were performed using a PCR mastercycler (Eppendorf, Hamburg, Germany) following the steps in Table 9. PCR products were purified using the Monarch® PCR & DNA cleanup kit according to the manufacturer's instruction.

Step	Temperature	Time
Initial denaturation	98 °C	30 s
Amplification – 35 cycles	98 °C	10 s
	Annealing temperature according to Table 8	30 s
	72 °C	30 s per kb
Final extension	72 °C	120 s
End	10 °C	Hold until use

Table 9: PCR steps for the amplification of OaPAC DNA fragments and pColdI_no-tag vector.

2.2.2.4. Ligation of Gene and Expression Vector

The final plasmids were obtained by ligation of the fragment DNA coding for OaPAC into the expression vector pColdI prepared via PCR or restriction digest. Ligation was performed using 5 μ L of Gibson Assembly Master Mix, 50 ng of vector DNA and a three-fold molar excess of fragment DNA, and filled to 10 μ L with nuclease-free water. The ligation solutions were kept 20 min at 50 °C before being used for transformations.

2.2.2.5. DH5 α Competent Cells Transformation

100 μ L of DH5 α competent cells were thawed on ice for 30 min, then mixed with 2 μ L of the ligation solution and incubated on ice for 30 additional min. A heat-shock was carried out on the cells with 42 $^{\circ}$ C for 30 s followed by 2 min on ice. 400 μ L of room-temperature SOC medium were added and the cells were incubated at 37 $^{\circ}$ C degrees with 180 rpm agitation for 1 h. 200 μ L were spread on of LB-agar plates supplemented with 100 μ g/mL ampicillin and incubated at 37 $^{\circ}$ C overnight.

2.2.2.6. Colony PCR

Several colonies were tested via colony PCR to verify the presence of the plasmid DNA. One fraction of each colony was transferred into a master mix containing 1x DreamTag buffer, 10 mM dNTPs, 10 μ M pColdI-F and 10 μ M pCold-R sequencing primers (Figure 5), 5 U DreamTaq polymerase, and filled to 25 μ L with nuclease-free water. The PCR amplifications were performed using a PCR mastercycler (Eppendorf, Hamburg, Germany) following the steps in Table 10. An agarose gel electrophoresis was performed to verify the presence of the plasmid with correct length for each colony.

Step	Temperature	Time
Initial denaturation	95 $^{\circ}$ C	1 min
Amplification – 30 cycles	95 $^{\circ}$ C	30 s
	60 $^{\circ}$ C	30 s
	72 $^{\circ}$ C	4 min
Final extension	72 $^{\circ}$ C	10 min
End	10 $^{\circ}$ C	Hold until use

Table 10: PCR steps for the colony PCR tests

2.2.2.7. Plasmid Preparation

The colonies containing the plasmids of interest were inoculated into 5 mL of 2x YT medium supplemented with 100 µg/mL ampicillin and cultured at 37 °C with 180 rpm agitation overnight. Subsequently, the cells were harvested, and plasmid DNA extracted and purified using the Monarch® Plasmid Miniprep Kit according to the manufacturer's instructions. All the pColdI_OaPAC plasmids were sequenced by Eurofins Genomics (Ebersberg, Germany) using pCold-F and pCold-R sequencing primers (Figure 5).

2.2.3. Gene Expression

2.2.3.1. BL21 Star™ (DE3), Rosetta (DE3) and ArcticExpress (DE3) Competent Cells Transformation

All the plasmids were transformed into the *Escherichia coli* stains BL21 Star™ (DE3) competent cells to enable gene expression. pColdI_his-tag_OaPAC₁₋₃₅₀ was also transformed into the *Escherichia coli* stains Rosetta (DE3) and ArcticExpress (DE3) competent cells for gene expression tests. ArcticExpress (DE3) competent cells are derived from the high-performance Agilent BL21-Gold competent cells (Agilent Technologies, Inc. 2010). They are suitable for low-growth temperature or cold-adapted technology in order to enhance protein folding and solubility. Chaperone proteins are simultaneously produced to improve protein processing at low temperature to increase the yield of recombinant proteins.

200 µL of competent cells were thawed on ice for 1 h. 3 ng of the different plasmids were added to the cells and swirled gently before incubation on ice for 30 min. A heat-shock was performed on the cells with 42 °C for 30 s followed by 2 min back on ice. 800 µL of room-temperature SOC medium were added and the cells were incubated at 37 °C degrees with 180 rpm agitation for 1 h. 200 µL or 500 µL were spread on of LB-agar plates supplemented with 100 µg/mL ampicillin and incubated at 37 °C overnight.

2.2.3.2. Glycerol Stock Preparation

A single colony was inoculated in 5 mL of 2x YT medium supplemented with 100 µg/mL ampicillin and cultured at 37 °C with 180 rpm agitation overnight. 500 µL of culture was combined with 500 µL of 50 % (v/v) glycerol, flash-cooled in liquid nitrogen and stored at -80 °C until use.

2.2.3.3. Cell Culture and Gene Expression for OaPAC

In order to prepare a pre-culture, some cells from the glycerol stock were cultured in 50 mL of 2x YT medium supplemented with 100 µg/mL ampicillin and incubated at 37 °C with 180 rpm agitation overnight. Six 5 L Erlenmeyer culture flasks containing 1 L of LB medium without antibiotics were inoculated with 15 mL of pre-culture each. Cells were grown at 30 °C for around 2 h until OD_{600nm} reached between 0.4 and 0.6. The pColdI-OaPAC plasmids were double induced with a cold shock on ice for 5 min followed by 10 min incubation at 12°C, and the addition of 1 mM IPTG. Cells were grown for an additional 16 h at 30 °C. The cells were harvested by centrifugation at 8,000 x g for 30 min and the cell pellet was frozen at -20 °C until use.

2.2.4. Protein Purification

All the purification steps presented below were performed at 4 °C or on ice.

2.2.4.1. Purification of His_tag-OaPAC₁₋₁₃₇ and His_tag-OaPAC₁₋₃₅₀

Cell pellets for 1 L culture of His_tag-OaPAC₁₋₁₃₇ or His_tag-OaPAC₁₋₃₅₀ were resuspended in 30 mL His_tag-OaPAC IMAC BINDING buffer containing one cOmplete™ Mini EDTA-free Protease Inhibitor tablet. After resuspension, cells were lysed by three cycles of high-pressure homogenization (EmulsiFlex-C3, Avestin, Mannheim, Germany) and centrifuged at 30 000 x g for 1 h. For His_tag-OaPAC₁₋₃₅₀, cells were alternatively lysed with a sonicator (Qsonica, Frankfurt am Main, Germany) setup at 50 % amplitude and for 3 cycles of 5 min with alternating 15 s on and 30 s off. The supernatant was collected and filtered through a 0.45 µm disposable vacuum filter.

The recombinant His_tag-OaPAC₁₋₁₃₇ and His_tag-OaPAC₁₋₃₅₀ proteins were first purified via immobilized metal affinity chromatography (IMAC) using a 5 mL HisTrap HP column equilibrated with His_tag-OaPAC IMAC BINDING buffer. His_tag-OaPAC₁₋₃₅₀ protein was eluted with a linear imidazole gradient up to 500 mM. Protein eluted between 20 and 40 % (v/v) elution buffer were pooled together and concentrated down to 500 µL using a centrifugal filter concentrator with a 30 kDa cutoff. His_tag-OaPAC₁₋₁₃₇ protein was eluted with a step imidazole gradient up to 500 mM. The column was first washed with 15 and 25 % (v/v) His_tag-OaPAC IMAC ELUTION buffer. His_tag-OaPAC₁₋₁₃₇ protein was then eluted with 50 % (v/v) elution buffer. Eluted fractions at 50 % (v/v) elution buffer were pooled together and concentrated down to 500 µL using a centrifugal filter concentrator with a 10 kDa cutoff.

The last step consisted of size exclusion chromatography (SEC) using a Superdex 200 Increase 10/300 GL or a HiLoad 26/600 Superdex 200 pg column for His_tag-OaPAC₁₋₃₅₀ and a Superdex 75 Increase 10/300 GL column for His_tag-OaPAC₁₋₁₃₇. The concentrated protein solution was injected onto the SEC column previously equilibrated with His-tag_OaPAC₁₋₁₃₇ SEC buffer. Eluted fractions containing protein material were analysed by SDS-PAGE and purified protein was concentrated before being flash-frozen in liquid nitrogen and stored at -80 °C.

2.2.4.2. Purification of OaPAC₁₋₃₅₀ and OaPAC₁₋₃₆₆

Cell pellets for each 1 L culture of OaPAC₁₋₃₅₀ or OaPAC₁₋₃₆₆ were resuspended in 30 mL OaPAC QHP BINDING buffer containing one cOmpleteTM Mini EDTA-free Protease Inhibitor tablet. After resuspension, cells were lysed by three cycles of high-pressure homogenization (EmulsiFlex-C3, Avestin, Mannheim, Germany) and centrifuged at 30 000 x g for 1 h. The supernatant was collected and filtered through a 0.45 µm disposable vacuum filter.

The recombinant proteins of interest (OaPAC₁₋₃₅₀ or OaPAC₁₋₃₆₆) were purified by fast protein liquid chromatography (FPLC). The supernatant was first loaded on a 20 mL anion exchange column (HiTrap Q HP 16/100) previously equilibrated with OaPAC QHP BINDING buffer. Proteins were eluted with a step salt gradient. The column was first washed with 10 % (v/v) OaPAC QHP ELUTION buffer and the protein of interest accompanied with some contaminants were eluted with 15 % (v/v) OaPAC QHP ELUTION buffer. Eluted fractions were pooled together and an ammonium sulphate precipitation was performed with 1.4 M ammonium sulphate. After precipitation, the solution was filtered through a 0.45 µm syringe filter and the buffer of the solution was exchanged with OaPAC CHT BINDING buffer using a PD10 desalting column. The next step consisted of cation exchange chromatography using the 20 mL Bio-Scale CHT20-I column equilibrated with OaPAC CHT BINDING buffer. OaPAC accompanied with some contaminants was eluted with a step potassium phosphate gradient at 5 % (v/v) OaPAC CHT ELUTION buffer, after a washing step without elution buffer. After the elution, the protein solution was concentrated down to 2 mL in a centrifugal filter concentrator with a 30 kDa cutoff and injected onto a HiLoad 26/600 Superdex 200 pg column equilibrated with OaPAC SEC buffer for size exclusion chromatography. Fractions of protein eluting of the column were analysed by SDS-PAGE. Fractions containing the purified protein in OaPAC SEC buffer were pooled and concentrated depending on the need. If not used immediately, protein was flash-frozen in liquid nitrogen and stored at -80 °C until use.

2.2.5. Basic Methods for Biochemical Characterization

2.2.5.1. Sodium Dodecyl Sulphate Polyacrylamide Gel Electrophoresis (SDS-PAGE)

Analysis of protein purity during and after purification was first performed with SDS-PAGE. Samples were denatured and reduced in 6x Laemmli SDS sample buffer at 95 °C for 5 min. Denatured and reduced samples, alongside an unstained protein standard, were loaded into the wells of precast 4–15 % (w/v) Mini-PROTEAN® TGX Stain-Free™ protein gels. Electrophoresis was carried out using a Mini-PROTEAN Tetra Vertical Electrophoresis Cell (BioRad, Hercules, CA, États-Unis) filled with SDS-PAGE running buffer. An electric field with 180 V and about 20 mA per gel allowed the proteins to migrate for 45 min. The stain-free imaging was performed after 45 s optimal auto-exposure of stain-free protein gels with an imaging system (ChemiDoc MP, BioRad, Hercules, CA, USA).

2.2.5.2. Determination of the Protein Concentration

Protein concentrations were estimated by measuring the absorbance at 280 nm using a NanoDrop™ One (Thermo Fisher Scientific, Waltham, MA, USA). Molar extinction coefficients at 280 nm were estimated using the ProtParam tool in the ExPASy Server (Wilkins *et al.*, 1999). A value of 18 000 M⁻¹ cm⁻¹ was added to the estimated extinction coefficients of OaPAC proteins to take into account the presence of FMN (Whitby, 1953; Kataoka *et al.*, 1992; Pace *et al.*, 1995; Kubota *et al.*, 2018). The calculated extinction coefficients for each protein are presented in Table 11.

Protein name	Extinction coefficient at 280 nm
OaPAC ₁₋₃₆₆ and OaPAC ₁₋₃₅₀	47 910 M ⁻¹ cm ⁻¹
OaPAC ₁₋₁₃₇	27 970 M ⁻¹ cm ⁻¹

Table 11: Extinction coefficients for OaPAC protein variants.

2.2.6. Oligomeric State and Stability

2.2.6.1. Dynamic Light Scattering

Long-term stability and determination of particle size distribution of His-tag-PAC₁₋₁₃₇ and OaPAC₁₋₃₅₀ and OaPAC₁₋₃₆₆ were performed by Dynamic Light Scattering (DLS) using a DynaPro Nanostar (Wyatt Technology, Santa Barbara, CA, USA).

After purification, proteins were flash-frozen in liquid nitrogen and kept at -80 °C until analysis. Samples were thawed on ice for 4 h before centrifugation at 21,000 x g for 1 h. The long-term stability of the three protein variants at 4°C was tested with DLS for 96 h. Disposable microcuvettes were filled with 10 µl protein solution and transferred into the pre-cooled DLS instrument. Measurements allowed calculation of the hydrodynamic radius (Rh) and polydispersity of particles present in the sample every h. For OaPAC₁₋₃₅₀, the same measurements were also carried out at 22 °C for 96 h.

2.2.6.2. Native Mass Spectrometry

OaPAC₁₋₃₅₀ purified with the protocol described in 2.2.4.2 was concentrated to 15 mg/mL. Before measurement, a SEC was run with OaPAC₁₋₃₅₀ in OaPAC MS buffer containing ammonium acetate only. After SEC, samples were diluted to 25 µM (1 mg/ml) for analysis. Native mass spectrometry data were collected and analysed by Kristina Lorenzen from EuXFEL (Schenefeld, Germany). Measurements were carried out using the Q-ToF MS instrument (MS Vision, Almere, the Netherlands) with positive electrospray ionisation time of flight mass spectrometry.

2.2.6.3. Small Angle X-ray Scattering

OaPAC₁₋₃₅₀ purified with the protocol described in 2.2.4.2 was concentrated to 25 mg/mL before being flash-frozen in liquid nitrogen. Before SAXS measurements, protein was thawed on ice for

4 h and a SEC was run with OaPAC₁₋₃₅₀ in OaPAC SEC buffer with 5 mM DTT at the CIBB laboratory of ESRF. Protein was diluted to obtain two replica aliquots with concentrations of 4 or 2 mg/mL corresponding to 100 and 50 μ M, respectively. A eight-fold molar excess of magnesium chloride was added to each sample, and ATP was added to one replica of the samples with a ATP:OaPAC molar ratio of four. Measurements were recorded at the BM29 BioSAXS beamline (ESRF, Grenoble, France) using a DECTRIS PILATUS3 X 2M (Tully *et al.*, 2023). Safe light conditions were respected in the hutch and the capillary was illuminated with red light only. Data were acquired at room-temperature for the two OaPAC₁₋₃₅₀ concentrations with and without ATP. Each sample was measured ten times with 1 second exposure and a buffer scattering signal was collected before and after each sample. Each condition was measured in triplicate. Data collected at the BM29 beamline were recorded under the proposal MX2518.

Two-dimensional (2D) scattering patterns were converted into one-dimensional (1D) scattering pattern using the automated data reduction pipeline available at the BM29 beamline (Tully *et al.*, 2023). 1D scattering patterns were averaged and subtracted to their corresponding buffer signals using the PRIMUS graphical interface from the ATSAS software suite version 3.0 (Manalastas-Cantos *et al.*, 2021). Guinier analysis (Guinier and Fournet, 1955) was carried out using the PRIMUS graphical interface. The radius of gyration (R_g) was estimated with a Guinier fit, choosing for the fit a $q_{\min}R_g$ below 0.65 and a $q_{\max}R_g$ around 1.3. Distance distribution analysis was performed using the program GNOM version 5.0 (Svergun, 1992) integrated into the PRIMUS graphical interface. Indirect Fourier Transform (IFT) to obtain the pair distance distribution ($P(r)$) function enabled the estimation of the maximal intramolecular distance (D_{\max}). Theoretical 1D scattering curves from OaPAC crystal structures obtained with SSX (PDB 9F1X OaPAC₁₋₃₅₀ orthorhombic crystal from with $P2_12_12$ space group (Kapetanaki *et al.*, 2024) and OaPAC₁₋₃₅₀ orthorhombic crystal from with $C222_1$ space group from this study) were calculated using CRY SOL version 3.0, included in the online ATSAS software suite (Franke *et al.*, 2017), and analysis of the fit to OaPAC₁₋₃₅₀ scattering curves in solution was carried out using the PRIMUS graphical interface from the ATSAS software suite version 3.0 (Manalastas-Cantos *et al.*, 2021). Twenty low resolution models were generated from OaPAC₁₋₃₅₀ SAXS data by *ab initio* modelling using DAMMIF version 1.1.2 included in the online ATSAS software suite (Franke and Svergun, 2009). All twenty models were selected as representative of the scattering data and were averaged using DAMAVER version 5.0 (Volkov and Svergun, 2003). The most representative model was

used for analysing the fit to the experimental data using the PRIMUS graphical interface. The averaged *ab initio* model was refined with DAMMIN version 5.3 (Svergun, 1999).

2.2.7. *In vitro* Adenylyl Cyclase Activity Assay

The study of the adenylyl cyclase domain enzymatic activity in solution was performed using an *in vitro* cAMP-Glo™ assay in which cAMP production was analysed. The assay is based on the principle that cAMP stimulates protein kinase A (PKA) holoenzyme activity, decreasing available ATP and leading to decreased light production in a coupled luciferase reaction.

A cyclic AMP (cAMP) standard curve was generated according to the manufacturer's instructions with a concentration of cAMP from 1 μM to 0.49 nM using a serial 1:1 dilution and with 20 μM ATP added in each well. A curve for the adenylyl cyclase activity of OaPAC₁₋₃₅₀ was generated by a serial dilution of 20 μM OaPAC₁₋₃₅₀ to 10 nM and with the addition of 20 μM ATP to enable its conversion into cAMP by the enzyme. The activity was measured after 40 s of blue light exposure using an excitation light source (pE-4000, CoolLED, Andover, United Kingdom) with a wavelength of 435 nm and 25 nm bandwidth. The reactions were prepared according to the manufacturer's instructions in a 384-well plate and the luminescence was recorded with a multimode microplate reader (Spark™ 10M, TECAN, Männedorf, Switzerland). Data analysis was performed with Origin software version 2024, using a sigmoidal dose-response equation for fitting the light response.

2.2.8. Spectroscopic Analysis in Solution

2.2.8.1. UV-Vis Absorption

UV-Vis absorption measurements of OaPAC₁₋₃₅₀ in solution were first carried out at the XBI laboratory to analyse the appearance of the specific redshift upon photoexcitation of BLUF domains. Spectral measurements were carried out with OaPAC₁₋₃₅₀ at a concentration of 125 μM

in OaPAC SEC buffer supplemented with 5 mM magnesium chloride, using a UV-Vis spectrophotometer (UV-2700, Shimadzu, Kyoto, Japan). Blue light excitation was performed by using an excitation light source (pE-4000, CoolLED, Andover, United Kingdom) with a wavelength of 435 nm and 25 nm bandwidth. Absorption spectra were recorded from the dark state and the light-activated state over a wavelength range of 300-550 nm using a 10 mm quartz cuvette. Transient absorption spectra to study the kinetic details of light activation (dark to light) and dark relaxation (light to dark) were measured at 492 nm with 10 scans recorded per second. Data analysis was performed with Origin software version 2024, using a one-phase exponential equation to fit the photoactivation and relaxation kinetics.

UV-Vis absorption measurements of OaPAC₁₋₃₅₀ in solution were also performed at the icOS (*in crystallo* optical spectroscopy) bench of the European Synchrotron Radiation Facility (ESRF, Grenoble, France) (von Stetten *et al.*, 2015). Data were collected with the help of Nicolas Caramello and Sylvain Engilberge from ESRF and were processed by Nicolas Caramello. Spectral measurements in solution were carried out with OaPAC₁₋₃₅₀ at a concentration of around 800 μ M in OaPAC SEC buffer supplemented with 5 mM magnesium chloride. The sample was pipetted onto a loop and placed on a SPINE standard holder in front of the dehumidifier for room-temperature measurements under red light conditions. The optical spectroscopy setup at icOS comprises up to three objectives. The white light was mounted opposite to the spectrophotometer with a CCD detector. The laser line for photoexcitation was mounted 90 °C from the others. The laser pulse was set up at 50 ms with a wavelength of 355 nm, and a laser fluence of 636.6 mJ/cm² (500 μ W laser power). Absorption spectra were measured with the commercial SpectraSuite software (Ocean Optics) and recorded for about 10 s after laser triggering.

2.2.8.2. Fourier-Transform Infrared Spectroscopy (FTIR)

All the FT-IR measurements were performed by our collaborators Marius Nagel and Tilman Kottke from Bielefeld University (Bielefeld, Germany).

OaPAC₁₋₃₅₀ and OaPAC₁₋₁₃₇ proteins in solution were transferred into 10 mM of substrate in OaPAC SEC buffer supplemented with 5 mM magnesium chloride by repeated ultracentrifugation, using a

Vivaspin 500 filter device with a cutoff of 30 kDa at 4 °C, and afterwards concentrated. The final concentration of the samples was 0.3 to 3.0 mM. 1.5 μ L of the samples was placed between two BaF₂ windows, which were sealed without any drying using vacuum grease. The path length was adjusted to reach an absorbance at 1650 cm^{-1} of 0.7 to 1.1. Full hydration was evident from an absorbance ratio of amide I / H₂O to amide II of 2.7 to 3.5.

The experiments were carried out on an IFS 66/S spectrometer (Bruker, Bremen, Germany) at 10 °C using a mercury cadmium telluride detector. A long wave pass filter with a cut off of 2040 cm^{-1} was used to remove stray light. The spectra were recorded at a scanner velocity of 150 kHz and a spectral resolution of 2 cm^{-1} . The Fourier Transform was performed using a zero-filling factor of 4.

The time-resolved difference spectra were obtained using the rapid-scan mode and induced by a blue LED light (445 nm, 25 mW/cm^2 , Philips Lumileds) with a diffusion disc placed in front. OaPAC₁₋₃₅₀ with non-hydrolysable ATP analogue ApC_{pp}, without any substrate and OaPAC₁₋₁₃₇ were illuminated for 10 s. OaPAC₁₋₃₅₀ with ATP was illuminated for 4 s. Data were collected directly before and after the illumination with a sequence of 32, 64, 128, eight times 256 and two times 1024 scans per experiment. For OaPAC₁₋₃₅₀ with ATP, with ApC_{pp}, without any substrate, and OaPAC₁₋₁₃₇ in total 16, 64, 16 and 32 experiments were averaged, respectively.

For reference measurements, 4 mM of cyclic adenosine monophosphate, adenosine triphosphate, pyrophosphate and phosphate were dissolved in OaPAC SEC buffer supplemented with 5 mM magnesium chloride and analysed using an attenuated total reflection setup. 100 μ L of the samples was placed on the internal reflection element with nine active reflections and the buffer was directly subtracted.

2.2.9. *In crystallo* Optical Spectroscopy

2.2.9.1. UV-Vis Absorption of Microcrystals

Experiments to verify the presence of the red-shift in crystallized OaPAC were first carried out at the icOS platform from ESRF, Grenoble, France (von Stetten *et al.*, 2015). Data were collected

with the help of Nicolas Caramello and Sylvain Engilberge from ESRF (Grenoble, France) and were processed by Nicolas Caramello. The setup was the same as described in 2.2.8.1. Crystals of OaPAC₁₋₃₅₀ with orthorhombic form in C222₁ or P2₁2₁2₁ space groups were mounted on a loop and placed on a SPINE standard holder for room-temperature measurements. Photoexcitation was performed with a 50 ms 355 nm-laser pulse with a laser fluence between 76.4 mJ/cm² (60 μW) and 636.6 mJ/cm² (500 μW).

Further experiments were conducted at the TR-icOS platform (Engilberge *et al.*, 2024) to study the effect of laser power on OaPAC crystal activation and to record time-dependent spectral changes of the absorbance in the crystals. Data were collected with the help of Nicolas Caramello and Samuel Rose from ESRF (Grenoble, France) and were processed by Nicolas Caramello. The white light with a pulse length of 1.3 μs was mounted opposite to the spectrophotometer which was equipped with a CMOS detector. A 420 nm-laser with pulses between 3 and 5 ns was triggered to initiate photoexcitation of the molecules inside the crystals.

For the first experiment, a slurry of OaPAC C222₁ crystals of around 20 x 12 x 4 μm³ were sandwiched between two COC films (Figure 6A). A power titration with 17.3, 46.4, 88.6, 150.7, 280.3 mJ/cm² laser fluence was conducted. For a sample of 4 μm thickness – as crystals were always adopting the same orientation in the COC sandwich – with an extinction coefficient at 420 nm of 8,500 M⁻¹ cm⁻¹ and a laser beam diameter of 130 μm (1/e²), this was equivalent to 1.1, 3.0, 5.7, 9.7 and 18 absorbed photons per molecules, respectively, according to the photon calculation Excel sheet by Grünbein *et al.* (Grünbein *et al.*, 2020). UV-Vis spectra were recorded between 300 and 550 nm. Spectra were recorded in the dark and 1 second after photoexcitation.

For the second experiment, a slurry of OaPAC C222₁ crystal of around 55 x 25 x 8 μm³ were sandwiched between two COC films (Figure 6B). The ns 420 nm-laser was setup at 143.1 mJ/cm², corresponding to 8.7 absorbed photons per molecules (8 μm thickness, 8,500 M⁻¹ cm⁻¹ extinction coefficient and 130 μm (1/e²) laser beam diameter). UV-Vis spectra were recorded in duplicate between 300 and 550 nm with a time delay after laser triggering between 3 μs and 12 s to follow the spectral changes.

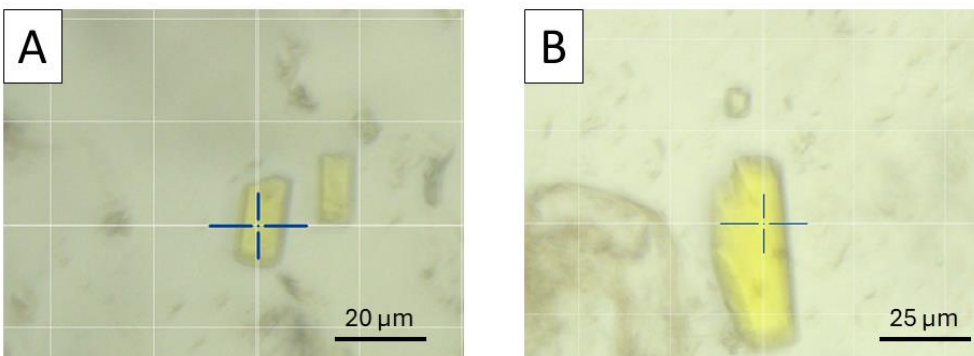


Figure 6: OaPAC crystals used at TR-icOS for UV-Vis absorption spectroscopy.

(A) OaPAC crystals used for power titration experiment. Crystal size is around $20 \times 12 \times 4 \mu\text{m}^3$. (B) OaPAC crystal used for time-resolved measurements. Crystal size is around $55 \times 25 \times 8 \mu\text{m}^3$.

2.2.9.2. Fourier-Transform Infrared Spectroscopy of Microcrystals

All the FTIR measurements were performed by our collaborators Marius Nagel and Tilman Kottke from Bielefeld University (Bielefeld, Germany). OaPAC microcrystals were concentrated by sedimentation overnight and removal of the supernatant. The FTIR measurements were recorded as explained in 2.2.8.2. Crystallized OaPAC was illuminated for 10 s before measurements and 32 experiments were averaged.

2.2.10. Crystallization and Structure Determination

2.2.10.1. Macrocrystal preparation for OaPAC₁₋₃₅₀ and OaPAC₁₋₃₆₆

96-well plates were used for vapor diffusion using the sitting drop method for the crystallization trials of OaPAC₁₋₃₅₀ and OaPAC₁₋₃₆₆. The reservoirs were filled with crystallization solutions from PACT, JCSG and Wizard crystallization screens, or with selected optimized crystallization solutions prepared with a liquid handling robot (Freedom EVO2 100/8, TECAN, Männedorf, Switzerland). All crystallization drops from one plate were set up at once using a robotic dispenser

(NT8 crystallization robot, FORMULATRIX, Oberursel, Germany) with 500 nL protein at 10 mg/mL and 500 nL from a 50 μ L reservoir solution (1:1 ratio). The plates were then sealed and incubated at 20 °C or 4 °C. The monitoring of crystal growth was performed using SONICC (FORMULATRIX Oberursel, Germany) or a stereomicroscope (SMZ18, Nikon, Amstelveen, Netherlands).

OaPAC₁₋₃₅₀ crystals with C222₁ space group grew with 100 mM SPG buffer, 1.2 M disodium succinate, 100 mM guanidine hydrochloride, 5 mM magnesium chloride (corresponding to OaPAC vapor diffusion crystallization buffer in Table 5). OaPAC₁₋₃₅₀ crystals with P2₁2₁2₁ space group grew with 100 mM sodium citrate pH 5.5, 10 % (v/v) PEG 20000, and 5 mM magnesium chloride. P2₁2₁2₁ crystals were crushed to create seeds used for the subsequent crystallization tests in order to improve diffraction quality.

The selected crystals for X-ray diffraction data collection grew in an orthorhombic crystal form with C222₁ space group with OaPAC vapor diffusion crystallization buffer, with or without ATP and under red light illumination or in the dark. Before cryo-cooling, a single crystal was cryo-protected with 20 % (v/v) glycerol added to the crystallization solution. After mounting in a LithoLoop™, crystals were flash-cooled in liquid nitrogen.

2.2.10.2. Macromolecular Crystallography (MX) data collection

Crystals for dark-state OaPAC grew up to a size of 200 x 60 x 40 μ m³ in an orthorhombic crystal form with space group C222₁, with one molecule in the asymmetric unit. Diffraction data were collected at 100 K at the ID23-2 beamline at ESRF, Grenoble, France using a DECTRIS PILATUS3 X 2M detector (Flot *et al.*, 2010). 3600 frames with 20 ms exposure were recorded with a 360° rotation range and 0.1° oscillation per frame. The X-ray beam was focused to 5 x 26 μ m², the energy was set at 14.2 keV and the transmission at 10 %. The high-resolution cutoff was 1.5 Å for this data set. Data recorded for the experiment at ESRF are available at data.esrf.fr/doi/10.15151/ESRF-DC-1329827085.

Crystals for dark-state OaPAC co-crystallized with 5 mM ATP had a size of 50 x 35 x 8 μ m³ and grew in an orthorhombic crystal form with space group C222₁ with one molecule in the asymmetric

unit. Diffraction data were collected at 100 K at the ID23-2 beamline at ESRF, Grenoble, France using a DECTRIS PILATUS3 X 2M detector (Flot *et al.*, 2010). 3000 frames with 20 ms exposure were recorded with a 300° rotation range and 0.1° oscillation per frame. The X-ray beam was focused to 5 x 5 μm^2 , the energy was set at 14.2 keV and the transmission at 1 %. The high-resolution cutoff was 2.1 Å for this data set. Data recorded for the experiment at ESRF are available at data.esrf.fr/doi/10.15151/ESRF-DC-1329817123.

For the cryo-trapping experiment, a single 150 x 50 x 30 μm^3 crystal was illuminated for 5 s at 200 mJ/cm^2 (10 absorbed photons per molecule) using an illumination system pE-400 (CoolLED, Andover, United Kingdom) with a wavelength of 435 nm and 25 nm bandwidth. The crystal was flash cooled in liquid nitrogen immediately after illumination. Light-activated OaPAC co-crystallized with 5 mM ATP grew in space group C222₁ with one molecule in the asymmetric unit. The high-resolution cutoff was 1.7 Å for this data set. Diffraction data were collected at 100 K at the P11 beamline at PETRA III, Hamburg, Germany using a DECTRIS EIGER2 X 16M detector (Burkhardt *et al.*, 2016). 3600 frames with 15 ms exposure were recorded with a 360° rotation range and 0.1° per frame. The X-ray beam was focused to 50 x 50 μm , the energy was set at 12.0 keV and the transmission at 35 %.

2.2.10.3. MX Data Processing, Model Building and Refinement

All data were processed and scaled using the program package XDS (Kabsch, 2010). All datasets were merged using AIMLESS (Evans and Murshudov, 2013) from the CCP4 suite (Agirre *et al.*, 2023). Initial models were obtained by molecular replacement using the PHENIX program suite (Adams *et al.*, 2010) with the OaPAC structure from Ohki *et al.* (PDB 4YUS) (Ohki *et al.*, 2016) as a search model. The models were refined using both the PHENIX program suite (Adams *et al.*, 2010) and the CCP4 suite (Agirre *et al.*, 2023) and manual model building was done using COOT (Emsley *et al.*, 2010). MX data and structure refinement statistics are shown in Appendix Table 1. Structural models have been deposited in the Protein Data Bank under accession codes 8QFE, 8QFF and 8QFG. The PyMOL Molecular Graphics System version 2.5.4 (Schrödinger and DeLano, 2020) was used to prepare all the figures representing the MX structural models of OaPAC.

2.2.10.4. Microcrystal Preparation for OaPAC₁₋₃₅₀ and Negative-Stain Transmission Electron Microscopy (TEM) Characterisation

OaPAC₁₋₃₅₀ microcrystals were obtained with batch crystallization (Boutet *et al.*, 2018). Microcrystals were grown after mixing 45 % (v/v) OaPAC₁₋₃₅₀ concentrated at 12 mg/mL, 10 % (v/v) seeds and 45 % (v/v) crystallization buffer containing 100 mM SPG buffer pH 7.0, 1.4 M disodium succinate, 100 mM guanidine hydrochloride, 5 mM magnesium chloride and 5 mM ATP. Microcrystals were grown in the dark at 4 °C. The seeds were produced by crushing macrocrystals grown with OaPAC vapor diffusion crystallization buffer using the sitting drop method with a glass stick. After a first round of seeding, the first batch of microcrystals was crushed with seed beads and five runs of 30 s vortexing to create the final seed stock for batch crystallization of microcrystals. By modifying the concentration and size of the seeds, it was possible to obtain a wide range of microcrystals size suitable for both synchrotron and XFEL experiments.

Crystals of OaPAC₁₋₃₅₀ in an orthorhombic crystal form with C222₁ space group grew up to a size of 25 x 12 x 6 μm³ and 7 x 3 x 2 μm³ using batch crystallization for TR-SSX and TR-SFX experiments, respectively. Microcrystals were concentrated by sedimentation and removal of the supernatant to 20 % pellet volume (v/v).

The monitoring of crystal growth was conducted with a stereomicroscope (SMZ18, Nikon, Amstelveen, Netherlands). If crystals were too small to be properly investigated with a stereomicroscope, a Transmission Electron Microscope (TEM) was used. A TEM grid (R2/2 Quantifoil grids, Science Services, Munich, Germany) was placed in the glow discharge system (GloQube Plus, Quorum, Laughton, United Kingdom) in order to provide a negative surface charge modification treatment to render the grid hydrophilic. A drop from the microcrystal slurry was applied onto the carbon side of the grid, blotted, washed with water and stained with uranyl acetate (2 % w/v). The grid was then analysed using an electron microscope (JEM-2100Plus, JOEL, Tokyo, Japan) at 200 kV acceleration voltage.

2.2.10.5. Time-Resolved Serial Femtosecond Crystallography (TR-SFX) Data Collection

The microcrystal slurry was filtered with a 10 μm gravity flow filter right before injection. The slurry was injected into the X-ray beam using a 3D printed (GT2, Nanoscribe, Heidelberg, Germany) double-flow focusing nozzle (DFFN) (Oberthuer *et al.*, 2017) or gas dynamic virtual nozzle (GDVN) (Vakili *et al.*, 2022) for a serial femtosecond crystallography (SFX) experiment at the SPB/SFX instrument of the European XFEL, Schenefeld, Germany (Mancuso *et al.*, 2019). Data recorded for the experiment at the European XFEL are available at doi:10.22003/XFEL.EU-DATA-002829-00 (proposal 2829).

OaPAC₁₋₃₅₀ microcrystals were photoexcited with the second harmonic of the EuXFEL pump-probe laser system at 421 nm (Pergament *et al.*, 2016; Palmer *et al.*, 2019; Koliyadu *et al.*, 2022). The optical pump pulses were stretched from their original duration of 50 fs to 250 fs by transmission through fused silica. The optical pump had a fluence of 19.8/21.6 or 100 mJ/cm^2 per pulse with a repetition rate of 188 kHz. Under these excitation conditions, 1.3 or 6.6 photons were absorbed on average per molecule, respectively. The calculation of the absorbed photon number was performed according to the photon calculation Excel sheet by Grünbein *et al.* (Grünbein *et al.*, 2020) with an extinction coefficient of 8,500 $\text{M}^{-1} \text{cm}^{-1}$ at 421 nm.

The X-ray probe beam was focused to 3 μm x 4 μm , with 9.3 keV photon energy, an estimated pulse length of ≤ 30 fs and 564 kHz intra-train pulse repetition rate. Data were acquired with the AGIPD detector operating in fixed medium gain mode (Allahgholi *et al.*, 2019). TR-SFX data were collected at 30 ps, 200 ps, 600 ps, 5 ns, 50 ns, 500 ns and 4.58 μs delays in a LIGHT-DARK1-DARK2 succession pattern (every 3rd pulse within an X-ray pulse train was pumped). A TRUE DARK without any optical laser was also collected.

2.2.10.6. TR-SFX Data Processing

All the TR-SFX offline data processing was performed by Sabine Botha from Arizona State University (Tempe, AZ, USA).

During the experiment, online monitoring was performed with Karabo (Fangohr *et al.*, 2018) and OnDA (Mariani *et al.*, 2016). Raw data were calibrated using the European XFEL's internal detector calibration pipeline. Initial hit finding was performed using CrystFEL version 0.10.1 (White *et al.*, 2012) with the following parameters (through the “Extra-xwiz” interface (Turkot *et al.*)): `-peaks=peakfinder8` (Barty *et al.*, 2014) `-min-snr=6` `-threshold=200` `-min-pix-count=1` `-max-pix-count=2` `-indexing=none` `-local-bg-radius=5` `-max-res=1200` `-min-peaks=0`. After manual inspection of the hit/peak finding results, custom python scripts were then used to extract image lists with at least 7 peaks for further processing. In a second pass, the pre-selected images were subjected to a 2nd round of hit/peak finding with the same parameters as before, apart from `-max-pix-count=20`, the addition of `-int-radius=2,4,6` `-min-peaks=10` and no maximum resolution set for peak finding. Indexing was attempted using `mosflm` (Powell *et al.*, 2013), `xgandalf` (Gevorkov *et al.*, 2019), `xds` (Kabsch, 2010) and `dirax` (Duisenberg, 1992) in that order.

Images were sorted into “LIGHT”, “DARK1” and “DARK2” based on the pulse IDs; the list of images were annotated accordingly and passed into the `partialator` program (White, 2019) from CrystFEL for merging using the “`—custom-split`” option, the unity model, a single iteration and `max-ADU` set to 110,000. All datasets were merged into point group `mmm`, and the space group was determined to be $C222_1$ using `AIMLESS` (Evans and Murshudov, 2013) from the CCP4 suite (Agirre *et al.*, 2023). The high-resolution cutoff was 1.8 Å for all data sets. A minimum of 40,000 indexed diffraction patterns were recorded for each data set.

2.2.10.7. TR-SFX Data Analysis, Model Building and Refinement

The dark structure reported in this manuscript was calculated from all of the DARK2 datasets for the 100 mJ/cm² laser fluence merged together for all time delays. We confirmed that no light contamination was visible in the DARK2 data sets by comparing them to the TRUE DARK data set collected without optical pump laser. The initial dark model was obtained by molecular replacement using the PHENIX program suite (Adams *et al.*, 2010) with the dark-state OaPAC co-crystallized with ATP solved at 100 K as search model.

q-weighted Fourier difference electron density maps were calculated with Xtrapol8 (de Zitter *et al.*, 2022) using a fraction of 60,000 diffraction patterns randomly chosen from all DARK data collected throughout the beamtime. The dark structure solved from that data set was used to phase the maps. No changes were visible when comparing LIGHT and DARK2 data sets with both laser intensities, showing that the selected time delays (ps and ns time scale) are too short to see changes in the electron density. However, the LIGHT-DARK1-DARK2 succession pattern was chosen as light contamination might occur in the first dark pulse data (DARK1), which could be tested for by comparing the DARK1 and DARK2 data. By investigating potentially light contaminated DARK1 data from the 100 mJ/cm² laser fluence exposure, strong differences surrounding the flavin chromophore became visible for some data sets. This indeed indicates a light contamination of our DARK1 data. Considering the light-contaminated DARK1 data as an additional “light”-state results in an additional time delay of 1.773 μ s (X-ray pulse period) between pump and probe pulse. Consequently, this resulted in calculated delay of 1034 ns (4.58 μ s minus 2 times 1.773 μ s), 1778 ns (5 ns plus 1.773 μ s) and 2273 ns (500 ns plus 1.773 μ s) for the DARK1 data and these new time-delays are referred to as 1 μ s, 1.8 μ s and 2.3 μ s, respectively. It should be noted that the aforementioned absorbed photon number calculation from the pump fluence represents the upper theoretical limit from the LIGHT data and the actual absorbed photons per molecule will be substantially lower in the light-contaminated data. Based on this, an exact photon dose could not be determined for the DARK1 data, but multi-photon effects can be excluded.

After q-weighted Fourier difference electron density map calculations between the light contaminated DARK1 data sets and the DARK2 data set, the occupancy of the light-activated state

was determined using Xtrapol8. An occupancy of around 25 % was obtained for the three time-delays, using the difference map method and singling out peaks with the highest integrated peak volume (de Zitter *et al.*, 2022). The difference map method only uses the X-ray data to estimate the occupancy, which avoid biases from prior knowledge on the triggered state or on the structure factor behaviour. This approach hinges on analysing the first extrapolated difference map obtained before structure refinement. Varying the reciprocal space occupancy (α), extrapolated difference maps are obtained with peaks height reaching its maximum when the occupancy is the closest to its real value. The occupancy value resulting in the extrapolated difference map with the greatest signal-to-noise ratio is considered the most likely. The estimation when integrating all peaks from the difference density did not converge toward a sharp occupancy estimation, however, after singling out the most significant peaks (around Tyr6, Gln48, Met92 and FMN), the signal to noise ratio was maximized at 25 % occupancy of the light activated state.

The mFo-DFc omit map-based method described by Barends *et al.* was also tested to determine occupancy of the 2.3 μ s light-activated state (Barends *et al.*, 2024). This method uses the changes in peak height in mFo-DFc omit maps between one atom or molecule position in the dark state to another position in the light-activated state to estimate the occupancy. The occupancy is calculated by dividing the peak height (ρ) of the light-excited atom position by the sum of the peak heights of both dark and light excited states atom positions:

$$Occ = \frac{\rho (\text{light state atom position})}{\rho (\text{light state atom position}) + \rho (\text{dark state atom position})}$$

An omit map was calculated with the 2.3 μ s delay DARK1 map and OaPAC SFX dark model using the simple omit map calculation tool of the PHENIX program suite (Adams *et al.*, 2010). Met92 SD atom positions in the dark state and in the light-activated state at 2.3 μ s were selected for the calculation.

Xtrapol8 was used to calculate extrapolated structure factor amplitudes of the light-activated state using the equation:

$$q|F_{extr}| = \alpha \times \frac{q}{(q)} \times (|F_{obs}^{light}| - |F_{obs}^{dark}|) + |F_{obs}^{dark}|$$

This extrapolation process is based on the assumption that structural rearrangements in the early photoactivation process of OaPAC are small, therefore the phases between the dark and the light-activated states are similar and extrapolated maps can be calculated by using the phases of the dark map. The extrapolated calculations generated some negative structure factor amplitudes, but for less than 5 % of structure factors, for each of the three extrapolated data sets (after 1 μ s, 1.8 μ s and 2.3 μ s calculated time delays). The “fref” option was used in Xtrapol8 in order to estimate their positive values (de Zitter *et al.*, 2022). With this approach, the assumption is that a strong negative difference amplitude is a consequence of measurement errors, and consequently the negative structure factors amplitudes are replaced by their corresponding values in the observed reference data set. This approach will however slightly bias the results towards the reference state, and should therefore only be used when less than 5 % of the total structure factor amplitudes are negative. The extrapolated electron density maps obtained after extrapolated structure factor determination were used to model the structural changes happening at the three time points collected.

All TR-SFX models were refined using both the PHENIX program suite (Adams *et al.*, 2010) and the CCP4 suite (Agirre *et al.*, 2023) and manual model building was done using COOT (Emsley *et al.*, 2010). SFX data and structure refinement statistics are shown in Appendix Table 2 and structural models (except 1 μ s) have been deposited in the Protein Data Bank under accession codes 8QFH, 8QFI and 8QFJ. The PyMOL Molecular Graphics System version 2.5.4 (Schrödinger and DeLano, 2020) was used to prepare all the figures representing the TR-SFX structural models of OaPAC.

In order to validate the data analysis and the results obtained with Xtrapol8, multi-copy refinement (Barends *et al.*, 2024) was performed. A new structural model of OaPAC₁₋₃₅₀ was created using COOT (Emsley *et al.*, 2010), corresponding to a combination of the dark state model at 75 % occupancy with fixed atom positions and a light-activated state model at 25 % occupancy, without pre-determination of the atom positions for the light-activated state. This new model was refined against the initial DARK1 electron density maps using the PHENIX program suite (Adams *et al.*, 2010). The light-activated state model was refined for atomic-positions in real and reciprocal space, as well as individual B-factors, but without occupancy refinement. Atomic positions of the light-activated state fraction of this model were then compared to the structural models of OaPAC light-activated states obtained with extrapolation.

2.2.10.8. Time-Resolved Serial Synchrotron Crystallography (TR-SSX) Data Collection

The microcrystal slurry was filtered with a 30 μm gravity flow filter before injection. 100 μL of slurry was applied onto a hit-and-return (HARE) chip (Mehrabi *et al.*, 2020; Bosman *et al.*, 2024) previously glow discharged. Excess liquid was pumped out and the chip was fixed to the sample holder before being mounted onto the translation stage of the T-REXX instrument (Pearson and Mehrabi, 2020) at the P14 end-station of Petra III synchrotron (Hamburg, Germany). A humidity chamber setup at 95 % humidity prevented dehydration and maintained the temperature at 20 $^{\circ}\text{C}$ during data collection. Data were recorded under the proposal MX947 with the help of David von Stetten from EMBL Hamburg, Germany.

For the dark state, the chips were raster scanned through the X-ray beam. One single diffraction pattern was recorded from each chip-well and diffraction patterns from one to two chips were merged to obtain a full data set. Each chip recorded 20736 images.

For the light-activated state, OaPAC₁₋₃₅₀ microcrystals were photoexcited with a 405 nm pulsed laser diode (NPL41B, Thorlabs, Bergkirchen, Germany). Pulses of 3 to 5 ns were repeated with a 10 MHz repetition rate to reach several ms exposure, equivalent to 55.1, 110.3, 220.5 and 441 mJ/cm^2 laser fluences (1, 2, 4 and 8 μJ laser intensities), respectively. For a sample of 6 μm thickness with an extinction coefficient at 405 nm of 6,000 $\text{M}^{-1} \text{cm}^{-1}$ and a laser beam diameter of 40 μm (FWHM), this was equivalent to 2.4, 4.7, 9.4 and 18.9 absorbed photons per molecule, respectively, according to the photon calculation Excel sheet by Grünbein *et al.* (Grünbein *et al.*, 2020). One single diffraction pattern was recorded from each chip-well and diffraction patterns from one to three chips were merged to obtain a full data set. The time delay was defined at 50 ms, 480 ms and 960 ms for the light-activated states recorded using HARE numbers 12 and 24 (Schulz *et al.*, 2018) for the 480 and 960 ms delay, respectively. The X-ray probe beam was focused to 15 x 10 μm^2 with 12.7 keV photon energy and a pulse length of 5 ms. Data were acquired with a DECTRIS EIGER2 x 4M detector.

2.2.10.9. TR-SSX Data Processing

During the experiment, online monitoring was performed with DOZOR (Melnikov *et al.*, 2018) and displayed on the GUI interface of MXCuBE (Oscarsson *et al.*, 2019). For the offline data processing, hit finding was performed using CrystFEL version 0.10.2 (White *et al.*, 2012) with the following parameters: `-peaks=zaef -min-snr=5 -threshold=20 -min-squared-gradient=100 min-pix-count=2 -max-pix-count=10 -int-rad=3,4,5 -high-res=1.95 -min-peaks=10`. Indexing was attempted with `xgandalf` (Gevorkov *et al.*, 2019) and `mosflm` (Powell *et al.*, 2013), in that order.

The images from the same beamtime were processed all together. The images with indexed hits were then passed into the `partialator` program (White, 2019) from CrystFEL for merging using the “`-custom-split`” option, the unity model, a single iteration and `max-ADU` set to 20,000. All datasets were merged into point group `mmm`, and the space group was determined to be $C222_1$ using AIMLESS (Evans and Murshudov, 2013) from the CCP4 suite (Agirre *et al.*, 2023). The high-resolution cutoff was 2 Å for all data sets from the first data collection (dark and 50 ms delay) and 2.05 Å for all data sets from the second data collection (dark and 480 and 960 ms delay).

2.2.10.10. TR-SSX Data Analysis, Model Building and Refinement

The dark structural models reported in this manuscript were obtained from DARK datasets of the first or second SSX data collection without any laser. The initial dark model was obtained by molecular replacement using the PHENIX program suite (Adams *et al.*, 2010) with the dark-state of OaPAC co-crystallized with ATP solved at room-temperature with SFX as search model. The dark SSX models were refined using the PHENIX program suite (Adams *et al.*, 2010) and manual model building was done using COOT (Emsley *et al.*, 2010).

q-weighted Fourier difference electron density maps were calculated with Xtrapol8 against the dark data sets (de Zitter *et al.*, 2022). The dark structure solved from the corresponding dark data set was used to phase the maps. By investigating the maps, strong differences became visible for all

the light data sets, except for the lowest laser fluence used of 55.1 mJ/cm². Structural changes of OaPAC on the ms time range were too large and/or unknown to use either the extrapolation process (de Zitter *et al.*, 2022) or mFo-DFc omit map-based occupancy determination followed by multi-copy refinement (Barends *et al.*, 2024) to retrieve the light-activated states model.

SSX data and structure refinement statistics are shown in Appendix Table 3. The PyMOL Molecular Graphics System version 2.5.4 (Schrödinger and DeLano, 2020) was used to prepare all the figures representing the TR-SSX structural models of OaPAC.

3. Results and Discussion

3.1. Background

Prior to the beginning of this thesis, two manuscripts involving crystallography experiments on OaPAC were already published (Ohki *et al.*, 2016; Ohki *et al.*, 2017). These manuscripts presented a description of the expression and purification strategies to produce OaPAC bound to non-cleavable N-terminal histidine-tag. The authors also briefly described another protocol to purify a histidine-tag-free OaPAC, which was used as a basis for the OaPAC purification strategy developed in this project. One crystallization condition was described in both papers, with which they grow microcrystals in orthorhombic crystal form with $P2_12_12_1$ space group using the vapor-diffusion technique.

Ohki *et al.* described the crystal structure of OaPAC in the dark (Ohki *et al.*, 2016) and after 20 s illumination (Ohki *et al.*, 2017). Yet, the light-activated structure of OaPAC revealed only minor changes, and no sign of non-cleavable ATP was visible in the active site, although the sample was co-crystallized with ApC_{pp}. Using mutation studies, they suggested the coiled-coil linker played a role in signal transduction from the BLUF to the AC domain. Nevertheless, no specific signalling pathway was proposed, and many questions remained to understand the signal transduction upon photoexcitation of the flavin chromophore.

Concurrently, a similar protein from another organism *Beggiatoa sp* named bPAC was investigated by Lindner and co-workers using crystallography and other complementary techniques (Lindner *et al.*, 2017; Lindner, 2018). In this study, the structure of bPAC was characterized, and the photoactivation mechanism was investigated. They examined the importance of the linker region, composed of the coiled-coil and the handle, to transmit the signal to the AC domain. Specifically, Lindner *et al.* suggested the tongue region interacting with the linker as a key regulator of the enzymatic domain response upon blue light exposure. Yet, their crystallographic observations were based on the structural model of a pseudo-lit state variant, and did not display intermediate steps during signal transduction.

3.2. Biophysical and Structural Characterization of OaPAC

3.2.1. Gene Expression and Protein Purification Optimization

OaPAC was cloned as described in the materials and methods section. After successful cloning of the different OaPAC constructs, expression tests were carried out using pCold_his-tag_OaPAC₁₋₃₅₀ to select the best parameters regarding growth media, DO of induction, temperature after induction, time of expression and lysis method. The three *E. coli* strains BL21 Star™ (DE3), Rosetta (DE3) and ArcticExpress (DE3) for recombinant protein expression were also compared.

Expression of His-tag_OaPAC₁₋₃₅₀ with a growth temperature of 10 °C for 5 days after induction led to a really low protein yield and was therefore abandoned (data not shown). Expression at 13 °C for 72 h was similar for all three strains tested (Figure 7A). The SDS-PAGE revealed a band at around 40 kDa - representing one protomer of OaPAC -, demonstrating a reasonable expression level. Yet almost no band corresponding to the soluble protein fraction after sonication was visible. To confirm that cell lysis by sonication was effective, as sonication could be inappropriate for very small volumes, the experiment was repeated with 5 cycles of freeze and thaw to test and compare the solubility. Once again, almost no band was visible for the three strains with this technique (Figure 7A), demonstrating that the soluble fraction of expressed protein at 13 °C was extremely low. Interestingly, expression at 13 °C with the strain ArcticExpress (DE3) was the lowest of all three *E. coli* strains tested, although the strain was developed with cold-adapted chaperones to increase solubility at low expression temperature (Agilent Technologies, Inc. 2010). Similar results as for 13 °C expression were observed for a culture at 18 °C after induction for 24 and 48 h (data not shown). Expression at 24 °C after induction led in general to a low yield (Figure 7B). Expression at 30 °C for 16 h was the most promising strategy, with the highest expression level and soluble fraction of expressed protein observed for BL21 Star™ (DE3) (Figure 7B). At 37 °C for 6 or 16 h, the expression was drastically reduced (data not shown).

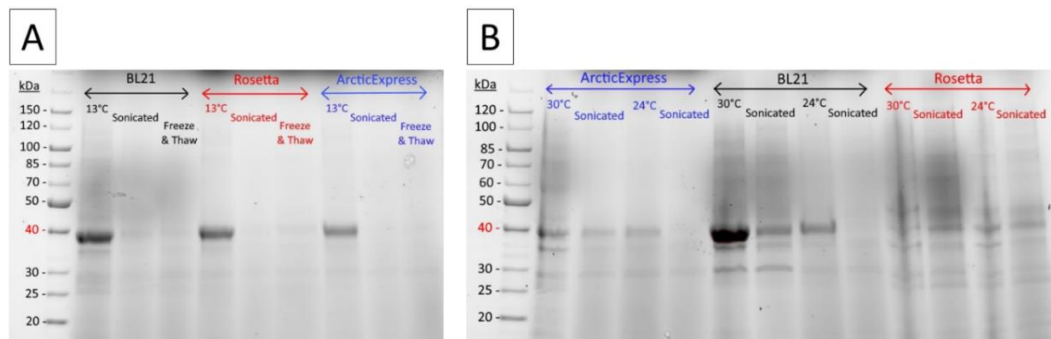


Figure 7: SDS-PAGE analysis of His-tag_OaPAC1-350 expression and solubility for different growth conditions. (A) His-tag_OaPAC₁₋₃₅₀ expression after double induction and expression at 13 °C for 72 h in BL21 Star™ (DE3) in black, Rosetta (DE3) in red and ArcticExpress (DE3) in blue. Although the expression level is reasonable, protein solubility tests after sonication or freeze and thaw lysis did not reveal any band for the three strains. (B) His-tag_OaPAC₁₋₃₅₀ expression after double induction and expression at 30 °C and 24 °C for 16 h in ArcticExpress (DE3) in blue, in BL21 Star™ (DE3) in black and Rosetta (DE3) in red. The gel reveals a strong band after expression at 30 °C with BL21 Star™ (DE3) and a weak band after sonication for this condition. The other conditions demonstrate a lower expression level and lower soluble fraction of the protein.

To confirm the preliminary results obtained with the expression test, an initial purification of His-tag_OaPAC₁₋₃₅₀ was conducted with the three *Escherichia coli* stains after gene expression at 30 °C for 16 h. After lysis using sonication and centrifugation, the supernatants were loaded onto a 5 mL HisTrap HP column for IMAC purification.

As OaPAC protein binds flavin *in vivo* and *in vitro*, monitoring the elution is facilitated by following the absorbance at 450 nm, where the flavin absorbance spectrum is at its maximum (Masuda *et al.*, 2005a; Hendriks *et al.*, 2009). The protein elutes when both absorbance at 280 nm and 450 nm are increasing simultaneously. Conveniently, OaPAC in solution exhibits a yellow colour, which also helps to follow the elution visually.

For BL21 Star™ (DE3) after expression at 30 °C, a clear peak with an increase of both absorbances was monitored during elution (Figure 8A), whereas only a small peak was observed for the expression in Rosetta (DE3) (Figure 8B) and no distinguishable peak for ArcticExpress (DE3) (Figure 8C). These results confirmed the preliminary observation from the expression test. Consequently, compared to Ohki *et al.*'s protocol, where the expression was optimized using *E. coli* stain ArcticExpress (DE3) and a temperature after induction of 10 °C and 5 days of culture (Ohki *et al.*, 2016), soluble His-tag_OaPAC₁₋₃₅₀ protein was found in higher yield when the related gene was expressed in *E. coli* BL21 Star™ (DE3) for 16 h at 30 °C after induction.

Gene expression was also optimized using LB as growth medium without supplementation of antibiotics, and the induction performed with cold shock and 1 mM IPTG at an OD_{600nm} between 0.4 and 0.6. The selected expression strategy was then applied to OaPAC₁₋₃₅₀, OaPAC₁₋₃₆₆ and His-tag_OaPAC₁₋₁₃₇ and enabled the production of all proteins to high yield, therefore no additional gene expression tests were carried out for the different OaPAC variants. Optimization of culture conditions has been shown to enhance gene expression level considerably in many studies (Weickert *et al.*, 1996; Zhang *et al.*, 2009; Francis and Page, 2010; Kaur *et al.*, 2018; Gutiérrez-González *et al.*, 2019; Damough *et al.*, 2021; Zhang *et al.*, 2022). As the amount of protein required for serial crystallography and especially TR-SFX experiments using liquid jet is extremely high (Weierstall, 2014; Sierra *et al.*, 2018; Cheng, 2020; Echelmeier *et al.*, 2020), optimizing expression significantly reduces the time required to prepare a sufficient amount of protein for these experiments.

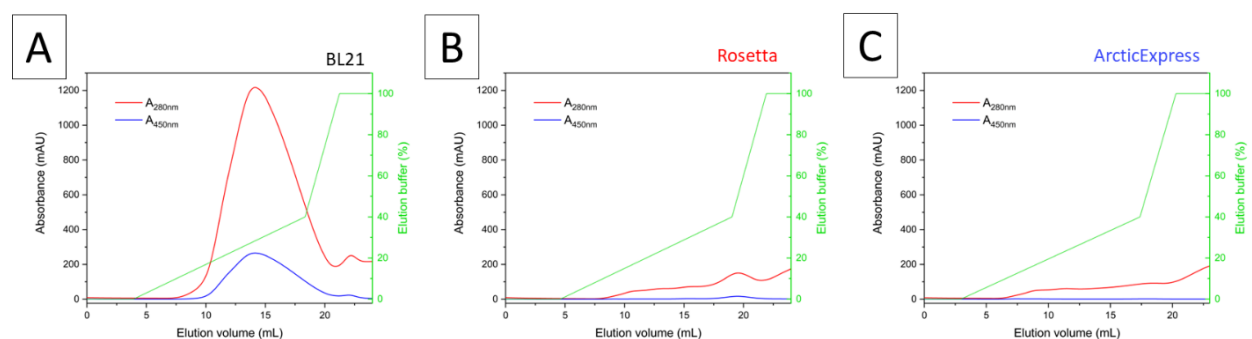


Figure 8: Comparison of IMAC purification of His-tag_OaPAC₁₋₃₅₀ after gene expression for 16 h at 30 °C with three different *E. coli* strains.

(A) Chromatograph of the affinity purification after gene expression in BL21 Star™ (DE3). The protein of interest elutes at an elution buffer concentration of about 30%, revealing a good expression of soluble His-tag_OaPAC₁₋₃₅₀. (B) Chromatograph of the affinity purification after gene expression in Rosetta (DE3) displayed almost no protein binding and elution. (C) Chromatograph of the affinity purification after gene expression in ArcticExpress (DE3) manifested no protein binding and elution.

The red curves correspond to the absorbance at 280 nm, whereas the blue curves correspond to the absorbance at 450 nm. The green curves display the gradient of elution buffer concentration during elution.

Figures were created with Origin software version 2024.

After determination of the optimal expression conditions, the purification strategy of OaPAC was optimized to achieve the highest yield and purity, essential for the following crystallography experiments. The first optimization was conducted on the lysis protocol. While Ohki *et al.* used sonication as lysis strategy (Ohki *et al.*, 2016), testing sonication and high pressure homogenization

with His-tag_OaPAC₁₋₃₅₀ revealed that a higher yield could be achieved with high pressure homogenization. The SEC chromatographs of a test purification disclosed a higher absorbance peak maximum and area under the curve for the sample prepared with a high-pressure homogenizer compared to a sonicator (Figure 9). After concentration of the purified protein, 60 % of the protein amount was recovered with sonication, compared to a 100 % standard for high-pressure homogenization. High-pressure homogenization was already found to yield better results during cell lysis compared to sonication for many proteins (Grabski, 2009; D'Hondt *et al.*, 2017). It allows a more complete as well as gentler cell disruption, lowering heat production which decreases protein degradation. Consequently, all the following lysate preparation for OaPAC were performed with high-pressure homogenization.

His-tag_OaPAC₁₋₃₅₀ and His-tag_OaPAC₁₋₁₃₇ purification did not require much additional optimization. Following a two-step protocol with IMAC followed by SEC purification led to a high protein yield with purity above 95 % and good stability. An example of a chromatograph of the final purification step for His-tag_OaPAC₁₋₃₅₀ is shown in Figure 10, when exchanging the SEC Superdex 200 Increase 10/300 column for a HiLoad 26/600 Superdex 200. The SDS-PAGE analysis after SEC indicates a high purity of the protein of interest, after separating contaminants with higher molecular weight, which elute earlier (Figure 10).

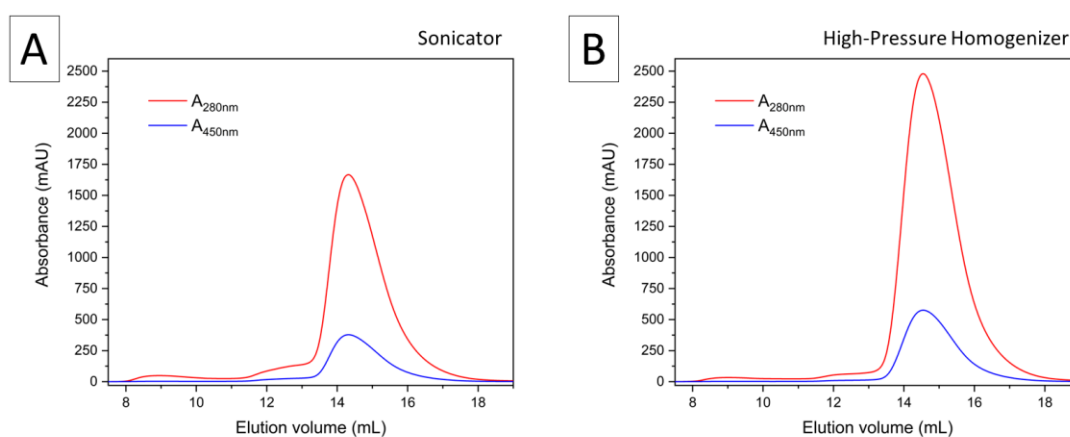


Figure 9: Comparison of cell lysis methods for the production of OaPAC proteins.

(A) SEC chromatograph of His-tag_OaPAC₁₋₃₅₀ after cell disruption with sonicator and a first purification step with affinity chromatography. The protein of interest is eluted after about 14.5 mL with a peak height maximum of 1750 mAU. (B) SEC chromatograph after lysate preparation with high-pressure homogenizer and a first purification step with affinity chromatography. The protein of interest is eluted after about 14.5 mL with a peak height maximum of 2500 mAU, confirming higher yield obtained after lysis with high-pressure homogenizer. The red curves correspond to the absorbance at 280 nm, whereas the blue curves correspond to the absorbance at 450 nm.

Figures were created with Origin software version 2024.

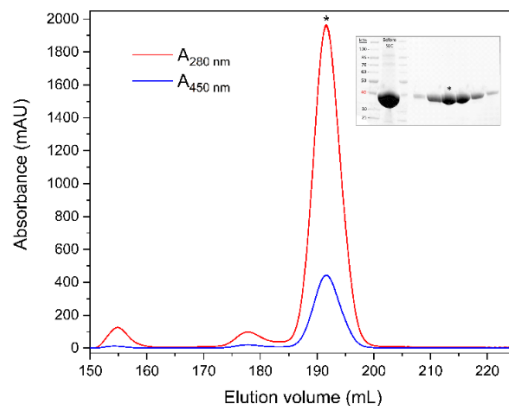


Figure 10: Optimized final purification step and SDS-PAGE analysis for His-tag_OaPAC₁₋₃₅₀.

Chromatograph of SEC corresponding to the second and final purification step for His-tag_OaPAC₁₋₃₅₀ using a HiLoad 26/600 Superdex 200 pg column. The protein of interest is eluted at about 192 mL (*). The contaminants present before SEC observed on the SDS-PAGE are separated from the peak where the protein of interest elutes, thanks to an elution distributed over a higher volume with the HiLoad column. The red curve corresponds to the absorbance at 280 nm, whereas the blue curve corresponds to the absorbance at 450 nm.

Figure was created with Origin software version 2024.

Removal of the hexa-histidine-tag from His-tag-OaPAC₁₋₃₅₀ proved unsuccessful, as observed by Ohki *et al.* previously (Ohki *et al.*, 2016). This inefficient cleavage might be due to an inaccessible histidine-tag and cleavage site, or a result of the high hydrophobicity of the amino acid sequence next to the cleavage site, as reported by (He *et al.*, 1993). The presence of the TEE, the N-terminal poly-histidine tag, the Factor Xa cleavage site and one additional amino acid, totalling 16 additional amino acids, was unfavourable. Increased disordering was noted in the BLUF domain after the first crystallization tests using His-tag-OaPAC₁₋₃₅₀, which could come from the additional amino acids as no electron density was observed for them (data not shown). Besides, non-native amino acids around the BLUF domain might affect the physiological signal transmission pathway of OaPAC upon blue light exposure, which would hinder the study of signal transmission in BLUF photoreceptors. Consequently, efforts were made to produce a native OaPAC₁₋₃₅₀ without additional amino acids before the N-terminus. OaPAC₁₋₃₅₀ was used for most of the subsequent characterization steps and crystallography experiments unless otherwise stated.

Purification of OaPAC₁₋₃₅₀ was based on the protocol described by Ohki *et al.* (Ohki *et al.*, 2016), although several parameters were optimized and a SEC step was added to generate the highest yield and purity possible. A combination of anion-exchange, ammonium sulphate precipitation and cation-exchange chromatography, followed by a final SEC purification led to the optimal purification strategy (Figure 11A-C). The use of step-gradient instead of linear gradient for both

ion-exchange chromatography steps greatly improved purity and reduced loss of protein. It was crucial to eliminate all the contaminants between 50 and 100 kDa during the anion and cation exchange chromatography and ammonium sulphate precipitation (Figure 11A-B), as the SEC could not separate them from OaPAC₁₋₃₅₀ (80 kDa). The SEC removed the majority of the remaining contaminant with an observed molecular weight of 120 kDa as well as potential OaPAC₁₋₃₅₀ aggregates formed during concentration steps or because of the long time required for the purification (Figure 11C).

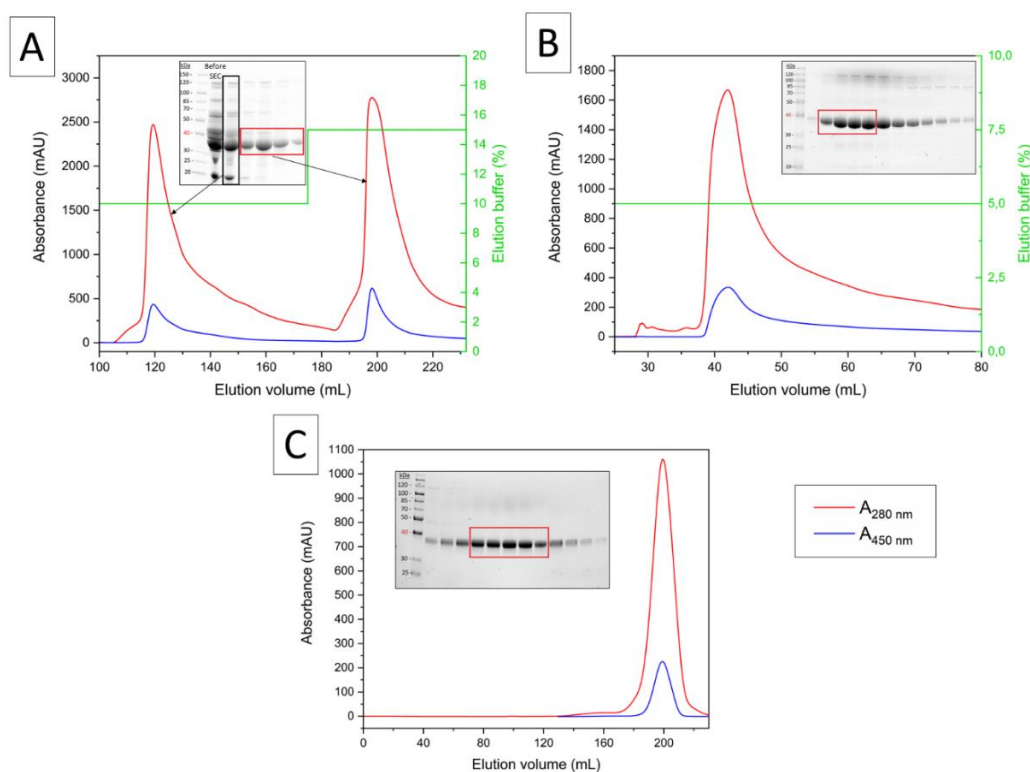


Figure 11: Purification strategy for OaPAC₁₋₃₅₀ and OaPAC₁₋₃₆₆ consists of a combination of anion-exchange, cation-exchange and size exclusion chromatography.

(A) Chromatograph of the anion exchange purification for OaPAC₁₋₃₅₀. Although a considerable amount of OaPAC protein is lost (which might be misfolded or aggregated), this anion exchange chromatography eliminates many contaminants from the first step. (B) Chromatograph of cation exchange chromatography for OaPAC₁₋₃₅₀ after anion exchange chromatography and ammonium sulphate precipitation steps. The protein interacts weakly with the resin and elutes early at 5 % (v/v) elution buffer with two major contaminants. As the contaminants revealed on the SDS-PAGE at 85 kDa cannot be removed during SEC, fractions containing this contaminant were carefully avoided for the subsequent steps. (C) Chromatograph of SEC corresponding to the fourth and final purification step for OaPAC₁₋₃₅₀. The protein of interest is eluted after approximately 200 mL. The contaminants present before SEC with a molecular weight of 120 kDa are separated from the peak where the protein of interest elutes. The symmetrical elution peak shape and the SDS-PAGE confirm a highly pure protein. The red curves correspond to the absorbance at 280 nm, whereas the blue curves correspond to the absorbance at 450 nm. The green curves display the gradient of elution buffer concentration during elution.

Figures were created with Origin software version 2024.

Buffer compositions were also improved for each step. As a result of the purification strategy optimization, 15 mg of Tag-free_OaPAC₁₋₃₅₀ could be retrieved for each litre of cell culture. Due to the robustness of the purification protocol, it was used for the purification of OaPAC₁₋₃₆₆ and also led to a high sample purity.

3.2.2. Protein Stability

Stability and homogeneity are essential components for a successful crystallization process (Durbin and Feher, 1996; Kim *et al.*, 2011), which is a requirement for X-ray diffraction based experiments. A stable protein *in vitro* is a prerequisite for conducting experiments that requires measurements for several h at room-temperature, such as the spectroscopic and biochemical characterization.

Structural stability and self-association or aggregation studies with DLS were conducted with all OaPAC variants in their final storage buffers. High stability was achieved for several days for OaPAC₁₋₃₅₀, OaPAC₁₋₃₆₆ and His-tag_OaPAC₁₋₁₃₇ at 4 °C (Figure 12). The mean hydrodynamic radius values were 3.5 nm with a standard deviation of 0.2 nm for OaPAC₁₋₃₅₀, and 4.2 nm with a standard deviation of 0.3 nm for OaPAC₁₋₃₆₆ (Figure 12A-B and Table 12), confirming a homodimeric form in solution (theoretical molecular weight of 80 kDa for OaPAC₁₋₃₅₀ and 83 kDa for His-tag_OaPAC₁₋₃₅₀). Ohki *et al.* already suggested the homodimeric structure of OaPAC in solution based on analytical ultracentrifugation analysis (Ohki *et al.*, 2016). The fact that no increase in radius nor in polydispersity was observed, even after four days at 4 °C, confirmed that the two protein variants were stable in solution (Figure 12A-B).

The mean hydrodynamic radius value for His-tag_OaPAC₁₋₁₃₇ was 2.2 nm with a standard deviation of 0.5 nm for 4 days of measurements (Figure 12C and Table 12). An increase in mean values and polydispersity was observed after around 20 h, revealing a lower stability for the shorter variant of OaPAC. Nonetheless, as His-tag_OaPAC₁₋₁₃₇ was only designed for spectroscopic analysis and not for crystallography experiments, the observed stability over 20 h with a mean radius value of 1.8 nm and 0.1 nm standard deviation was satisfactory (Figure 12C and Table 12). The results confirmed His-tag_OaPAC₁₋₁₃₇ to be a homodimer in solution (theoretical molecular weight of 37 kDa).

Notably, a shorter variant of His-tag_OaPAC was initially designed with residues 1 to 95 only but the variant was extremely unstable in solution, although it could be expressed and purified easily. The missing coiled coil from this variant, which enables OaPAC homodimerization, affected not only the oligomeric state of His-tag_OaPAC₁₋₉₅ but also the general stability of the protein. Homodimerization is an essential process for PAC activity, as both protomers are involved in ATP binding in both active sites (Lindner *et al.*, 2017). Therefore, studying shorter variants of OaPAC is only reasonable if the homodimeric structure is kept intact.

The stability of OaPAC₁₋₃₅₀ was also tested at room-temperature to verify the possibility of crystallizing the protein at room-temperature as well as for spectroscopic measurements and activity assays requiring several h of measurements or incubation time at room-temperature. After four days of measurements, the mean hydrodynamic radius of OaPAC₁₋₃₅₀ was 3.7 nm with a standard deviation of 0.2 nm (Figure 12D and Table 12). A slight increase in mean values was observed continuously, revealing a slightly lower stability of the protein at room-temperature compared to 4 °C. Nevertheless, no substantial aggregation was observed, even after four days at room-temperature. Therefore, these results showed that crystallization at room-temperature was possible, as well as the following spectroscopic and enzymatic properties analysis.

Consequently, optimization of the purification protocols and choice of buffers was successful to obtain the stable proteins and homogeneous samples required for the subsequent analysis steps.

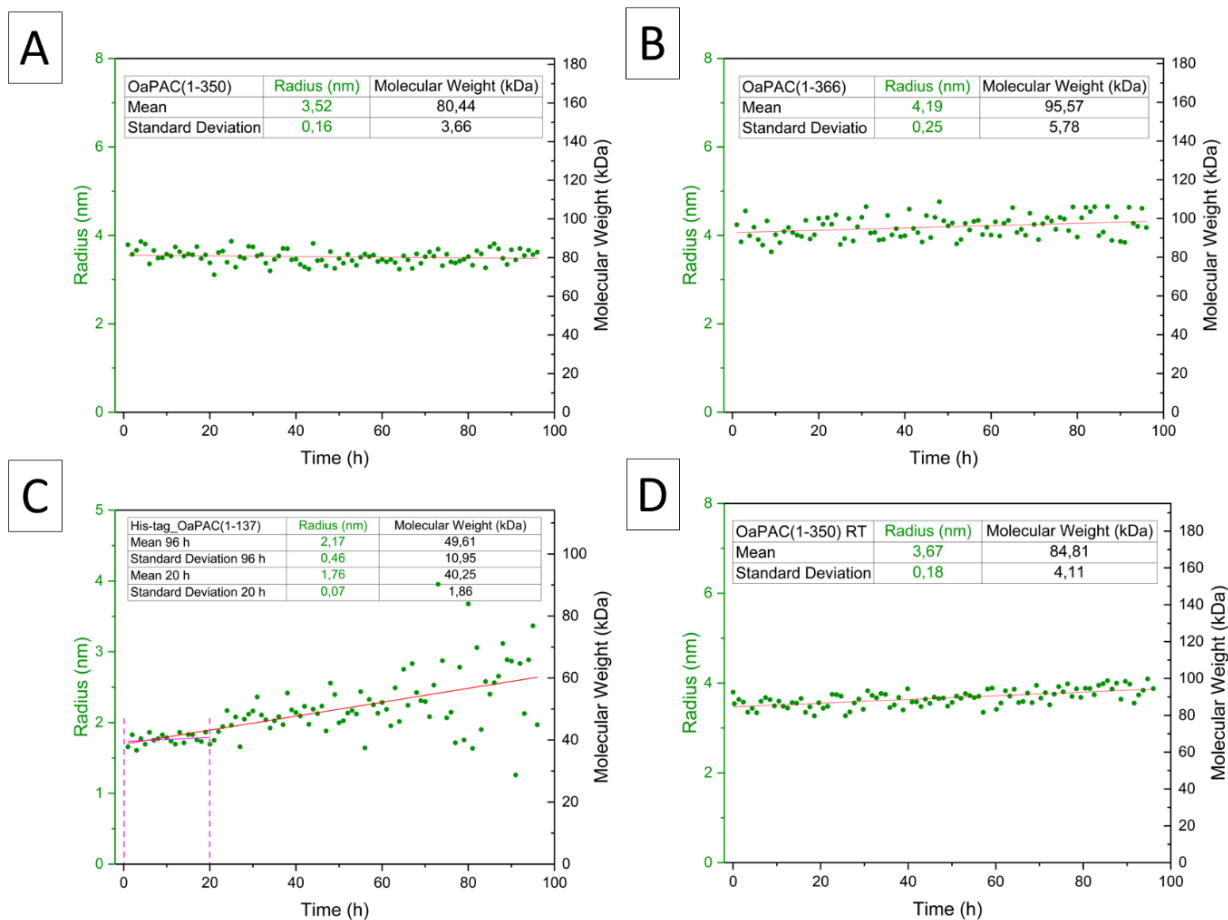


Figure 12: Protein stability analysis of three OaPAC variants after purification, flash-freezing and thawing, based on DLS-measurements.

Graphs representing hydrodynamic radius measurements (green) and associated molecular weight of OaPAC variant over 96 h. The mean and standard deviation values over 96 h or 20 h are indicated in the table. (A) For OaPAC₁₋₃₅₀ at 4 °C, hydrodynamic radius values are stable over the time recorded. (B) For OaPAC₁₋₃₆₆ at 4 °C, hydrodynamic radius values are stable over the time recorded. (C) For His-tag_OaPAC₁₋₃₅₀ at 4 °C, hydrodynamic radius values are stable over 20 h (pink delimitation) and are increasing after that. (D) For OaPAC₁₋₃₅₀ at 22 °C, hydrodynamic radius values are slowly increasing over time, showing a slightly lower stability at 22 °C.

Figures were created with Origin software version 2024. Data analysis was performed using a linear fit (red line).

	OaPAC ₁₋₃₅₀ Radius at 4 °C	OaPAC ₁₋₃₆₆ Radius at 4 °C	His-tag_OaPAC ₁₋₁₃₇ Radius at 4 °C	His-tag_OaPAC ₁₋₁₃₇ Radius at 4 °C for 20 h only	OaPAC ₁₋₃₅₀ Radius at 22 °C
Equation	$y = a + b \cdot x$	$y = a + b \cdot x$	$y = a + b \cdot x$	$y = a + b \cdot x$	$y = a + b \cdot x$
Intercept	3.55 ± 0.03	4.06 ± 0.05	1.70 ± 0.08	1.73 ± 0.03	3.47 ± 0.03
Slope	-0.001 ± 0.001	0.003 ± 0.001	0.010 ± 0.001	0.003 ± 0.003	0.004 ± 0.001
Residual Sum of Squares	2.40	5.61	12.78	0.10	2.06
Pearson's R	-0.13	0.29	0.60	0.24	0.62
R-Square (COD)	0.02	0.081	0.36	0.058	0.38
Adj. R-Square	0.007	0.071	0.351	0.006	0.378
Number of Points	96	96	96	20	96
Radius mean (nm)	3.5	4.2	2.2	1.8	3.7
Radius SD (nm)	0.2	0.3	0.5	0.1	0.2
MW mean (kDa)	80.4	95.6	49.6	40.3	84.8
MW SD (kDa)	3.7	5.8	11.0	1.9	4.1

Table 12: Equation parameters and values from data analysis of OaPAC variants stability performed by the Origin software version 2024 using a linear fit as shown in Figure 12.

3.2.3. Spectroscopic and Enzymatic Properties of OaPAC₁₋₃₅₀

BLUF photoreceptors bind FAD or FMN *in vitro* (Hendriks *et al.*, 2009) and display the typical flavin visible absorption spectrum in the dark with a double peak and a maximum absorption at approximately 443 nm (Figure 13A). Under continuous 435 nm-LED illumination, the maximum

absorption red-shifts around 13 nm to peak at 456 in the light-activated state, as previously described (Masuda and Bauer, 2002), confirming the change of hydrogen bond network in OaPAC in solution. To verify that OaPAC could also be activated with a shorter laser pulse and other wavelengths, OaPAC₁₋₃₅₀ in solution was exposed for 50 ms to a 355 nm-laser and a spectrum was recorded at the icOS platform (von Stetten *et al.*, 2015) after 1 s delay (Figure 13B). Data were collected with the help of Nicolas Caramello and Sylvain Engilberge from ESRF and were processed by Nicolas Caramello. The light-activated spectrum shows a similar red-shift of 12.5 nm at the maximum absorption near 450 nm. Of note, Ohki *et al.* only observed a 9.6 nm red-shift under illumination for the same protein, potentially indicating an incomplete signalling state formation (Ohki *et al.*, 2017).

As the maximum change in absorption upon blue light exposure occurs at 492 nm for BLUF photoreceptors (Figure 13A), the absorption at 492 nm was used to monitor photoactivation and relaxation kinetics of OaPAC₁₋₃₅₀ in solution. Both photoactivation and relaxation revealed an exponential change in the absorbance at 492 nm (Figure 13C-D). Similar to Ohki *et al.* (Ohki *et al.*, 2017), the kinetics can be characterized, with a margin of error, by a single-phase exponential equation that does not exhibit a burst phase (Table 13), and changes were fully reversible. Under the conditions used, the activation rate for OaPAC₁₋₃₅₀ in solution was $k = 2.10 \text{ s}^{-1}$ with a half-life of 0.33 s and the relaxation rate was ten times slower with $k = 0.19 \text{ s}^{-1}$ and a half-life around 3.74 s. The relaxation rate is slower than kinetics observed by Ohki *et al.* with the same protein ($k = 0.25 \text{ s}^{-1}$ and $t(1/2) = 2.8 \text{ s}$) (Ohki *et al.*, 2016). Differences can be caused by different protein concentrations and illumination conditions, but can also be due to an incomplete signalling state formation in the Ohki *et al.* study, as revealed by the smaller red-shift in the absorption spectrum after photoexcitation (Ohki *et al.*, 2017). Collado *et al.* observed a 14 nm red-shift in the absorption spectrum and also obtained a half-life around 3.5 s (time constant of 5 s) when analysing the dark recovery rate of OaPAC in solution at 444 nm (Collado *et al.*, 2022).

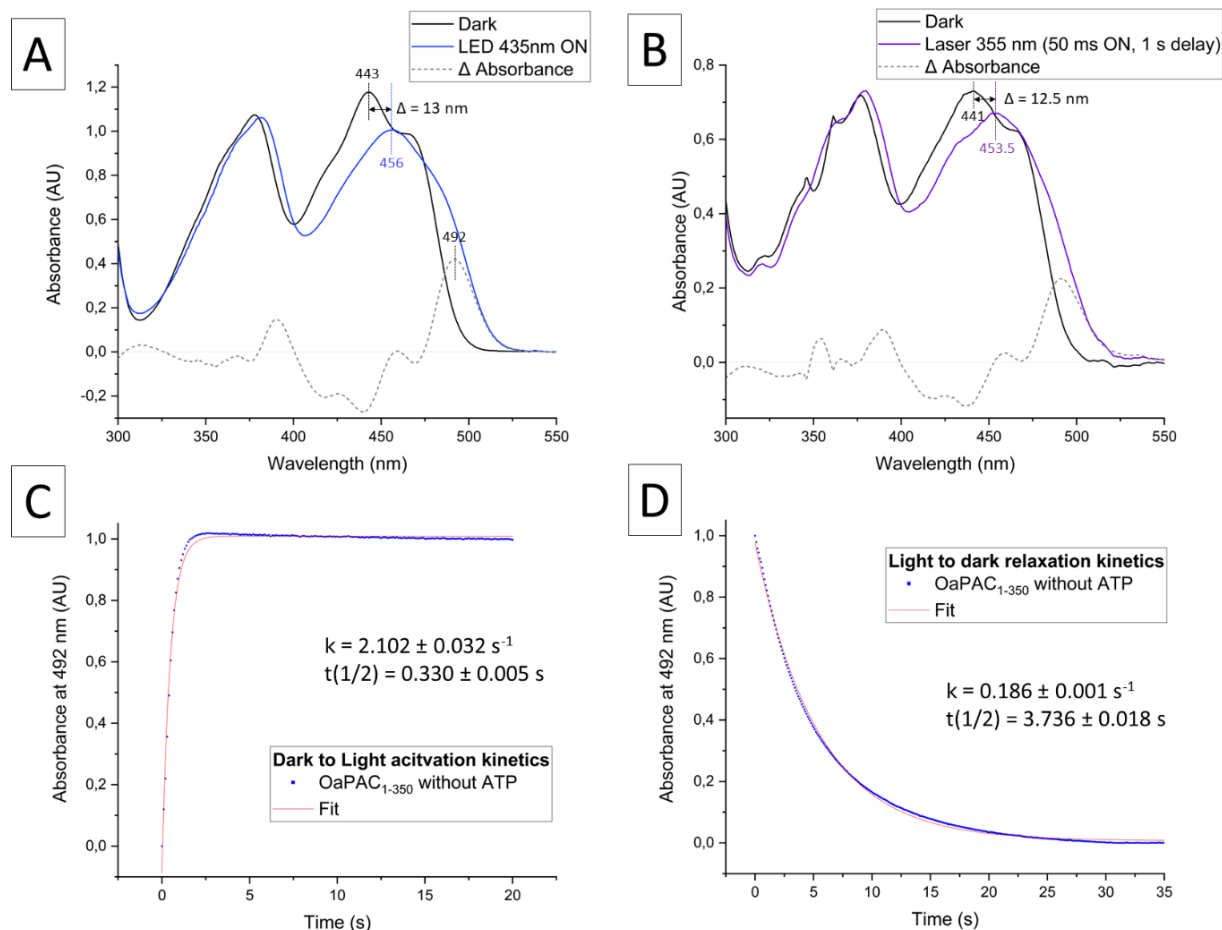


Figure 13: Spectral properties of OaPAC₁₋₃₅₀ in solution.

(A) Room-temperature UV-Vis absorption spectra of OaPAC₁₋₃₅₀ in solution measured in the dark or under continuous illumination with LED light at 435 nm. Blue and dark lines show the light- and dark-adapted states, respectively. A red-shift of 13 nm of the absorption maximum at around 450 nm occurs upon light excitation. The grey dashed line corresponds to the difference in absorbance between the light- and dark-adapted states. The maximal change between both absorption spectra is observed at 492 nm. (B) Room-temperature UV-Vis absorption spectra of OaPAC₁₋₃₅₀ in solution measured under red light or after 50 ms laser illumination at 355 nm and 1 s delay. Purple and dark lines show the light- and dark-adapted states, respectively. A red-shift of 12.5 nm of the absorption maximum at around 450 nm is observed upon light excitation. The grey dashed line corresponds to the difference in absorbance between the light- and dark-adapted states. (C) Photoactivation kinetics of OaPAC₁₋₃₅₀ in solution. The photoactivation was monitored by absorbance change at 492 nm. At time 0, the 435 nm-LED light was turned on. (D) Relaxation kinetics of PAC₁₋₃₅₀ in solution after LED illumination. The relaxation was monitored by absorbance change at 492 nm. At time 0, the 435 nm-LED light was turned off.

Figures were created with Origin software version 2024. Data analysis was performed using a one-phase exponential equation to fit (red line) the photoactivation and relaxation kinetics.

	Dark to light kinetics fit	Light to dark kinetics fit
Model	One-phase exponential activation	One-phase exponential decay
Reduced Chi-Sqr	0.0002	0.0001
R-Square (COD)	0.9891	0.9984
Adj. R-Square	0.9890	0.9984
Residual Sum of Squares	0.0369	0.0293
k (s ⁻¹)	2.102 ± 0.032	0.186 ± 0.001
t(1/2) (s)	0.330 ± 0.005	3.736 ± 0.018

Table 13: Values from data analysis of OaPAC₁₋₃₅₀ activation and relaxation kinetics performed by the Origin software version 2024 using a one-phase exponential fit as shown in Figure 13.

The spectral properties of OaPAC₁₋₃₅₀ confirmed the presence of the signalling state upon blue light illumination in the BLUF domain, but activity of the AC domain needed to be verified to confirm the full functionality of the protein. To test this, an activity assay was used which detects cAMP levels in solution. For this activity assay, light-dependent AC activity enabling ATP conversion to cAMP is linked to a decrease in luminescence signal. The assay was performed after 40 s blue light illumination of OaPAC₁₋₃₅₀ in the presence of ATP to analyse the production of cAMP by the AC domain. The response depending on the protein concentration was characterized with a sigmoidal dose-response equation and revealed a decrease in luminescence reaching its minimum at 10 μM OaPAC concentration (Figure 14A), confirming the capability of OaPAC₁₋₃₅₀ AC domain to properly convert ATP into cAMP.

Complementary FTIR measurements were performed by Marius Nagel and Tilman Kottke from Bielefeld University to follow ATP conversion in solution. After 4 s blue light illumination of OaPAC₁₋₃₅₀ in the presence of ATP, characteristic difference signals of ATP and products were observed in the spectral range 900-1300 cm⁻¹ (Figure 14B-D). Difference absorption signals after photoexcitation and 5.2 min delay agreed with the presence of cAMP, pyrophosphate and phosphate, being the product and byproducts of the adenylate cyclase activity (Figure 14B). More precisely, the subtraction of the ATP signals from cAMP signals results in a spectrum which differs from the ATP turnover spectrum in OaPAC₁₋₃₅₀ (Figure 14C). ATP and cAMP reference spectra were subtracted from the OaPAC₁₋₃₅₀ spectrum, and the remaining signals could be assigned to that of pyrophosphate and phosphate (Figure 14D). Consequently, the remaining difference signals of

OaPAC after illumination can be clearly assigned to ATP and the products of its photo-induced turnover to cAMP, confirming the full functionality of OaPAC₁₋₃₅₀ in solution.

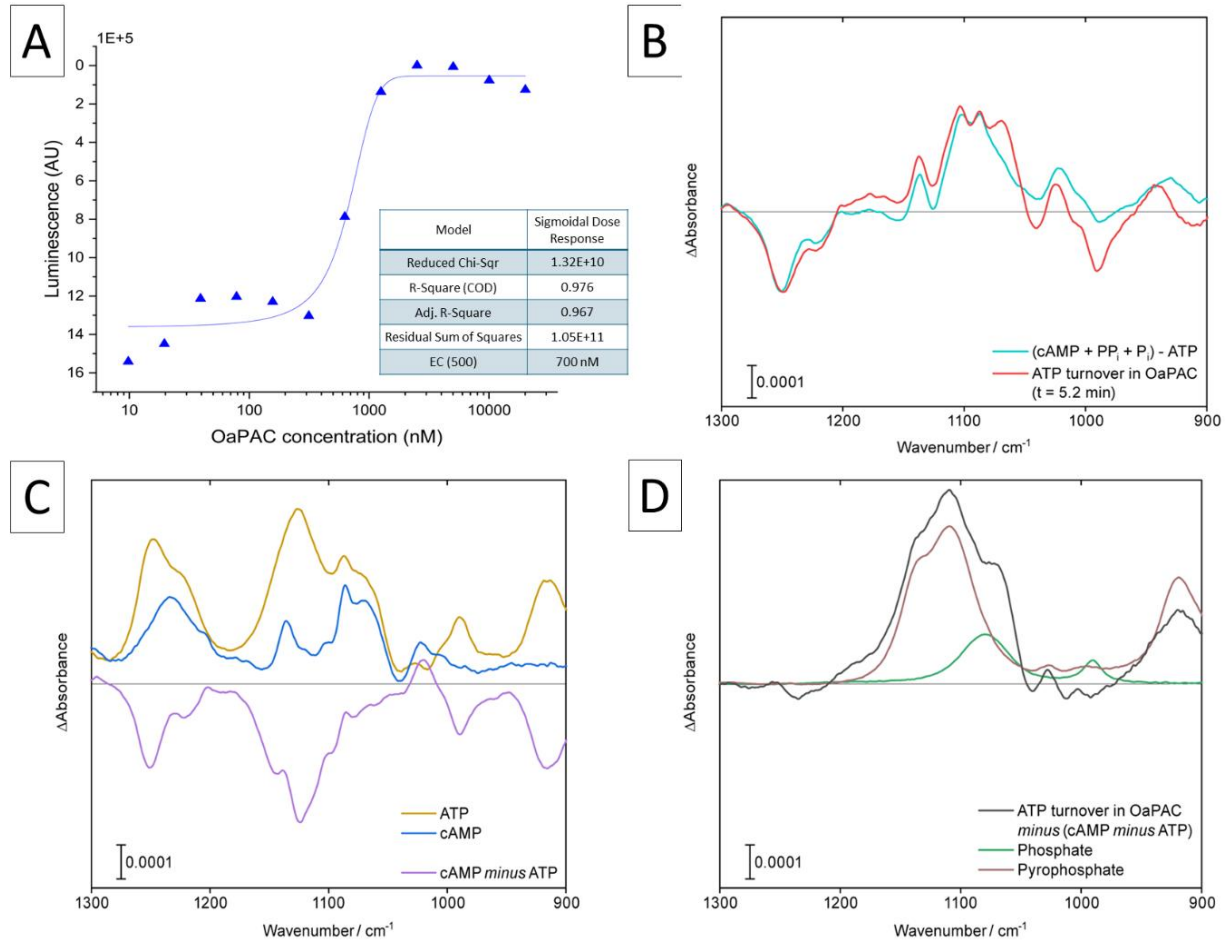


Figure 14: ATP turnover analysis in OaPAC₁₋₃₅₀ in solution using activity assay and FTIR spectroscopy.

(A) Results of a cAMP-Glo activity assay (Promega) for testing the adenylyl cyclase activity of OaPAC₁₋₃₅₀. The blue triangles represent the measured luminescence after the assay depending on the protein concentration. The luminescence decreases with increased OaPAC₁₋₃₅₀ concentration, meaning that ATP conversion to cAMP increases. Figure was created with Origin software version 2024. Data analysis was performed using a sigmoidal dose-response equation to fit (blue line) the luminescence variation. Values from data analysis and fit are presented in the table embedded in the graph. (B) Recorded light-minus-dark FTIR difference signal from ATP (red) in the 1300 to 900 cm^{-1} region matches the expected signal of cAMP, pyrophosphate (PPi) and phosphate (Pi) minus ATP (cyan), confirming the conversion of ATP to cAMP in OaPAC₁₋₃₅₀ upon blue light excitation. Figure from (Chretien et al., 2024). (C) Reference spectra of ATP (yellow) and cAMP (blue) in solution and resulting 'cAMP minus ATP' spectrum (purple) are shown. Figure from (Chretien et al., 2024). (D) Subtraction of cAMP and ATP from OaPAC₁₋₃₅₀ difference spectrum in solution (black) matches well the contribution of byproducts pyrophosphate (brown) and phosphate (green) from the conversion of ATP to cAMP. Figure from (Chretien et al., 2024).

3.2.4. Crystallization

Crystallization trials for OaPAC₁₋₃₅₀ and OaPAC₁₋₃₆₆ were performed initially with three crystallization screens using the sitting drop vapor diffusion technique. Plates were prepared under ambient light or dark/red light conditions and were incubated at 20 and 4 °C for several days. For OaPAC₁₋₃₆₆, no crystal was observed for any of the conditions, even after several optimization trials. OaPAC₁₋₃₅₀ crystallized easily and showed two major crystal morphologies (Figure 15A,D). By testing the diffraction of two different populations, it was revealed that OaPAC₁₋₃₅₀ crystals were found in two different space groups: C222₁ for condition A, with a resolution reaching around 2.2 Å, and P2₁2₁2₁ for condition D with a resolution not greater than 4 Å. Optimization of the orthorhombic crystal form with C222₁ space group led to the establishment of the best crystallization condition composed of 100 mM SPG buffer pH 7.0, 1.2 M disodium malonate, 100 mM guanidine hydrochloride and 5 mM magnesium chloride, reaching a resolution of 1.5 Å in the dark without ATP and 2.1 Å with ATP (Figure 15B-C and Table 14). Optimization of the orthorhombic crystal form with P2₁2₁2₁ space group was unsuccessful when screening around crystallization conditions, additives and temperature, always resulting in long and thin needle shaped crystals (Figure 15D). Several rounds of seeding using crystals from condition D led to bigger and thicker crystals without and co-crystallized with ATP (Figure 15E-F and Table 14), but the resolution was only improved to 3.5 Å. As 3.5 Å is not sufficient to distinguish small conformational changes during signal transmission of OaPAC, efforts were made to optimize the resolution further but were unsuccessful. The condition used for OaPAC crystallization in P2₁2₁2₁ was similar to the one described by Ohki *et al.*, for which the crystal diffracted at 2.9 Å resolution (Ohki *et al.*, 2016). Notably, bPAC also crystallized in a P2₁2₁2₁ space group and the best resolution achievable was 3.3 Å, whereas bPAC crystallized in P1 with a resolution of 1.8 Å (Lindner, 2018), suggesting an intrinsic lower ordering of the molecules in the P2₁2₁2₁ crystals. Recently, Kapetanaki *et al.* published a structure of OaPAC solved in P2₁2₁2 space group at cryogenic temperature at 1.95 Å (1.8 Å at RT with SSX and 1.75 Å with SFX) (Kapetanaki *et al.*, 2024). However, the published structure displayed a reduced accessible solvent area in the ATP binding pocket, resulting in a close active site conformation most likely preventing substrate binding. Addition of ATP proved indeed unsuccessful in obtaining ATP-bound crystal structure with this

space group. In order to thoroughly study the enzymatic domain activity with TRX, ATP binding in the crystal is, however, essential.

Interestingly, OaPAC₁₋₃₅₀ crystals could be grown under ambient light, while none grew under constant blue light illumination, possibly as structural changes upon illumination destabilized the crystal growth. This suggests that OaPAC requires a strong light signal to be activated, as crystal growth was not destabilized by ambient light. Nakasone *et al.* also suggested OaPAC cyclase responded non-linearly to light intensity and hence could only be activated under strong light conditions in nature (Nakasone *et al.*, 2023).

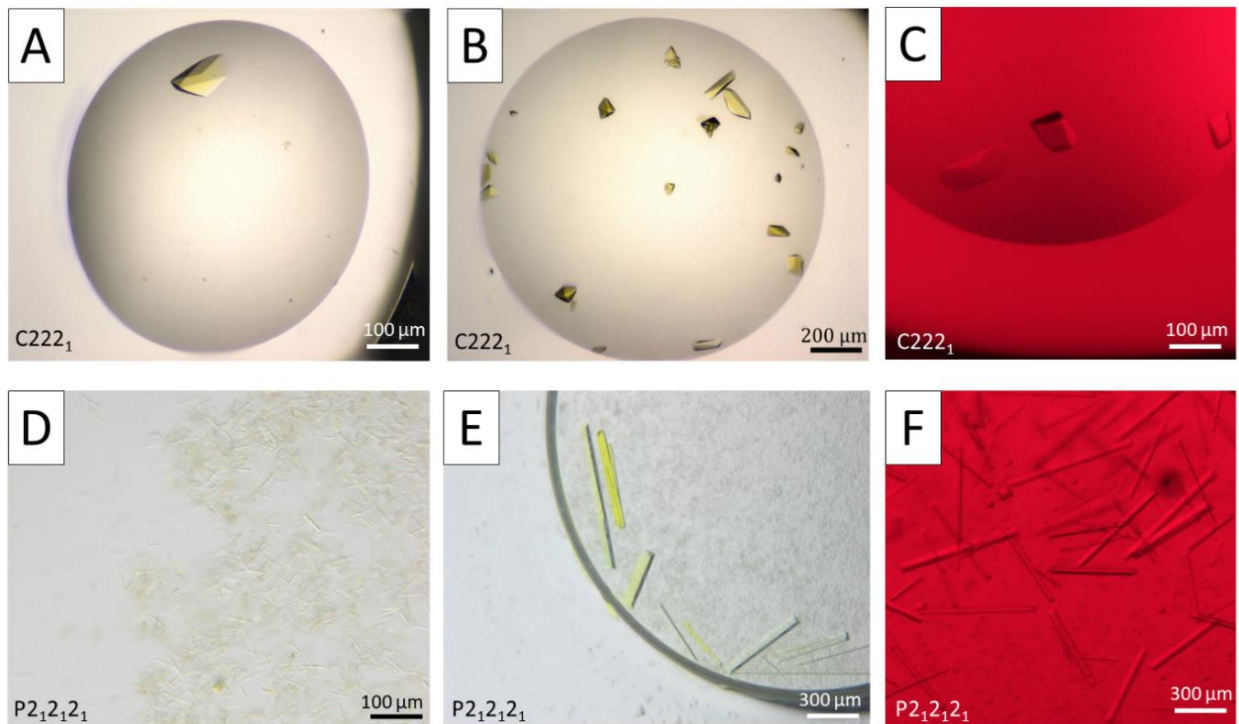


Figure 15: OaPAC₁₋₃₅₀ crystallization trial at 4 °C.

(A) Image of a single macrocrystal of OaPAC₁₋₃₅₀ grown in C222₁ space group using hanging drop vapor diffusion. (B) Image of several OaPAC₁₋₃₅₀ macrocrystals grown in C222₁ space group using hanging drop vapor diffusion with an optimized crystallization condition. Images (A) and (B) were recorded with the SONICC instrument (FORMULATRIX, Beldford, USA). (C) Image of three OaPAC₁₋₃₅₀ macrocrystals grown in C222₁ space group under red light using hanging drop vapor diffusion with an optimized crystallization condition. (D) Image of several OaPAC₁₋₃₅₀ macrocrystals grown in P2₁2₁2₁ space group using hanging drop vapor. (E) Image of several OaPAC₁₋₃₅₀ macrocrystals grown as in (D) after three cycles of seeding with crushed crystals from (D) for the first seeding cycle. (F) Image of several OaPAC₁₋₃₅₀ macrocrystals grown in P2₁2₁2₁ space group under red light using hanging drop vapor diffusion after three cycles of seeding with crushed crystals from (D) for the first seeding cycle. Images (C) to (F) were recorded with a stereomicroscope (SMZ18, Nikon, Amstelveen, the Netherlands).

	Space group	Crystallization buffer	Growth condition
A	C222 ₁	100 mM SPG buffer pH 7.0, 1.2 M disodium malonate	Ambient Light
B	C222 ₁	100 mM SPG buffer pH 7.0, 1.2 M disodium malonate, 100 mM guanidine hydrochloride, 5 mM MgCl ₂	Ambient Light
C	C222 ₁	100 mM SPG buffer pH 7.0, 1.2 M disodium malonate, 100 mM guanidine hydrochloride, 5 mM MgCl ₂ , 5 mM ATP	Dark/Red Light
D	P2 ₁ 2 ₁ 2 ₁	100 mM sodium citrate pH 5.5, 10 % (v/v) PEG 20000, 5 mM MgCl ₂	Ambient Light
E	P2 ₁ 2 ₁ 2 ₁	100 mM sodium citrate pH 5.5, 10 % (v/v) PEG 20000, 5 mM MgCl ₂ + Seeds	Ambient Light
F	P2 ₁ 2 ₁ 2 ₁	100 mM sodium citrate pH 5.5, 10 % (v/v) PEG 20000, 5 mM MgCl ₂ , 5 mM ATP + Seeds	Dark/Red Light

Table 14: Description of the crystallization conditions used to obtain the crystals shown in Figure 15.

To confirm the formation of the signalling state in OaPAC crystals, both orthorhombic crystal forms with C222₁ and P2₁2₁2₁ space groups were tested at the icOS platform (von Stetten *et al.*, 2015) for UV-Vis absorption. A single crystal was exposed for 50 ms with a 355 nm-laser and light-activated spectra were recorded after 1 s delay (Figure 16). Data were collected with the help of Nicolas Caramello and Sylvain Engilberge from ESRF and were processed by Nicolas Caramello. Crystals with both C222₁ and P2₁2₁2₁ space groups displayed the typical red-shift upon photoactivation, confirming the presence of the signalling state in the BLUF domain upon blue light illumination of OaPAC crystals. Similar to OaPAC₁₋₃₅₀ in solution with the same setup (Figure 13B), C222₁ crystals exhibited a 12.5 nm shift (Figure 16A), while only a 11 nm-shift was observed for P2₁2₁2₁ crystal.

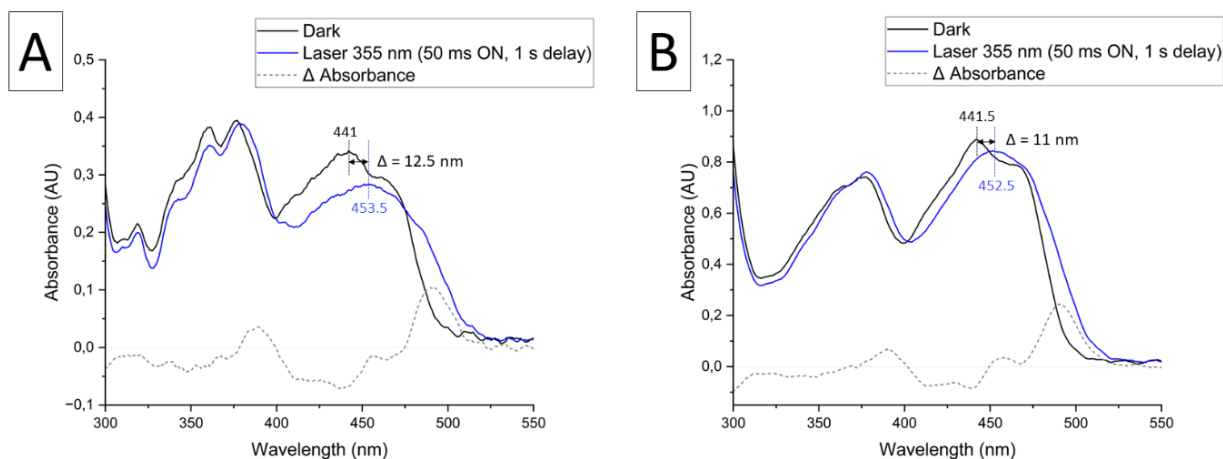


Figure 16: Spectral properties of OaPAC₁₋₃₅₀ crystals.

(A) In crystallo optical spectroscopy analysis of OaPAC₁₋₃₅₀ C222₁ crystals. UV-Vis absorption measurements were performed at room-temperature under red light (referred to as dark) or after 50 ms laser illumination at 355 nm and 1 s delay. Blue and dark lines show the light- and dark-adapted states, respectively. A red-shift of 12.5 nm at around 450 nm is observed. (B) In crystallo optical spectroscopy analysis of OaPAC₁₋₃₅₀ P2₁2₁2₁ crystals. UV-Vis absorption measurements are performed as in (A). A red-shift of 11 nm at around 450 nm is observed.

The grey dashed lines correspond to the difference in absorbance between the light- and dark-adapted states.

Figures were created with Origin software version 2024.

Interestingly, with a 50 ms laser pulse at low laser fluence, the P2₁2₁2₁ crystal showed signs of damage with cracks appearing where the laser spot hit the crystal (Figure 17A-B), and the crystal started dissolving with a laser fluence around 8 times stronger (Figure 17C-D), suggesting a disruption of the crystal packing due to the protein structure rearranging in reaction to light. In addition to poor resolution, this loss of long-range order in P2₁2₁2₁ crystal packing upon light-induced structure rearrangements was a significant barrier to using these crystals in TRX experiments. Crystals growing in the P2₁2₁2₁ space group were therefore not selected for further studies. On the other hand, the C222₁ crystals showed no sign of visible damage, even after photoexcitation with high laser fluence (Figure 17E-F), while still displaying the complete red-shifted absorption upon photoexcitation (Figure 16A). C222₁ crystals were therefore selected for subsequent use and analysis.

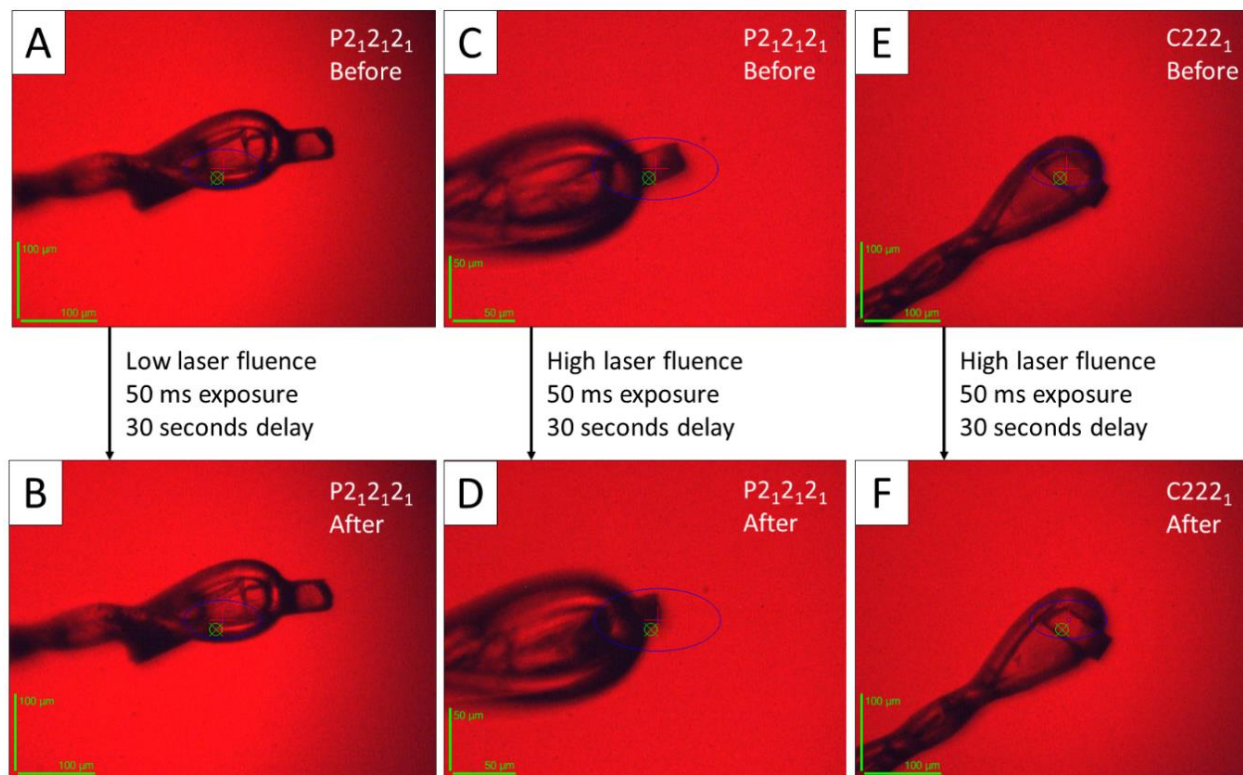


Figure 17: OaPAC₁₋₃₅₀ crystal images recorded before and after 355 nm-laser exposure.

OaPAC₁₋₃₅₀ P₂₁₂₁₂₁ crystal before (A) and after (B) 50 ms exposure with 355 nm-laser at 76.4 mJ/cm² and around 30 s delay. The P₂₁₂₁₂₁ crystal shows damage with cracks (B) even at low laser fluence. OaPAC₁₋₃₅₀ P₂₁₂₁₂₁ crystal before (C) and after (D) 50 ms exposure with 355 nm-laser at 636.6 mJ/cm² and around 30 s delay. The P₂₁₂₁₂₁ crystal dissolves (D) at high laser fluence. OaPAC₁₋₃₅₀ C₂₂₂₁ crystal before (E) and after (F) 50 ms exposure with 355 nm-laser at 636.6 mJ/cm² and around 30 s delay. The C₂₂₂₁ crystal shows no sign of visible damage (F) even at high laser fluence.

The crystallization of C₂₂₂₁ crystals was optimized for batch crystallization to obtain microcrystals suitable for TRX experiments (Figure 18). OaPAC₁₋₃₅₀ at 12 mg/mL was mixed in a one-to-one ratio with OaPAC batch crystallization buffer, with an increased concentration of disodium succinate to 1.4 M compared to 1.2 M for vapor diffusion crystallization. Seeds were prepared by crushing OaPAC C₂₂₂₁ crystals with seed beads and vortexing. By varying the concentration of seeds from 2 to 10 % (v/v) of the final crystallization volume, it was possible to control crystal size and obtain crystals of 7 x 3 x 2 μm³ for TR-SFX experiment (Figure 18A) and 25 x 12 x 6 μm³ for TR-SSX experiment (Figure 18B). Crystals were concentrated to 20 % pellet volume (v/v) (Figure 18C) to ensure a satisfactory hit rate. Crystal size and morphology were homogeneous within a batch for each experiment. Microcrystals hardly visible using a stereomicroscope were observed under the TEM after negative staining (Figure 18D). The crystalline state of the slurry could be

confirmed and lattice spacing in different orientations could be analysed (Figure 18E). It confirmed that the crystal lattice dimensions were in line with the dimensions obtained from the C222₁ crystals at cryogenic conditions. Strikingly the crystal lattice could be seen with such high resolution that it could be overlaid with a reconstructed two-dimensional crystal packing from the crystallographic data (Figure 18F), confirming that these microcrystals also grew in the selected C222₁ space group.

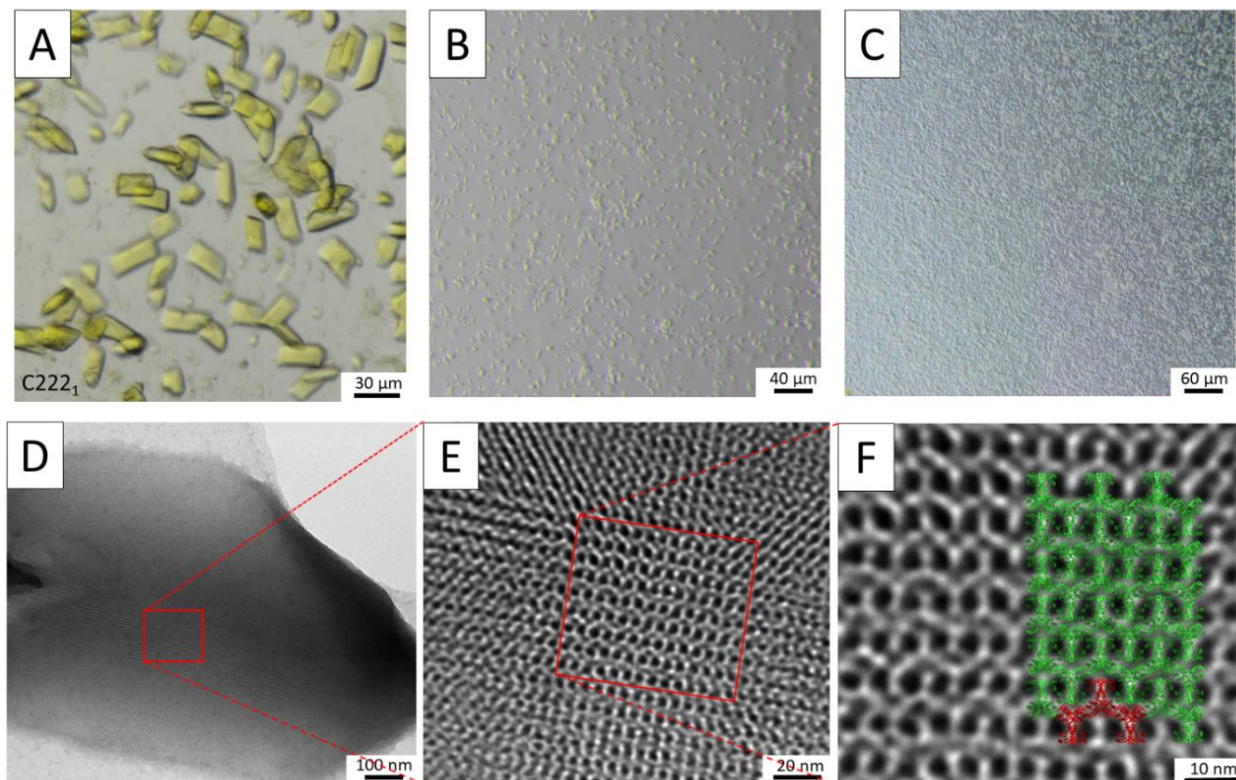


Figure 18: Microcrystal slurry suitable for TR-SSX and TR-SFX experiments.

(A) OaPAC₁₋₃₅₀ microcrystals of approximately $28 \times 12 \times 8 \mu\text{m}^3$ used for TR-SSX data collection at the T-REXX instrument (Petra III, Hamburg, Germany). (B) Unconcentrated slurry of $7 \times 3 \times 2 \mu\text{m}^3$ microcrystals used for TR-SFX data collection at the SPB/SFX instrument (EuXFEL, Schenefeld, Germany). (C) Microcrystal slurry corresponding to (B) after concentration by sedimentation to 20 % pellet volume (v/v). (D) OaPAC₁₋₃₅₀ microcrystal observed under the transmission electron microscopy after negative staining, confirming the crystalline form of the sample. (E) Crystal lattice of the well-ordered microcrystal shown in (D). (F) Superposition of the crystal lattice shown in (E) with a reconstructed crystal packing obtained from previous X-ray diffraction data from OaPAC₁₋₃₅₀. The matching overlay confirmed that both crystals belong to the same space group.

The smaller crystals used for TR-SFX are ideal for homogeneous photoexcitation (Panneels *et al.*, 2015; Schulz *et al.*, 2022). Molecules present at the back of the crystals will receive a similar photon dose compared to molecules at the front, as little absorption occurs when light travels through thin crystals. Additionally, the use of a liquid-jet for sample delivery at the SPX/SFX instrument also requires crystals to be smaller than 10 microns, to limit the risk of nozzle clogging during sample delivery (Grünbein and Nass Kovacs, 2019; Wijn *et al.*, 2022).

For TR-SSX experiment at the T-REXX instrument, smaller crystals than $25 \times 12 \times 6 \mu\text{m}^3$ were first tested but gave too weak diffraction. The P14 end-station offers a beam flux of around 2×10^{12} ph/s with a beam of $15 \times 10 \mu\text{m}^2$, which is relatively weak. In addition, the crystals seemed to adopt a preferential orientation on the chip with the smallest dimension (6 μm width) aligned along the X-ray beam axis, therefore the thinner crystals were insufficient to generate decent diffraction. Luckily, the use of fixed-target chips for TR-SSX experiment did not impose strong limitations on crystals size (Mehrabi *et al.*, 2020).

3.2.5. Dark State Structural Model of OaPAC₁₋₃₅₀

A structural model of OaPAC₁₋₃₅₀ without ATP could be solved in orthorhombic form in the C222₁ space group at 1.5 Å resolution at cryogenic temperature (PDB 8QFE). Data collection and refinement statistics are shown in Appendix Table 1. The overall secondary structure is comparable to previously determined OaPAC (Ohki *et al.*, 2016) and bPAC (Lindner *et al.*, 2017) structures (Figure 19A). However, OaPAC was crystallized by Ohki *et al.* in either an orthorhombic space group (PDB 4YUT) or in a hexagonal space group (PDB 4YUS), with a 2.4 Å C α RMSD and a 2.2 Å C α RMSD when compared to OaPAC from this study (PDB 8QFE), respectively. The differences likely arise from the different crystal packing for each structure, influencing certain domains and amino acids to adopt specific conformations based on the neighbouring proteins in the crystals.

A representation of the OaPAC model without ATP (PDB 8QFE) can be found in Figure 19B, with annotation of the secondary structure elements. OaPAC shows the typical BLUF domain arrangement with an alpha/beta-sandwich-like fold, which consists of 5 stranded β -sheet surrounded by α -helices in a $\beta\alpha\beta\beta\alpha\beta$ arrangement, as previously described (Hendriks *et al.*, 2009;

Ohki *et al.*, 2016). In solution, OaPAC was observed to bind both FMN and FAD molecules (Appendix Figure 1). However, in the crystal, the AMP moiety was not visible in the electron density. The bound flavin molecule was only modelled as FMN, sitting on top of the β -sheet between the two α -helices. The BLUF domain is not in direct contact with the AC domain, but a central α -helix acts as a linker. Indeed, the fifth β -strand of the BLUF domain is connected to the N-terminus of the central α -helix 3 by a short loop region, and the C-terminus of the second helix linker is in return in contact with the AC domain of the second protomer.

The α -helix 3 linker forms a coiled coil with the α -helix from the second protomer to create the dimerization interface (Figure 19B), which is a unique feature of PAC photoreceptors in the BLUF family (Ohki *et al.*, 2016; Lindner *et al.*, 2017). OaPAC is found as an homodimer in the crystal, as expected from DLS measurements (Figure 12) and mass spectrometry data (Appendix Figure 1) in solution.

The AC domain follows a much more complex folding, with an 8 stranded β -sheet and 8 α -helices, consistent with a typical class III AC-fold (Figure 19B). AC domains from both protomers face each other in an antiparallel fashion. Unlike bPAC (Lindner *et al.*, 2017), OaPAC does not present an asymmetry of the tongue region between β -sheets 9 and 10, which is consistent with Ohki *et al.* and Kapetanaki *et al.*'s results on OaPAC (Ohki *et al.*, 2016; Kapetanaki *et al.*, 2024). The C-terminal region, composed of α -helices 11 and 12, is highly disordered, and deviates the most between the four PAC structural models (Figure 19A).

The structural model of OaPAC with ATP was also solved in the orthorhombic form with C222₁ space group at 2.1 Å resolution at cryogenic temperature (PDB 8QFF). Data collection and refinement statistics are shown in Appendix Table 1. The two structural models mainly differ around the two active sites, and a detailed analysis of ATP binding and the overall active site arrangement is given in section 3.4.1. Additionally, a near radiation damage-free structure of OaPAC with ATP was solved in the orthorhombic form with C222₁ space group at 1.8 Å resolution at room-temperature (PDB 8QFH) using SFX at the EuXFEL. Data collection and refinement statistics are shown in Appendix Table 2. The obtained structure is similar to the structure with ATP at cryogenic temperature with 0.40 Å C α RMSD over 350 residues. A detailed analysis of ATP binding at room-temperature is given in section 3.4.1.

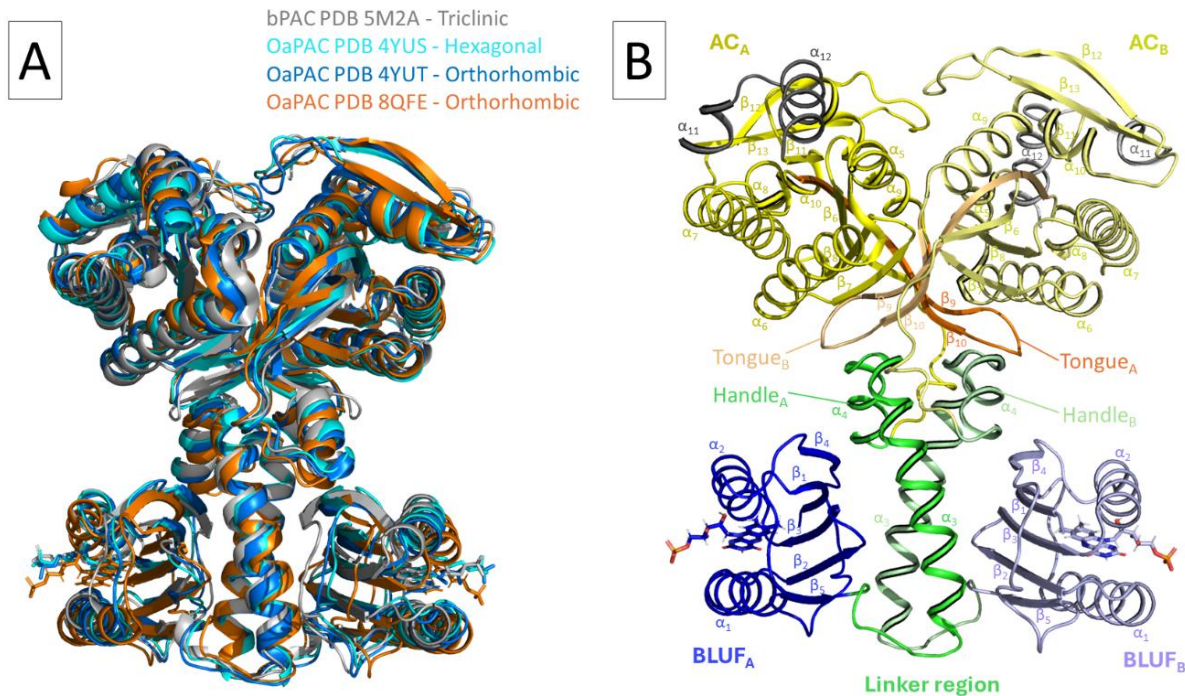


Figure 19: Structural models of OaPAC and bPAC.

(A) Overlay of the structural models of Lindner *et al.* with triclinic space group in grey (PDB 5M2A) (Lindner *et al.*, 2017), Ohki *et al.* with hexagonal space group in cyan (PDB 4YUS), orthorhombic space group in blue (4YUT) (Ohki *et al.*, 2016), and Chretien *et al.* with orthorhombic space group in orange (PDB 8QFE) (Chretien *et al.*, 2024). (B) Annotation of secondary structure elements of OaPAC in cartoon representation with the BLUF domain of one protomer in dark blue and the other protomer in light purple, AC domain in yellow shades and linker region in green shades. The tongue region of both protomers in the AC domains is highlighted in orange and light orange. No asymmetry is observed in the tongue region.

Figures prepared by the PyMOL Molecular Graphics System, Version 2.5.4 Schrödinger, LLC (Schrödinger and DeLano, 2020). Both figures are modified from Chretien *et al.* (Chretien *et al.*, 2024).

When comparing the three dark state structures with and without ATP, three regions appear to display higher temperature factors compared to the rest of the protein (Figure 20). The C-terminal region, which was thought to be generally disordered, is one of them. C or N-terminal regions are known to be generally flexible or even unstructured (Savvides *et al.*, 2004; Bourhis *et al.*, 2005; Belle *et al.*, 2008; Valsecchi *et al.*, 2013; Laptenko *et al.*, 2016), therefore increased temperature factors in these regions are not surprising. Disordered regions can be key regulators in signalling pathways and essential in cellular processes (Wright and Dyson, 1999; Iakoucheva *et al.*, 2002; Dyson and Wright, 2005; Galea *et al.*, 2008). 16-amino acids from the C-terminal were already truncated due to activity inhibition in OaPAC (Hirano *et al.*, 2019), supporting a regulatory role of the flexible C-terminal tail of OaPAC.

The two loops between β -sheets 4 and 5 and between β -sheet 5 and α -helix 3 also display higher flexibility (Figure 20 and Figure 21A). Interestingly, overlaying the amino acid positions of the three structures for both of these regions reveals significant differences between them (Figure 21B-C). The loops are displaced when aligning the three models, and residues composing these loops are modelled at different positions and/or with different orientations. Some residues such as Asp102 and Phe103 even exhibit alternative conformations within one model (Figure 21B). This increased flexibility in both loops might indicate dynamic regions useful for signal transduction, and were therefore of interest during this study. Lindner *et al.* studied bPAC using hydrogen-deuterium exchange mass spectrometry (HDX-MS) and also highlighted the C-terminus as well as residues 80 to 105, composed of both loops and β -sheet 5, to be more dynamic than the rest of the structure (Lindner *et al.*, 2017).

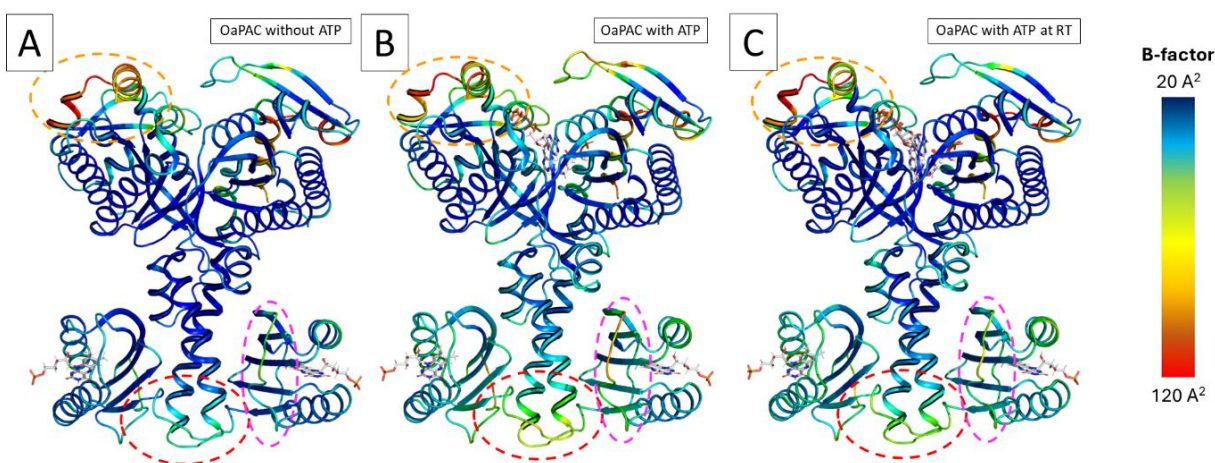


Figure 20: Temperature factors analysis of OaPAC₁₋₃₅₀ structural models derived from X-ray crystallography data collection at cryogenic temperature and at room-temperature, with and without ATP.

The cartoon models are coloured depending on temperature factor values. The highest temperature-factor is represented in red and the lowest in blue. The FMN chromophore and ATP ligand are represented in white with sticks. (A) Structural model of OaPAC₁₋₃₅₀ without ATP from an X-ray diffraction experiment at cryogenic temperatures. (B) Structural model of OaPAC₁₋₃₅₀ when co-crystallized with ATP from an X-ray diffraction experiment at cryogenic temperatures. (C) Structural model of OaPAC₁₋₃₅₀ when co-crystallized with ATP from a serial X-ray diffraction experiment at room-temperature.

The temperature factors are higher in the three highlighted regions: the C-terminal region (circled in orange), the loop between β -sheets 4 and 5 (circled in red) and the loop between β -sheet 5 and the α -helix linker (circled in magenta). These represent the regions with increased flexibility.

Figures prepared by the PyMOL Molecular Graphics System, Version 2.5.4 Schrödinger, LLC (Schrödinger and DeLano, 2020).

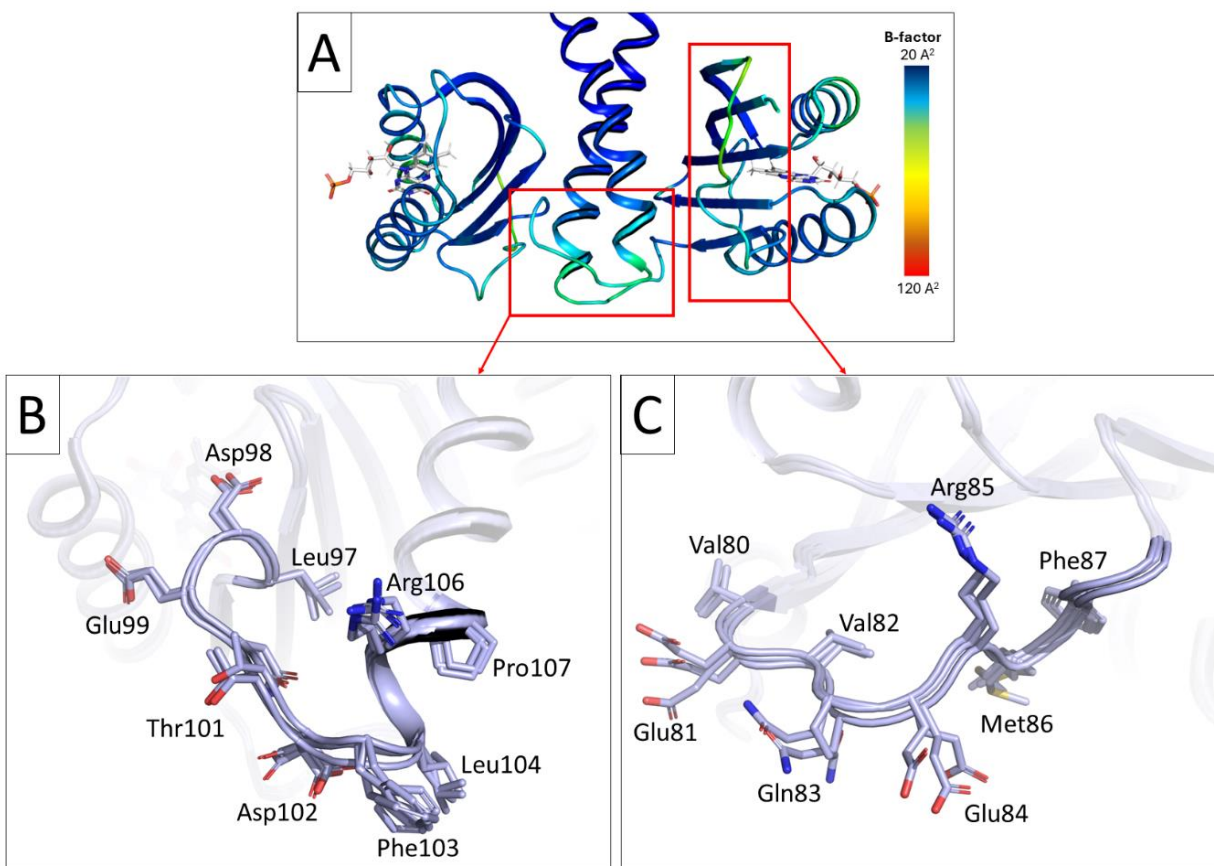


Figure 21: Close-up of the flexible region in the BLUF domain of OaPAC₁₋₃₅₀.

(A) Close-up on the temperature factors of the BLUF domain and linker region of the structural model of OaPAC₁₋₃₅₀ as shown in Figure 20A. Low temperature factors are represented in dark blue and colours moving toward yellow represent higher temperature factors. (B) Close-up on the overlaid structures of the loop between β -sheet 5 and the α -helix linker revealing increased flexibility. (C) Close-up on the overlaid structures of the loop between β -sheets 4 and 5 revealing increased flexibility. The three models overlaid in (B) and (C) represent the structural models of OaPAC₁₋₃₅₀ without ATP and when co-crystallized with ATP at cryogenic temperature, as well as OaPAC₁₋₃₅₀ with ATP at room-temperature.

Figures prepared by the PyMOL Molecular Graphics System, Version 2.5.4 Schrödinger, LLC (Schrödinger and DeLano, 2020).

A closer look at the BLUF domain structural model reveals five amino acids that are involved in interactions with the flavin chromophore (Figure 22A). Lys29 (α -helix 1) shares a hydrogen bond with FMN phosphate with a NZ-OP1 distance of 3.3 Å. Asn30 (α -helix 1) ND2 and OD1 atoms interact with FMN O4 and N3 (3.1 and 2.9 Å, respectively). FMN O2' and O3' share hydrogen bonds with Asp67 (α -helix 2) OD2 within 2.8 and 3.3 Å, respectively. Arg63 (α -helix 2) NH2 and NE interact with FMN O2 and O4', respectively (2.7 and 3.0 Å). Finally, Gln48 (β -sheet 3) shows an amide tautomer in the dark state, which enables its NE2 atom to share hydrogen bonds with FMN O4 and N5 with distances of 2.9 and 3.3 Å, respectively. Gln48 also forms a hydrogen bond

with Tyr6 (β -sheet 1) OH through its OE1 atom (2.8 Å). Met92 (β -sheet 5) is found near Gln48 in a Met_{in} conformation, while Trp90 is solvent exposed (Trp_{out}) pointing away from the flavin binding site (Figure 22A). Gln48 in its amide tautomer form and Met92 buried in the chromophore pockets are consistent with several studies revealing a Met_{in} and Trp_{out} conformation of BLUF domain in the dark state (Kita *et al.*, 2005; Jung *et al.*, 2006; Winkler *et al.*, 2013; Collette *et al.*, 2014; Ohki *et al.*, 2016; Lindner *et al.*, 2017; Karadi *et al.*, 2020). Additionally, the orientation of the glutamine side chain can be confirmed by the differing geometries in the interactions involving the sulphur atom of a methionine residue. The perpendicular to the sulphide plane, formed by the Met92 CG, SD and CE atoms, shows an angle less than 40° with the NE2-H group of Gln48, the latter therefore acts here as an electrophile (Pal and Chakrabarti, 2001). This enables a hydrogen-bond-like interaction between Gln48 nitrogen and Met92 sulphur (3.5 Å distance). Interaction of Met92 SD with the nucleophile Gln48 OE1 would not be favourable with this geometry, confirming the orientation of the glutamine in the dark state structure. Methionine residues which exhibit this specific interaction with a N-H group are usually buried in the protein core, and demonstrate importance in the stability of the protein (Pal and Chakrabarti, 2001). This conformation is favourable for a stable dark state structure. Recently, description of an OaPAC structural model crystallized in another space group (P2₁2₁2) confirmed the involvement of Lys29, Asn30, Gln48 and Asp67 in the hydrogen bond network of the chromophore pocket (Kapetanaki *et al.*, 2024). A similar Met_{in} and Trp_{out} conformation in the dark state was observed, with the same Gln48 NE2 - Met92 SD distance of 3.5 Å.

β -sheet 5 adopts an S-shape structure in the dark state (Figure 22B). The kink on the β -sheet brings Met92 closer to the flavin chromophore, as described above. β -sheet 5 is located in-between the two flexible loops shown in Figure 21, therefore this specific structure might play a role in signal transduction. The loop between β -sheet 5 and the α -helix 3 linker exhibits many intramolecular hydrogen bonds (Figure 22C). Lys109 NZ interacts with Leu97 O and Asn100 O (2.8 and 3.3 Å, respectively), and Asp102 O forms two hydrogen bonds with Ile105 N and Arg106 N (3.3 Å).

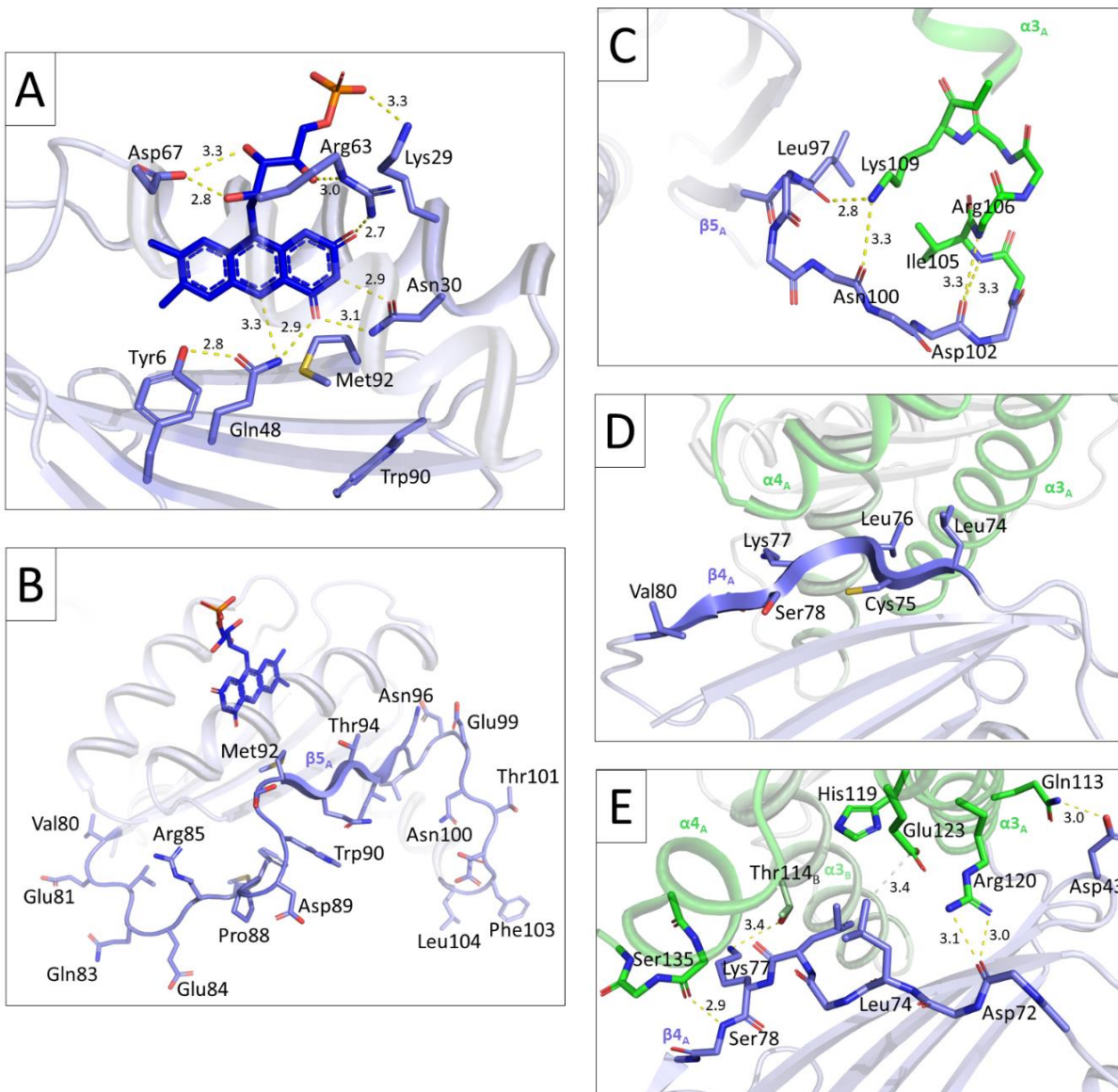


Figure 22: Structural details of the BLUF domain in ATP-bound OaPAC₁₋₃₅₀ at cryogenic temperature.

(A) View of BLUF domain core (blue) in cartoon representation and involved amino acids in the chromophore binding pocket in stick representation. The hydrogen bond network is highlighted in yellow dashed lines. The conserved Tyr6, Gln48 and Met92 are close to the flavin chromophore, while Trp90 is in a Trp_{out} conformation and is solvent exposed. (B) View of BLUF domain β -sheet 5 and the adjacent loops. Amino acids 80 to 104 are represented in sticks. The β -sheet 5 adopts a S-shape pattern in the dark state. (C) View of the loop between β -sheet 5 (blue) and α -helix 3 (green) and hydrogen bonds (yellow dashed lines) between amino acids of in the loop. The side chain of Lys109 before α -helix 3 interacts with Leu97 and Asn100, while Asp102 interacts with Ile105 and Arg106. (D) View of BLUF domain β -sheet 4. Amino acids 74 to 80 are represented in sticks. The β -sheet 4 reveals a kink between Leu76 and Lys77 in the dark state, bringing the β -sheet of the BLUF domain (blue) closer to the α -helix region (green). (E) View of the interactions (dashed lines) between BLUF domain (blue) and the top of the α -helix region (green). Asp43 on the loop between β -sheets 2 and 3 shares a hydrogen bond with Gln113 on α -helix 3. Arg120 (α -helix 3) interacts with Asp72 (loop between α -helix 2 and β -sheet 4), and Ser135 (α -helix 4) interacts with Ser78 (β -sheet 4). Lys77 on β -sheet 4 is also in contact with Thr144 on α -helix 3 from the other protomer. Glu123 (α -helix 3) has van der Waals contact with Leu74 (β -sheet 4).

The hydrogen bond interactions are highlighted in yellow dashed lines and van der Waals contacts in white dashed lines, with distances in Å. Figures prepared by the PyMOL Molecular Graphics System, Version 2.5.4 Schrödinger, LLC (Schrödinger and DeLano, 2020).

On the other side of the BLUF domain, β -sheet 4 also adopts an S-shape pattern, with a kink bringing the section between Cys75 and Ser78 closer to the linker region (Figure 22D). This enables the Ser78 backbone amide nitrogen and Ser135 (α -helix 4) backbone carbonyl oxygen to share a hydrogen bond (2.9 Å), while Lys77 NZ shows an interaction with Thr144 OG1 (α -helix 3 on protomer B) with a distance of 3.5 Å (Figure 22E). On the BLUF domain, β -sheet 4 is the closest to the AC domain, while still separated by the α -helices 3 and 4 (Figure 22D). Additionally, other interactions between the α -helix 3 linker and the BLUF domain can be observed (Figure 22E). Arg120 NH1 and NH2 (α -helix 3) interact with Asp72 (loop between α -helix 2 and β -sheet 4) backbone carbonyl oxygen within 3.0 and 3.1 Å, respectively, as also observed for bPAC (Lindner, 2018). Glu113 (α -helix 3) shares a hydrogen bond with Asp43 (loop between β -sheets 2 and 3), displaying a NE1-OD2 distance of 3.0 Å. Compared to bPAC (Lindner, 2018), Leu76 has no Van der Waals contact with His119, which is 5.6 Å away, but Leu74 CD2 also has a van der Waals interaction with Glu 123 CD (3.4 Å).

Numerous interactions between the BLUF domain and the linker region (Figure 22C-E) suggest that signal transmission could follow many different pathways in OaPAC. Possible pathways are studied with TRX in chapter 3.3.

A closer look at the AC domain structural model highlights the secondary structure region between α -helices 3 and 4 and the active site (Figure 23A). The presence of non-polar residues with hydrophobic side chains between the C-terminus of α -helix 3 and α -helix 4 (Leu122, Tyr125, Ile130, Phe131, Ile133, Ile134) leads to a tightly packed structure that interacts with the AC domain (Figure 23B). Specifically, the tongue region of the other protomer, composed of the loop between β -sheets 9 and 10, is located on top of the linker region and enables Tyr125_A OH and O to share hydrogen bonds with Asn256_B OD1 and Lys262_B NZ, respectively (2.7 and 3.2 Å). The region between α -helix 6 and β -sheet 7 is also positioned on top of α -helix 4, enabling the two conformers of Gln193_A to interact with Ser129_A with an OE2-OG distance of 2.6 or 2.7 Å, depending on the conformer. In the same region, the backbone carbonyl oxygen atom of Val194_A also interacts with Gln127_A NE2 (3.3 Å). These strongly interacting regions between OaPAC linker and AC domain constitute interesting potential pathways for signal transmission to the AC domain.

AC domains from both protomers face each other in an antiparallel fashion, which creates two ATP binding pockets in which both protomers are involved in each ATP binding site (Figure 23A,D).

Both the tongue region and β -sheet 7 line up with ATP binding pocket, creating a direct pathway for the signal to reach the active site from the linker region (Figure 23C). Specifically, the C-terminus of β -sheets 7 (protomer A) and 10 (protomer B) are in close proximity with the ATP, with the loop between β -sheets 7 and 8 of protomer A and the region between β -sheet 10 and α -helix 9 of protomer B surrounding the ribose (Figure 23D). Further details of ATP binding and interactions with these secondary structures will be described in section 3.4.1.

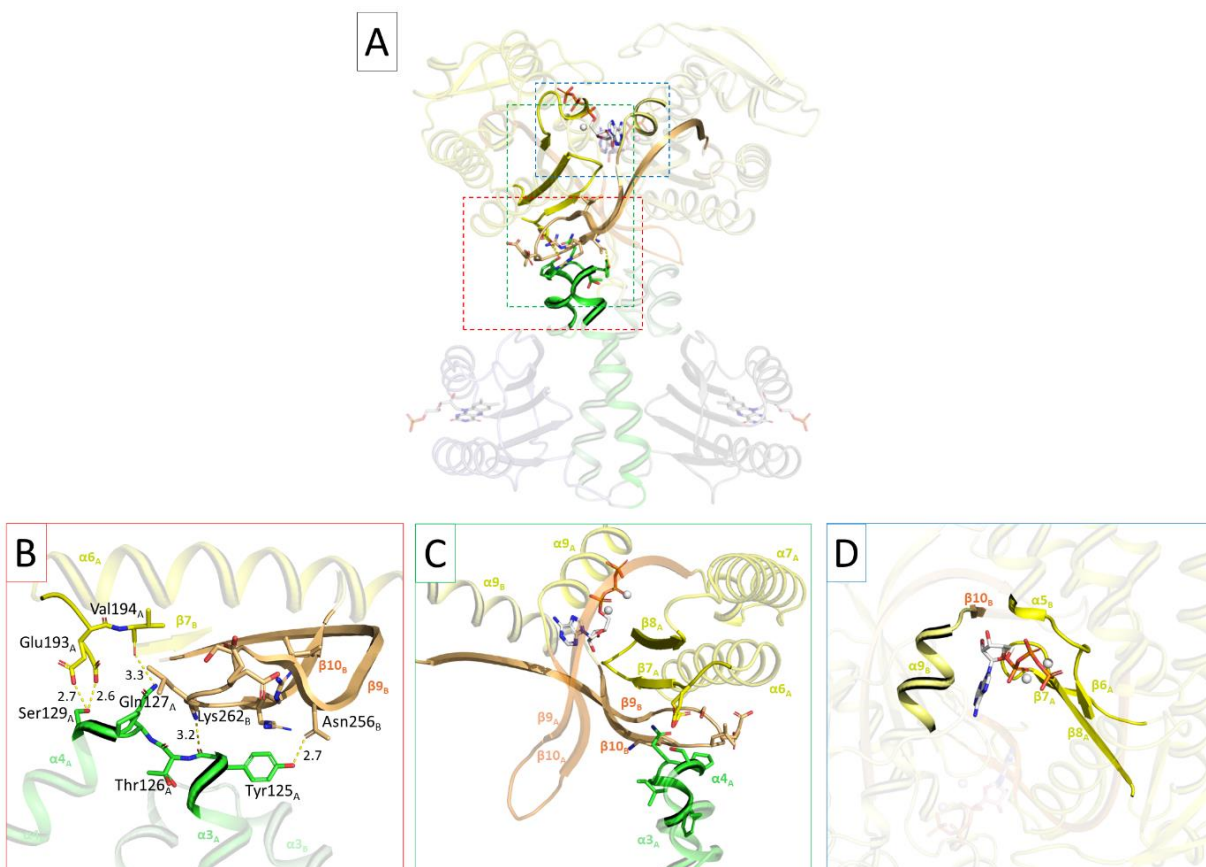


Figure 23: Structural details of the AC domain in ATP-bound OaPAC₁₋₃₅₀ at cryogenic temperature.

(A) View of OaPAC₁₋₃₅₀ with highlighted region of interest. The linker region is represented in green, the AC domain in yellow and the tongue region is highlighted in orange. ATP is represented in white with sticks. The red, green and blue dashed boxed are detailed in quadrants B, C and D, respectively. (B) View of the interactions between linker region (green) and AC domain (yellow/orange). Tyr125 on α -helix 3 (protomer A) shares two hydrogen bonds with Asn256 and Lys262 (protomer B) on the tongue region. Ser129 on α -helix 4 (protomer A) on the handle region interacts with Glu193 from the same protomer found in two conformations. Gln127 shares a hydrogen bond with Val194 in the same protomer. (C) View of the path from the linker region to the ATP binding site in OaPAC₁₋₃₅₀. Both the tongue region of protomer B (orange) and β -sheet 7 of protomer A (yellow) provide a direct path to reach the ligand from the linker region (green). (D) View of the ATP binding site. Regions implicated in ATP binding are highlighted in solid colour. In protomer A, the regions between β -sheet 6 and α -helix 5, and between β -sheets 7 and 8 are involved. In protomer B, the region between the end of β -sheet 10 and the beginning of α -helix 9 is involved.

Figures prepared by the PyMOL Molecular Graphics System, Version 2.5.4 Schrödinger, LLC (Schrödinger and DeLano, 2020).

3.3. Characterization of OaPAC Photoactivation and Signal Transduction Mechanisms

3.3.1. Early Photoactivation Mechanism of OaPAC

To gain deeper insights into the response of BLUF photoreceptors and especially OaPAC upon blue light activation, and to address the divergent views within the scientific community regarding the initial photoexcitation events, a TR-SFX experiment was carried out at the SPB/SFX instrument of the EuXFEL facility (Pandey *et al.*, 2020; Koliyadu *et al.*, 2022). This TR-SFX investigation aimed to elucidate the structural rearrangements occurring in the surrounding of the flavin chromophore in OaPAC when co-crystallized with ATP in the orthorhombic crystal form with C222₁ space group. For this experiment, I prepared the sample with the help of Lea Brings, Huijong Han, Christina Schmidt and Robin Schubert; injection was handled by Katerina Dörner, Mohammad Vakili and Agnieszka Wrona; beamline setup and data collection was performed by the SPB/SFX beamline scientists Raphaël de Wijn, Jayanath C. P. Koliyadu, Romain Letrun, Adam Round, Tokushi Sato and Radu-Costin Secareanu; data processing was done by Sabine Botha and I performed the data analysis.

The *in crystallo* optical spectroscopy experiments carried out in this study, such as TR-FTIR and TR UV-Vis absorption spectroscopy did not achieve a sufficient time-resolution to decipher the best time-points to target during the TR-SFX experiment. Therefore, values from the literature were used as a reference to design the experiment. According to a time-resolved infrared spectroscopy (TRIR) study in the fs-ps time range by Collado *et al.*, OaPAC in solution exhibits four distinguishable intermediate states after photoexcitation (Collado *et al.*, 2022). Time constants of 3.9, 24 and 184 ps were observed, and the last component did not show any decay phase in the recorded time. At 3.9 ps, the flavin excited state was decayed. The formation of the radical pair FADH• and Tyr• was prominent at 24 ps and relaxed around 184 ps.

These results are similar to values observed for other BLUF photoreceptors such as AppA. Several research groups used time-resolved fluorescence and ultrafast transient absorption spectroscopy to investigate the multiexponential decays of the excited state and observed up to four time constants

of around 3 ps, 30 ps, 200 ps, 600 ps and a few ns, (Dragnea *et al.*, 2005; Gauden *et al.*, 2005; Zirak *et al.*, 2005). As the flavin excited state is not observable using TR-SFX at the expected resolution (between 1.5 and 2.1 Å based on the MX data), the fastest species corresponding to ~ 3 ps was not probed. On the ps time scale, OaPAC crystals were probed at 30 ps, 200 ps and 600 ps (Table 15), with the aim to observe changes related to forward CPET, glutamine rotation and reverse PCET. According to Lukacs *et al.*, after 1 ns delay, the flavin chromophore returns to the ground state, but with a modified hydrogen bond network (Lukacs *et al.*, 2022). 5 ns delay was also probed in this TR-SFX study to visualise the chromophore binding pocket with an altered but stable hydrogen bond network representing the signalling state (Table 15).

Additionally, several hypotheses propose dynamic changes in the late ns and early μ s time range (Majerus *et al.*, 2007; Brust *et al.*, 2013). Consequently, 50 ns, 500 ns and 4.58 μ s were probed to follow the early changes in the protein conformation after formation of the signalling state (Table 15). 4.58 μ s was the longest time delay achievable at the SPX/SFX instrument applying the liquid jet sample delivery approach using GDVN/DFFN. The time delays are obtained by modifying the distance between the X-ray interaction region and the laser interaction region in the liquid jet. As the length of a stable liquid jet after exiting the nozzle is limited, a delay greater than 4.58 μ s would have required exciting the sample directly inside the nozzle, which was not feasible at that time but was tested during a second beamtime.

A dark data set, named TRUE DARK, was first collected without laser and serves as reference for the collected TR-SFX data (Table 15). For the light induced data, a pulse pattern with every 3rd X-ray pulse being pre-pumped by the optical laser light was used, with a laser pump repetition rate of 188 kHz and a X-ray probe repetition rate of 564 kHz, to ensure that no light contamination would be possible in the subsequent light-activated diffraction pattern (Figure 24). If each pulse was pumped with the optical laser, which had a focal spot of 35 μ m diameter (FWHM), subsequent pulses could be contaminated by the previous laser pulse and crystals would be activated twice with different timing. Using two non-probed pulses in-between enabled us to verify that the third pulse really corresponded to the protein structure in the dark state. With this setup, a total of three data sets per time point were collected, namely the LIGHT, the DARK1 (potentially light-contaminated) and the DARK2 data sets.

	TRUE DARK	30 ps	200 ps	600 ps	5 ns	50 ns	500 ns	4.58 μ s							
Sample	OaPAC ₁₋₃₅₀ C222 ₁ crystals single batch														
Cell param.	a = 54.3 Å, b = 145.8 Å, c = 105.3 Å, $\alpha = 90^\circ$, $\beta = 90^\circ$, $\gamma = 90^\circ$														
X-ray param.	3 μ m x 4 μ m, 9.3 keV, 1 mJ, 564 kHz, ≤ 30 fs														
Laser	No	Yes, 421 nm													
Laser param.	N/A	35 μ m (FMWH), 188 kHz													
Laser fluence (mJ/cm ²)	N/A	19.4	100	19.4	100	21.6	21.6	100	100	21.6	100	19.4	100	21.6	100
Delivery method	Liquid jet														
Nozzle	DFFN	GDVN	GDVN	GDVN	GDVN	DFFN	GDVN	GDVN	GDVN	GDVN	GDVN	GDVN	GDVN	GDVN	GDVN
Date of data collection	04.05.2022	05.05.2022	05.05.2022	05.05.2022	05.05.2022	04.05.2022	04.05.2022	05.05.2022	05.05.2022	04.05.2022	05.05.2022	05.05.2022	05.05.2022	04.05.2022	05.05.2022
Run numbers	43-47	184-191	175-182	192-195 + 200-203	168-174	48-59	63-72	136-138 + 143-144	162-167	90-103	145-150	204-209	156-161	77-89	151-155
Number of frames	2,510, 892	4,348, 032	4,615, 161	4,510, 641	3,942, 615	6,181, 755	6,283, 059	2,512, 299	3,771, 564	7,989, 951	3,769, 755	3,775, 986	3,770, 157	6,940, 731	3,144, 645

Table 15: Description of data collection setup and results during TR-SFX beamtime at the SPX/SFX instrument of EuXFEL with proposal 2829.

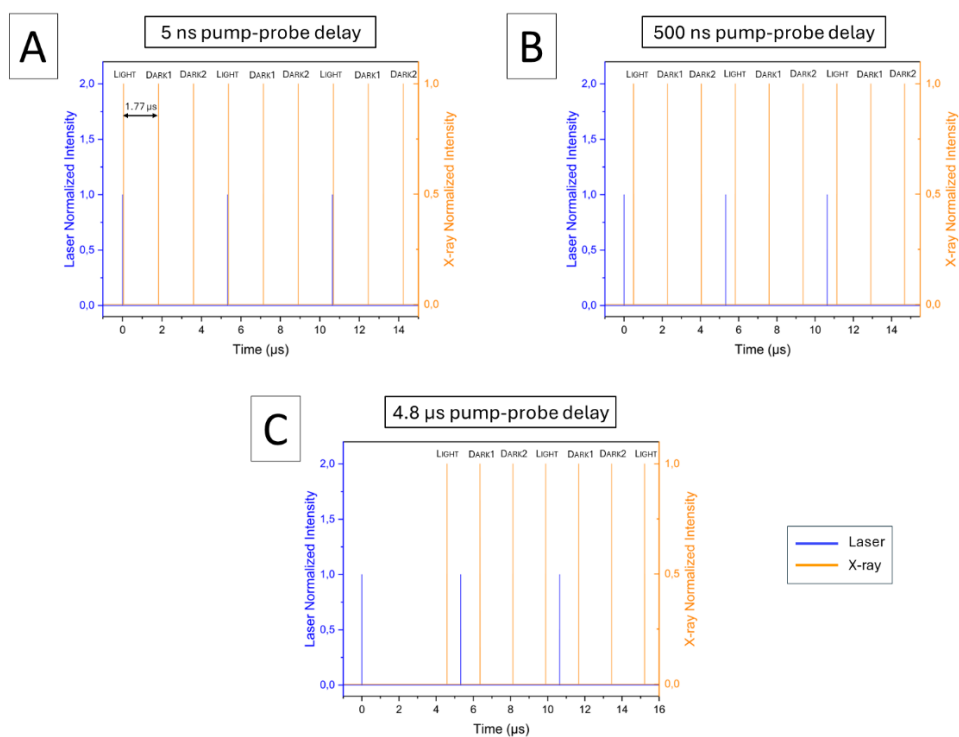


Figure 24: Oscilloscope trace of the TR-SFX experiment illustrating the applied pump-probe pulse pattern in LIGHT-DARK1-DARK2 succession.

(A) Data were recorded with a time delay between pump pulse (blue) and first probe pulse (orange) of 5 ns (LIGHT) and 1.78 μ s for the second probe pulse (DARK1). The X-ray pulses are separated by 1.77 μ s. (B) Data were recorded with a time delay between pump pulse (red) and first probe pulse (blue) of 500 ns (LIGHT) and 2.3 μ s for the second probe pulse (DARK1). (C) Data were recorded with a time delay between pump pulse (red) and first probe pulse (blue) of 4.58 μ s (LIGHT) and 1 and 2.8 μ s for the probe pulses that appear before the real light pulse (DARK1 and DARK2). Figures were created with Origin software version 2024. Figures (A,B) are modified from Chretien et al. (Chretien et al., 2024).

All the induced light data sets were analysed by calculating difference electron density maps against the dark data set. Attention was put into analysing differences around the chromophore. Yet, no interpretable difference was observed for any of the LIGHT data sets, regardless of the weighting used for map calculation (q, k or no weighting (Terwilliger and Berendzen, 1995; Ursby and Bourgeois, 1997; Schmidt *et al.*, 2010)). When analysing images from the second pulse, *i.e.* the potentially light-contaminated DARK1 images, strong differences could be observed for 3 of the data sets pumped with 100 mJ/cm²: 5 ns, 500 ns and 4.58 μ s (Figure 25).

For these light-contaminated DARK1 data sets, the time delay corresponds to the initial delay set-up for this data collection plus 1.77 μ s, which is the time between two X-ray pulses (Figure 24A-B). The last data set with 4.58 μ s time delay is the only exception, as here both DARK1 and DARK2 images are potentially light-contaminated. DARK1 is contaminated similarly as in the other data sets and DARK2 is exposed by a subsequent pump pulse, due to the long travel time in the liquid jet at this large time delay (Figure 24C).

This resulted in three new “light” data sets with calculated time delays of 1.034 ns (4.58 μ s *minus* two times 1.773 μ s), 1.778 ns (5 ns *plus* 1.773 μ s) and 2.273 ns (500 ns *plus* 1.773 μ s), named 1, 1.8 and 2.3 μ s delay, respectively. Differences were also observed for the contaminated pulse of the 50 ns DARK1 data, but were less interpretable than the light contaminated 1.778 ns data, although the time delay for the light contaminated pulse was almost identical (1.823 ns) (Appendix Figure 2). A detailed summary of the data collection results for these four data sets is shown in Table 16. The number of indexed lattices and obtained resolution was similar for each sub data set, indicating that the laser beam did not damage the crystals during the experiment.

	5 ns – 100 mJ/cm ²			50 ns – 100 mJ/cm ²			500 ns – 100 mJ/cm ²			4.58 μs – 100 mJ/cm ²		
Data set	LIGHT	DARK1 Contaminated	DARK2	LIGHT	DARK1 Contaminated	DARK2	LIGHT	DARK1 Contaminated	DARK2	LIGHT	DARK1 Contaminated	DARK2 Contaminated
Time delay	5 ns	1.8 μs	0	50 ns	1.8 μs	0	500 ns	2.3 μs	0	4.58 μs	1 μs	2.8 μs
Absorbed photons per molecules (according to theoretical calculations)	6.6	< 6.6	0	6.6	< 6.6	0	6.6	< 6.6	0	6.6	< 6.6	< 6.6
Total nb of hits	147,201			141,094			205,695			147,709		
Hit rate	3.9 %			3.7 %			5.5 %			4.7 %		
Total nb of indexed lattices	153,871			142,782			210,575			151,875		
Indexed rate	104.5 %			101.2 %			102.4 %			102.8 %		
Indexed hit rate (disregarding multi-indexing)	97.3 %			96.9 %			97.8 %			97.9 %		
Indexed lattices per data set	51,838	50,786	51,247	47,928	47,101	47,751	70,798	68,993	79,784	50,874	50,054	50,947

Table 16: Description of hit rate and indexed lattices during the data processing of four data sets (5, 50, 500 ns and 4.58 μs delay) and corresponding light (LIGHT), light-contaminated (DARK1) and dark (DARK2) sub-data sets.

Q-weighted Fourier difference electron density maps for the three pump-probe delays (1, 1.8 and 2.3 μs) were calculated against the dark data set using Xtrapol8 (de Zitter *et al.*, 2022) and several changes in the vicinity of the flavin chromophore are highlighted (Figure 25B,E,H). A subset of 60,000 indexed pattern from the DARK2 data set was used as reference, which enabled a better correlation between the DARK2 and the light contaminated DARK1 (1, 1.8 and 2.3 μs) data sets. Up to 1.9 Å resolution, good correlation was observed with an R factor between both data sets (R_{iso}) < 0.2 and an isomorphism-indicating correlation coefficient CC_{iso} > 0.8. The resolution for the extrapolation process was therefore cut at 1.9 Å. Xtrapol8 was used to determine occupancies of the light-excited state and thereby extrapolate structure-factor amplitudes, allowing modelling of the structural changes happening at these three time points. The light excited states could be estimated at 25 % occupancy for all the time points using the difference map method (de Zitter *et al.*, 2022). The estimation when integrating all peaks from the difference density maps did not converge towards a sharp occupancy estimation, yet, after singling out the most significant peaks (including around Tyr6, Gln48, Met92 and FMN) and peaks with the highest integrated peak volume around residues with increased signal to noise ratio (Met92), the normalized difference map ratio was maximized at around 25 % occupancy (Appendix Figure 3). Data collection and refinement statistics for the dark and light-activated states models are shown in Appendix Table 2.

Fourier difference density maps and extrapolated electron density maps provide some evidence of the involvement of the conserved amino acids Tyr6, Gln48 and Met92 in the early steps after photoexcitation (Figure 25B-C, E-F, H-I). It is well known that these residues in the flavin binding pocket are highly conserved among BLUF photoreceptors (Anderson *et al.*, 2005; Gauden *et al.*, 2006a; Okajima *et al.*, 2006; Yuan *et al.*, 2006; Stelling *et al.*, 2007; Bonetti *et al.*, 2008; Barends *et al.*, 2009; Iwata *et al.*, 2011; Brust *et al.*, 2013; Ohki *et al.*, 2017; Goings *et al.*, 2020), making them likely candidates as key residues for the early photoinduced rearrangements.

Firstly, after a pump probe delay of 1.0 μs , Gln48 moves slightly closer to the tyrosine residue. Especially, the hydrogen bond between Gln48 OE1 and Tyr6 OH is strengthened (Figure 25A-D). This change in the hydrogen bond network could be representative of the forward CPET described in the literature (Collado *et al.*, 2022; Zhou *et al.*, 2022), which can have an influence on Gln48 OE1-Tyr6 OH distance and on Gln48 NE2-FMN N5 distance. Interestingly, at the same time, Met92 is also displaced, with its CE and CG atoms being slightly further away from Gln48 NE2, as suspected from the reduced electron density observed around both atoms (Figure 25B-D). This displacement might also be induced by the change in hydrogen bond network around Gln48.

Subsequently, following a pump probe delay of 1.8 μs in this experiment, several new changes manifest, implicating the aforementioned residues (Tyr6, Gln48 and Met92) (Figure 25E-G). Among these changes, the most notable involves Gln48, which has undergone a complete 180° rotation around its CG-CD axis. This leads to a thorough rearrangement of the hydrogen bond network around the flavin. Gln48 NE2 interacts in the light-activated state with Tyr6 OH and FMN N5 (2.9 and 3.2 Å, respectively), breaking its bond with FMN O4 (Figure 25G). The distance between Tyr OH and Gln48 OE1 (dark)/NE2 (light) is slightly increased in the light state. The rotation also establishes an interaction between Gln48 OE1 and FMN O4 (2.9 Å). Additionally, Gln48 OE1 exhibits dipole interactions with Met92 CE (3.3 Å), and an intramolecular interaction with Met92 SD, positioned 3.1 Å away, while the distances between Gln48 NE2–Met92 CE or SD were 3.6 Å and 3.4 Å in the dark state, respectively. Of note, a small movement of the flavin increases its distance from Asn30 ND2 and OD1 compared to the dark state. Meanwhile, Met92 continues its motion, moving away from the flavin binding pocket, inducing a 1 Å displacement from its original position. This phenomenon was previously observed by Jung *et al.* in the context of AppA (Jung *et al.*, 2006). Specifically, the conformation of Met92 varied, with CE rotating 90° downward, now facing towards β -sheet 2, in comparison to its orientation in the dark state and after

1 μ s. The displacement of Met92 changes the geometry of its interaction with Gln48, as the perpendicular to the sulphide plane formed by the Met92 CG, SD and CE atoms does not exhibit an angle of less than 40° with Gln48 NE2-H as revealed in the dark state. The orientation observed here shows the Gln48 side chain lying along the extension of the CG-SD axis, which is only favourable for an interaction between a divalent sulphur atom with a nucleophile (Pal and Chakrabarti, 2001), confirming the rotation of Gln48 to enable its OE1 group to favourably interact with Met92 SD.

The rotational behaviour of Gln48 has been a subject of ongoing debate for the past two decades. Several studies have supported the presence of a glutamine tautomerization accompanied by a rotation of its side chain (Domratcheva *et al.*, 2008; Khrenova *et al.*, 2013; Goings *et al.*, 2020; Hontani *et al.*, 2023; Salvadori *et al.*, 2024). Yet, few studies suggest that the presence of a keto-enol tautomerization is sufficient to induce a stable signalling state (Sadeghian *et al.*, 2008; Ohki *et al.*, 2017). Although it is challenging to assign the tautomeric state of a glutamine solely with X-ray crystallography data, this TR-SFX analysis strongly supports the occurrence of a glutamine rotation in the initial stages of photoactivation. Interestingly, this finding contradicts the observation made by Ohki *et al.* for OaPAC, where only a 40° rotation of Gln48 was reported after 20 s of illumination (PDB 5X4T) (Ohki *et al.*, 2017).

Since the presented TR-SFX data has a limited resolution of 1.9 Å, it is not possible to verify the proton and electron transfer from Tyr6 to the flavin. However, one can speculate that the 1.8 μ s data (Figure 25G) corresponds to the end of the early photoexcitation event, when the flavin is returned to the ground state after reverse PCET, leaving an altered hydrogen bond network due to the rotation and keto-enol tautomerization of the glutamine. This state represents the characteristic red-shift spectral signature of the flavin.

The last structural model corresponding to 2.3 μ s after photoexcitation exhibits more significant alterations around the chromophore binding pocket (Figure 25H). Specifically, Gln48 and Met92 undergo additional movement to respond to photoexcitation (Figure 25I-J). Gln48 undergoes an additional 40° rotation, totalling a rotation of 220° from its original orientation in the dark state. Concomitantly, Gln48 also moves further away from Tyr6, extending the NE2-OH distance from 2.9 Å after 1.8 μ s to 3.5 Å at 2.3 μ s delay (Figure 25J). This shift causes Gln48 OE1 to be more distant from FMN O4, with an OE1-O4 distance of 3.2 Å compared to 2.9 Å after 1.8 μ s. Notably,

a similar 40° rotation was observed by Ohki *et al.* after 20 s of illumination in OaPAC, albeit without the initial 180° rotation of the side chain (Ohki *et al.*, 2017). This additional 40° rotation likely plays a role in stabilizing the hydrogen bonding network around the flavin chromophore, particularly with Met92. Indeed, the rotation coincides with the additional displacement of Met92, which moves further away from the chromophore pocket. This displacement is evident in the Fourier difference electron density map (Figure 25H) and has been transposed into extrapolated density maps (Figure 25I), showing Met92 has moved 1.5 Å away from its original location (Figure 25J). Met92 displacement triggers movements in the backbone of neighbouring residues. The amino acids within the loop region between β -sheet 4 and 5 (Glu79 to Ser91), as well as those in β -sheet 5 and the subsequent loop until α -helix 3 (Gln93 to Phe103), are destabilized by the methionine movement. Hence, the alterations surrounding the flavin binding pocket appear to initiate a signal transmission involving more distal amino acids from the chromophore approximately 2.3 μ s after photoexcitation in this study.

Notably, hydrogen bonds involving Asn30 are once again altered, with a decrease of the Asn30 OD1-FMN N3 distance at 2.3 μ s. Interaction between Asn30 and the flavin chromophore seems to be continuously modified, although no real trend or correlation with the signalling state are observed. One can question if this dynamic behaviour is of importance for the signalling state and signal transmission, or whether the changes are only a passive product of the major change concerning the Gln48. Jung *et al.* described the asparagine in AppA to be important in breaking its interaction with His105 (corresponding to Ser91 in OaPAC) and stabilizing the light state (Jung *et al.*, 2006). Here, Asn30 shares a hydrogen bond with the carbonyl oxygen of Ser91 in all the structures, and the ND2-O distance only varies from 3.1 to 2.9 Å between the models. These small changes might be attributed to noise added during the extrapolation process (Barends *et al.*, 2024) and therefore viewed as not significant, especially at 1.9 Å resolution where a small 0.3 Å change is within the error of the model. However, the asparagine residue is highly conserved among BLUF photoreceptors (Gomelsky and Klug, 2002) and shares important interactions with the flavin chromophore and the backbone between Met92 and Trp90, two amino acids known to play a role in signal transmission (Masuda *et al.*, 2005c; Jung *et al.*, 2006; Masuda *et al.*, 2008; Yuan *et al.*, 2011; Brust *et al.*, 2013; Karadi *et al.*, 2020). Consequently, Asn30 might have an important role in signal transmission, which will be further discussed in section 3.3.5.

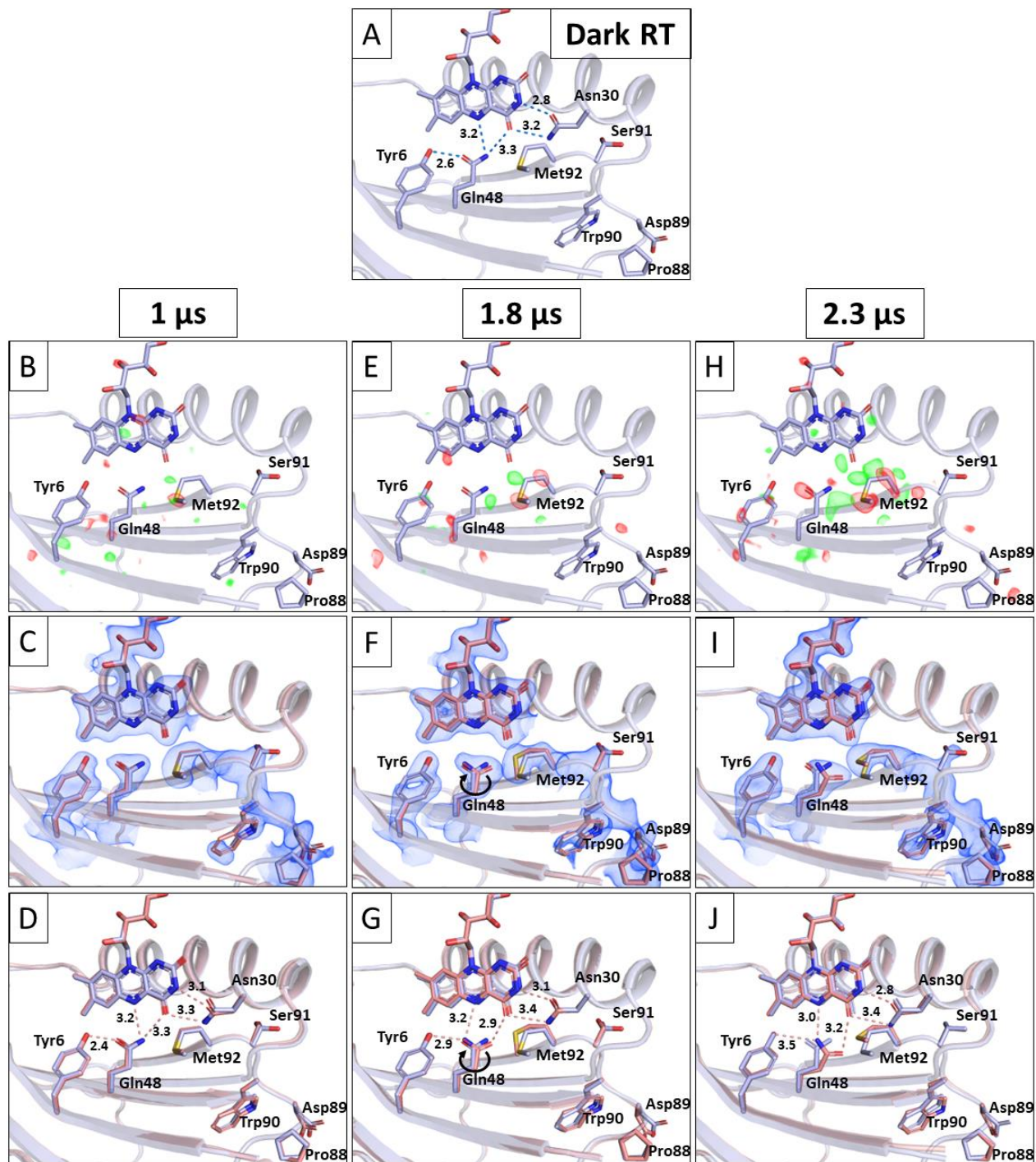


Figure 25: BLUF activation via blue light excitation of flavin chromophore in *OaPAC* revealed by TR-SFX and extrapolation process.

(A) Structural details of the chromophore binding pocket in *OaPAC*₁₋₃₅₀ dark state at room-temperature.

View of the BLUF domain core in cartoon representation and involved amino acids in the chromophore binding pocket in stick representation. The conserved Tyr6, Gln48 and Met92 are close to the flavin chromophore, while Trp90 is in a *Trp_{out}* conformation solvent-exposed, as in Figure 22A at cryogenic temperature. In dashed line is highlighted the hydrogen bond distances in Å within the chromophore pocket hydrogen bond network involved in the early step upon photoexcitation.

(B-J) Structural models of excited OaPAC (salmon) with pump-probe delays of 1.0 μs (B-D), 1.8 μs (E-G) and 2.3 μs (H-J) are shown and involved amino acids in stick representation along with the dark model (light blue). (B,E,H) $F_{\text{light}} - F_{\text{dark}}$ difference maps contoured at +3 rmsd (green) and -3 rmsd (red) reveal initial changes around the flavin chromophore after excitation. (C,F,I) Extrapolated Fourier difference density maps ($2F_{\text{o}} - F_{\text{c}}$) contoured at 1 rmsd for the different pump-probe delays, calculated against the dark data set using Xtrapol8 to allow building of the structural model of the excited state. (D,G,J) Hydrogen bond distances in \AA around the flavin chromophore upon BLUF excitation at the investigated pump-probe delays.

Figures prepared by the PyMOL Molecular Graphics System, Version 2.5.4 Schrödinger, LLC (Schrödinger and DeLano, 2020).

Figures modified from Chretien *et al.* (Chretien *et al.*, 2024).

It is important to note that the kinetics observed in this crystallographic study are significantly slower compared to OaPAC in solution, for which the forward CPET, glutamine rotation and reverse PCET already happens within hundreds of ps (Collado *et al.*, 2022). The first rearrangements are only visible at 1 μs in this TR-SFX study and could not be observed for the faster time points studied up to 500 ns. The glutamine rotation and potentially the final signalling state seems to only occur between 1 and 1.8 μs , which is 3 orders of magnitude slower than has been proposed for OaPAC in solution (a few ns) (Collado *et al.*, 2022; Lukacs *et al.*, 2022). Slower kinetics have been documented on numerous occasions in crystallographic studies (Ferrari *et al.*, 2003; Wilmot, 2003; Hadjidemetriou *et al.*, 2022). This variation in dynamics can probably be attributed to distinct protein environments resulting to the crystal packing or the composition of the crystallization solution (Makinen and Fink, 1977; Schulz *et al.*, 2022).

One could question whether the rotation of the glutamine happens even earlier but is not distinguishable. Indeed, a perfect rotation would signify a strict replacement of the oxygen by the nitrogen and *vice versa*, meaning the difference in density would be unnoticeable as oxygen and nitrogen have almost the same electron density. However, with the geometry of interaction between the methionine and the glutamine present at 1 μs delay, as explained before, favourable interaction requires Met92 SD to interact with an electrophile, here Gln48 N-H group, as in the dark state. Therefore, it is unlikely that the rotation happens before 1 μs in this study.

The attribution of the pulse IDs was verified with the oscilloscope trace of the pump laser (Figure 24) and with the metadata recorded during the beamtime. Yet, several aspects are still unresolved. The light contaminated 1.823 ns data sets exhibited weaker differences than the light contaminated 1.778 ns data set, and all the ps data sets of the light contaminated pulse (30, 200 and 600 ps *plus* 1.77 μs) did not result in interpretable differences, although the time delay is almost identical for all of them (1,773 ns). Additionally, if the second pulse of the 4.58 μs data set, namely the 1 μs

time delay, is light contaminated, then the third pulse at 2.8 μs (Table 16) should also exhibit differences due to light contamination because of the specific pulse sequence for this data set (Figure 24C), but this was not the case. Last but not least, if no difference is observed at fast time delays (ps to ns) only because of slower reaction kinetics in the C222₁ crystal, then the 4.58 μs light data set should exhibit features at least similar to the light contaminated 2.3 μs data set, which is also not the case. As a result, these unresolved questions negatively impact the confidence in the results of this TR-SFX experiment. Inconsistencies may result from issues with the setup at the SPB/SFX beamline (laser, pulse pattern and detector) or from OaPAC not being a suitable target for TR-SFX due to a low quantum yield and small structural rearrangements at fast time scale.

The determination of the occupancy in TRX experiment is non-trivial. Estimating the occupancy using extrapolated maps such as in the Fo-Fo difference map method in Xtrapol8 (de Zitter *et al.*, 2022) was first thought to underestimate the occupancy by half (Schmidt, 2023). However, a later study showed that the occupancy was only slightly underestimated using this technique (Barends *et al.*, 2024). Nonetheless, attempts were made to verify the occupancy obtained with Xtrapol8 using another difference map method described by Barends *et al.* (Barends *et al.*, 2024). This method is based on the changes in peak height in mFo-DFc omit maps for one atom or molecule moving between one position in the dark state to another position in the light-activated state. By calculating the peak height of the light-excited atom position divided by the sum of the peak heights of both dark and light excited states positions, it is possible to retrieve the occupancy of the light-excited state. However, this method requires prior knowledge of the atom/molecule position in the light-activated state, as well as a clear distinction between its position in the dark and in the light excited states.

In this TR-SFX study, changes are too limited to obtain a clear distinction between the atom positions in the dark and light-activated states of Met92 or Gln48 for instance, which render the occupancy determination with this method laborious. Nevertheless, the method was tested with the 2.3 μs structural model which offers the biggest deviation of atom position between the dark and light-activated states among the three models for Met92 SD atom (Figure 25). An mFo-DFc omit map was calculated using the SFX dark state structural model of OaPAC and the original DARK1 map (2.3 μs delay). The peak height at the Met92 SD atom positions in the dark state and in the light-activated state enabled the determination of 32 % occupancy for the 2.3 μs light-activated state. As Met92 positions between the dark and light-activated states are not completely distinct

and the adjacent Met92 CG atom in the dark state would influence the peak height at the Met92 SD light-activated state position (Figure 25J), the occupancy might have been overestimated when using the omit map-based method. Additionally, the position of Met92 SD atom in the 2.3 μ s light-activated state is not certain, which might lead to incorrect occupancy estimation.

Recently, it has been discussed that the extrapolation process of TRX data tends to introduce errors (Schmidt, 2023; Barends *et al.*, 2024). Indeed, the calculation of structure factor amplitudes is equivalent to summing up an appropriately scaled light *minus* dark difference map to the electron density map of the dark state. By this, features introduced by the extrapolation process are at half scale only and noise is introduced during the process. Barends *et al.* demonstrated that for an occupancy below 0.3, extrapolation-based methods clearly underestimated the real changes even for large rearrangements, while at high occupancy, even small changes could be well reproduced. Consequently, structures of light-activated states modelled from extrapolated maps with occupancies below 0.3 were biased toward the dark state (Barends *et al.*, 2024). Using multi-copy refinement, which makes fewer assumptions than the extrapolation process, a better modelling of the structural changes was possible in their study, and this even when the triggered state presented a low occupancy (below 0.3). Assuming the estimated occupancy with Xtrapol8 of around 25 % is correct, multi-copy refinement was tested for a structural model composed of 75 % dark state with fixed atom positions and a 25 % light-activated state where atoms were refined, without pre-determination of the atom's position for the light-activated state. The light-activated model was refined for atomic-positions in real and reciprocal space, as well as individual B-factors (temperature factors), but without occupancy refinement. Structural models for the three pump-probe delays after multi-copy refinement using the original DARK1 electron density maps are shown in Figure 26.

After 1 μ s, the refined model exhibits a more pronounced shortening of the hydrogen bond between Tyr6 OH and Gln OE1, with 2.2 Å in the multi-copy refinement model against 2.4 Å for the extrapolated model and 2.6 Å in the dark state (Figure 26A and Figure 25A,D). A slight shortening of the Gln48 NE2-FMN O4 hydrogen bond distance is also observed, which was not present in the extrapolated model. Last, the movement of Met92 is also more pronounced here, with a 45° flip of the CE atom in the SD-CE axis (Figure 26B). This leads to an increase of the Gln48 NE2-Met92 SD distance as already described for the extrapolated data. Interestingly, as a consequence of the Met92 flip the interaction between Met92 SD and Gln48 NE2 changes and is not favoured anymore

as in the dark state. Indeed, the specific angle of less than 40° described previously (Pal and Chakrabarti, 2001) is not observed here, suggesting that Met92 SD would have a favourable interaction with Gln48 OE1, acting as a nucleophile here instead. The refinement process did not lead to a glutamine side chain rotation for this data, but it is plausible that the rotation happens already after 1 μs according to the position of Met92 in the multi-copy refinement process. Consequently, multi-copy refinement for the 1 μs exhibits to some degree similar features as observed with the extrapolated data, although the changes are more pronounced. This corroborates the tendency of extrapolated data with low occupancy to bias the light-activated state toward the dark state (Barends *et al.*, 2024).

The structural model for 1.8 μs shows a complete rotation of the highly conserved glutamine side chain (Figure 26C-D). As described in the extrapolated data, this creates a new hydrogen bond between Gln48 OE2 and FMN O4, although a slight difference in the rotation leads to an increase in the distance to 3.4 \AA here compared to 2.9 \AA (Figure 26C and Figure 25G). Met92 continues its motion away from the flavin binding pocket, with more than 1 \AA displacement when compared to its original position in the dark state. As a result, both structural models exhibit similar movements after 1.8 μs (Figure 26D), although distances appear different.

The last structural model, corresponding to 2.3 μs after photoexcitation, defined with multi-copy refinement also exhibits similar features to the extrapolated model for the same time delay (Figure 26E-F and Figure 25J). Indeed, the movement of the methionine away from the chromophore binding pocket is highly similar in both cases, with a 1.5 \AA displacement of Met92 compared to its original position in the dark. However, the distance between Met92 SD and Gln48 OE1 is increased (4.1 \AA) compared to the extrapolated data (3.8 \AA). This is due to Gln48 showing a more restricted displacement away from Tyr6 (2.9 \AA against 3.5 \AA). Yet, Gln48 exhibits a similar 220° rotation when compared to the dark state. As a result, changes are comparable between both methods to obtain the light-activated state at 2.3 μs , except that the extrapolated data exhibits a more extreme displacement of Gln48 away from Tyr6.

Overall, the same patterns of displacement and rotation are observed with both multi-copy refinement and extrapolation methods, but the bond distances are clearly distinct in many cases. This indicates that TR-SFX data can be extremely complex to analyse when the light-activated state occupancy is low. The data shown here certainly demonstrates rotation of the highly conserved

glutamine and movement of the Met92 away from the flavin binding pocket, but it is difficult to clearly describe the changes in hydrogen bond distances around the flavin.

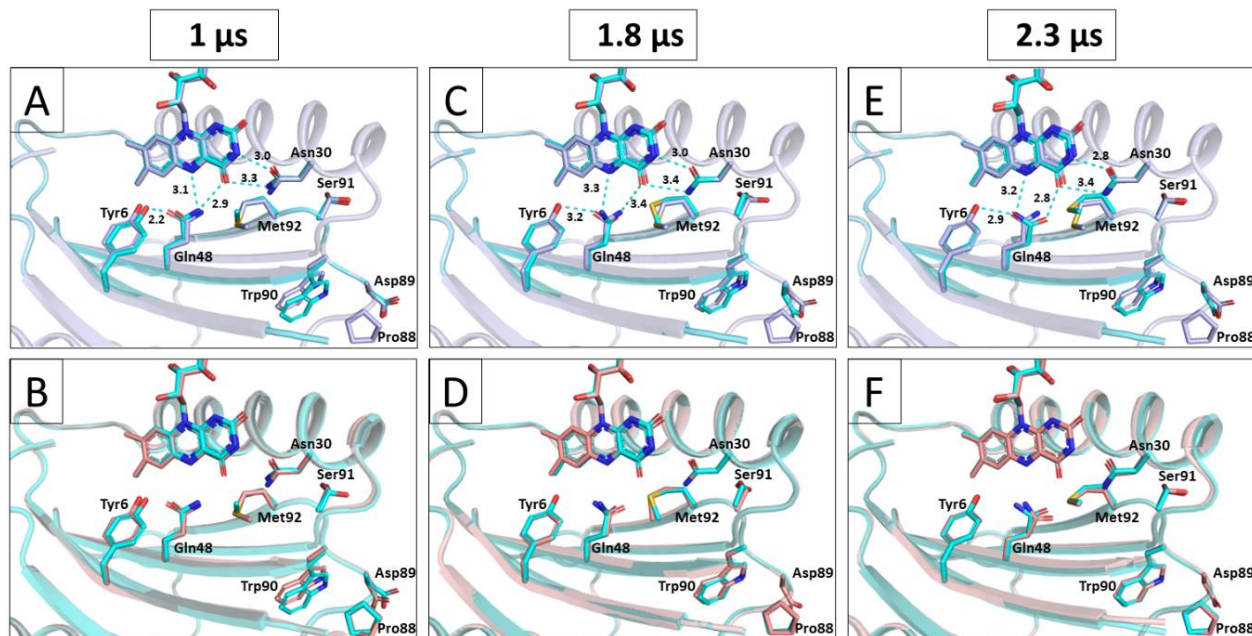


Figure 26: BLUF activation via blue light excitation of flavin chromophore in OaPAC revealed by TR-SFX and multi-copy refinement.

Structural models of excited OaPAC solved with multi-copy refinement (orange) with pump-probe delays of 1.0 μs (A-B), 1.8 μs (C-D) and 2.3 μs (E-F) are shown and involved amino acids in stick representation along with the dark model (light blue) or the corresponding model of excited OaPAC solved by extrapolation process (salmon). (A,C,E) Hydrogen bond distances in \AA around the flavin chromophore upon BLUF excitation at the investigated pump-probe delays.

Figures prepared by the PyMOL Molecular Graphics System, Version 2.5.4 Schrödinger, LLC (Schrödinger and DeLano, 2020).

3.3.2. Laser Power Titration

To better understand why molecules in the crystals illuminated with the lower laser fluence (theoretically 1.3 absorbed photon per molecule) did not exhibit any reaction for the light contaminated DARK1 (1, 1.8 and 2.3 μs) data sets, a laser power titration was carried out at the TR-icOS platform of ESRF (Engilberge *et al.*, 2024). The degree of photoactivation of the molecules in the 4 μm -thick C222₁ crystals was tested after illumination with a 420 nm ns laser ranging from 17.3 to 280.3 mJ/cm^2 laser fluence, corresponding to 1.1 to 18 absorbed photons per

molecules, according to the calculation described by Grünbein *et al.* (Grünbein *et al.*, 2020). Data were collected with the help of Nicolas Caramello and Samuel Rose from ESRF and were processed by Nicolas Caramello. The tested laser intensities and the presence or absence of red-shift in the UV-Vis absorption spectra are listed in Table 17. Interestingly, up to a theoretical value of 3 absorbed photons per molecules, no clear red-shift was observed after light excitation (Figure 27A-B). This demonstrates that none or an extremely low fraction of molecules in the crystal reacted to the light trigger. With 46.4 mJ/cm² (3 absorbed photons per molecule), a slight change of the UV-Vis spectrum compared to the dark was noted (Figure 27B). This might indicate the initiation of the hydrogen bond rearrangements for a slightly larger fraction of molecules in the crystals, although photoactivation is clearly still incomplete. From 88.6 mJ/cm² (5.7 absorbed photons per molecule), the red-shift was maximized (Figure 27C). Indeed, between 88.6 and 280.3 mJ/cm², the light-activated state displayed the typical red-shift upon photon excitation and a clear increase in absorbance at 492 nm (Figure 27C-E). Due to the noise in the spectra, it was not possible to properly determine the red-shift distance for these data. For the subsequent analysis using the TR-icOS platform, thicker crystals (around 8 μm thick) were used to increase the signal to noise ratio. Notably, no bleaching was observed for the highest laser intensities tested (Appendix Figure 4), suggesting that no flavin damage was occurring even when multiphoton absorption was likely happening.

15 mJ/cm² using the setup at the SPB/SFX instrument of EuXFEL is equivalent to 1 absorbed photon per molecule, theoretically. Yet, structural rearrangements around the flavin necessary for obtaining the lit state are not detectable with UV-Vis absorption up to a theoretical value of 3 absorbed photons per molecules. Consequently, it seems logical that no reaction was detected for the low laser fluence used during the TR-SFX experiment. For all the later TRX experiments, laser fluence was chosen to yield a theoretical number of absorbed photons per molecules of 5.7 minimum.

	17.3 mJ/cm ²	46.4 mJ/cm ²	88.6 mJ/cm ²	150.7 mJ/cm ²	280.3 mJ/cm ²
Absorbed photons per molecules (according to theoretical calculations)	1.1	3.0	5.7	9.7	18.0
Red-shift after 1 s	No	No	Yes	Yes	Yes

Table 17: Power titration experiment for C222₁ crystals of OaPAC₁₋₃₅₀.

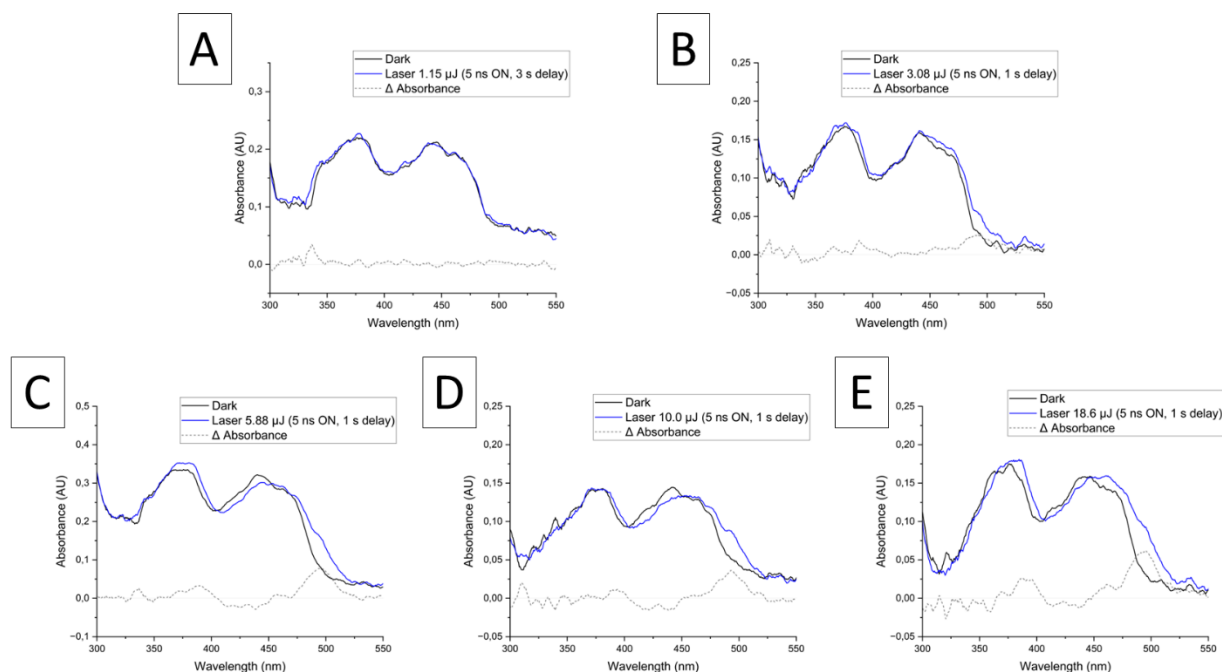


Figure 27: Laser power titration analysis of C2221 OaPAC₁₋₃₅₀ crystals.

In crystallo optical spectroscopy analysis of OaPAC₁₋₃₅₀ C2221 crystals after excitation with increasing laser intensities. UV-Vis absorption measurements were performed at room-temperature under red light (referred to as dark) or after 5 s laser illumination at 420 nm and 1 to 3 s delay. Blue and dark lines show the light- and dark-adapted states, respectively. The grey dashed lines correspond to the difference in absorbance between the light- and dark-adapted states. (A-B) No red-shift of the maximum absorption around 450 nm is present for laser intensities of 17.3 and 46.4 mJ/cm². (C-D) A red-shift at around 450 nm is noticed for laser intensities between 88.6 and 280.3 mJ/cm², with the maximum increase of the absorbance around 492 nm.

Figures were created with Origin software version 2024.

OaPAC in the crystal not reacting at low laser fluence might indicate that the theoretical calculation is slightly incorrect, or that the parameters used for the calculation are inaccurate. However, it is also possible that OaPAC requires a strong light signal to react. Nakasone *et al.* used a combination of transient grating and activity assay to describe the non-linear response of OaPAC to light intensity, proposing that OaPAC is only activated under strong light conditions. Interestingly, they established that both protomers of OaPAC must be activated for the enzyme to successfully convert ATP to cAMP. This indicates that limiting the number of photons during TRX crystallography to one absorbed photon per molecule to avoid multiphoton effect (Grünbein *et al.*, 2020; Barends *et al.*, 2024; Do *et al.*, 2024) might not be adequate for enzymes dependent on strong light excitation like OaPAC. Following this calculation will result in extremely low occupancy of the light-activated state, most likely not visible in the electron density.

3.3.3. Slow Conformational Changes in OaPAC₁₋₃₅₀ Crystals Revealed by Time-Resolved Optical Spectroscopy

After determination of the required laser fluence to initiate the signalling state in OaPAC, a time series of UV-Vis absorption spectrum was recorded for an OaPAC C222₁ crystal after photoexcitation with 143.1 mJ/cm² fluence (8.7 absorbed photons per molecules, theoretically). Spectra were recorded between 10 μs and 12 s (Figure 28), being the limit range of the TR-icOS setup at the time of the experiment (Engilberge *et al.*, 2024). The crystal exhibited the typical red-shift of BLUF photoreceptors upon photoexcitation within a few ms, while the largest red-shift of 11.5 nm was observed after 900 ms (Figure 28A-B). Interestingly, after a spectroscopically stable phase over 30 ms (together with the incomplete red-shift), the absorbance at 492 nm slowly increased until 900 ms, before the decay to the ground state occurred (Figure 28C). In solution this second slow increase in absorbance was not observable, because the achievable time resolution was limited (Figure 13C). Decay kinetics could not be calculated due to the incomplete recovery of the dark state on the recorded time range (Figure 28C), but a time constant between 10 and 15 s could be approximated, which is two to three times slower, compared to the recovery of OaPAC in solution. Dark spectra, recorded before each time point during the time series analysis, are shown in Appendix Figure 5 and confirmed that OaPAC returned to the dark state before each new photoexcitation.

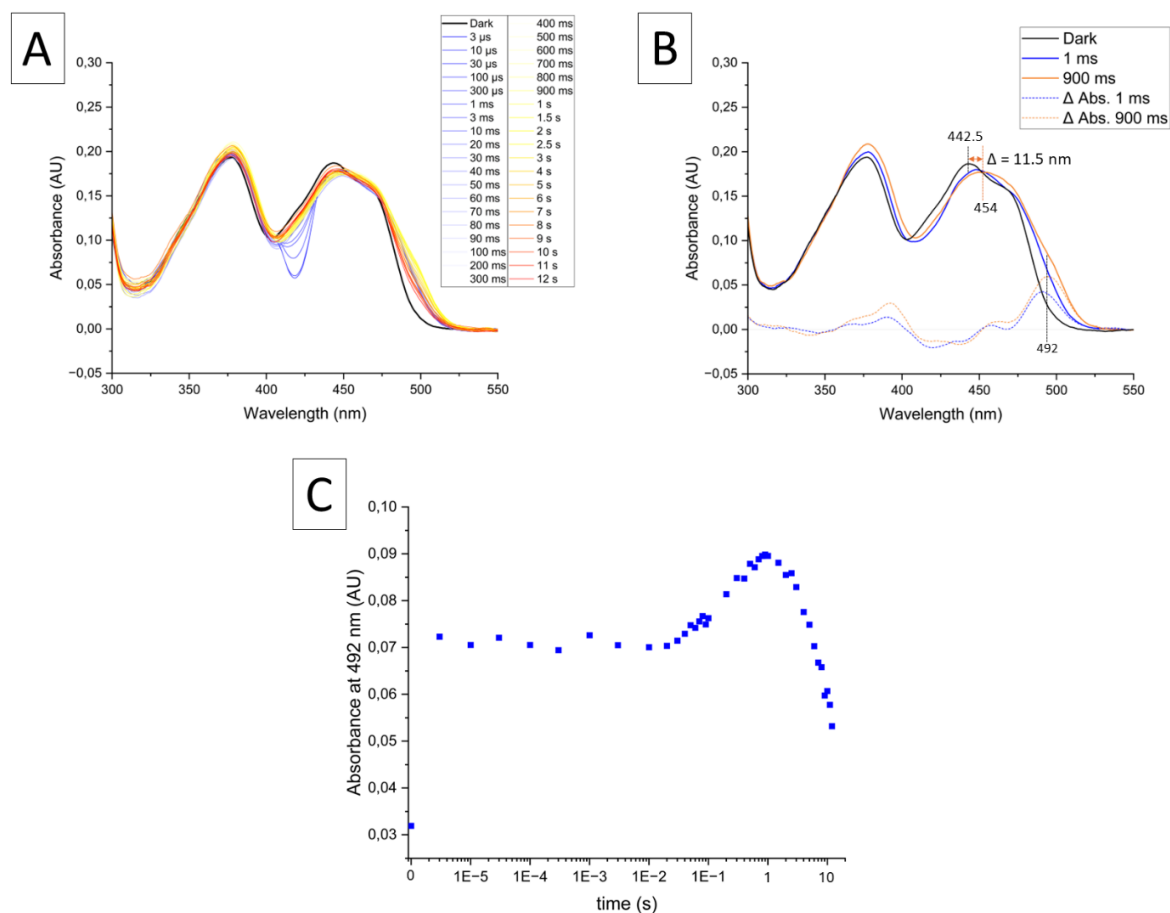


Figure 28: Time-resolved analysis of OaPAC₁₋₃₅₀ C222₁ crystal UV-Vis absorption recorded at the TR-icOS platform. (A) Time series of an OaPAC₁₋₃₅₀ C222₁ crystal UV-Vis absorption spectra, measured in the dark and after a ns 420 nm-laser pulse and a delay time between 3 μ s and 12 s. The dark line shows the dark-adapted state. The time series is coloured following a gradient with blue from the fastest to red for the slowest time delays. (B) Room-temperature UV-Vis absorption spectra of OaPAC₁₋₃₅₀ C222₁ crystal measured in the dark or after 1 and 900 ms delay after 4 ns 420 nm-laser excitation. Blue, orange and dark lines show the light-adapted state after 1 and 900 ms delay and dark-adapted state, respectively. A red-shift of 11.5 nm of the absorption maximum at around 450 nm is observed upon light excitation. The dashed lines correspond to the difference in absorbance between the light- and dark-adapted states. (C) Change in absorbance during the time series shown in (A) was monitored at 492 nm. Time 0 represents the absorbance in the dark state. The values exhibit an increased absorbance at the fastest measured point at 3 μ s. A second increase in absorbance at 492 nm is observed after 30 ms and peaking at 900 ms, before it decreases again. Figures were created with Origin software version 2024.

From prior ultrafast spectroscopy studies, there has been general consensus that the red-shifted state is formed within ns and that the reaction is then spectroscopically silent (Gauden *et al.*, 2005; Gauden *et al.*, 2006a; Okajima *et al.*, 2006; Mathes *et al.*, 2011; Kennis and Mathes, 2013; Mathes and Götze, 2015). Yet, these studies were focussed on ultrafast time scales or used truncated BLUF variants, therefore they might have missed slower changes in the UV-Vis absorption spectrum.

Recently, Tokonami *et al.* performed UV-Vis absorption studies over a longer time scale for eight different full length BLUF photoreceptors and demonstrated that AppA and OaPAC (multi-domain proteins) and PapB and Sy PixD/Slr1694 (short BLUF proteins) exhibited clear slower reaction kinetics in a second phase on the ms time scale (Tokonami *et al.*, 2022). A slow increase in absorbance was also noted for the three other BLUF photoreceptors tested (BlrP1, YcgF and TePixD/Tll0078) but was less pronounced. Specifically, for OaPAC, a slow increase in absorbance was observed after the fast, initial rise, peaking at 150 ms (time constant of 36 ms). Yet, this slower reaction phase was absent in the truncated version of OaPAC composed of the BLUF sensor domain only, meaning that the absorbance change in the ms time range was related to rearrangement in the AC domain or the linker region during signal transmission linked to amino acids interacting with the flavin. As reaction kinetics in the crystal seem to be slower than in solution, it is plausible that the slow rise in absorbance observed from 30 to 900 ms before decay in the crystal (time constant around 235 ms) (Figure 28C) corresponds to the slow rise peaking at 150 ms in solution in the study of Tokonami *et al.* (time constant of 36 ms) (Tokonami *et al.*, 2022).

Nakasone *et al.* also noted a second phase of rise and decay on the ms time scale when studying OaPAC with transient grating (Nakasone *et al.*, 2023). Specifically, they only observed this rising phase for OaPAC full length and OaPAC₁₋₁₂₆ (BLUF and α -helix 3) with time constants of 36 and 31 ms, respectively, while OaPAC₁₋₁₀₂ (BLUF domain alone) and a full length Trp90Ala mutant did not exhibit this pattern. They attributed this slow reaction phase to motions in the AC domain and α -helix linker regulated by the tryptophan.

Before trying to elucidate structural rearrangements associated with the second absorbance increase phase, attempts were made to obtain structural models of OaPAC in the spectroscopically stable phase between 3 μ s and 30 ms, to compare it with the 2.3 μ s model obtained from TR-SFX.

At the T-REXX instrument, because of the fairly weak diffraction of the crystals, it was not possible to reach a time resolution better than 50 ms. A data collection was carried out at the ID29 beamline of ESRF, where the highest photon flux enables X-ray exposure of less than 100 μ s. A data set was collected around 200 μ s after laser excitation, but unfortunately did not lead to any interesting data, as the difference electron density maps did not reveal any reasonable change between the dark and the 200 μ s-light-activated state. In-nozzle excitation was also tested at the SPB/SFX instrument

from EuXFEL. In this experiment, instead of exciting the crystals in the liquid jet, the laser beam was positioned at the tip of the nozzle, which enabled delays between laser excitation and X-ray probing in the tens to hundreds of μs time range to be reached. However, with this setup, light contamination of subsequent pulses within a train was too pronounced, rendering the expected time delays unreliable. Additionally, it appeared that the pump laser beam was damaging the nozzle. Unfortunately, no other possibility arose during the timeline of this PhD to try collecting new data to elucidate structural models of OaPAC in the spectroscopically stable intermediate phase from 3 μs to 30 ms.

3.3.4. Signal Transduction on the Millisecond Time Scale

To decipher the structural rearrangement associated with the slow reaction phase, visible as a rise in absorbance at 492 nm on the ms time scale, a TR-SSX experiment was carried out at the T-REXX instrument of Petra III P14.EH2 beamline. This TR-SSX investigation elucidated the structural rearrangements occurring in OaPAC when co-crystallized with ATP in the orthorhombic crystal form with $C222_1$ space group at the three different time delays 50, 480 and 960 ms. Data were collected on two different beamtime days. A detailed breakdown of data collection and data processing for each dataset is shown in Table 18. Surprisingly, although sample preparation was similar for both beamtimes, electron density for the ATP was not observable in the active site for the data collected during the second beamtime (480 and 960 ms).

For this TR-SSX experiment, I carried out the sample preparation, sample loading on fixed target and data processing and analysis, while David von Stetten (beamline scientist at T-REXX/P14.EH2, Hamburg, Germany) was in charge of the beamline setup and data collection. Data collection and refinement statistics are shown in Appendix Table 3.

	TRUE DARK	50 ms			TRUE DARK	480 ms		960 ms	
Sample	OaPAC ₁₋₃₅₀ C222 ₁ crystals batch 1				OaPAC ₁₋₃₅₀ C222 ₁ crystals batch 2				
Cell parameters	a = 54.3 Å, b = 145.8 Å, c = 105.5 Å, $\alpha = 90^\circ$, $\beta = 90^\circ$, $\gamma = 90^\circ$				a = 53.7 Å, b = 146.4 Å, c = 103.5 Å, $\alpha = 90^\circ$, $\beta = 90^\circ$, $\gamma = 90^\circ$				
ATP visible	Yes				No				
X-ray parameters	10 x 15 μm , 12.7 keV, 5 ms, $\sim 2 \times 10^{12}$ ph/s								
Laser	No	Yes, 405 nm			No	Yes, 405 nm		Yes, 405 nm	
Laser parameters	N/A	40 μm (FMWH), 10 MHz, 10,000 pulses, 1 ms total	40 μm (FMWH), 10 MHz, 40,000 pulses, 4 ms total	40 μm (FMWH), 10 MHz, 80,000 pulses, 8 ms total	N/A	40 μm (FMWH), 10 MHz, 40,000 pulses, 4 ms total	40 μm (FMWH), 10 MHz, 80,000 pulses, 8 ms total	40 μm (FMWH), 10 MHz, 40,000 pulses, 4 ms total	40 μm (FMWH), 10 MHz, 80,000 pulses, 8 ms total
Laser fluence	N/A	55.1 mJ/cm ²	220.5 mJ/cm ²	441 mJ/cm ²	N/A	110.3 mJ/cm ²	220.5 mJ/cm ²	110.3 mJ/cm ²	220.5 mJ/cm ²
Delivery method	Fixed target HARE chips								
Date of data collection	06.07.2023	06.07.2023	06.07.2023	06.07.2023	12.12.2023	12.12.2023	12.12.2023	12.12.2023	12.12.2023
Total number of frames	41,472	41,472	20,736	60,908	20,736	41,472	41,472	41,472	41,272
Total number of hits	15,924	24,136	12,928	29,808	5,872	12,030	10,293	9,291	10,212
Hit rate	38.4 %	58.2 %	62.3 %	48.9 %	28.3 %	29.0 %	24.8 %	22.4 %	24.7 %
Total nb of indexed lattices	12,181	17,524	9960	22,645	7,530	16,010	11,966	11,375	14,387
Indexed rate	76.5 %	72.6 %	77.0 %	76.0 %	128.2 %	133.1 %	116.3 %	122.4 %	140.9 %
Indexed rate (disregarding multiindexing)	59.6 %	56.8 %	59.8 %	58.8 %	92.7 %	89.9 %	89.2 %	86.8 %	86.1 %

Table 18: Description of data collection setup and data processing results during TR-SSX beamtimes at the T-REXX instrument of PETRA III P14.EH2 beamline with proposal MX947.

Q-weighted Fourier difference electron density maps for the three pump-probe delays (50, 480 and 960 ms) were calculated against their respective dark data set using Xtrapol8 (de Zitter *et al.*, 2022) and several changes in the vicinity of the flavin chromophore surrounding are highlighted (Figure 25B,E,H). Up to 2.1 Å resolution, good correlation was observed with an R factor between both data sets ($R_{\text{iso}} < 0.25$) and an isomorphism-indicating correlation coefficient $CC_{\text{iso}} > 0.8$. The resolution for the analysis process using Xtrapol8 was therefore cut at 2.1 Å.

Fourier difference electron density maps provide some evidence on the involvement of the conserved amino acids Gln48, Trp90, Ser91 and Met92 in the second phase during signal transmission (Figure 29 and Figure 30). For the data set corresponding to 50 ms pump-probe delay and 55.1 mJ/cm² laser fluence, no significant difference around the flavin chromophore was observed (Figure 29A-B). At this laser fluence, only 2.4 absorbed photons per chromophore were theoretically calculated according the illumination guideline of Grünbein *et al.* (Grünbein *et al.*, 2020), and it has been shown by *in crystallo* spectroscopy that more than 3 absorbed photons (theoretically calculated) were necessary to activate the system. No difference in the difference electron density map for this data set was therefore expected, confirming the results from the power titration.

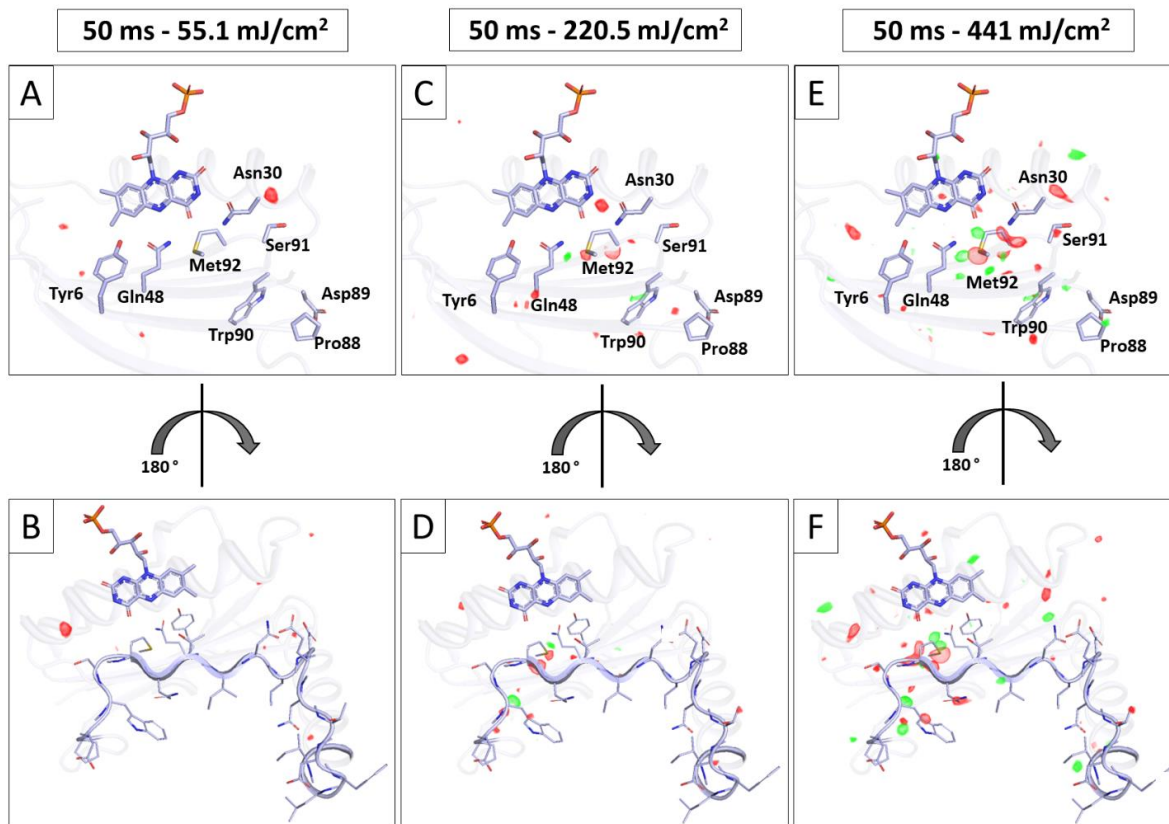


Figure 29: Signal transmission in the BLUF domain of OaPAC revealed at 50 ms pump-probe delay by TR-SSX. $F_{o-light}-F_{o-dark}$ difference maps contoured at +3.5 r.m.s.d. (green) and -3.5 r.m.s.d. (red) reveal changes around the flavin chromophore and the BLUF domain at 50 ms pump-probe delay after photoexcitation of OaPAC₁₋₃₅₀ with three laser fluences 55.1 mJ/cm² (A-B), 220.5 mJ/cm² (C-D) and 441 mJ/cm² (E-F). The BLUF domain of OaPAC in the dark state at RT is shown in light blue in cartoon representation and involved amino acids in stick representation. (A, C, E) Structural details and changes in the chromophore binding pocket. Most of the changes are focused around the conserved Met92. (B, D, F) Structural details and changes behind the flavin highlighting β -sheet 5 and the loop preceding the α -helix 3 linker. After 50 ms, the changes are mainly focused around the flavin binding pocket. Figures prepared by the PyMOL Molecular Graphics System, Version 2.5.4 Schrödinger, LLC (Schrödinger and DeLano, 2020).

Analysis of the difference electron density maps after 50 ms pump-probe delay at higher laser fluence demonstrate clear changes around Gln48 and Met92 (Figure 29C,E), as observed after a few μ s in the TR-SFX experiment (Figure 25). Predictably, changes are similar between the two higher laser fluences 220.5 and 441 mJ/cm² and increase with increased laser fluences (Figure 29C-F). Specifically, Met92 seems completely displaced, which affects the backbone region around Ser91 and Met92 (Figure 29E-F). However, structural changes seem to be localized around the flavin chromophore and did not advance away from the chromophore pocket even after 50 ms (Figure 29D,F). It is probable that the 50 ms delay here is probing the OaPAC structural

arrangement in the optically stable phase defined in the previous section. Indeed, 50 ms is in the transition phase at the beginning of the slow absorbance rise (Figure 28C), therefore it is likely that structural rearrangements related to signal transmission in the second phase have only just started and not yet advanced enough at 50 ms to reveal changes further than the chromophore binding pocket.

Assuming the increase in absorbance from 30 ms after photoexcitation is due to an intermediate state that accumulates and reaches maximum occupancy around 900 ms, then difference electron density maps should exhibit similar patterns at 480 and 960 ms, but with more pronounced differences at 960 ms. This hypothesis seems plausible with the data obtained from TR-SSX experiment (Figure 30). An increase in difference signals is observed with increased laser fluence for each time point and also between 480 and 960 ms when comparing the same laser fluence, although the latter is not so explicit. Interestingly, already at 480 ms pump-probe delay, structural rearrangements have propagated further away from the chromophore binding site (Figure 30B,D,F,H). Specifically, the loop between β -sheet 5 and α -helix 3 exhibits strong differences between the dark state and the light-activated states. The backbone of Ser91 and Met92 are largely displaced, as well as all the amino acids between Asn96 and Leu104. The FTIR study by Masuda *et al.* revealed changes in the β -sheet 5 structure during signal transduction (Masuda *et al.*, 2005c), which correlate with the strong negative absorbance on the backbone between Ser91 and Met92 right at the beginning of β -sheet 5 (Figure 29 and Figure 30). Jung *et al.* also speculated from crystallography results that the kink in the β -sheet 5, which represents the dark-adapted state, is modified for a regular β -strand in the light-adapted state of AppA (Jung *et al.*, 2006). Wu *et al.*, when comparing NMR spectra of BlrP1 in the dark and light-activated states, noted significant chemical shifts corresponding to changes in β -sheet 5 and both loops preceding and succeeding it (Wu and Gardner, 2009). Interestingly, these later results and this TR-SSX study indicate that rather large structural rearrangements are observed in the BLUF domain during signal transduction, which contradicts the findings of Ohki *et al.*, who cryo-trapped OaPAC₁₋₃₅₀ in a light-activated state after 20 s continuous illumination (Ohki *et al.*, 2017). They only observed a slight 40° rotation of Gln48, accompanied with a Met92 movement of around 1.4 Å, but without change in the backbone related to a straightening or any other modification of β -sheet 5. Additionally, they did not note any changes in the loop before α -helix 3.

The appearance of changes at 480 and 960 ms pump-probe delays, which were absent at 50 ms, correlates with the observed slow phase of absorbance rise from UV-Vis spectroscopy (Figure 28). This second phase therefore indicates, that signal transduction to more distant amino acids in the BLUF domain also involves residues neighbouring the flavin chromophore, which cause additional changes in the UV-Vis spectra. From this TR-SSX study, Met92 is the most likely candidate for the transmission of the signal. Masuda *et al.* showed the importance of the conserved methionine in PixD signal transduction by demonstrating that a Met93Ala mutant (corresponding to Met92Ala in OaPAC) was not able to properly respond to light, as many FTIR signals related to signal transduction in the wild type were absent in the mutant (Masuda *et al.*, 2008).

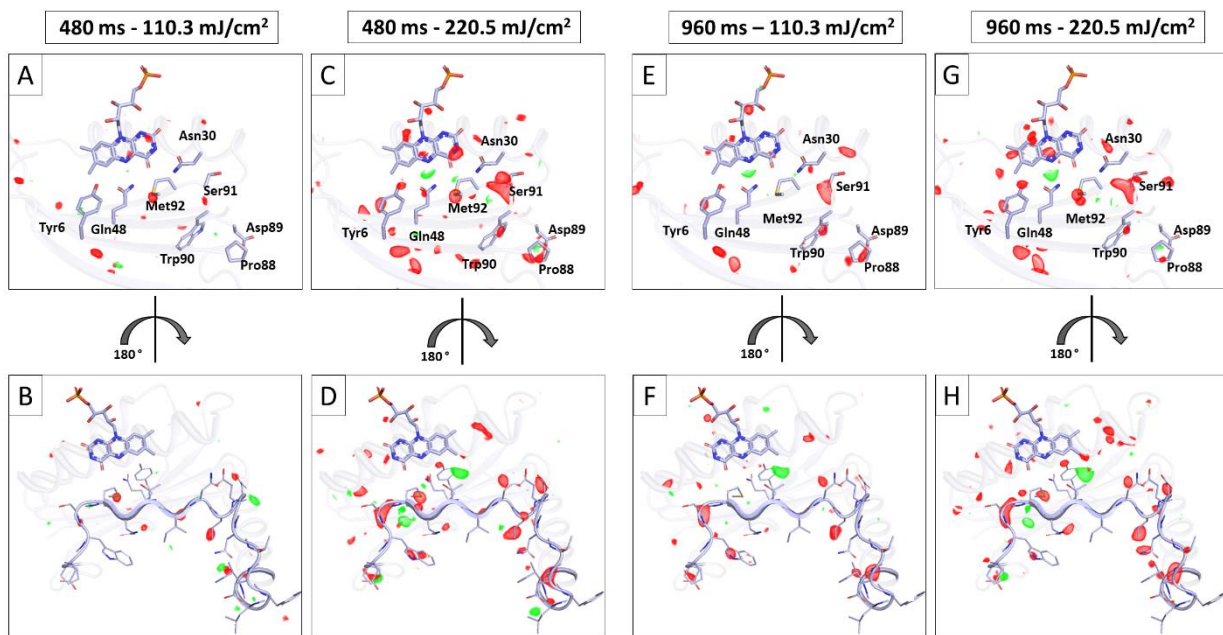


Figure 30: Signal transmission in the BLUF domain of OaPAC₁₋₃₅₀ revealed at 480 and 960 ms pump-probe delays by TR-SSX.

F_{o-light}-F_{o-dark} difference maps contoured at +3.5 r.m.s.d. (green) and -3.5 r.m.s.d. (red) reveal changes around the flavin chromophore and the BLUF domain at 480 ms (A-D) and 960 ms (E-H) pump-probe delay after photoexcitation of OaPAC₁₋₃₅₀ with two laser fluences 110.3 mJ/cm² (A-B, E-F) and 220.5 mJ/cm² (C-D, G-H). The BLUF domain of OaPAC in the dark state at RT is exhibited in light blue in cartoon representation and involved amino acids in stick representation. (A, C, E, G) Structural details and changes in the chromophore binding pocket. Structural rearrangements are observed around Tyr6, Gln48, Ser91 and Met92. (B, D, F) Structural details and changes behind the flavin highlighting β -sheet 5 and the loop preceding the α -helix 3 linker. After 480 and 960 ms, the changes have advanced, and structural rearrangements happen in the backbone and the side chain of amino acids on β -sheet 5 and the preceding and following loops.

Figures prepared by the PyMOL Molecular Graphics System, Version 2.5.4 Schrödinger, LLC (Schrödinger and DeLano, 2020).

Examination of the AC domain also revealed a few changes. Compared to 50 ms time delay, differences are visible in the region between α -helices 7 and 8 at 480 and 960 ms, while the rest of the AC domain seems unchanged (Figure 31). Although it would be expected that more changes are happening in the AC domain at these two late time delays, the absence of ATP in the second experiment might be the reason for the small changes of the AC domain during signal transduction.

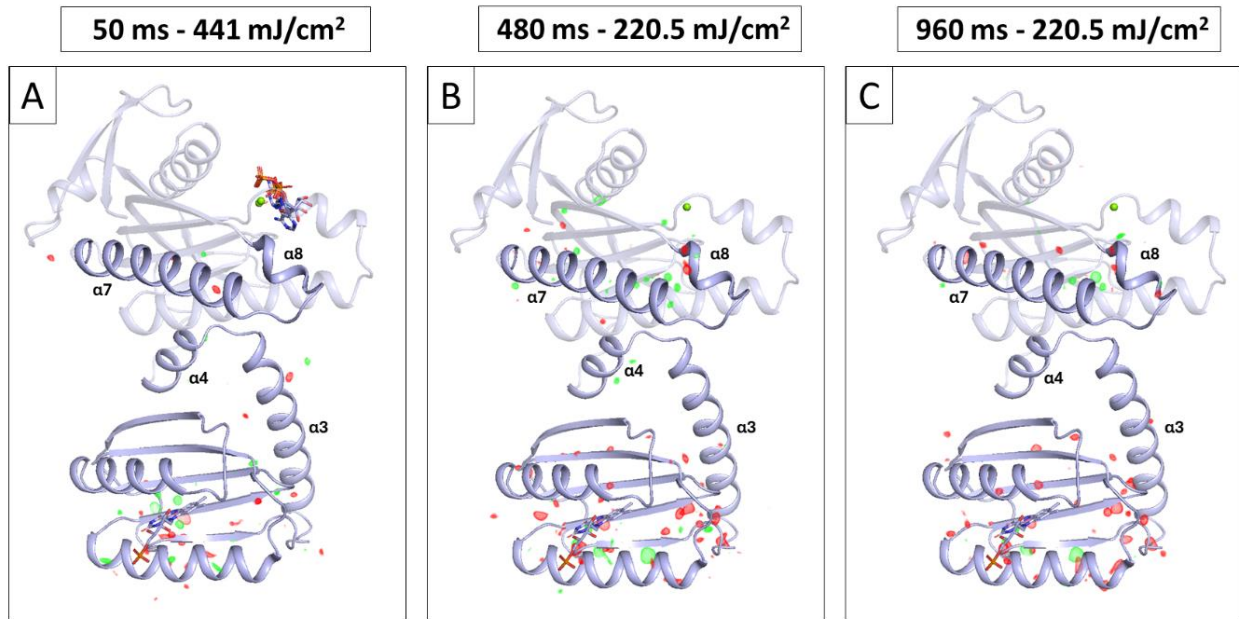


Figure 31: Signal transmission in *OaPAC*₁₋₃₅₀ revealed at 50, 480 and 960 ms pump-probe delays by TR-SSX.

*F*_{o-light}-*F*_{o-dark} difference maps contoured at +3.5 rmsd (green) and -3.5 rmsd (red) reveal changes in the BLUF domain and the AC domain at the three pump-probe delays 50 ms (A) 480 ms (B) and 960 ms (D) after photoexcitation. *OaPAC* in its dark state at RT is exhibited in light blue in cartoon representation. Changes in the BLUF domain are clear; while only few rearrangements are observed in the AC domain after 480 and 960 ms.

Figures prepared by the PyMOL Molecular Graphics System, Version 2.5.4 Schrödinger, LLC (Schrödinger and DeLano, 2020).

After analysis of the difference electron density maps, attempts were made to obtain a structural model of the light-activated states at the three time delays to better understand the structural rearrangements involved in signal transduction. Xtrapol8 could not be used to estimate occupancies or extrapolate structure-factor amplitudes, as the structural changes happening on the ms time scale were too large. Indeed, the extrapolation process works on the assumption that the dark and light-activated states have highly similar phases (de Zitter *et al.*, 2022), which is incorrect when structural changes between the two states become larger. Consequently, calculating occupancies and extrapolated maps for the TR-SSX data did not lead to interpretable results. Similarly,

occupancy determination following the method described by Barends *et al.* was not suitable as prior knowledge on the intermediate light-activated state is necessary to apply this method (Barends *et al.*, 2024). As multicopy refinement requires a known occupancy, it was also impossible to obtain structural models using this strategy.

3.3.5. Steady State of OaPAC₁₋₃₅₀ Light-Activated State in C222₁ Crystal

In order to investigate the later events during signal transduction from the BLUF domain to the AC domain after blue light excitation, cryo-trapping experiments were performed to capture a steady state of the reaction. Several exposure times, laser fluences and crystal size combinations were tested in an attempt to obtain the light-activated state close to full occupancy, which would greatly simplify data analysis. Indeed, long light exposure induced a change in the unit cell dimensions due to large structural rearrangements, rendering the dark and light-activated crystals non-isomorphous. Neither the extrapolation process nor mFo-DFc omit map-based occupancy determination followed by multicopy refinement can resolve a light-activated state and its occupancy with a non-isomorphous reference crystal and/or when the changes are too significant between the two states (de Zitter *et al.*, 2022; Barends *et al.*, 2024).

A crystal of OaPAC was co-crystallized with ATP and grew up to a size of 150 x 50 x 30 μm^3 . The crystal was flash cooled immediately after 5 s constant light exposure with a 200 mJ/cm^2 laser fluence and manual rotation of the crystal during exposure. By this, full occupancy of the light-activated state could be achieved and reversion to the dark state was prevented. X-ray diffraction data of the light-activated sample were collected at 100 K at the synchrotron. Light-activated OaPAC co-crystallized with 5 mM ATP grew in space group C222₁ with one molecule in the asymmetric unit and unit-cell parameters $a = 52.5 \text{ \AA}$, $b = 141.4 \text{ \AA}$, $c = 104.7 \text{ \AA}$, $\alpha = 90^\circ$, $\beta = 90^\circ$, $\gamma = 90^\circ$. Compared to OaPAC co-crystallized with ATP in the dark, with unit cell parameters $a = 54.5 \text{ \AA}$, $b = 146.4 \text{ \AA}$, $c = 104.9 \text{ \AA}$, $\alpha = 90^\circ$, $\beta = 90^\circ$, $\gamma = 90^\circ$, a shortening of 2 and 5 \AA of the a and the b axes were observed, respectively. The structural model of cryo-trapped OaPAC could be solved at

1.7 Å resolution and the electron density map around the flavin chromophore is presented in Figure 32A.

When comparing the structural models of the dark state and the steady-state, activated by 5 s of light exposure, both at cryogenic temperature, notable differences were observed in the BLUF domain and particularly around the flavin chromophore (Figure 32B and Appendix Figure 6). The C α RMSD was 1.36 Å when comparing both dimers and 1.93 Å for an all-atom RMSD. A difference electron density map was calculated in real space using MatchMaps (Brookner and Hekstra, 2024) to overcome the loss of isomorphism between the two crystals (Appendix Figure 6). Several significant changes around the chromophore in the sensor domain deserve attention.

Most importantly, Trp90 moves from the Trp_{out}/solvent exposed conformation to a Trp_{in} conformation upon light exposure, taking the position of Met92, which is now in a Met_{out} conformation (Figure 32B). Concurrently, the Gln48 side chain displays a 205° rotation when compared to the dark state. The orientation of the glutamine in this model allows a favourable interaction between Gln48 OE1 and Trp90 NE1 (Pal and Chakrabarti, 2001), which would not be the case if Gln48 had not performed a side chain rotation compared to the dark state. By this, Gln48 OE1 shares a new hydrogen bond with Trp90 NE1 (3.4 Å) (Figure 32C). The formation and breakage of a hydrogen bond between the carbonyl group of Gln63 and the indole nitrogen of Trp104 in AppA was already proposed by Masuda *et al.* as critical for the light signalling pathway (Masuda *et al.*, 2005c; Masuda *et al.*, 2007). The onset of the Met_{in} to Met_{out} transition was already visible in the TR-SSX (Figure 29 and Figure 30) as well as the TR-SFX data, where Gln48 has undergone a 180° rotation after 1.8 μs delay and Met92 was moving away from the flavin binding pocket simultaneously (Figure 25). The movement of Met92 is accompanied by the displacement of Trp90, which can use the space freed by Met92 to settle near the chromophore binding pocket.

Additionally, the hydrogen bond network between the highly conserved amino acids Tyr6 and Gln48 and the chromophore is altered (Figure 32C-D). In the dark state at cryogenic conditions, Gln48 NE1 shares a hydrogen bond with FMN O4 (2.9 Å) and FMN N5 (3.3 Å), and Gln48 OE1 with Tyr6 OH (2.8 Å). In the steady state, the rotated Gln48 side chain exhibits interactions between Gln48 OE1 and FMN O4 (3.1 Å) and between Gln48 NE1 to FMN N5 (3.1 Å). The hydrogen bond between Gln48 NE1 (replacing OE1) to Tyr6 OH also stretches to 3.4 Å compared to 2.8 Å in the dark state. The rotation of Gln48, as well as the movement of Gln48 away from Tyr6 (0.6 Å

displacement), is similar after the continuous 5 s illumination compared to 2.3 μ s delay in the TR-SFX study using the extrapolation process (Figure 25J). The alteration in the hydrogen bond configuration towards FMN O4 aligns perfectly with the distinctive shifts observed in the IR difference spectra of BLUF domains (Domratcheva *et al.*, 2016). Indeed, the steady state presented in this cryo-trapped data represents the Z-Z glutamine tautomer with hydrogen bonding properties distinct from those of the dark state's glutamine in its amide tautomer.

The Met_{out}/Trp_{in} transition triggers the breakage of the hydrogen bond between Asn30 ND2 and Ser91 carbonyl oxygen and creates a new amino-aromatic interaction between Asn30 ND2 and Trp90 NE1 (3.1 Å) (Figure 32C-D), which was discussed by Jung *et al.* as an important step to stabilize the signalling state (Jung *et al.*, 2006). The tryptophan to alanine mutation in AppA and the asparagine to alanine mutation in Tll0078-TePixD both resulted in an increase in the relaxation rate (Kita *et al.*, 2005; Masuda *et al.*, 2005c). This suggests that preventing the highly conserved asparagine from interacting with the semi-conserved tryptophan destabilizes the light-activated state. Additionally, the Asn32Ala mutation in Tll0078-TePixD also revealed an incomplete red-shifted spectrum upon light excitation (Kita *et al.*, 2005), as observed by Ohki *et al.* in OaPAC hexagonal crystal form. This indicates an incomplete reaction during signal transduction and might explain the absence of Trp_{in} conformation in their 20 s cryo-trapped data (Ohki *et al.*, 2017).

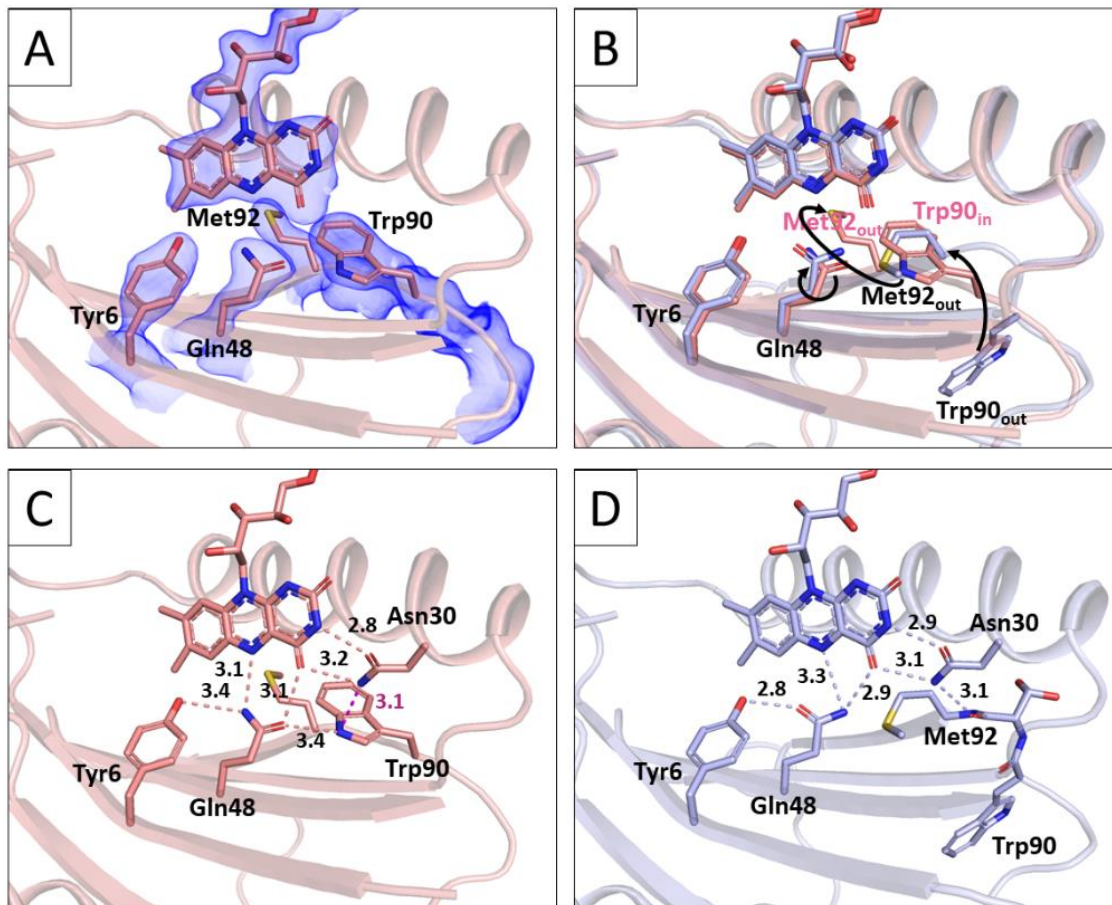


Figure 32: Transition from Trp_{out} to Trp_{in} in OaPAC revealed by cryo-trapped data after 5 s of continuous light excitation.

(A) Electron density map ($2F_o - F_c$) contoured at 1 rmsd around FAD chromophore in 5 s cryo-trapped data from OaPAC showing the Met_{out}/Trp_{in} conformation. (B) Structural model of excited OaPAC (salmon) is shown and involved amino acids in stick representation along with the dark model (light blue). Trp_{out} to Trp_{in} transition as well as Met_{in} to Met_{out} transition and Gln48 rotation are visualized by arrows. (C) Hydrogen bond distances (black) and amino-aromatic interaction (magenta) around the flavin chromophore of the Trp_{in} state. (D) Hydrogen bond distances around the flavin chromophore of the Trp_{out} dark state.

Figures prepared by the PyMOL Molecular Graphics System, Version 2.5.4 Schrödinger, LLC (Schrödinger and DeLano, 2020). Figures modified from Chretien et al. (Chretien et al., 2024).

This cryo-trapping result corroborates the significance of Gln48 rotation in the photoactivation process. Additionally, the map shows the $Trp_{in/out}$ and $Met_{in/out}$ conformations, which have been subjects of debate since the initial investigations into BLUF photoreceptors. To date, it has been documented that most BLUF variants exhibit a Trp_{out} conformation in the dark state, such as OaPAC (Ohki et al., 2016), bPAC (Lindner et al., 2017), AppA (Jung et al., 2006), BlrB (Jung et al., 2005), BlrP1 (Barends et al., 2009; Wu and Gardner, 2009), BlsA (Chitrakar et al., 2020), TePixD/TII0078 (Kita et al., 2005) and SyPixD/Srl1694 (Yuan et al., 2006) in 9 subunits out of 10. Yet, some of them also present a Trp_{in} conformation like SyPixD/Srl1694 (Yuan et al., 2006)

in 1 subunit out of 10 and AppA in the presence of imidazole (Anderson *et al.*, 2005). Nonetheless, there has been no structural evidence demonstrating that the transition between these conformations occurs during light exposure as a component of the signalling pathway. In fact, this finding diverges from previous observations on OaPAC, where a structure illuminated for 20 s displayed only minor alterations upon blue light excitation and no Trp_{out} to Trp_{in} transition (Ohki *et al.*, 2017). Specifically, this prior report indicated a rotation of Gln48 by only 40°, whereas the observations presented here reveal a complete rotation of the side chain. Furthermore, Met92 shifted away from Gln48 only after 20 s in the hexagonal crystal form, extending the distance from 2.6 Å to 3.3 Å, and Trp90 underwent a minor 40° rotation. In contrast, this data demonstrates a complete Trp_{in}/Met_{out} switch and a significant structural reorganization of the loop between β -sheet 4 and 5, as well as β -sheet 5 and the following loop, already after 5 s of illumination (Figure 33).

Interestingly, recording data from a 20 s constant illumination was impossible for the orthorhombic crystal form, due to a considerable decrease in resolution when the crystal was illuminated for more than 5 s. This decrease occurred even when the LED light intensity was significantly reduced. This suggests that prolonged light exposure disrupts the crystal lattice as OaPAC undergoes its enzymatic activity. Possibly, the crystal packing of the hexagonal crystal form, as reported by Ohki *et al.*, prevented the larger structural rearrangements necessary for the Trp_{in}/Met_{out} switch in their study (Ohki *et al.*, 2017). This may have also enabled the crystal to maintain a high level of order during longer exposure to blue light without disrupting the crystal lattice.

The significance of the semi-conserved methionine in inducing the signalling state was initially demonstrated for AppA by Masuda *et al.* with the FTIR analysis of AppA Trp104Ala mutant (Masuda *et al.*, 2005c). Later, Brust *et al.* also suggested the tryptophan as a key residue in transmitting signals from the FAD chromophore to the protein backbone after their time-resolved FTIR study of AppA (Brust *et al.*, 2013). Additionally, studies on AppA (Karadi *et al.*, 2020), BlrP1 (Barends *et al.*, 2009), SyPixD/Srl1694 (Yuan *et al.*, 2006) and BlrB (Sadeghian *et al.*, 2008), and have already proposed the transition from Trp_{out} to Trp_{in} conformation as one of the initial steps in signal transmission to the effector domain, but this phenomenon has not been previously described for PAC. To date, structures of OaPAC (Ohki *et al.*, 2017) and bPAC (Lindner *et al.*, 2017; Lindner, 2018) only noted the presence of a Trp_{out} conformation in the light-adapted state. A few studies also contradicted the drastic movement of the tryptophan upon photoexcitation, and argued that only minor changes in the tryptophan or also the methionine are necessary for signal transduction in

BLUF photoreceptors (Toh *et al.*, 2008; Dragnea *et al.*, 2010; Unno *et al.*, 2010). However, these studies were performed on truncated versions of AppA (1-125 to 1-133), which is known to alter or restrict signal transmission (Hasegawa *et al.*, 2006), and can be the origin of the different results obtained by these studies.

The Met_{out}/Trp_{in} transition reported in the steady state is accompanied by the reorganization of the loop before β -sheet 5 (Val80 to Trp90) and β -sheet 5 itself (Ser91 to Asn96) (Figure 33B-C). The sequence between Pro88 and Gln93, which reveals a kink in the dark structure, is flattened by the Met_{out}/Trp_{in} transition. Consequently, all the subsequent amino acids are moved two amino acids further towards the C-terminus and β -sheet 5 loses its S-pattern to reveal a straighter β -strand (Figure 33D). Temperature factors in the following loop from Leu97 to Phe103 increase to over 100 Å², indicating that the flexibility of the loop is extremely high and that this section is disordered in the steady state. Probably, Asp98 to Thr101 move out to reduce the C-terminal shift, which gets fully compensated from Leu104 at the beginning of the α -helix linker. Interestingly, both loops before β -sheet 5 were already suspected to be involved in signal transduction as they exhibited higher flexibility in the dark state (Figure 21).

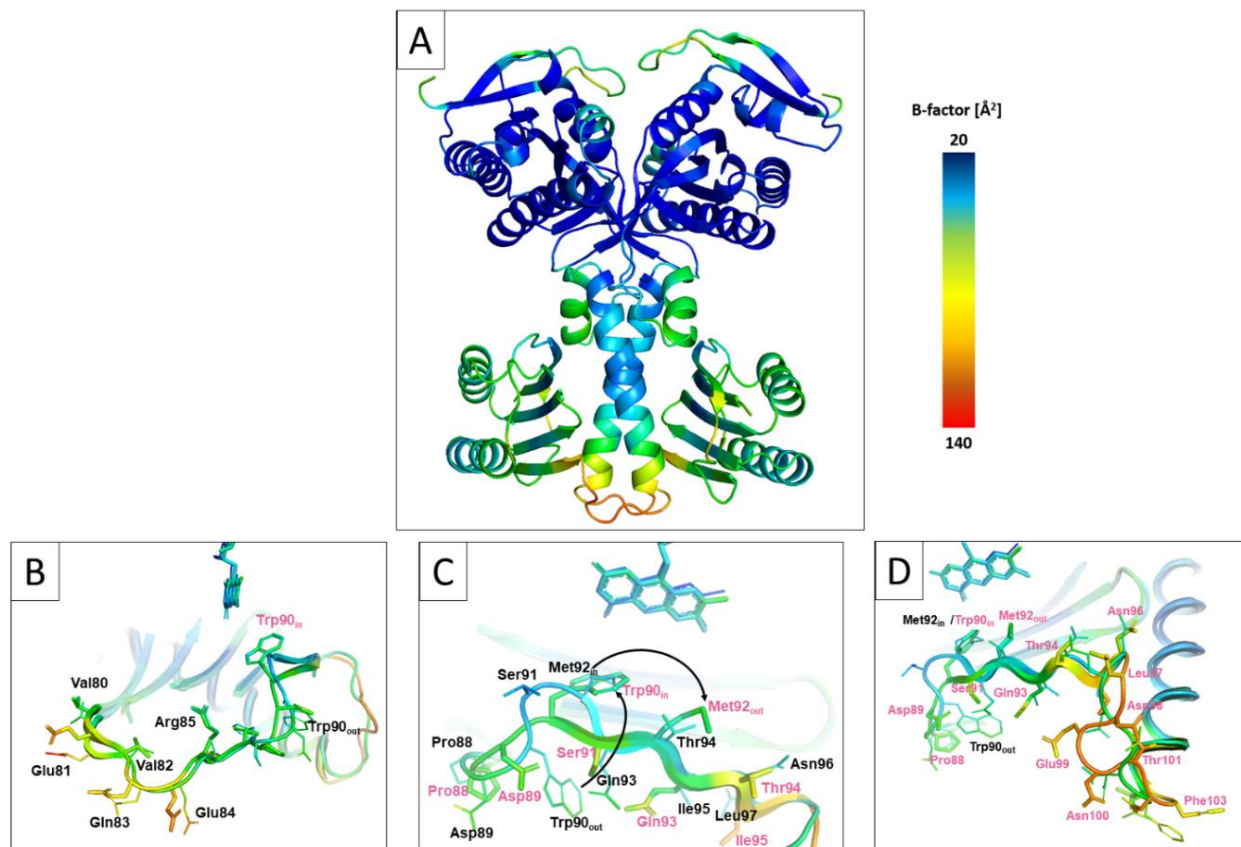


Figure 33: OaPAC shows a restructuring of β -sheet 5 and both loops preceding and succeeding it together with the $\text{Met}_{\text{out}}/\text{Trp}_{\text{in}}$ transition upon light excitation.

(A) OaPAC secondary structure from 5 s cryo-trapped data coloured according to temperature factors. Lower temperature factors coloured in blue indicate low flexibility, while high temperature factors coloured in red indicate a high degree of flexibility. (B-D) Trp_{in} transition is facilitated by mobilization of neighbouring amino acids (Val80 to Phe103), as can be seen by the increase in temperature factors. Significantly displaced amino acids in the Trp_{in} model are labelled in salmon. S-pattern shape of β -sheet 5 in the dark structural model straightens to accompany the two-amino acid shift in the Trp_{in} model (C). This shift is compensated for by an increased flexibility in the loop between β -sheet 5 and α -helix 3 (D).

Figures prepared by the PyMOL Molecular Graphics System, Version 2.0 Schrödinger, LLC (Schrödinger and DeLano, 2020).

Figures modified from Chretien *et al.* (Chretien *et al.*, 2024).

Masuda *et al.* studied AppA Trp104Ala mutant (corresponding to Trp90Ala in OaPAC) with FTIR spectroscopy and demonstrated that certain signals related to changes in a β -sheet structure during signal transduction were abolished in the mutant, confirming that the semi-conserved tryptophan is essential to transmit the signal through this distinct β -sheet structure alteration (Masuda *et al.*, 2005c). Brust *et al.* used vibrational spectroscopy to investigate the relaxation pathway of AppA, revealing a hierarchical pathway where the H-bonded residues in the chromophore binding pocket returned to the ground state more slowly than distant residues (Brust *et al.*, 2013). The study of a Trp104Ala mutant in AppA demonstrated an acceleration of the relaxation to the ground state by a

factor of 80, and structural changes in more distant residues observed in AppA wild type were suppressed in the mutant, suggesting that long ranged structural rearrangements critical for the protein activity cannot develop if the semi-conserved tryptophan is not present in the protein. Jung *et al.* also speculated that the kink in β -sheet 5 corresponds to the dark-adapted state of AppA, whereas the straightened β -strand corresponds to the light-adapted state (Jung *et al.*, 2006). The cryo-trapped data shown here agrees with these two proposals, as it supports the crucial role of Trp90 specifically in straightening β -sheet 5 during the signal transmission in the light-adapted state of OaPAC.

The slow reaction kinetics observed in the ms time range with OaPAC using Transient grating and UV-Vis absorption spectroscopy are suppressed for the Trp90Ala mutant, as well as in the truncated version of OaPAC containing the BLUF domain only (Tokonami *et al.*, 2022; Nakasone *et al.*, 2023). For both mutants, conformational changes related to signal transduction upon light excitation were limited to changes with fast kinetics, and in the Trp90Ala mutant, enzymatic activity was abolished. This suggests that the slower structural rearrangements associated with AC domain activity are mediated by the semi-conserved tryptophan residue in OaPAC. It also confirms that study of truncated BLUF photoreceptors provides misleading information when studying signal transduction. Here, although kinetics in the crystal are slower than in solution (time constant of 235 against 36 ms), the slow rise in absorbance observed with UV-Vis spectroscopy (Figure 28C) seems also to be associated with signal transduction through the Met_{out}/Trp_{in} transition.

The importance of the coiled-coil in transmitting the signalling state in OaPAC was suggested by Ohki *et al.* (Ohki *et al.*, 2016). They showed that mutations of Leu111 and Leu115, which exhibit hydrophobic interactions between both α -helices 3 at the dimer interface, suppressed the cyclase activity. Additionally, mutating Tyr125 on α -helix 3 or Asn256 on β -sheet 10 in the tongue region of the AC domain, which share an inter-subunit hydrogen bond, also led to loss of enzymatic activity. Interestingly, this interaction is part of the critical hydrogen bond network at the interface between the linker region (C-terminus of α -helix 3 and α -helix 4) and the tongue region of the AC domain, which was suggested to play a crucial role in transmitting the signal to the active site. These findings confirm the role of α -helix 3 in signal transduction, necessitating critical non-polar and polar interactions across the dimer interface. Consequently, this supports the essential functional role of Trp90 in communicating the signalling state to the linker region in OaPAC.

The OaPAC structural model obtained from the cryo-trapping experiment was superposed with the difference electron density map obtained from the TR-SSX data introduced in the previous chapter (Figure 34). The strong increase in electron density behind the flavin chromophore observed at 480 and 960 ms matches perfectly with the Met92 in a Met_{out} conformation (Figure 34B-C), while this increase in density is not yet visible after 50 ms pump-probe delay (Figure 34A). This confirms that the changes in the UV-Vis absorbance spectrum on the ms time scale are associated with the Trp_{in} conformation altering a second time the hydrogen bond network in the chromophore binding pocket. Additionally, displacement of the backbone of Ser91 in the 5 s cryo-trapped data also correlates with the changes in electron density at 480 and 960 ms (Figure 34B-C), confirming the straightening of β -sheet 5 is associated with the Trp movement already at 480 ms after photoexcitation in the crystal.

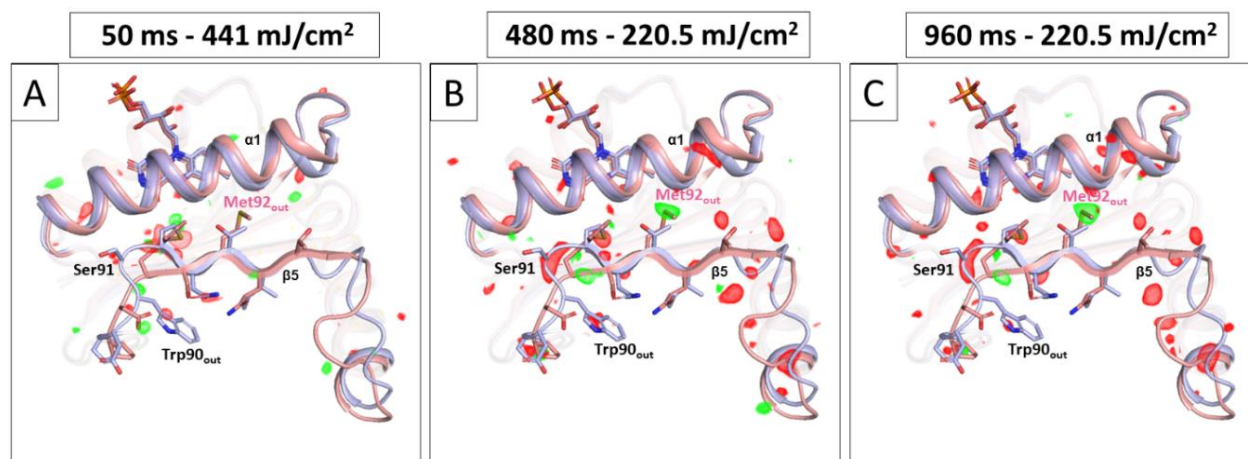


Figure 34: Overlay of OaPAC₁₋₃₅₀ structural model from the cryo-trapping experiment with the TR-SSX data. The structural model from the cryo-trapping experiment (salmon) is overlaid with OaPAC structural model at room-temperature from the TR-SSX experiment (light blue), as well as the Fo-light-Fo-dark difference maps contoured at +3.5 rmsd (green) and -3.5 rmsd (red) at the three pump-probe delay times: 50 ms (A), 480 ms (B) and 960 ms (C). At 480 (B) and 960 ms (C) delays, the 5 s cryo-trapped structural model matches well with the changes in electron density from the TR-SSX data.

Figures prepared by the PyMOL Molecular Graphics System, Version 2.5.4 Schrödinger, LLC (Schrödinger and DeLano, 2020).

With these results, it is possible to propose that the Met_{out}/Trp_{in} transition present in OaPAC is of crucial importance in the signalling mechanism. It appears to drive the entire β -strand 5 into a new conformation, thereby inducing subsequent structural changes necessary for signal transmission.

Interestingly, Lindner *et al.* proposed that in bPAC, the kink in β -sheet 4 at the top of the BLUF domain serves as a pathway for signal transmission from the flavin chromophore to the C-terminus of α -helix 3 and/or α -helix 4, before proceeding through the tongue region of the AC domain (Lindner *et al.*, 2017). However, the TR-SSX and cryo-trapping data for OaPAC do not support the first part of this mechanism. Instead, the findings suggest signal transmission occurs via β -sheet 5 to the coiled-coil linker. Residues of β -sheet 4 near α -helices 3 or 4 do not reveal significant change upon light excitation, while the loop located between β -sheet 5 and α -helix 3 exhibits substantial movements, associated with a notable increase in temperature factors in that region, confirming the loop's involvement in signal transduction (Figure 33).

Looking at structural rearrangements located further away from the BLUF domain, a movement of both BLUF domains in the homodimer away from each other as well as closer to the AC domains is observed (Figure 35A). For example, the distance between Ile22 C α in α -helix 1 (BLUF domain) and Glu224 C α in α -helix 7 (AC domain) is reduced from 40.7 Å to 38.7 Å in the cryo-trapped data. This movement causes the shortening of the unit cell axis described previously, with the a axis shortened by 2 Å and the b axis strongly shortened by 5 Å after 5 s light exposure, compared to the dark state at cryogenic temperature. Recently, Kapetanaki *et al.* also observed the same distance shortening in a constitutively active Tyr6Trp mutant of OaPAC with the BLUF domain moving closer to the AC domain when compared to the wild type, slightly changing the ATP cavity (Kapetanaki *et al.*, 2024).

Additionally, the data also indicate that the α -helix 4 is involved in signal transduction to the AC domain, as revealed by the increased temperature factors (Figure 33A), the non-isomorphous difference map (Appendix Figure 6) and the conformational changes in this region (Figure 35B). Specifically, Gln127 to Ser129, as well as the side chain of Phe131, moves 1 Å closer to the tongue of the AC domain from monomer B. These changes modify the hydrogen bond network slightly, with a breakage of the hydrogen bond between Tyr125_A carbonyl oxygen and Lys262_B side chain, and Gln127_A NE2 sharing a hydrogen bond with Thr195 O (3.1 Å) instead of Val194 O in the dark state (3.3 Å). Lindner *et al.* already proposed that the tongue between β -sheets 9 and 10 serves as the link enabling signal transmission from the linker region to the AC domain (Lindner *et al.*, 2017). They revealed a structural flexibility in that region for bPAC, with one tongue in an upper position compared to the tongue from the other monomer in the dark state, suggesting this flexibility is functionally relevant for signal transduction in PAC photoreceptors. In OaPAC, the asymmetry is

not present for either the dark or the light-activated structural models presented here. Yet, in the cryo-trapped structure, most of the amino acids at the interface between the handle and the tongue also exhibit high flexibility, as indicated by residues in α -helix 4 and the loop between β -sheets 9 and B adopting multiple conformations (Figure 35B). The changes in hydrogen bonds due to the α -helix 4 structural rearrangement and the high flexibility in that region might be a continuation of signal transmission to the AC domain.

Finally, few interesting changes are observed in the AC domain after 5 s continuous illumination. The C-terminus of OaPAC is significantly disordered after blue light exposure. Glu326 and Asn327 at the end of β -sheet 13 and Glu128 in the subsequent loop are the last residues that can be clearly modelled in the electron density of the cryo-trapped structure. Interestingly, their position varies significantly from those in the dark-state structure, confirming that the C-terminus undergoes structural rearrangements (Figure 35A). As a result, α -helix 5, which is located next to the C-terminal α -helix 12, appears to be destabilized (Figure 33A), causing a slight shift in residues Val158 to Leu157 (Figure 35C). Specifically, the distances between ATP O3' and Ser161 CA or Glu165 CA are increased from 5.6 to 5.9 Å or from 10 to 11 Å compared to the dark state, respectively. This observation might explain the strong influence of the OaPAC C-terminus on the adenylate cyclase activity (Hirano *et al.*, 2019), as α -helix 5 is crucial for coordinating the ATP phosphates in the active site. Notably, the changes observed in the TR-SSX data after 480 and 960 ms between α -helices 7 and 8 (Figure 31B-C) are not observed here, with both helices matching the structural model of OaPAC in its dark state well.

Interestingly, the changes revealed by the cryo-trapped data compared to the dark-state structural model are primarily confined to structural rearrangements within the BLUF domain, with only minor changes detected in the AC domain. An evaluation of the temperature factors for the entire structural model of OaPAC showed consistently higher values in the BLUF domain and the linker region, especially for both loops preceding and succeeding β -sheet 5 and for α -helix 4, while the AC domains are particularly unaffected by the light exposure and do not exhibit significant increases in temperature factors compared to the dark state (Figure 33A). Additionally, no sign of cAMP production is detected in the cryo-trapped data, with ATP still clearly visible in the electron density, although the reaction is expected to progress further towards ATP conversion to cAMP after 5 s of continuous blue light exposure.

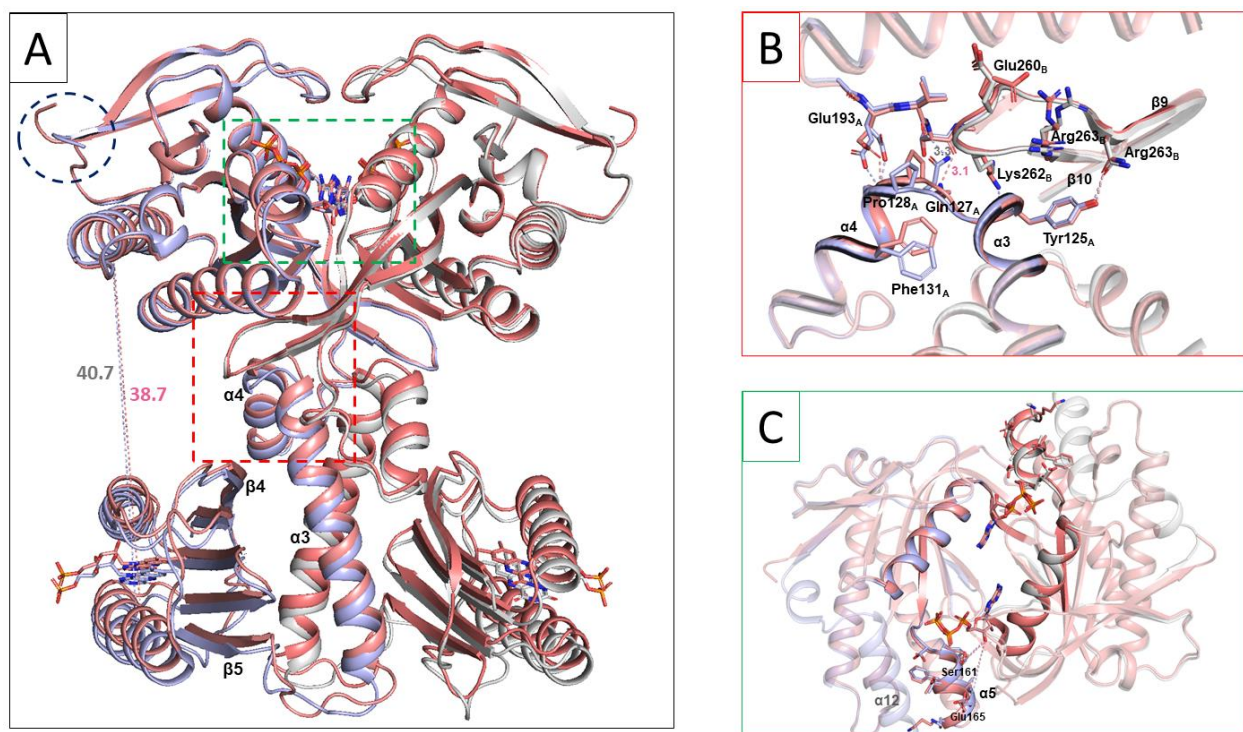


Figure 35: Analysis of changes in the linker region and AC domain upon light exposure in the C222₁ crystals. (A) BLUF domain moves about 2 Å closer to the AC domain in 5 s cryo-trapped OaPAC (salmon) compared to the dark-state model (light blue/grey). Regions which exhibit light-induced rearrangements are highlighted with dashed lines. Figure is modified from Chretien et al. (Chretien et al., 2024). (B) Side chain rearrangements in the α -helical linker region between the BLUF and AC domains in 5 s cryo-trapped OaPAC (salmon) compared to the dark-state model (light blue/grey). (C) View of the top of the active sites, showing the displacement of α -helix 5 in the cryo-trapped model (salmon) compared to the dark state (light blue/grey). α -helix 5 is located near the C-terminal α -helix 12. Figures prepared by the PyMOL Molecular Graphics System, Version 2.5.4 Schrödinger, LLC (Schrödinger and DeLano, 2020).

3.3.6. FTIR Study to Understand the Absence of ATP to cAMP Turnover in OaPAC₁₋₃₅₀ Crystals

To better understand the absence of ATP to cAMP conversion in OaPAC C222₁ crystals, FTIR light-minus-dark difference spectra were recorded from a crystal slurry in the orthorhombic space group. FTIR spectra from OaPAC₁₋₃₅₀ and OaPAC₁₋₁₃₇ containing only the BLUF domain and the linker region (α -helices 3 and 4) were also recorded in solution (Figure 36A and Appendix Figure 7). FTIR data were collected and analysed by Marius Nagel and Tilman Kottke from Bielefeld University. The data enabled us to determine which signals originated from the AC domain or from the rest of the protein. While analysing the overlay spectra of OaPAC in solution after scaling, it

can be observed that most of the prominent bands between 1680 and 1600 cm^{-1} are from the AC domain, except for one signal at 1655 cm^{-1} that persists even in the truncated construct, indicating it is not solely due to the AC domain (Figure 36A and Appendix Figure 7). The most prominent signals of the BLUF plus linker domain are observed at 1695 and 1710 cm^{-1} . A double difference analysis of both spectra is shown in Appendix Figure 7 to better visualize the contributions of the AC domain.

Comparing these spectra with the one of crystallized OaPAC in $C222_1$ space group reveals that the difference signal in the crystal is similar to that of OaPAC₁₋₁₃₇, which only includes the BLUF domain and the linker region (Figure 36A). A double difference analysis of crystallized OaPAC and OaPAC₁₋₁₃₇ spectra exhibits almost no remaining signal. This demonstrates that the AC domain does not undergo significant conformational changes in this crystal form, although ATP was present, which corroborates the cryo-trapping results presented in the previous section.

The lack of response of the AC domain upon blue light exposure in both the crystallographic and FTIR data can be attributed to the many crystal contacts surrounding the effector domain in the $C222_1$ crystal form (Figure 36B). Analysis of the crystal packing indicates that the movements of the enzymatic domain are sterically hindered by the surrounding molecules. While there are only a few crystal contacts around the BLUF domain, four adjacent molecules restrict the movement of the AC domains, allowing only minimal displacement. As result, although the sensor domain of OaPAC in the $C222_1$ crystals can be properly photoexcited and undergo conformational changes as part of the activation and signal transmission processes up to α -helix 4 the same way as in solution, the tight crystal packing prevents large rearrangements in the AC domain.

The volume occupied by protein in crystals is known to be closer to the volume occupied by proteins in the intracellular space, compared to purified protein in solution which is extremely diluted (Fulton, 1982). Furthermore, protein crystals are soft matter which contain widespread solvent channels, theoretically allowing diffusion of small molecules into the crystals to reach catalytic pockets (Moffat, 2001). In practice however, this does not guarantee the protein to be active in crystalline state, as some specific inter-protein interactions forced by the crystal packing might hinder essential structural changes at specific positions (Makinen and Fink, 1977; Konold *et al.*, 2020). Besides steric hindrance, the composition of the crystallisation solution might also affect the activity of the protein, if pH or unusual components are incompatible with the reaction for

instance. Sometimes, reaction kinetics will differ to that of the protein in solution (Ferrari *et al.*, 2003; Wilmot, 2003; Hadjidemetriou *et al.*, 2022). All these limitations due to the crystalline state reflect the difficulties in observing the entire signal transduction with TRX and cryo-trapping when studying BLUF photoreceptors. Specifically, this explains why, in this study, most structural rearrangements related to signal transduction did not propagate past the interface between the linker region and the AC domain. Additionally, it might also explain why only the BLUF domain moved closer to the AC domain, although Lindner *et al.* observed an opening of the AC domain upon blue light exposure to enlarge the active site cavity (Lindner *et al.*, 2017).

One can question whether the limited reaction in the C222₁ crystals suppresses the potential signalling pathway proposed by Lindner *et al.* via β -sheet 4 to the linker region (Lindner *et al.*, 2017). However, as the signals in crystallized OaPAC and in solution are similar for the BLUF domain and the linker region all the way to α -helix 4, it is unlikely that this pathway is suppressed in the crystal packing. It is more likely that the signal transmission pathway in OaPAC is initiated as observed in the TR-SSX and cryo-trapping study via β -sheet 5 to α -helix 3 and then α -helix 4.

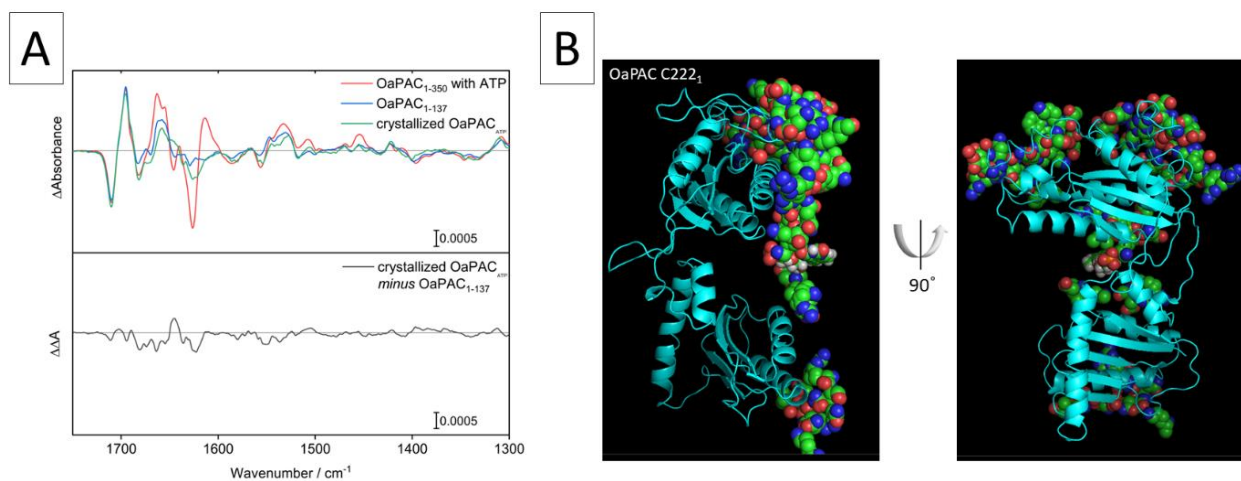


Figure 36: FTIR and crystal packing analysis of OaPAC C222₁ crystals.

(A) Light-minus-dark FTIR difference spectra of OaPAC₁₋₃₅₀ and OaPAC₁₋₁₃₇ and crystallized OaPAC in C222₁ space group and double difference spectrum between OaPAC₁₋₁₃₇ and crystallized OaPAC to isolate AC domain response in the crystals. The effector domain response is absent in the crystals. Figure modified from (Chretien *et al.*, 2024). (B) Crystal packing analysis of OaPAC crystals revealing crystal contacts in the C222₁ space group. Steric hindrance is important around the AC domain.

Figure (B) prepared by the PyMOL Molecular Graphics System, Version 2.5.4 Schrödinger, LLC (Schrödinger and DeLano, 2020).

To determine whether the other orthorhombic space group in which OaPAC crystal grew during the crystallization tests is more suitable to observe the AC domain response in the crystal, FTIR analysis of the $P2_12_12_1$ crystals was performed as well. Investigation of the crystal packing of bPAC $P2_12_12_1$ crystals (Lindner *et al.*, 2017) indicates both domains and especially the AC domain exhibit more room for movement in this crystal form (Figure 37A). This might imply that the movements of the enzymatic domain will not be sterically hindered by the surrounding molecules.

FTIR analysis on the OaPAC $P2_12_12_1$ crystals was performed by Marius Nagel and Tilman Kottke from Bielefeld University (Figure 37B-C). Surprisingly, apart from the BLUF domain signals at 1695 and 1710 cm^{-1} , signals between 1680 and 1600 cm^{-1} seem to deviate greatly from OaPAC₁₋₃₅₀ in solution (Figure 37B). Additionally, although OaPAC was co-crystallized with ATP, no peak was observed in the 900 to 1300 cm^{-1} region, which is known to exhibit signal related to ATP or cAMP (Barth and Mäntele, 1998). Of note, OaPAC C222₁ exhibited clear peaks in this region, which will be explained with more details in the next chapter (see section 3.4.3). Notably, residual signals were observed even several min after light excitation and remained until around 10 min of relaxation (Figure 37C). The remaining signals decayed more slowly after six illuminations and relaxations of the same crystal slurry and were less pronounced after ten illuminations. These residual signals appeared to be artefacts matching well the absorption of the protein in the dark in solution (Figure 37D). This indicates that remaining signals are due to $P2_12_12_1$ crystals dissolving upon light exposure and reforming only within min, as the sample during FTIR measurements is highly concentrated and enables direct recrystallization. $P2_12_12_1$ crystal dissolution was already observed during UV-Vis absorption measurement at the TR-icOS platform as described in section 3.2.4.

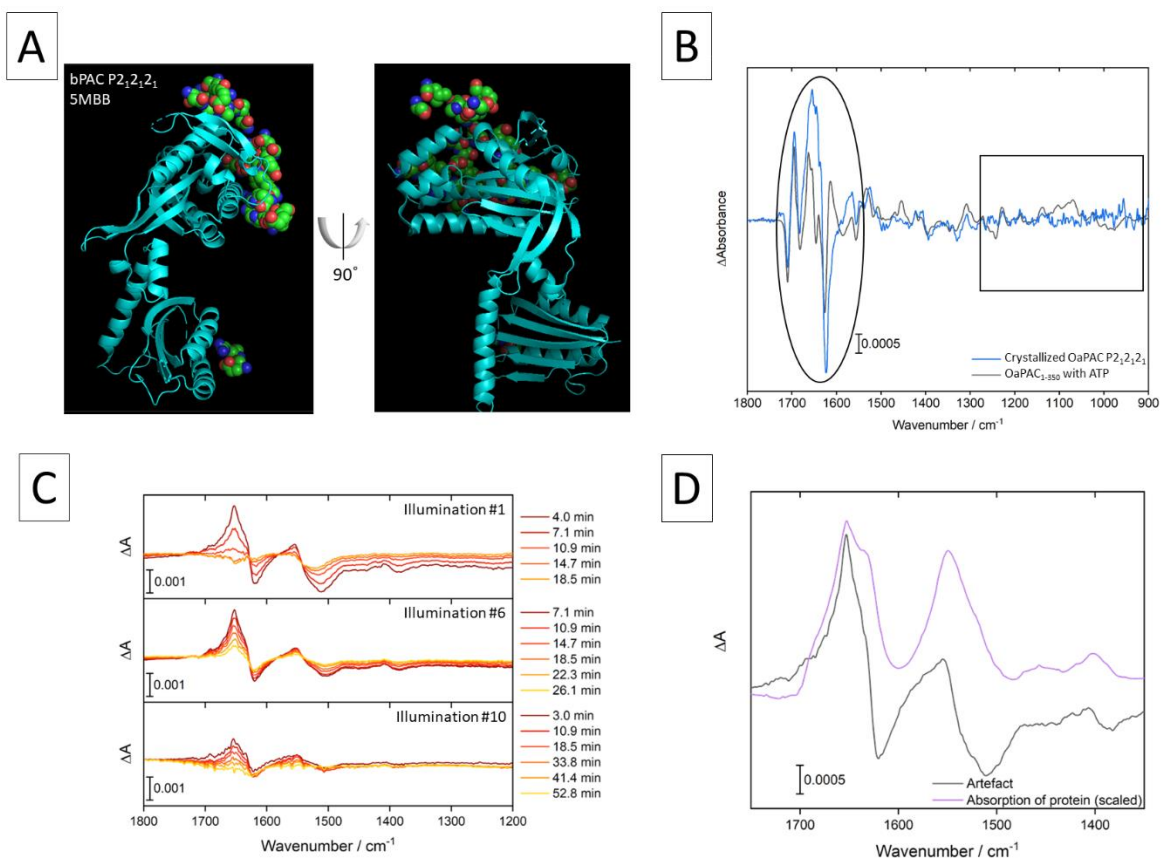


Figure 37: Crystal packing and FTIR analysis of P212121 crystals.

(A) Crystal packing analysis of bPAC P212121 crystals revealing fewer crystal contacts than in the C2221 space group. Specifically, steric hindrance is less important around the AC domain. Figure prepared by the PyMOL Molecular Graphics System, Version 2.5.4 Schrödinger, LLC (Schrödinger and DeLano, 2020). (B) Light-minus-dark FTIR difference spectra of OaPAC1-350 and crystallized OaPAC in P212121 space group. In the circle is highlighted the signals corresponding to BLUF or AC domain structural rearrangement upon light exposure. The two spectra do not match together. In the rectangle is highlighted the region exhibiting ATP or cAMP signals. Peaks are absent for OaPAC P212121 crystals in this region. (C) Light-minus-dark FTIR difference spectra of crystallized OaPAC in P212121 space group reveals remaining signal after several min of relaxation, and signals change with increased number of illuminations. (D) The residual signal shown in (C) 4 min after photoexcitation of the crystals matches the signal of OaPAC absorption in the dark in solution. Figures B, C and D are courtesy of Marius Nagel and Tilman Kottke.

Consequently, although OaPAC P212121 crystals exhibit less tight crystal packing compared to the C2221 crystals, they are not suitable for studying OaPAC signal transduction by crystallography as the crystals disintegrate upon photoexcitation. This might indicate that structural rearrangements in the AC domain are rather large during signal transduction, as a tight crystal packing does not allow for the full rearrangements to occur and a loose crystal packing led to disruption of the crystal lattice and crystal damage. The most likely explanation is an opening of the AC domain to enable enlargement of the ATP binding cavities and conversion to cAMP, as hypothesized by Lindner *et al.* (Lindner *et al.*, 2017).

3.4. Enzymatic Domain, Allosteric Communication & Relaxation

3.4.1. Binding Configuration of ATP in the Active Site

To reveal the features of native ATP binding in OaPAC, crystals of OaPAC without ATP (named ATP-free) and OaPAC crystals co-crystallized in the presence of ATP (named holo) were analysed using macromolecular X-ray crystallography at cryogenic temperature. In both cases, OaPAC grew in an orthorhombic crystal form with $C2_12_12_1$ space group in the dark. The structural model of ATP-free OaPAC could be refined to 1.5 Å, while the holo-OaPAC model was refined to 2.1 Å. Data collection and refinement statistics are shown in Appendix Table 1.

Holo OaPAC crystals demonstrated clear electron density for ATP in both active sites, as demonstrated by the Fo-Fc Polder map contoured at 3 rmsd shown in Figure 38A. This data represents the first structure of native ATP bound to a wild-type photoactivatable adenylate cyclase. Until now, ATP has only been observed in a mutated, constitutively active version of bPAC (Tyr7Trp mutant) (Lindner *et al.*, 2017). ATP was not observed for OaPAC crystallized in the orthorhombic crystal form with $P2_12_12$ space group (personal communication from Kapetanaki), just as the non-hydrolysable ATP analogue ApC_{pp} was not visible in the hexagonal crystal form with $P6_122$ space group (Ohki *et al.*, 2016). ATP also does not bind in the OaPAC orthorhombic $P2_12_12_1$ crystal used in this study, as described in previously in section 3.3.6.

Additionally, binding of ATP was also analysed at room-temperature using serial X-ray crystallography. Once again, ATP-free and holo OaPAC grew in orthorhombic crystal form with $C2_12_12_1$ space group in the dark. The structural model of ATP-free OaPAC could be solved at 2.05 Å with SSX at the T-REXX instrument of Petra III, while holo-OaPAC model was solved at 2.0 Å with SSX and 1.8 Å with SFX at SPX/SFX instrument of EuXFEL. Data collection and refinement statistics are shown in Appendix Table 3 for the SSX data and in Appendix Table 2 for the SFX data.

The three holo structures are similar to each other with 0.38 Å carbon α RMSD between the cryo and SFX structures over 350 residues, 0.64 Å between the cryo and SSX structures, and 0.58 Å

between the two room-temperature structures. Yet, both SFX and SSX structures revealed the presence of a second ATP conformation at room-temperature with between 40 to 50 % occupancy (annotated A and B) (Figure 38B and Appendix Figure 8). In the second ATP conformation B, the phosphates are unchanged with only a 0.3 Å displacement in comparison to the conformation A, but the ribose adopts a different conformation with 23° rotation, and the adenine is dragged away by approximately 5 Å, changing the torsion angle C8-N9-C1'-O4' from 45° to 77°.

At cryogenic- and room-temperatures, ATP binding is coordinated by many interactions in the active site (Figure 38C-D). Between β-sheet 6 and α-helix 5, Ser159_A, Phe160_A and Ser161_A share hydrogen bonds with the phosphates directly. Additionally, Asp156_A, Asp200_A, Ile157_A are involved in coordinating the phosphates via the two magnesium ions. The water molecules W1, W3, W4, W5 and W7 also interact with the phosphates, sharing hydrogen bonds to stabilize them.

The coordination of ATP in the active site of OaPAC is shown as a 2D representation in Figure 39 to better reveal the hydrogen and coordination bonds network and distances. Asp156_A (β-sheet 5) and Asp200_A (loop between β-sheets 7 and 8) are key residues to coordinate ATP in the active site via the magnesium ions (Tesmer *et al.*, 1999; Hahn *et al.*, 2015; Grigorenko *et al.*, 2020), sharing magnesium coordinating bonds with distances between 2 to 2.5 Å. The triad Ser159_A, Ser160_A and Ser161_A is less than 3 Å away from the phosphates and specifically stabilises PG and PB via hydrogen bonding to their backbone amide nitrogen. Similarly, Arg283_A (α-helix 9) is crucially involved in coordinating the phosphate binding via hydrogen bonds with PG OG1 and OG2. The second protomer is also involved in ATP binding in the active site with Gly269_B N, forming a hydrogen bond with the O2' of the ribose.

Surprisingly, the second ATP conformation does not appear to significantly affect the structural conformation of the surrounding amino acids in the active site (Figure 39B-C). The loss of a coordination bond between Cys201_A and Mg2 is observed, along with the formation of hydrogen bonds between Asn273_B and ATP. Asn273_B moves closer to the ATP, creating hydrogen bonds between Asn273_B ND2 and ATP O1A (3.0 Å for ATP conformation A and 2.7 Å for ATP conformation B). However, the rest of the coordination network seems particularly unaffected. This is mainly due to the adenosine being loosely coordinated in the active site (Figure 38C-D and Figure 39). The adenine is not coordinated by hydrogen bonds but engages primarily in hydrophobic interactions with surrounding amino acids. Specifically, at cryogenic temperature in

ATP conformation A, the adenine has many hydrophobic interactions with the second protomer such as β -sheet 5 (Phe154_B) and α -helix 9 (Leu268_B, Val 272_B, Asn273_B and Ala276_B) (Figure 39A-B). Due to the 5 Å displacement of the adenine, hydrophobic interactions with Phe154_B and Ala276_B disappear in conformation B, leaving the space to Ile198_B, Met203_B (loop between β -sheets 7 and 8), and Ile267_B and Asp270_B (α -helix 9) (Figure 39C).

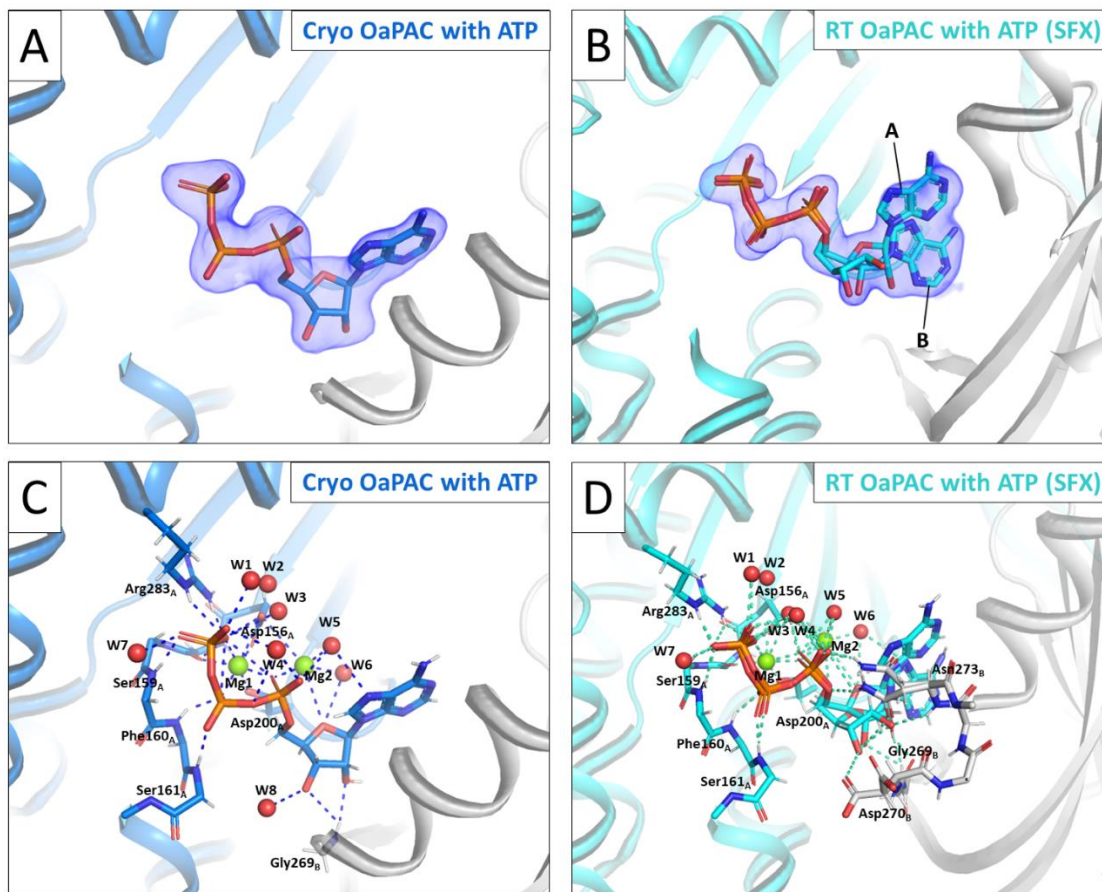


Figure 38: Details of ATP binding coordination in OaPAC active site.

Cartoon representation of the structural model of holo OaPAC at cryogenic temperature (blue) or room-temperature (cyan) and the second protomer in grey, with involved amino acids and substrate in stick representation. (A) ATP binding in a single conformation at cryogenic temperature is visible without bias, as shown by the F_o-F_c Polder map contoured at 3 rmsd. (B) ATP binding in two distinct conformations at room-temperature according to the SFX structure is visible without bias, as shown by the F_o-F_c Polder map contoured at 3 rmsd. (C) Details on ATP coordination at cryogenic temperature. A large hydrogen and magnesium coordination bond network is involved in coordinating ATP binding. (D) Details on ATP coordination at room-temperature according to the SFX structure. Similarly, a large hydrogen and magnesium coordination bond network is involved in coordinating ATP binding. Additional amino acids are involved due to the presence of a second ATP conformation.

Figures prepared by the PyMOL Molecular Graphics System, Version 2.5.4 Schrödinger, LLC (Schrödinger and DeLano, 2020). Figures (A,B,C) are modified from (Chretien et al., 2024).

Additionally, the ribose only shares hydrogen bonds with W6 and W8 or Gly269_B (Figure 38C-D). A water molecule near Mg2 has been previously described as essential for the proton transfer route during ATP conversion to cAMP (Hahn *et al.*, 2015; Grigorenko *et al.*, 2020). This water molecule could correspond to W6 in our model, situated 2.2 Å from Mg2 in the cryo structure and 2.4 Å at room-temperature, and 3.4 Å away from the ribose ATP O4' (Figure 39).

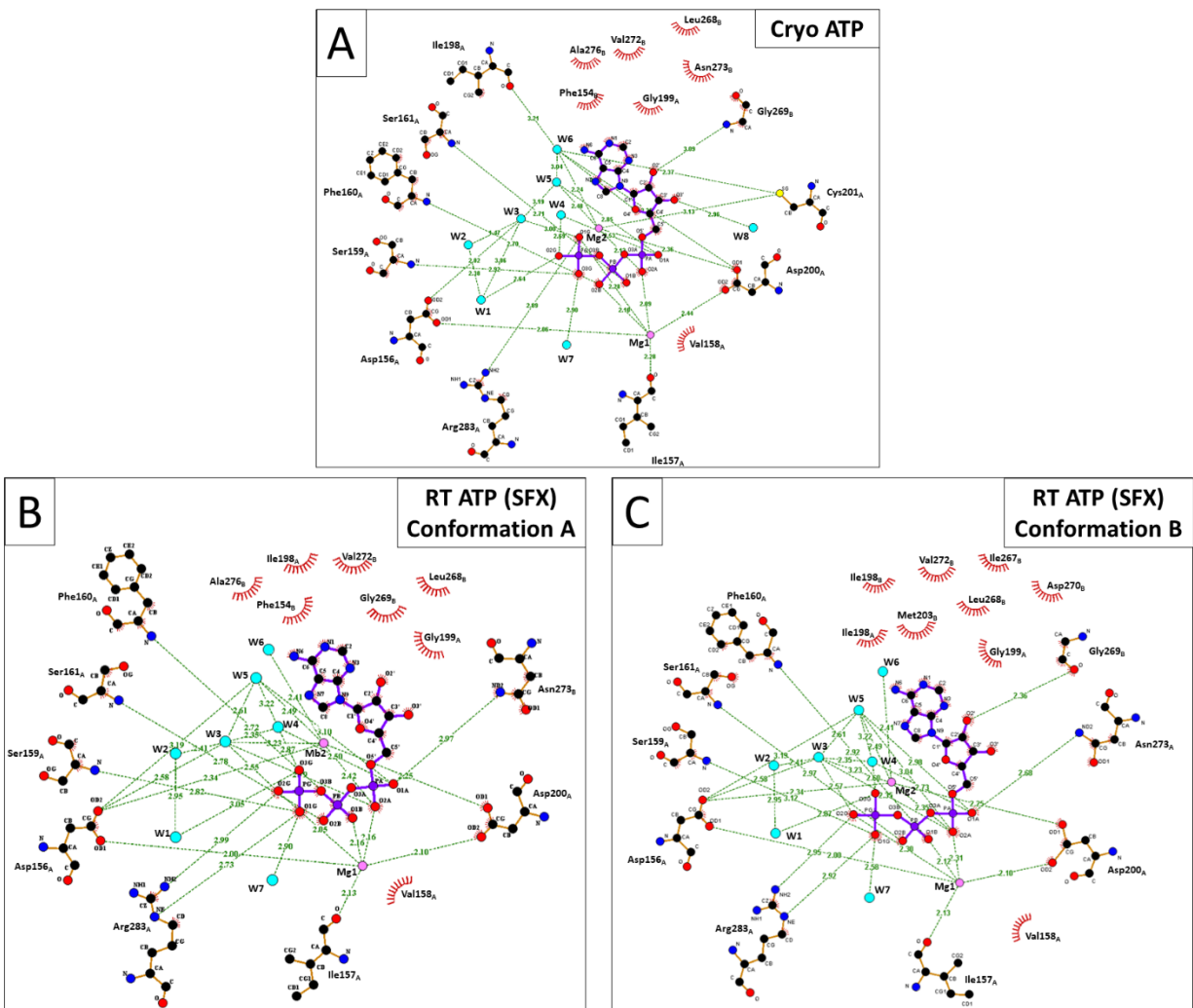


Figure 39: Representation of hydrogen bond and magnesium coordination bond network coordinating ATP in the active site of OaPAC.

(A) ATP coordination in OaPAC at cryogenic temperature. (B-C) ATP coordination in two conformations, both with ~50% occupancy, in OaPAC SFX structure at room-temperature. As ATP is coordinated mainly via the phosphates, the adenosine moiety has flexibility to adopt both conformations in the active site.

Figures prepared with LigPlot⁺ version 2.2 (Laskowski and Swindells, 2011). Figures from Chretien *et al.* (Chretien *et al.*, 2024).

Notably, the ATP molecule has a degree of flexibility in the active site, with the adenine capable of moving freely within a 5 Å range. However, the conformation observed at cryogenic temperature and both conformations at the room-temperature are energetically unfavourable for ATP turnover, according to literature (Grigorenko *et al.*, 2020). Grigorenko *et al.* identified the most favourable ATP configuration in the enzyme active site after characterizing the lowest energy barrier for initiating ATP conversion to cAMP. In this configuration, the ribose O3' atom is oriented toward one of the magnesium ions (Mg²⁺) and is about 3 Å away from the phosphate PA, enabling the in-line nucleophilic attack necessary for ATP turnover. This configuration supports proton translocation to the adjacent aspartate residue (Asp200), marking the first step of the enzymatic reaction. However, in the structural models presented above, the ATP substrate binds differently than in Grigorenko *et al.* model. The distance between the ribosyl O3' and ATP PA is more than 5 Å, too far for a nucleophilic O3' attack on the phosphate. Specifically, the ribose ring is rotated away from the phosphate, preventing the O3' atom from the ribose to coordinate Mg²⁺ as it is pointing to the opposite direction in the active site. Consequently, W6, coordinated by Mg²⁺, cannot interact with the ribosyl O3' to facilitate proton transfer. Our ATP conformation represents a higher energy state, unsuitable for low-energy proton translocation (Grigorenko *et al.*, 2020), necessitating additional structural changes before it can be converted into cAMP. Of note, Hahn *et al.* proposed another probable mechanism for ATP to cAMP conversion, which differs from Grigorenko *et al.*, but still identified the ATP configuration with the ribosyl O3' facing the magnesium ion as the starting point (Hahn *et al.*, 2015).

The second ATP conformation in the room-temperature structure shows onset of ribose rotation, but the distance between ATP O3' and PA stays greater than 5 Å (Figure 38B,D). In fact, the most favourable ATP conformation described by Grigorenko *et al.* (Grigorenko *et al.*, 2020) or Hahn *et al.* (Hahn *et al.*, 2015) cannot bind in the active site configuration seen here in OaPAC crystal structures. Although the adenine exhibits a certain degree of movement, the active site cavity is too limited to enable a fully rotated ribose and the adenine conformation associated with it. Nevertheless, the low coordination of the adenosine moiety might indicate that rearrangements necessary for ATP conversion to cAMP occur after a slight opening of the AC domain upon light excitation, as this would provide the necessary additional space for the ribose rotation.

So far and to the best of my knowledge, none of the crystallographic studies revealing ATP or analogues binding in active sites of AC enzymes have been able to observe the ATP in the specific

configuration described by Grigorenko or Hahn and co-workers (Hahn *et al.*, 2015; Grigorenko *et al.*, 2020), but all have reported ATP with a ribose pointing at the opposite direction and/or with a too large ATP O3' – PA distance (Tesmer *et al.*, 1999; Steegborn *et al.*, 2005; Mou *et al.*, 2009; Kleinboelting *et al.*, 2014; Bharambe *et al.*, 2016; Lindner, 2018; Linder *et al.*, 2020). This might indicate that the native binding of ATP in adenylate cyclase active site does not follow the most energetically favourable conformation and requires additional rearrangements for turnover.

Comparing ATP-free and holo OaPAC reveals a few differences in the active site and in the overall structure. The unit cell parameters change at cryogenic temperature from $a = 52.9$, $b = 146.2$ and $c = 103.6$ Å without ATP to $a = 54.5$, $b = 146.4$ and $c = 104.9$ Å with ATP, and at room-temperature (SSX) from $a = 53.7$, $b = 146.4$ and $c = 103.5$ Å without ATP to $a = 54.3$, $b = 145.8$ and $c = 105.5$ Å with ATP ($a = 54.3$, $b = 145.8$, $c = 105.3$ Å for SFX). The increase in a and c axis indicates a slight opening of the dimer with a movement of the AC domains away from each other. The opening does not affect the structure of OaPAC much, with 0.484 Å carbon α RMSD between ATP-free and holo structures when comparing both dimers at cryogenic temperature, and 0.458 Å at room-temperature (SSX).

Several side chains around the active site rearrange to coordinate ATP binding (Figure 40). At cryogenic temperature, Asp156_A rotates approximately 80° to interact with Mg1 and W3, facilitating ATP coordination in collaboration with Asp200_A (Figure 40A). Asp200_A, which shares a magnesium coordination bond with Mg1 in both structures, also rotates 30° to interact with the second Mg2 ion, absent in the ATP-free OaPAC structure. Ile198A undergoes a significant displacement, with its side chain rotating 180° to expand the hydrophobic pocket for the adenosine moiety in the active site. The side chain of Phe154_B comes closer to the adenine (3.6 Å in holo OaPAC vs. 3.9 Å in ATP-free). The Asn273_B side chain rotates 180° around CB, displacing Asn273_B CG by 2.1 Å to create additional space for the adenosine. Arg283A shifts 4.2 Å away from the surface, enabling its NH2 atom to share a new hydrogen bond with ATP O1G (2.9 Å) to coordinate the ATP phosphate (Figure 39A and Figure 40A) (Figure 1D and Supplementary Figure S2A). Last, Phe154 side chain rotates 20° around its CB-CG axis upon substrate binding. Lindner *et al.* also revealed that the side chain of Phe155 (corresponding to Phe154 in OaPAC) in the bPAC mutant (Tyr7Phe) moves away to allow ATP binding (Lindner, 2018).

As the adenine is mainly coordinated by hydrophobic interactions, the 5 Å displacement in ATP conformation B does not affect the surrounding residues much (Figure 40B and Appendix Figure 9). Indeed, the rearrangements are similar at room-temperature when compared to cryogenic temperature, except for Asn273_B which is found in two conformations in holo OaPAC due to the second ATP conformation. Additionally, at room-temperature (SSX and SFX), Asp156_A is rotated 70° compared to its position in holo OaPAC at cryogenic temperature. This rotation allows Asp156_A to interact with both magnesium ions, whereas at cryogenic temperature, Asp156_A interacts with Mg1 and W3. The conformation at room-temperature seems more adapted for a strong coordination of ATP binding via both magnesium ions. In previous studies by Lindner *et al.*, the constitutively active bPAC mutant revealed that Glu157 (corresponding to Asp156 in OaPAC) rotates upon ATP binding to facilitate ATP coordination via Mg2 (Lindner, 2018). Additionally, two studies on mammalian type V adenylate cyclase using computational modelling agreed on the presence and the importance of the aspartate (Asp396 corresponding to Asp156 in OaPAC) in the coordination shells of both Mg1 and Mg2 (Hahn *et al.*, 2015; Grigorenko *et al.*, 2020).

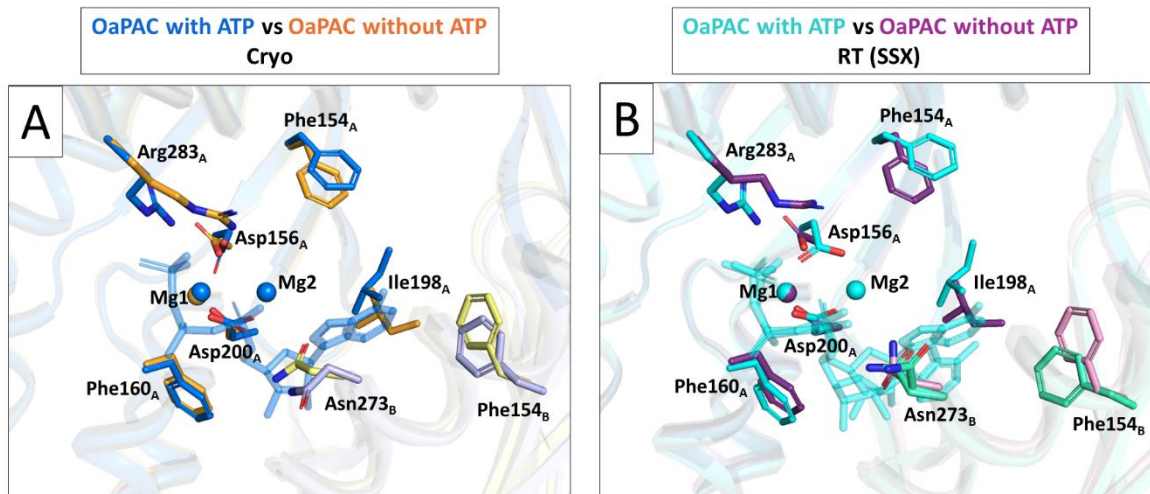


Figure 40: Details of active site rearrangement upon ATP binding in OaPAC.

Side chain rearrangements upon ATP binding at cryogenic temperature with ATP-free OaPAC in orange/yellow and holo OaPAC in blue/grey (A) and at room-temperature with ATP-free in purple/pink and holo in cyan/green-cyan (B). The changes mainly involve Asp156_A, Ile198_A, Asp200_A, Arg283_A, Phe154_B, Asn273_B. Two magnesium ions are involved in the coordination of ATP, while only one magnesium ion (Mg1) is present in the ATP-free state.

Figures prepared by the PyMOL Molecular Graphics System, Version 2.5.4 Schrödinger, LLC (Schrödinger and DeLano, 2020). Figure (A) is modified from (Chretien *et al.*, 2024).

Notably, while two magnesium ions are involved in ATP coordination in holo OaPAC (Mg1 and Mg2), only one magnesium ion (Mg1) is found to bind in the ATP-free structure (Figure 40). Early on, studies demonstrated that two metal ions were necessary for ATP turnover, with the first ion (corresponding to Mg1) mainly involved in the nucleotide binding coordination and the second ion (Mg2) involved in the catalytic activity (Black *et al.*, 1994; Tesmer *et al.*, 1999; Steegborn *et al.*, 2005). This indicates that Mg2 is recruited during/after substrate binding to enable ATP turnover.

Recently, crystallography study of OaPAC revealed that the active site without substrate presented one calcium ions instead of a magnesium (Mg1), although magnesium was present in the crystallization solution (Kapetanaki *et al.*, 2024). Similarly, Steegborn *et al.* noted the presence of calcium in the first ion site in the ATP binding pocket (Steegborn *et al.*, 2005). However, calcium ions were not able to bind in the second site, whereas bicarbonate could and would increase the catalytic activity, suggesting that calcium is not the right ion for ATP turnover. ATP has a high affinity for magnesium ions and the latter are abundant in intracellular fluid, explaining why magnesium ion is usually found to bind ATP (Garbers and Johnson, 1975; Black *et al.*, 1994). Typically, one magnesium ion always binds ATP to strongly coordinate the phosphate, while sometimes for a few enzymes a second magnesium ion weakly binds to help with group transfer (Black *et al.*, 1994). Consequently, most of the studies converge on magnesium being the physiologically relevant ion for ATP binding and catalysis in AC enzymes, although some suggest manganese ions could also replace them (Hahn *et al.*, 2015; Azher, 2018; Grigorenko *et al.*, 2020).

In addition to the binding of calcium ions, the recent OaPAC structure solved from orthorhombic crystal form in P2₁2₁2 space group (Kapetanaki *et al.*, 2024) reveals interesting features of ATP-free OaPAC which can be compared to ATP-free OaPAC from this study (C222₁). Specifically, both structures solved at room-temperature with SSX using the T-REXX instrument of P14.EH2 beamline (Petra III, Hamburg, Germany) are compared in Figure 41. The overall secondary structure is conserved, but many of the secondary structure elements are displaced in the P2₁2₁2 model when compared to the C222₁ model (Figure 41A). A carbon alpha RMSD of 2.5 Å is observed over 350 residues and of 3.3 Å when comparing both dimers. The most significant change is noted for β-sheet 12, which is moved further down in the P2₁2₁2 structure. Specifically, the tip of the β-strand where Ser311 is located is displaced 7.7 Å closer to the core of the AC domain, rearranging the subsequent loop completely.

A closer look at the AC domain reveals that the rearrangement of β -sheet 12 and the subsequent loop completely alter the active site structure (Figure 41B). The loop between β -sheets 12 and 13 forces the displacement α -helix 9 closer to its dimer counterpart. Additionally, α -helix 5 is also moved around 2 Å closer to the dimer interface. Both movements and especially the α -helices 9 from both protomers coming closer together significantly reduces the active site pocket volume. When overlaying the P2₁2₁2 structural model with the ATP binding pocket of holo OaPAC from this study, it appears that not only the active site cavity is greatly reduced but also the α -helix 9 N-terminus collides with the ATP (Figure 41C). Consequently, the active site observed in the P2₁2₁2 model reveals a closed configuration, compared to the open active site conformation obtained so far with the C222₁ models. This closed conformation prevents ATP binding, which explains why a structural model of holo OaPAC was not achievable with this crystal form and space group.

One can question whether the closed active site conformation observed in Kapetanaki *et al.* study (Kapetanaki *et al.*, 2024) is actually the native ATP-free OaPAC confirmation. It is possible to speculate that OaPAC retains a closed conformation until ATP is available. The latter would trigger an opening of the dimer interface to enlarge the ATP binding pocket and reach the open conformation observed in this study. Only then, ATP would be able to bind the enzyme and wait until light exposure for turnover.

Yet, some details of the orthorhombic crystal form with P2₁2₁2 space group might indicate that the closed configuration is rather an artefact of the crystallization process. Analysis of the crystal packing indicates that the open configuration is sterically hindered by the surrounding molecules (Figure 41D). While the C222₁ crystals already reveal many crystals contacts surrounding the effector domain (Figure 36B), the P2₁2₁2 crystals demonstrate even closer packing of the neighbouring molecules around the AC domain, forcing some secondary structure elements to move closer to the AC domain core (Figure 41D). Specifically, the 7.7 Å displacement of the β -sheet 12 C-terminal is imposed by one of the surrounding molecules, which prevent the β -strand from adopting the conformation observed in the open form. Additionally, the OaPAC C-terminus with α -helix 12, as well as the loop between α -helices 7 and 8, are affected by binding of two surrounding molecules in the crystals, resulting in the displacement of the neighbouring α -helix 5 moving 2 Å closer to the dimer interface. Consequently, the presence of an OaPAC closed active site conformation might be attributed to the many crystal contacts surrounding the effector domain in the P2₁2₁2 crystal form and forcing the protein to adopt a non-native conformation. Nevertheless,

it is still plausible that the crystal packing is only a consequence and not a cause of the closed conformation, which would then represent the native ATP-free OaPAC conformation.

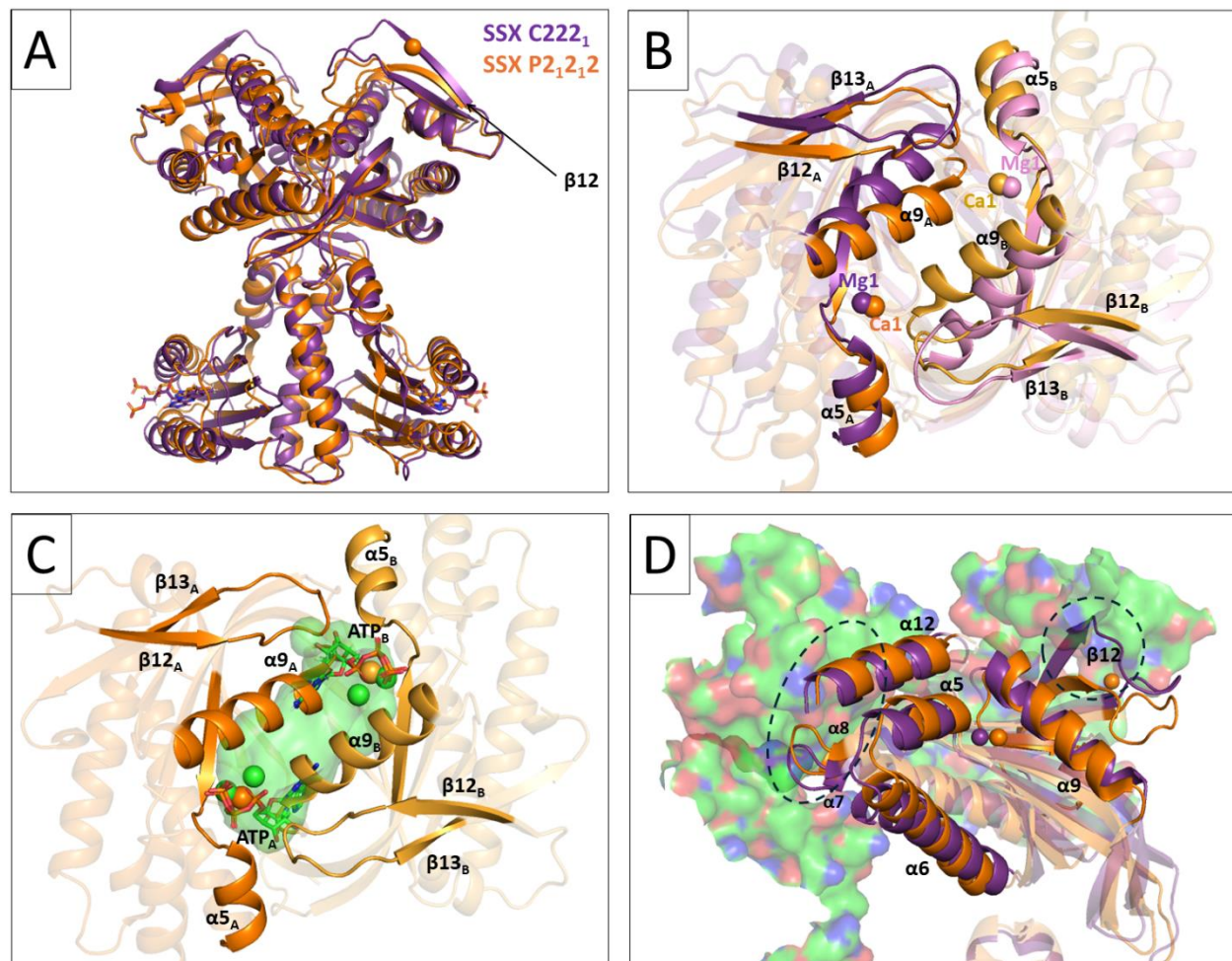


Figure 41: Analysis of ATP-free OaPAC closed conformation and open conformation.

Overlay of the structural models of Kapetanaki et al. with orthorhombic $P2_12_12$ space group solved with SSX in orange (PDB 9F1X) (Kapetanaki et al., 2024) and ATP-free OaPAC with orthorhombic $C222_1$ space group solved with SSX in purple. (A) Homodimer overlay, revealing similar secondary structures but significant displacement. (B) Close-up view of the active site in the AC domain. The displacement of α -helices 5 and 9 induces the closing of the ATP binding site. (C) Overlay of the closed active site conformation with ATP and magnesium binding at room-temperature as well as active site cavity (green) from the open conformation. (D) Crystal packing analysis of OaPAC crystals revealing crystal contacts in the $P2_12_12$ space group. Steric hindrance is important around the AC domain, forcing β -sheet 12 and α -helix 12 to adopt an arrangement closer to the core of the AC domain.

Figures prepared by the PyMOL Molecular Graphics System, Version 2.5.4 Schrödinger, LLC. (Schrödinger and DeLano, 2020).

3.4.2. SAXS Analysis of OaPAC₁₋₃₅₀ in the Presence and Absence of ATP

Additional experiments were carried out to investigate whether large structural rearrangements in OaPAC and especially the AC domain occur upon substrate binding in the dark. Recently published results suggest that ATP binding might result in transition of the AC domain from a closed to an open conformation whereas, according to data presented in this study, the binding of ATP does not particularly affect the AC domain configuration. To test both hypotheses, SAXS data were collected at the BioSAXS BM29 beamline of ESRF (Grenoble, France) (Tully *et al.*, 2023) on both, OaPAC₁₋₃₅₀ in the absence and in the presence of ATP (4 ATP:1 OaPAC molar ratio) in the dark in solution. X-ray scattering curves of three independent measurements for each OaPAC concentration (2 and 4 mg/mL), with or without ATP are presented in Appendix Figure 10. The measurements indicate no sign of aggregation or radiation damage, and the noise from the scattering curves is reduced at the highest concentration tested. For comparison purposes, the three measurements for each condition were averaged and overlaid with the other conditions (Figure 42). The overlaid X-ray scattering curves do not indicate clear differences between OaPAC with or without ATP, with only a slight change in the Porod region, while the curves in the Guinier region are alike (Figure 42A). A comparison of the Kratky plots also reveals clear Gaussian curves, peaking around $q_{\max} = 0.058 \text{ \AA}^{-1}$ for both conditions, indicating that OaPAC adopts a globular and rather compact shape with or without substrate present (Figure 42B). Analysis of the Porod-Debye plots discloses a clear plateau for each condition, which confirms that OaPAC₁₋₃₅₀ is well-folded in solution in the presence or absence of ATP (Figure 42C).

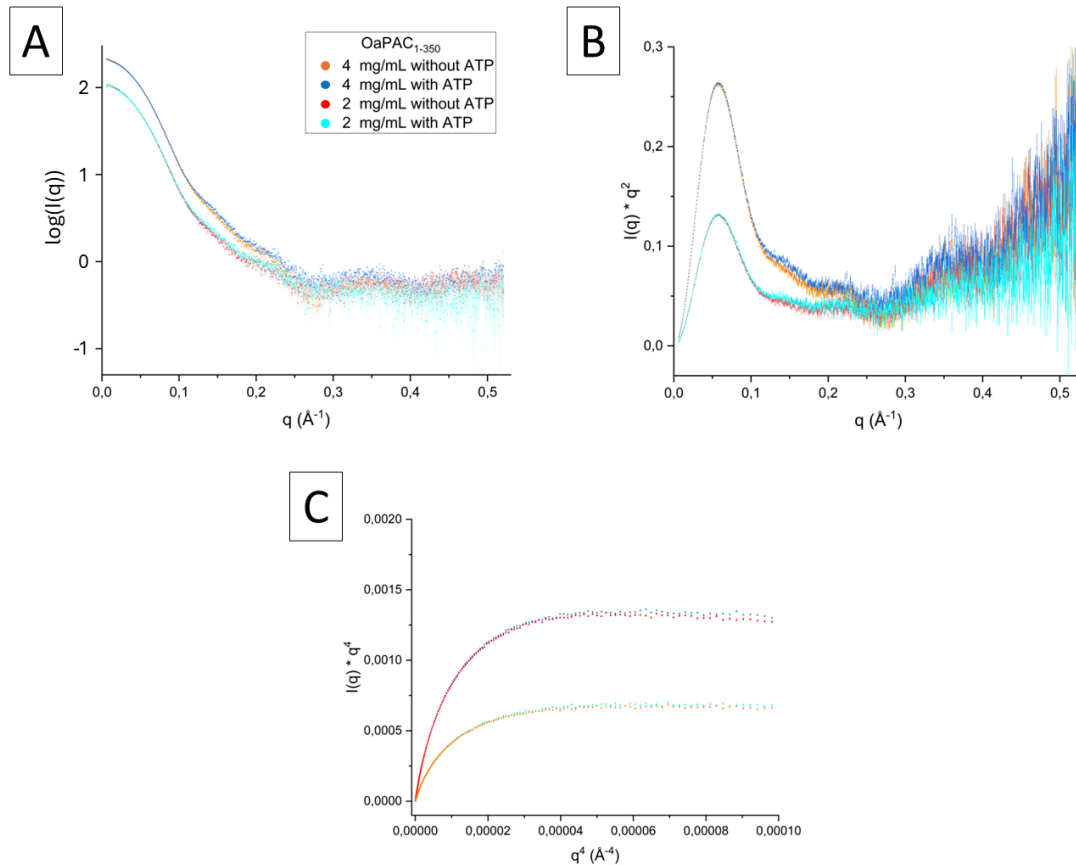


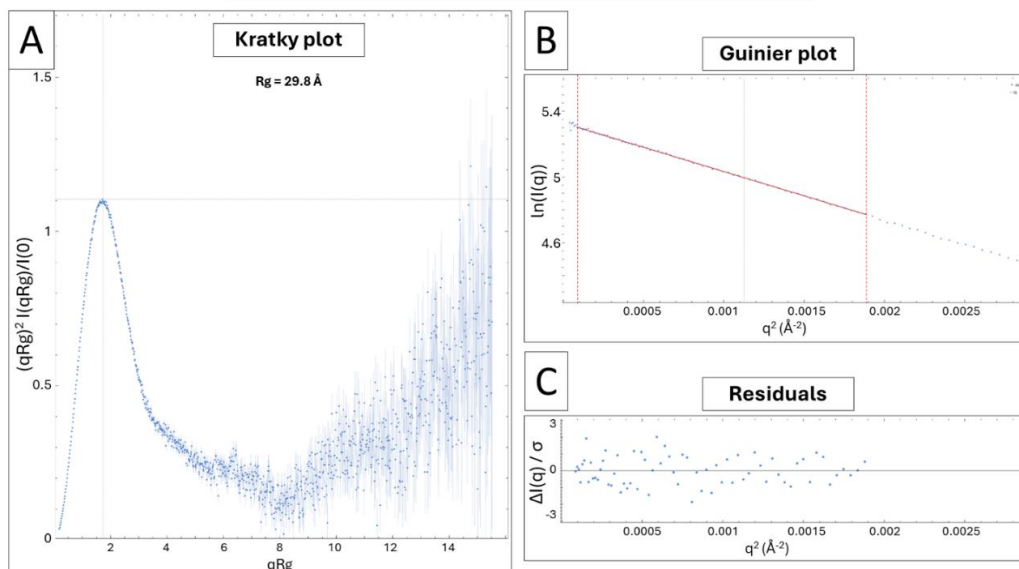
Figure 42: SAXS data from OaPAC₁₋₃₅₀.

Overlay of the SAXS data from OaPAC at 4 mg/mL without ATP (orange) or with ATP (blue) and at 2 mg/mL without ATP (red) or with ATP (cyan) averaged from three measurements for each condition. (A) X-ray scattering curves, (B) Kratky plots and (C) Porod-Debye plots, revealing no significant change in the protein upon ATP binding.

Figures were created with Origin software version 2024.

Each individual measurement was analysed using the ATSAS software suite version 3.0 (Manalastas-Cantos *et al.*, 2021). Details of the Guinier (Guinier and Fournet, 1955) and distance distribution (Svergun, 1992) analysis of the first measurement of OaPAC₁₋₃₅₀ at 4 mg/mL in the absence and presence of ATP are shown in Figure 43 and Figure 44, respectively. A detailed analysis of all other measurements is presented in Appendix Figure 11 to 20. Both the Guinier and distance distribution analysis confirm that the samples were monodisperse and indicate that no aggregation or radiation damage occurred during the measurements. The distance distribution function exhibits a Gaussian curve with a slight asymmetry (Figure 43D, Figure 44D), indicating that OaPAC₁₋₃₅₀ displays a quasi-globular shape in solution, corroborating the indications from the Kratky plots. This result is in agreement with previous SAXS analysis of OaPAC₁₋₃₆₆ (Nakasone *et al.*, 2023; Ujfalusi-Pozsonyi *et al.*, 2024).

**Guinier analysis of OaPAC₁₋₃₅₀ 4 mg/mL without ATP
Measurement 1**



Distance distribution analysis

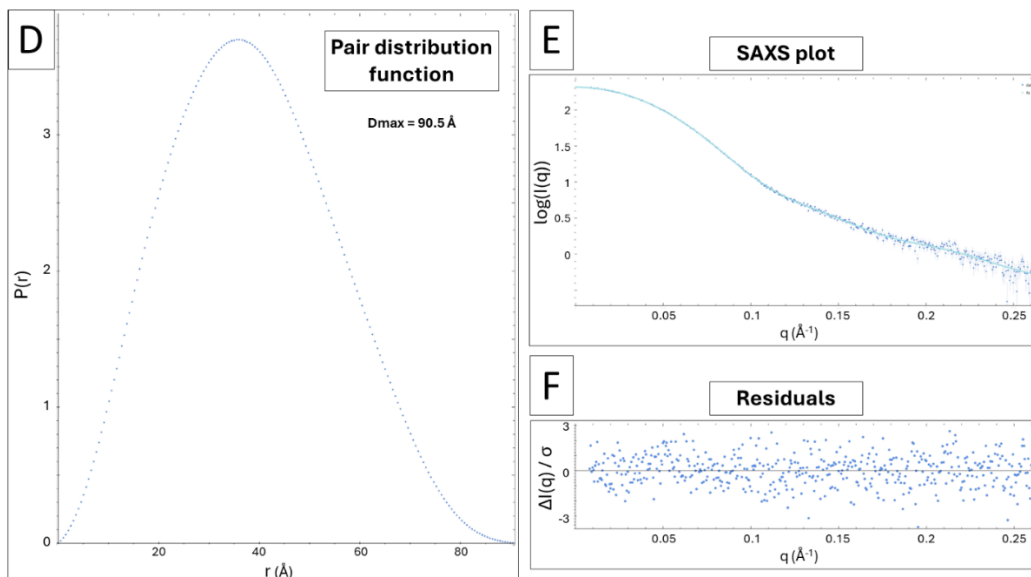


Figure 43: SAXS data analysis of the first measurement of OaPAC₁₋₃₅₀ at 4 mg/mL without ATP.

(A-C) Guinier analysis of OaPAC₁₋₃₅₀ at 4 mg/mL without ATP measurement 1 with dimensionless Kratky plot (A), Guinier plot and its linear fit (red) (B) and corresponding normalized residual plot of the Guinier plot fit (C). The analysis reveals a radius of gyration R_g of 29.8 Å and a compact and globular shape of OaPAC₁₋₃₅₀ without ATP in solution.

(D-F) Distance distribution analysis using GNOM version 5.0 (Svergun, 1992) with Pair distribution function $P(r)$ plot (D), fit of the X-ray scattering curve by Fourier transform of the $P(r)$ function (light blue) (E) and corresponding normalized residual plot of the SAXS plot fit (F). The analysis reveals a D_{max} of 90.5 Å and a compact and globular shape with a slight asymmetry of OaPAC₁₋₃₅₀ without ATP in solution.

Analysis and corresponding figures were produced with the PRIMUS graphical interface from the ATSAS software suite version 3.0 (Manalastas-Cantos et al., 2021).

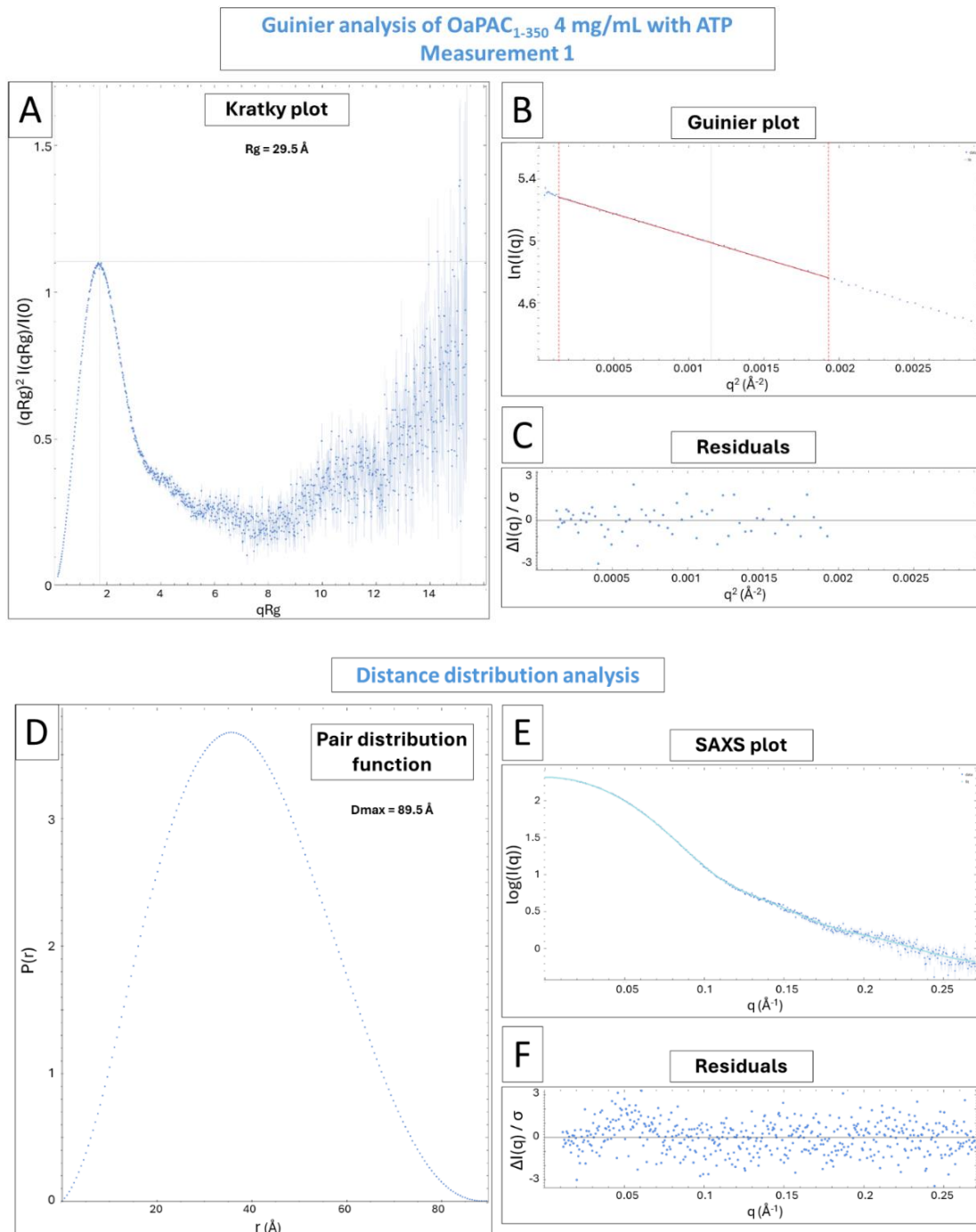


Figure 44: SAXS data analysis of the first measurement of OaPAC₁₋₃₅₀ at 4 mg/mL with ATP.

(A-C) Guinier analysis of OaPAC₁₋₃₅₀ at 4 mg/mL with ATP measurement 1 with dimensionless Kratky plot (A), Guinier plot and its linear fit (red) (B) and corresponding normalized residual plot of the Guinier plot fit (C). The analysis reveals a radius of gyration Rg of 29.5 Å and a compact and globular shape of OaPAC₁₋₃₅₀ with ATP in solution.

(D-F) Distance distribution analysis using GNOM version 5.0 (Svergun, 1992) with Pair distribution function P(r) plot (D), fit of the X-ray scattering curve by Fourier transform of the P(r) function (light blue) (E) and corresponding normalized residual plot of the SAXS plot fit (F). The analysis reveals a Dmax of 89.5 Å and a compact and globular shape with a slight asymmetry of OaPAC₁₋₃₅₀ with ATP in solution.

Analysis and corresponding figures were produced with the PRIMUS graphical interface from the ATSAS software suite version 3.0 (Manalastas-Cantos et al., 2021).



Results of the analysis are detailed in Table 19. The three individual measurements for each condition are consistent with each other, confirming that measurements are reproducible. Determination of the radius of gyration (R_g) with the Guinier analysis (Svergun *et al.*, 1987) or the distance distribution ($P(r)$) analysis using GNOM (Svergun, 1992) also reveal similar values, with Guinier $R_g = 29.5 \text{ \AA}$ for OaPAC 4 mg/mL with ATP against 29.8 \AA without, and 29.9 \AA for OaPAC 2 mg/mL with ATP against 30.1 \AA without. This might indicate that OaPAC is slightly more compact in the presence of ATP (4 ATP:OaPAC molar ratio), although the slight decrease in R_g might only be the result of measurement error. Similarly, volume analysis using GNOM in ATSAS software suite (Manalastas-Cantos *et al.*, 2021) reveals a slight reduction of the Porod volume in the presence of ATP. The $P(r)$ function reveals similar maximum intramolecular distance (D_{max}) values for OaPAC in the absence or presence of ATP, but demonstrates a decrease in D_{max} value with increased concentration, with $D_{max} = 89.5 \pm 0.5 \text{ \AA}$ and $90.7 \pm 0.3 \text{ \AA}$ for OaPAC 4 mg/mL with or without ATP, respectively, against $94.0 \pm 0.5 \text{ \AA}$ and $94.8 \pm 0.8 \text{ \AA}$ for OaPAC 2 mg/mL with or without ATP, respectively. A change within 5 % of the D_{max} values is usually not considered significant with SAXS data (Svergun *et al.*, 1987; Svergun, 1992; Putnam *et al.*, 2007), and might simply be a result of the better signal to noise ratio obtained with higher protein concentration. The obtained values for ATP-free OaPAC 4 mg/mL in the dark are in agreement with reported values for OaPAC₁₋₃₆₆ of a $R_g = 30 \pm 1 \text{ \AA}$ and a $D_{max} = 88 \pm 3 \text{ \AA}$ (Nakasone *et al.*, 2023) and for his-tag_OaPAC₁₋₃₆₆ using SEC-SAXS with $R_g = 31.4 \pm 0.52 \text{ \AA}$ and $D_{max} = 90 \text{ \AA}$ (Ujfalusi-Pozsonyi *et al.*, 2024). ATP-free OaPAC exhibits a R_g/R_h ratio of 0.81 with $\sim 30 \text{ \AA}$ for R_g and $R_h = 37 \pm 2 \text{ \AA}$ according to study of OaPAC₁₋₃₅₀ at room-temperature using

dynamic light scattering (Figure 12D), which is slightly higher than a R_g/R_h ratio of 0.77 for a hard sphere but significantly lower than 1 which characterises elongated particles (Guinier and Fournet, 1955; Dudás and Bodor, 2019), confirming that OaPAC₁₋₃₅₀ adopts a quasi-globular shape with a slight elongation in solution.

Surprisingly, the observations made here for the radius of gyration and the maximum intramolecular distance in the presence of ATP are in contradiction with the SAXS analysis of Ujfalusi-Pozsonyi *et al.*, which demonstrated an ATP dependent increase of the R_g and D_{max} in his-tag_OaPAC₁₋₃₆₆ (Ujfalusi-Pozsonyi *et al.*, 2024). Specifically, they calculated a Guinier R_g of 30.63 ± 0.31 Å for OaPAC at 3 mg/mL in the absence of substrate against 34.93 ± 0.38 Å in the presence of ATP (4.3 ATP:1 OaPAC molar ratio), indicating a higher flexibility when the substrate is bound; and a D_{max} increase from 90 to 131 Å, suggesting an expansion of the protein upon ATP binding. The major difference is the use of his-tag_OaPAC₁₋₃₆₆ which is the full-length protein with 16 additional non-native amino acids in N-terminus, while OaPAC₁₋₃₅₀, corresponding to native OaPAC with a truncation of 16 C-terminal amino acids, was used in this study. One can hypothesize that the increase in R_g in Ujfalusi-Pozsonyi *et al.*'s study is due to the C-terminal region extending upon ATP binding, while the R_g and D_{max} remains relatively constant in this study as the C-terminal region is absent. Interestingly, Hirano and co-workers studied the influence of the C-terminus on OaPAC activity and discovered that this region negatively affected the AC activity (Hirano *et al.*, 2019). The presence of the C-terminus in OaPAC reduced the ATP turnover to cAMP, while a deletion between 9 to 18 amino acids increased the photoactivity up to 60-fold, but did not seem to affect the structural changes involved in signal transmission. Consequently, one might speculate that the C-terminal region extends upon ATP binding and disturbs or slows down the ATP conversion to cAMP by covering the top of the active site cavity. However, as no crystallographic structure of full length OaPAC₁₋₃₆₆ has been solved so far, it is difficult to really determine the role of the C-terminus in ATP binding and AC activity.

Analysis of Ujfalusi-Pozsonyi *et al.* OaPAC titration series with ATP reveals an upturn at low q values and an extended tail on the $P(r)$ plot for some data, which could indicate aggregation or bad buffer subtraction (Ujfalusi-Pozsonyi *et al.*, 2024). Specifically, this observation is concomitant with the increase in ATP concentration. Aggregation or bad buffer subtraction affect the estimated values during Guinier and distance distribution analysis and can lead to incorrectly assigned increase in R_g and D_{max} values (Svergun *et al.*, 1987; Svergun, 1992; Putnam *et al.*, 2007).

Consequently, it is also possible that the increasing R_g and D_{max} values observed with increased ATP concentrations could be a result of the underlying aggregation issue. Nonetheless, it is also plausible that these SAXS data reflect a combination of increased aggregation and extension of the C-terminus, which rearranges upon ATP binding.

Measurement	4 mg/mL without ATP			4 mg/mL with ATP			2 mg/mL without ATP			2 mg/mL with ATP		
	1	2	3	1	2	3	1	2	3	1	2	3
Guinier Rg (Å)	29.8	29.8	29.8	29.5	29.5	29.5	30.2	30.1	30.1	29.8	29.9	29.9
I(q=0) of Guinier analysis	205.87	204.23	201.43	204.53	214.51	214.39	101.74	103.05	102.79	105.33	105.53	108.11
q _{min} Rg _{of} Guinier plot fit (Å)	0.028	0.046	0.023	0.034	0.037	0.041	0.059	0.047	0.062	0.049	0.037	0.049
q _{max} Rg _{of} Guinier plot fit (Å)	1.29	1.29	1.29	1.29	1.29	1.32	1.34	1.37	1.40	1.29	1.37	1.37
GNOM P(r) Rg (Å)	29.7	29.7	29.8	29.5	29.5	29.5	30.1	30.1	30.0	29.9	29.8	29.8
I(q=0) of GNOM P(r) analysis	205.90	204.40	201.40	204.80	214.90	214.80	101.60	103.20	102.80	105.70	105.50	108.20
P(r) Dmax (Å)	90.5	90.5	91.0	89.5	90.0	89.0	95.0	94.0	95.5	94.0	93.5	94.5
Porod Volume of GNOM P(r) analysis (Å ³)	116,550	116,107	116,513	111,579	111,124	111,018	118,446	117,076	118,273	114,014	111,817	112,292
Quality estimate of GNOM P(r) analysis	0.99	0.98	0.98	0.99	0.99	0.99	0.96	0.97	0.97	0.98	0.98	0.98
Mean Guinier Rg (Å)	29.8 ± 0.1			29.5 ± 0.1			30.1 ± 0.1			29.9 ± 0.1		
Mean P(r) Dmax (Å)	90.7 ± 0.3			89.5 ± 0.5			94.8 ± 0.8			94.0 ± 0.5		



Table 19: SAXS parameters and statistics of OaPAC₁₋₃₅₀ study

obtained with Guinier and distance distribution analysis.

Analysis was performed with the PRIMUS graphical interface from the ATSAS software suite version 3.0 (Manalastas-Cantos et al., 2021).

To investigate how well the structural models derived from X-ray crystallography fit the X-ray scattering data of OaPAC in solution, CRY SOL (Franke *et al.*, 2017) was used to fit the atomic structures of OaPAC open conformation at room-temperature (C222₁ model) and closed conformation at room-temperature (P2₁2₁2 model) with the experimental data of OaPAC in the absence and presence of ATP (Figure 45). Analysis of the scattering curves in solution and respective fit with the crystallography structures reveal that for both conditions, the open conformation of OaPAC matches the SAXS data better (Figure 45A,D). The normalised residual plots for OaPAC closed conformation demonstrates that the theoretical SAXS curve of the latter significantly differs from the experimental data (Figure 45C,F). The Correlation Map test indicating the randomness of residuals, the reduced χ^2 test indicating the randomness of normalised residuals and the Anderson-Darling test verifying the standard normal distribution of residuals all display significantly lower values (Table 20). Yet, although the open AC domain conformation exhibits a better fit than the closed conformation, the normalized residuals (Figure 45B,E) alongside the statistics from the pairwise similarity tests (Table 20) also demonstrate important differences. Interestingly, the crystallographic model representing an open AC domain conformation fits the ATP-free OaPAC SAXS curve in solution rather poorly but still exhibits better statistics than the closed conformation, suggesting that OaPAC presents an even more open conformation in the absence of substrate, leading to an increased protein volume, as observed when comparing OaPAC Porod volume without and with ATP (



Table 19). The open OaPAC conformation fits better

with the OaPAC SAXS scattering curve in solution in the presence of ATP, with a p-value for the correlation map test above 0.05 and for the Anderson-Darlin test around 0.036.

Consequently, the absence of increase in R_g or D_{max} for OaPAC₁₋₃₅₀ upon ATP binding, as well as the relatively good fit of the OaPAC crystal structure of the open AC domain conformation (C222₁ model) to OaPAC X-ray scattering data in solution in the presence of ATP, and the really poor fit between OaPAC closed AC domain conformation (P2₁2₁2 model) and ATP-free OaPAC X-ray scattering data, seem to indicate that OaPAC does not transition between the closed to the open conformation upon ATP binding as hypothesised previously. On the contrary, these SAXS data rather indicate a slight reduction in volume upon ATP binding, but generally indicate that the binding of ATP does not induce large rearrangements of the overall protein conformation.

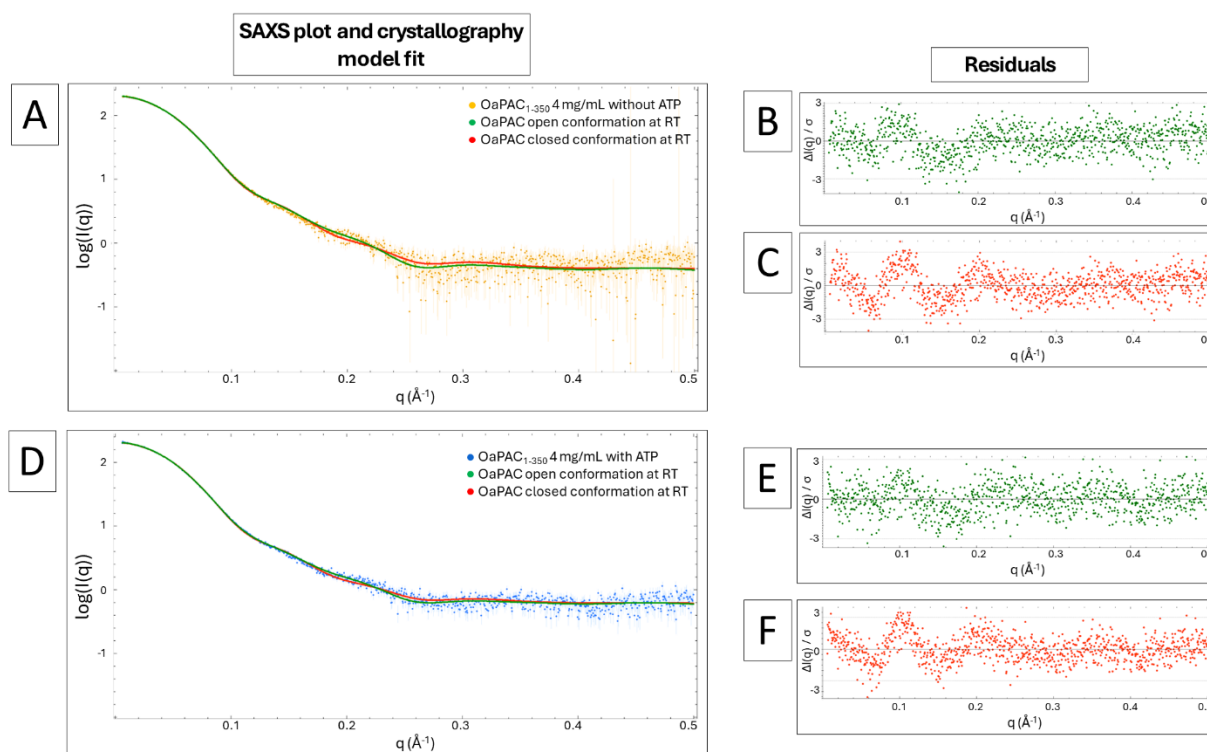


Figure 45: Analysis of the fit between the X-ray scattering data of OaPAC₁₋₃₅₀ in solution and the crystallography models of OaPAC₁₋₃₅₀.

(A,D) Scattering curve of OaPAC 4 mg/mL (measurement 1) without ATP (orange) and with ATP (blue) overlaid with the theoretical scattering data from OaPAC open conformation using the room-temperature serial X-ray crystallography model with space group C222₁ presented in the previous section (green) and the theoretical scattering data from OaPAC closed conformation using the room-temperature serial X-ray crystallography model with space group P2₁2₁2 (PDB 9FIX) (red). Theoretical scattering curves calculated using CRYSQL version 3.0 (Franke et al., 2017). (B) Corresponding normalized residual plot of the fit shown in (A) between OaPAC in solution without ATP and OaPAC atomic structure with an open AC domain conformation. (C) Corresponding normalized residual plot of the fit shown in (A) between OaPAC in solution without ATP and OaPAC atomic structure with a closed AC domain

conformation. (E) Corresponding normalized residual plot of the fit shown in (D) between OaPAC in solution with ATP and OaPAC atomic structure with an open AC domain conformation. (F) Corresponding normalized residual plot of the fit shown in (E) between OaPAC in solution with ATP and OaPAC atomic structure with a closed AC domain conformation.

Analysis and corresponding figures were produced with the PRIMUS graphical interface from the ATSAS software suite version 3.0 (Manalastas-Cantos et al., 2021).

	OaPAC without ATP			OaPAC with ATP		
	Correlation Map Test	Reduced χ^2 Test	Anderson-Darling Test	Correlation Map Test	Reduced χ^2 Test	Anderson-Darling Test
Open conformation C222 ₁	4.31e-08	2.71e-08	1.04e-03	0.0562	2.4e-05	0.0360
Closed conformation P2 ₁ 2 ₁ 2	1.35e-08	0	5.28e-09	5.40e-08	0	1.11e-07

Table 20: P-values from the pairwise similarity tests between OaPAC SAXS data in solution without or with ATP and OaPAC crystallographic model fit depending on the AC domain conformation obtained with CRY SOL as shown in Figure 45.

An *ab initio* molecular envelope of OaPAC₁₋₃₅₀ was determined using the output of the analysis with ATP-free OaPAC₁₋₃₅₀ at 4 mg/mL (measurement 1). Twenty models were produced with DAMMIF, which enables the rapid identification of the *ab initio* shape by simulated annealing using a single phase dummy atom model (Franke and Svergun, 2009). Models are compared by DAMAVER (Volkov and Svergun, 2003) and the most representative DAMMIF model is displayed in Figure 46A, alongside the fit to the experimental X-ray scattering data. The normalised residual plot presents a fairly good random distribution (Figure 46B), and the Correlation Map and the Anderson-Darling tests exhibit p-values of 0.621 and 0.369, respectively (Table 21). The reduced χ^2 test demonstrates slightly less good statistics, with a p-value of 0.025. The twenty models were all selected as representative of the experimental data and were averaged with DAMAVER before final refinement with DAMMIF (Svergun, 1999) (Figure 46C). The *ab initio* molecular envelope exhibiting a quasi-globular shape agrees with the Kratky and P(r) plots. Of note, the reconstruction was also performed using the SAXS data of holo OaPAC₁₋₃₅₀ at 4 mg/mL (measurement 1) and led to a highly similar surface, but the fit to the experimental data was slightly less good (Appendix Figure 21). The averaged conformation of OaPAC₁₋₃₅₀ without substrate in solution is in line with the structural model of OaPAC₁₋₃₅₀ obtained with X-ray crystallography (orthorhombic crystal form with C222₁ space group), although the crystallography model does not completely cover the averaged volume of OaPAC in solution (Figure 46C). For instance, the maximum intramolecular distance in the crystal structure is found between Gln31 from one protomer and Trp307 from the

second protomer and exhibits values ranging from 86.5 to 87.4 Å at cryogenic and room-temperatures (PDB 8QFE, 8QFF and 8QFH and unpublished SSX structures), while D_{max} in solution according to the SAXS data of OaPAC at 4 mg/mL reaches around 90 Å. This might indicate that OaPAC₁₋₃₅₀ is slightly enlarged in solution when compared to the crystal structures, and suggests that the homodimer presents a less flexible conformation in the crystal most likely due to the crystal packing. Of note, the structural model presenting a closed AC domain conformation exhibits an even shorter maximum distance between 83.9 and 85.2 Å (PDB 9F1W, 9F1X and 9F1Y), suggesting that this conformation is even more distant from OaPAC conformation in solution.

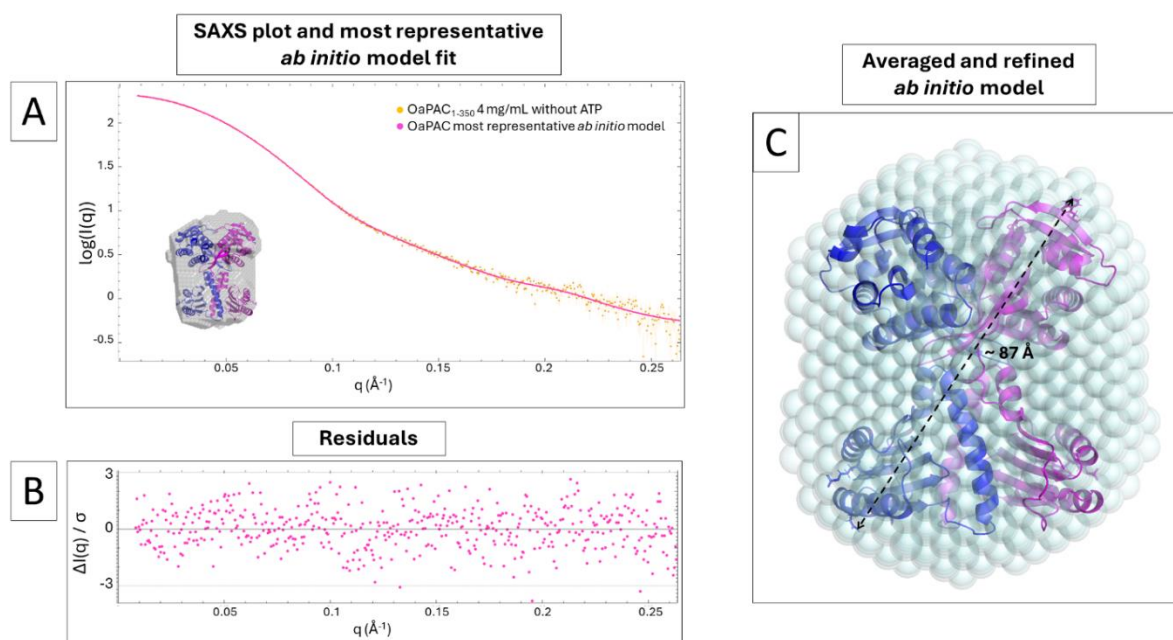


Figure 46: *Ab initio* modelling obtained from the SAXS data of OaPAC₁₋₃₅₀ in the absence of substrate.

(A) Scattering curve of OaPAC₁₋₃₅₀ at 4 mg/mL without ATP measurement 1 (orange) and fit of the most representative *ab initio* model of OaPAC (pink) obtained with DAMMIF version 1.1.2 (Franke and Svergun, 2009). The molecular envelope of the most representative model superposed with OaPAC crystallography structure (C222₁ model) is shown on the left bottom corner. (B) Corresponding normalized residual plot of the fit shown in (A). (C) *Ab initio* model of OaPAC obtained from 20 models out of 20 produced by DAMMIF averaged with DAMAVER version 5.0 (Volkov and Svergun, 2003) and refined with DAMMIN version 5.3 (Svergun, 1999). The molecular envelope is displayed in sphere representation. OaPAC crystallography structure in orthorhombic form with space group C222₁ at room-temperature is presented in cartouche representation and overlaid to the SAXS *ab initio* model. The maximum intramolecular distance of ~ 87 Å in the crystal structure is slightly reduced compared to the D_{max} obtained from the $P(r)$ function (~ 90 Å). Analysis and corresponding figures (A,B) were produced with the PRIMUS graphical interface from the ATSAS software suite version 3.0 (Manalastas-Cantos et al., 2021). Figure (C) was prepared by the PyMOL Molecular Graphics System, Version 2.5.4 Schrödinger, LLC (Schrödinger and DeLano, 2020).

OaPAC without ATP			
	Correlation Map Test	Reduced χ^2 Test	Anderson-Darling Test
OaPAC most representative <i>ab-initio</i> model	0.621	0.025	0.369

Table 21: *P-values from the pairwise similarity tests between OaPAC SAXS data in solution without ATP and OaPAC most representative ab initio model fit obtained with DAMMIF as shown in Figure 46.*

3.4.3. FTIR Study on Signal Transduction in the Presence or Absence of ATP

After verifying that ATP does bind OaPAC in the dark without introducing large structural rearrangements, subsequent investigations were carried out to decipher the enzyme reaction in solution during ATP turnover. For this, OaPAC₁₋₃₅₀ was studied using FTIR spectroscopy in the dark and after 4 s of blue light illumination. Time-resolved light *minus* dark FTIR difference spectra were recorded for several s and are presented in Figure 47A. FTIR data were collected and processed by Marius Nagel and Tilman Kottke from Bielefeld University. The contributions from the BLUF domain or the AC domain to the FTIR spectra were distinguished by comparing the signals with truncated OaPAC₁₋₁₃₇ (composed of the BLUF domain and the linker region) (Appendix Figure 7). Difference bands were accordingly assigned and labelled with squares for BLUF domain and linker region and triangles for AC domain contributions (Figure 47A). Other signals contained mixed contributions. The difference spectra exhibit the specific carbonyl signature of BLUF photoreceptors at 1710(-) and 1695(+) cm⁻¹, indicative of alterations in hydrogen bonding to the flavin C4=O4 upon photoexcitation (Hasegawa *et al.*, 2005; Masuda *et al.*, 2005b; Stierl *et al.*, 2014).

Regarding the reaction further away from the BLUF domain, the band at 1663(+) cm⁻¹ (Figure 47A) likely corresponds to the AC α -helical rearrangement signal around 1650(+) cm⁻¹ observed in bPAC, as it exhibits a similar characteristic peak shape, including a low frequency shoulder (Stierl *et al.*, 2014). Interestingly, this shoulder was also thought to originate from the AC domain reaction in bPAC, as it was lacking in the truncated bPAC₁₋₁₂₄ mutant (containing the BLUF domain

and α -helix 3). In this study, a positive signal at 1655(+) cm^{-1} is also visible in the OaPAC₁₋₁₃₇ mutant spectra (containing the BLUF domain and α -helices 3 and 4), suggesting that this signal originates from rearrangements of the α -helix 4 handle. Changes in α -helix 4 have already been suggested as crucial for signal transduction in BLUF photoreceptors (Domratcheva *et al.*, 2008; Schroeder *et al.*, 2008; Barends *et al.*, 2009; Dragnea *et al.*, 2010; Yuan *et al.*, 2011; Lindner *et al.*, 2017). Besides, α -helix 4 also revealed structural rearrangements and higher flexibility in OaPAC light excited cryo-trapped structure described in this study.

Other significant difference signals originating from the AC domain are also evident at 1626(-) and 1614(+) cm^{-1} (Figure 47A). In bPAC, the corresponding negative signal detected at 1631(-) cm^{-1} could be determined, based on its characteristic frequency, as a β -sheet rearrangement in the enzymatic domain (Stierl *et al.*, 2014). It is improbable that this signal originates from a restrained β -sheet 5 response in the BLUF domain as discussed by Stierl *et al.*, as signalling from the flavin to the linker region via β -sheet 5 remains intact in OaPAC₁₋₁₃₇. Notably, the positive band at 1614 cm^{-1} has not been observed in YcgF (Hasegawa *et al.*, 2006) or in bPAC (Stierl *et al.*, 2014) and is surprisingly low in frequency for an amide I signal of secondary structure elements (Barth and Zscherp, 2002). Steady-state measurements on OaPAC and OaPAC₁₋₁₄₁ under deuterated conditions did not reveal any notable positive band in this region either (Collado *et al.*, 2022). This could be explained by a strong downshift to 1560 cm^{-1} or by band compensation effects.

As a result, this time-resolved FTIR study reveals that in addition to α -helix 4, both a β -sheet and an α -helix in the AC domain are rearranged during signal transfer, as well as an unknown third secondary structure element. Many elements could be potential candidates for rearrangements, including β -sheets 9 and 10 of the tongue region and α -helix 6, which are located near the linker region. Additionally, β -sheets 7 and 8 and α -helices 5 and 9 around the ATP could be part of signal transduction too, considering that α -helix 5 also revealed a displacement away from the active site in OaPAC light excited cryo-trapped data.

In addition to contributions from the BLUF and the enzymatic domains, distinctive negative difference signals from ATP and positive differences signals from cAMP and byproducts (Figure 47A) are detectable in the spectral range of 900–1300 cm^{-1} (Barth and Mäntele, 1998), as discussed previously in section 3.2.3, confirming that the enzyme is active in solution. After 67.9 s, the differences from structural rearrangements in the protein have relaxed, and only ATP turnover

contributions remain. Since ATP is bound in an energetically unfavourable conformation for cAMP production in our crystals, one could argue that this conformation does not represent the native binding of ATP in OaPAC but is only an artifact of the crystal packing. Possibly, OaPAC could open up upon light excitation to enable ATP binding directly in another conformation. To investigate this possibility, FTIR difference spectra were recorded without ATP and with the non-hydrolysable ATP analogue ApCpp (Figure 47B). When compared to holo OaPAC, ATP-free OaPAC discloses a significant FTIR difference signal reduction. Specifically, all main difference peaks attributed to contributions of the enzymatic domain (1614(+), 1626(-), 1663(+) cm^{-1}) and the shoulder attributed to the α -helix 4 change (1655(+) cm^{-1}) disappear when ATP is absent, while signals are largely restored if ApCpp is present. Consequently, the enzymatic domain seems to remain largely unchanged upon blue light excitation when ATP or analogues are not present. This indicates that under illumination, the AC domain does not rearrange prior to substrate binding to enlarge the active site pocket and enable the binding of ATP in the most energetically favourable conformation directly before turnover. Similarly, Lindner *et al.* demonstrated that in the bPAC Tyr7Phe mutant, no light-dependent increase in ATP affinity was detected, suggesting that ATP does directly bind in the dark naturally and does not require light for active site opening to increase ATP binding affinity (Lindner *et al.*, 2017). The result of this FTIR study supports the binding of ATP in a non-energetically favourable conformation first, followed by a likely opening of the AC domains from both protomers to slightly enlarge the active site cavity and facilitate the full rotation of the ribose along with the adenine, enabling the in-line nucleophilic attack on the ATP PA phosphate as a first step of the ATP conversion to cAMP.

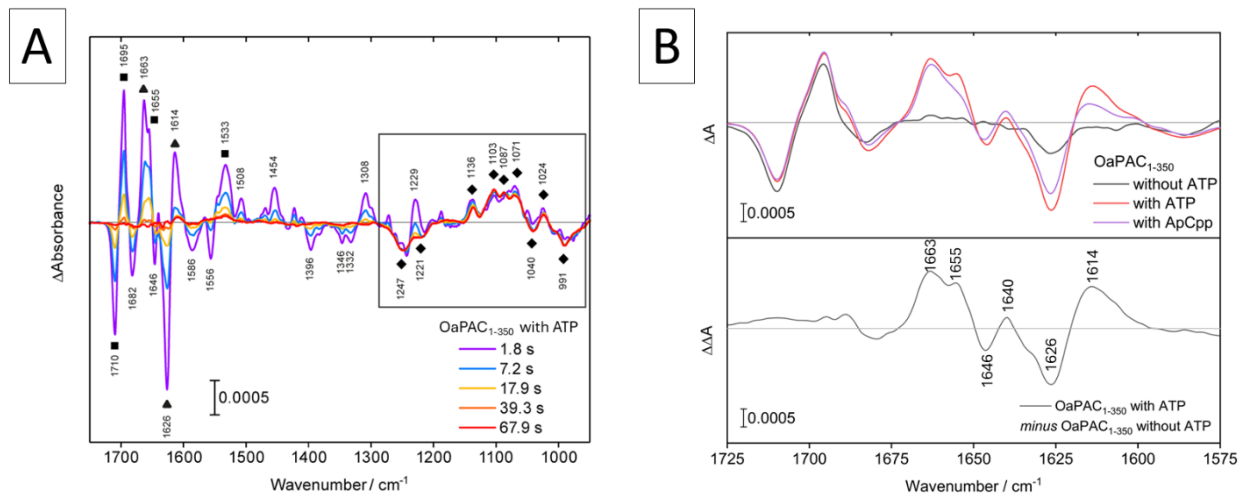


Figure 47: Light-minus-dark FTIR difference spectra of OaPAC in solution in the presence or absence of ATP and analogues.

(A) Time-resolved FTIR spectroscopy revealing difference signal evolution in holo OaPAC after 4 s of illumination. Contributions by the BLUF domain, AC domain and ATP turnover are marked with squares, triangles and diamonds, respectively. Other bands represent mixed contributions. The black frame highlights the characteristic spectral range of ATP conversion to cAMP. Figure is from Chretien et al. (Chretien et al., 2024). (B) The presence of ATP (red line) and the non-hydrolysable ATP analogue ApCp (purple line) strongly influences the light-minus-dark FTIR difference spectrum of OaPAC. In the absence of ATP (black line), the contributions from the AC domain of OaPAC to the difference spectrum nearly vanish completely. The double difference spectrum between OaPAC with and without ATP shows significant signals mainly originating from the AC domain. Addition of ApCp leads to a nearly complete recovery of the light-induced response of the AC domain.

3.4.4. Allosteric Regulation and Relaxation in OaPAC

To achieve a better understanding of the structural rearrangements involved during ATP turnover to cAMP, the effect of ATP on OaPAC relaxation and its kinetics were studied with TR-FTIR spectroscopy. FTIR data were collected and processed by Marius Nagel and Tilman Kottke from Bielefeld University.

Relaxation of structural changes was followed at 1710(-) and 1696(+) cm^{-1} for the BLUF domain and at 1615(+) cm^{-1} for the AC domain. The evolution of the difference spectra at 1696(+) cm^{-1} is shown in Figure 48A for holo OaPAC₁₋₃₅₀, ATP-free OaPAC₁₋₃₅₀ and OaPAC₁₋₁₃₇. Interestingly, the signal at 1696(+) cm^{-1} for the BLUF domain of holo OaPAC decayed significantly slower than for ATP-free OaPAC and OaPAC₁₋₁₃₇. The evolution of the difference spectra at 1710(-) cm^{-1} also revealed a similar pattern (data not shown). Specifically, the decay at 1710(-) / 1696(+) cm^{-1} of holo OaPAC₁₋₃₅₀ BLUF domain demonstrated a time constant of $\tau = 8.9 \pm 0.5$ s, while the BLUF

domain of ATP-free OaPAC₁₋₃₅₀ and OaPAC₁₋₁₃₇ revealed time constants of $\tau = 5.8 \pm 0.7$ s and $\tau = 6.3 \pm 0.2$ s, respectively (Figure 48B). Of note, the relaxation of the BLUF domain in ATP-free OaPAC₁₋₃₅₀ derived from FTIR ($k = 0.17$ s⁻¹ and $\tau = 5.8 \pm 0.7$ s) is similar to the relaxation observed with UV-Vis spectroscopy ($k = 0.19$ s⁻¹ and $\tau = 5.4 \pm 0.2$ s). When ApCcp is present, the relaxation kinetics of the BLUF domain is similar to OaPAC in the presence of ATP ($\tau = 8.6 \pm 0.8$ s) (Figure 48B). Notably, the kinetics of OaPAC measured by Ohki *et al.* without the presence of ATP are slightly faster ($k = 0.246$ s⁻¹ and $\tau = 4.0$ s) (Ohki *et al.*, 2016). Surprisingly, the addition of ApCcp did not significantly alter the BLUF kinetics observed with UV-Vis spectroscopy in their study compared to ATP-free OaPAC ($k = 0.269$ s⁻¹ and $\tau = 3.7$ s). As in the same study, the co-crystallized ATP analogue was not visible in the electron density of OaPAC hexagonal crystals although ApCcp is non-cleavable, the unchanged relaxation kinetics raise the question of whether ApCcp was binding to OaPAC in their study at all. The significant change in relaxation kinetics for the BLUF domain depending on the presence of ATP or analogues, as well as the absence of AC domain reaction when the substrate is absent from the environment, clearly indicates an allosteric regulation of the protein depending on ATP binding. Additionally, the relaxation of the enzymatic domain was derived from the evolution of the peak at 1615(+) cm⁻¹ and yielded $\tau = 2.9 \pm 0.6$ s in the presence of ATP and $\tau = 4.6 \pm 0.6$ s in the presence of ApCcp (Figure 48B). Of note, the relaxation kinetics of the AC domain without substrate could not be calculated as the AC domain does not react without ATP or analogues. Interestingly, the relaxation of the AC domain with ATP appears to be significantly faster than the relaxation of the BLUF domain (three times faster). This confirms the allosteric feedback effect of ATP binding and more generally of the AC domain on the sensor domain relaxation and its lifetime. Consequently, two scenarios can be postulated. In the presence of ATP, photoexcitation of the flavin chromophore will lead to structural rearrangements in the BLUF domain and signal transduction to the AC domain to activate the enzyme. After ATP conversion to cAMP, the AC domain relaxes back and subsequently allows the sensor domain to relax to the ground state. On the other hand, without ATP, photoexcitation of the flavin chromophore will lead to structural rearrangements in the BLUF domain and partial signal transduction until the BLUF-AC domain interface. In the absence of ATP, the AC domain cannot be activated and therefore the BLUF domain relaxes faster to the ground state.

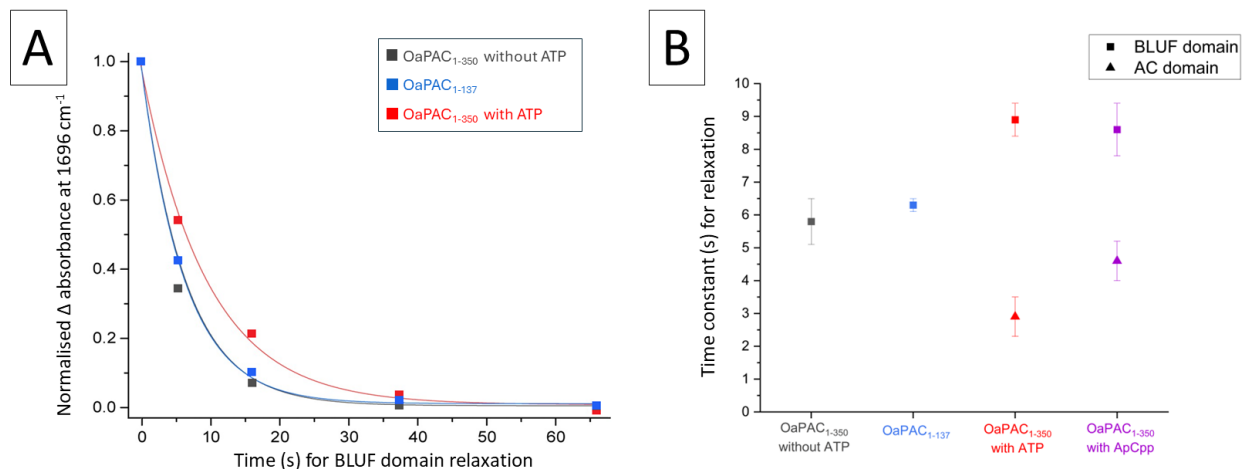


Figure 48: Relaxation kinetics of structural changes after photoexcitation of OaPAC observed with TR-FTIR.

(A) The evolution of the time-resolved FTIR difference absorbance was plotted at 1696 cm^{-1} for OaPAC₁₋₃₅₀ in the presence (red) and absence of ATP (grey) and for OaPAC₁₋₁₃₇ (blue) and analysed by single exponential functions. Figure modified from (Chretien et al., 2024). (B) Time constants of OaPAC₁₋₃₅₀ without ATP (grey), OaPAC₁₋₁₃₇ (blue), OaPAC₁₋₃₅₀ with ATP (red) and OaPAC₁₋₃₅₀ with ApCcp (purple) derived from FTIR difference signals evolution for the relaxation of the BLUF domain at 1710(-) / 1696(+) cm^{-1} (squares) and for the AC domain at 1615(+) cm^{-1} (triangles). The AC domain exhibits a significantly faster relaxation ($\tau = 2.9 \pm 0.6$ s) than the BLUF domain ($\tau = 8.9 \pm 0.5$ s) in the presence of ATP. Relaxation of BLUF becomes faster when ATP or analogues are absent and in the truncated OaPAC₁₋₁₃₇ protein, suggesting a tight allosteric communication.

Figures were created with Origin software version 2024.

Allosteric communication from the sensor toward the effector domain is evident for multi-domain photoreceptors. Specifically, the BLUF domain of bPAC was confirmed to be a true allosteric activator of the AC domain, as five different truncated bPAC variants, containing the AC domain only or the AC domain with parts of the linker region, did not achieve conversion of ATP into cAMP (Lindner, 2018). However, the results shown here demonstrate for the first time the allosteric feedback effect of ATP binding in the AC domain towards the BLUF domain in PAC photoreceptors, with the ATP binding pocket being a dual active site and allosteric site. Yet, it is unclear how the binding of the ATP controls the allosteric regulation of BLUF in detail. There is no apparent hydrogen bond breakage upon ATP binding at the interface between the BLUF and the linker region or between the linker region and the AC domain. The slight displacement of the AC domain observed in holo OaPAC crystal structure and/or the slight reduction in OaPAC volume observed by SAXS upon ATP binding in solution might be a sufficient signal for the sensor domain to perceive the binding, but there is no strong evidence to support this hypothesis.

A non-isomorphous difference map calculated in real space using MatchMaps (Brookner and Hekstra, 2024) confirms that the BLUF domain is not affected by ATP binding (Figure 49A-B). Yet, in addition to changes in the active site, differences in electron density are observed in the tongue region between β -sheets 9 and 10. Specifically, the amino acid orientations are similar in the presence and the absence of ATP, but the tongue is slightly displaced and moves a little bit closer to the handle and linker region (α -helices 4 and 3) upon ATP binding (Figure 49C). Consequently, it is possible that the information regarding substrate binding is transmitted to the BLUF domain via the tongue region in the AC domain.

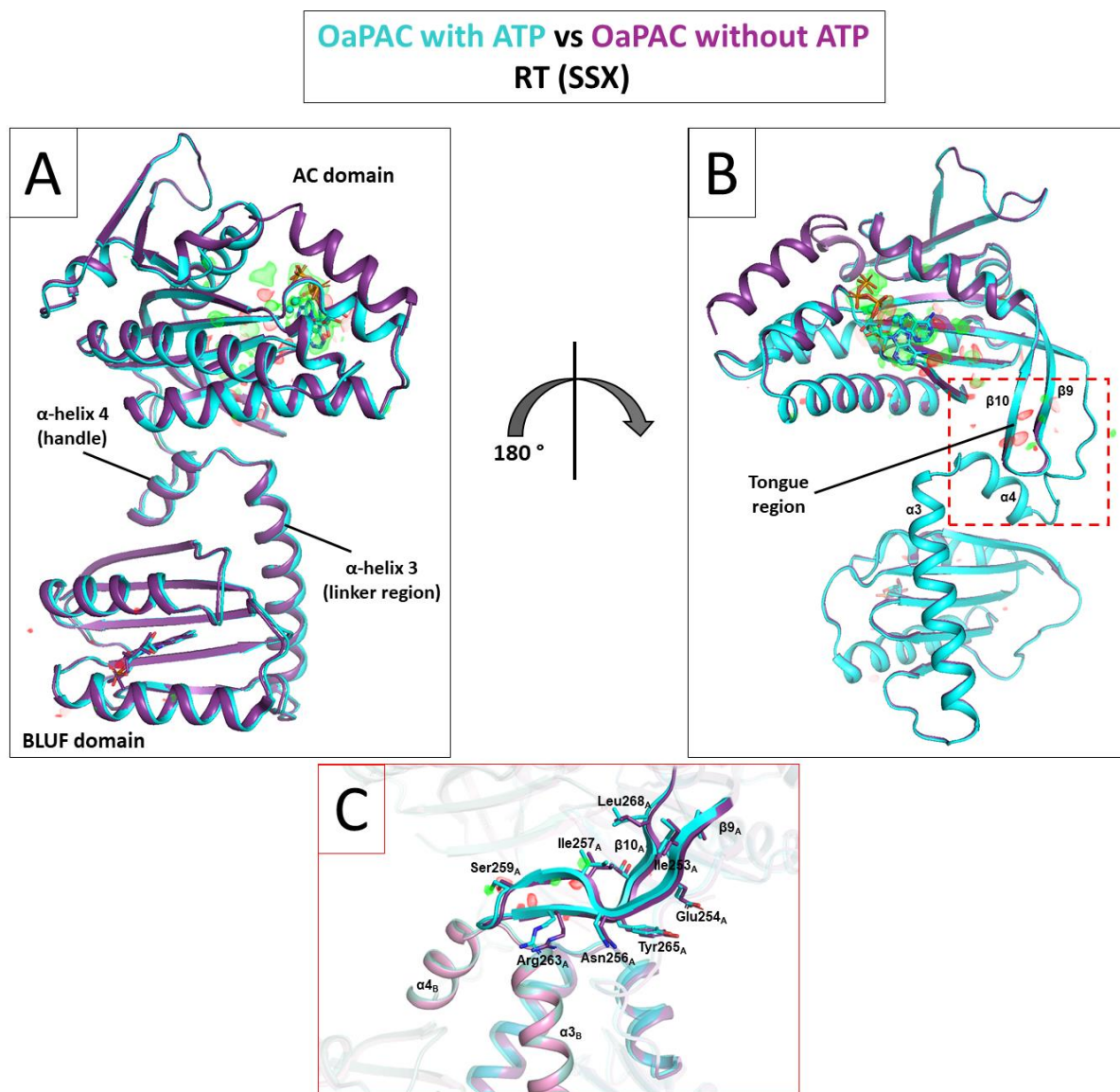


Figure 49: Difference map revealing changes in the active site and the tongue region between holo and ATP-free OaPAC.

Non-isomorphous electron density difference map between holo OaPAC (cyan) and ATP-free OaPAC (purple) data collected at room-temperature with SSX was calculated in real space to overcome poorly-isomorphous crystals using MatchMaps (Brookner and Hekstra, 2024). The differences contoured at +3 rmsd (green) and -3 rmsd (red) reveals, in addition to changes in the active site, a displacement of the tongue region upon ATP binding. (A-B) Overview of OaPAC differences upon ATP binding with 180° rotation between both views. (C) Close-up view of the tongue and helix linker regions.

Figures prepared by the PyMOL Molecular Graphics System, Version 2.5.4 Schrödinger, LLC (Schrödinger and DeLano, 2020).

4. Conclusion

4.1. Early Photoactivation Events in BLUF Photoreceptors

Understanding the early photoactivation events of BLUF photoreceptors is crucial for elucidating their function and photoactivation mechanism. Early photoactivation in BLUF domains involves a series of ultrafast processes that initiate signal transduction. Upon absorption of blue light, the flavin chromophore undergoes photoexcitation, leading to a series of structural changes within the flavin binding pocket. These changes typically occur within ps to ns and include alterations in hydrogen bond networks and protonation states. Specifically, the conserved glutamine residue plays a pivotal role in this process by altering its position and interactions with the flavin chromophore, which in turn affects the overall protein conformation.

OaPAC has been used as a model to study the early photoexcitation mechanism in BLUF photoreceptors using TR-SFX. The advantage of using OaPAC is the precise control of the sensor domain and the possibility to quantify the outcome of the effector domain. Structural differences observed in this study revealed details of the early lit state intermediates. By combining this insight with prior spectroscopic studies on BLUF photoreceptors, it is now possible to propose that BLUF proteins follow a specific pathway upon blue photon absorption, composed of a forward PCET/CPET of the Tyr-Gln-flavin triad, followed by a side chain rotation of the highly conserved glutamine concomitant to the displacement of the nearby methionine. Eventually, the reverse PCET locks Gln48 in an unusual rotated imidic acid tautomer form a few ns after photoexcitation in solution (Brust *et al.*, 2013) ($\sim 1 \mu\text{s}$ in OaPAC C222₁ crystal form) which represents a stable lit state conformation, setting the stage for downstream signalling events (Figure 50). The rearrangement of Gln48 has been a topic of debate for the past twenty years, as a few studies argued that the keto-enol tautomerization alone was sufficient to create a stable lit state (Sadeghian *et al.*, 2008; Ohki *et al.*, 2017). The pathway proposed here involves changes in the hydrogen bond networks around the flavin that create the red-shift at the absorption maximum around 450 nm. Nevertheless, the red-shift is not complete up until 150 ms in solution (Tokonami *et al.*, 2022;

Nakasone *et al.*, 2023) and 900 ms in OaPAC orthorhombic crystal form with C222₁ space group. This indicates that additional rearrangements occur around the flavin after tens of ms that further change the hydrogen bond network in the chromophore binding pocket again.

4.2. Importance of the Semi-Conserved Tryptophan Residue in Signal Transduction in BLUF Photoreceptors

Using a combination of TR-SSX and cryotrapping studies provided crucial insights on the structural rearrangements in the BLUF domain necessary for signal transduction. Consequently, in this study, compelling evidence for a Met_{out}/Trp_{in} transition in OaPAC upon light excitation was obtained. This transition plays a crucial role in transmitting the signal to the effector domain, making Trp90 a key player in signal transduction following blue light excitation of the chromophore. Trp90 induces a conformational change in the entire β -strand 5, leading to subsequent structural changes in the following loop and α -helix linker region necessary for signal transmission. The Met_{out}/Trp_{in} switch disrupts the hydrogen bond between Asn30 ND2 and Ser91 carbonyl oxygen and enables the formation of a new hydrogen bond between Gln48 OE1 and Trp90 NE1 (3.4 Å), as well as a new amino-aromatic interaction between Asn30 ND2 and Trp90 NE1 (3.1 Å). These interactions, previously proposed to be vital for stabilizing the signalling state (Jung *et al.*, 2006), confirm the importance of the Met_{out}/Trp_{in} switch in signal transduction. Yet, despite these findings, questions remain regarding the precise role of the Met_{out}/Trp_{in} transition. This might have a functional importance for signal transmission to the AC domain via the α -helices 3 and 4 linking the BLUF domain to the AC effector domain, or it might only stabilize the light-activated state, contributing to the long-lived nature of OaPAC light-activated state.

The semi-conserved Trp90 has been suggested to be linked to the slower dynamics observed in signal transduction in AppA and OaPAC (Masuda *et al.*, 2005c; Laan *et al.*, 2006; Brust *et al.*, 2013; Tokonami *et al.*, 2022; Nakasone *et al.*, 2023). Several spectroscopic studies reported that AppA Trp104Ala or Trp104Phe mutants (analogous to Trp90Ala and Trp90Phe in OaPAC) could

exhibit fast rearrangements around the flavin binding pocket similar to the wild type, but were missing significant slower light-induced structural rearrangements during signal transmission in the mutants which exhibited a relaxation rate 80 to 700 times faster when compared to the wild type (Masuda *et al.*, 2005c; Laan *et al.*, 2006; Brust *et al.*, 2013). Similarly, the Trp104Ala AppA and Trp90Ala OaPAC mutants did not exhibit the slow increase in absorbance at 492 nm and in transient grating signals on the ms time scale related to slow conformational changes during signal transmission (Tokonami *et al.*, 2022; Nakasone *et al.*, 2023). Last, Ohki *et al.* suggested the importance of the coiled-coil in transmitting the signalling state in OaPAC (Ohki *et al.*, 2016). They discovered the necessity of critical non-polar and polar interactions across the dimer interface in signal transduction. Consequently, these studies and the cryotrapping results presented in the thesis support the notion that the semi-conserved tryptophan is a critical component in the signal transduction pathway and plays a dual role in both stabilizing the chromophore binding pocket and the long-lived light state, and in initiating the conformational changes necessary for signal propagation to the linker region, before it can be transmitted to the AC domain.

Interestingly, for bPAC, Lindner *et al.* proposed the kink of β -sheet 4 to be a potential signal transmission pathway from the flavin binding pocket to the linker region (α -helices 3 and 4) before proceeding to the tongue region of the effector domain (Lindner *et al.*, 2017). However, the data presented in this study do not support this pathway for OaPAC. Instead, the data strongly suggest signal transmission via β -sheet 5 to α -helix 3. Neither the β -sheet 4 kink near α -helix 3 nor α -helix 4 demonstrate significant changes upon photoexcitation in either TR-SSX or cryotrapping studies, while amino acids in the loop between β -sheet 5 and α -helix 3 reveal strong changes and a significant increase in temperature factors, confirming the involvement of the loop in signal transmission.

The Met_{out}/Trp_{in} transition impacts the hydrogen bond network around the flavin and induces the additional changes in the UV-Vis absorption spectrum observed for OaPAC in solution (Tokonami *et al.*, 2022; Nakasone *et al.*, 2023) and in the crystalline state (C222₁ crystals). Interestingly, although the movement of the methionine away from the chromophore binding pocket is initiated already on the early μ s time scale in OaPAC C222₁ crystals (and most likely on the ns time scale in solution), the final transitioned Met_{out}/Trp_{in} conformation is only observed on the ms time scale (time constants of 235 ms in the crystal and of 36 ms in solution).

Taken all together, these findings allow proposal of the following signal transduction pathway in OaPAC: after local conformational changes around the flavin binding pocket, the signal is transmitted to the linker region via the Met_{out}/Trp_{in} switch, which rearranges β -sheet 5, linked to α -helix 3, with a time constant of 36 ms in solution (Tokonami *et al.*, 2022; Nakasone *et al.*, 2023) and 235 ms in OaPAC C222₁ crystal (Figure 50). Both α -helices 3 and 4 show structural changes alongside signal transduction from the β -sheet 5 to the N-terminal part of the linker region. The signalling state of the BLUF sensor domain is stabilised by a new amino-aromatic interaction formed between Asn30 ND2 and Trp90 NE1 (3.1 Å) and a hydrogen bond between Gln48 OE1 and Trp90 NE1 (3.4 Å).

Due to the high diversity in BLUF multi-domain photoreceptors, especially in term of effector domains, a consensus signal transmission pathway for all BLUF photoreceptors cannot be described. Nevertheless, conservation of the BLUF sensor domain secondary structure suggests that structural rearrangements happening in the BLUF domain are likely conserved among the BLUF family. Consequently, it is possible to speculate that the Met_{in} to Met_{out} and Trp_{out} to Trp_{in} transition is a common feature to transmit the signal to the N-terminal part of the α -helix linker (or C-terminal α -helix) in many BLUF photoreceptors. Transient absorption studies at 492 nm revealed that slower structural rearrangements around the flavin on the ms time scale were also present for other BLUF protein, including AppA, PapB and PixD/Slr1694, indicating that the Met_{out}/Trp_{in} transition might also occur for those proteins (Tokonami *et al.*, 2022).

4.3. Signal Transduction to the AC Domain in PAC Photoreceptors

Signal transduction in BLUF multi-domain photoreceptors involves the transfer of the light-induced signal from the BLUF sensor domain to downstream effector domains, such as the AC domain. This process is mediated by a series of conformational changes that propagate from the linker region through the effector domain. Although the limited AC domain structural rearrangements happening in the C222₁ crystal due to the constraints imposed by the crystal lattice

did not allow to observe the complete signal transmission, the last part of the signal transduction pathway in OaPAC can be postulated based on previous spectroscopic and crystallographic studies, the minor changes observed with time-resolved crystallography and cryotrapping, and on the FTIR study presented in this work.

In the presence of ATP, the signal is further transmitted on the ms to s time scale from the C-terminus of α -helix 3 and the handle (α -helix 4) to the tongue region of the AC domain from the other protomer (β -sheets 9 and 10) (Figure 50), probably through the interaction between Tyr125 (α -helix 3) and Asn256 (β -sheet 10). A slight change in angle between the handle and the tongue creates an opening of both AC domains which impacts α -helices 5 and 9 and the C-terminus and enables the rotation of the ATP ribose and adenine to initiate ATP turnover to cAMP. After the conversion, the AC domain relaxes to the ground state ($\tau = 2.9 \pm 0.6$ s), followed by the relaxation of the α -helix linker region and the BLUF domain ($\tau = 8.9 \pm 0.5$ s) (Figure 50). On the other hand, in the absence of ATP, the interaction between the handle (α -helix 4) and the tongue (β -sheets 9 and 10) is modified. As a result, the signal is not transmitted further from the linker region and the BLUF domain relaxes to the ground state faster ($\tau = 5.8 \pm 0.7$ s).

The FTIR data presented in this work suggests that blue light induces rather large structural rearrangements in the AC domains along with their opening only when ATP is already bound in the dark state, leading to an enlarged active site and the opportunity for the ATP adenosine moiety to rotate into the most energetically favourable conformation for pyrophosphate cleavage and cAMP production. Interestingly, Nakasone *et al.* studied OaPAC in solution with SAXS and did not observe any increase in R_g or D_{max} between the dark and the blue light excited states that would corroborate the opening of the AC domains (Nakasone *et al.*, 2023). Yet, they performed the measurements without ATP or analogues present in the solution, preventing the reaction of the effector domain. This highlights that many studies might have missed bigger changes in the AC domain as they only studied PAC photoreceptors in the absence of ATP. Similarly to studies of truncated BLUF photoreceptors, spectroscopy, scattering or crystallography experiments in the absence of substrate are also misleading and might overlook important changes during signal transduction.

The pathway proposed here involves a *trans* transmission of the signal from the sensor domain of one protomer to the effector domain of the second protomer, and necessitates the concomitant

photoexcitation of both protomers to enable the opening of the AC domains and the turnover of both ATPs to cAMPs. This pathway would explain why the ATP binding sites are at the interface of both AC domains, which requires a synchronized reaction of both protomers to enable the conversion.

Study of OaPAC using transient grating spectroscopy and enzymatic assays revealed that light-induced changes in the AC domain and ATP conversion to cAMP only occurred when both protomers were simultaneously activated (Nakasone *et al.*, 2023), demonstrating that the structural rearrangement of a single BLUF domain is not sufficient to induce the opening of the AC domains. Additionally, preliminary FTIR measurements seem to suggest that only one ATP can be converted per active site per photoexcitation cycle (2 ATPs converted in total per cycle) (data not shown). These findings suggest that OaPAC is a rather inefficient cyclase enzyme, as it necessitates strong light conditions to initiate cAMP production and a return to the ground state before new ATPs can be converted into cAMPs.

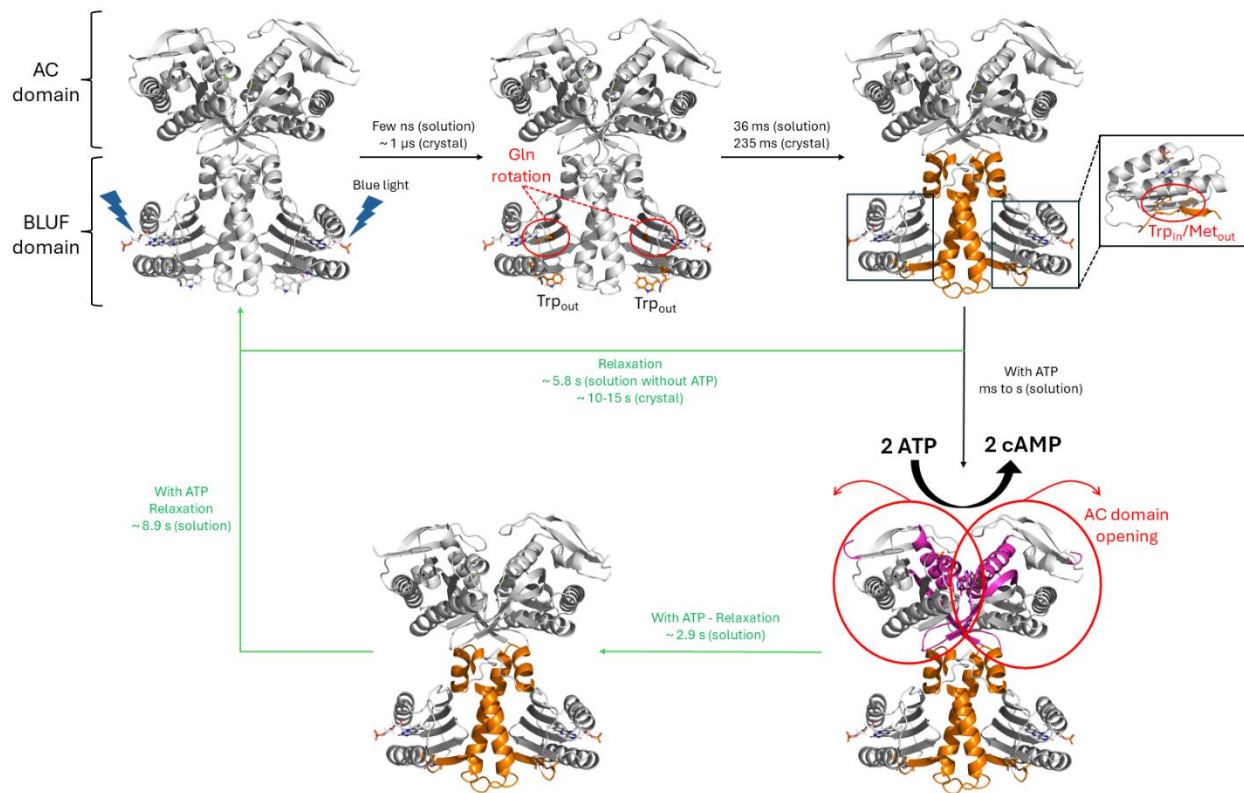


Figure 50: Proposed signal transmission pathway of OaPAC photoreceptor.

Signal transduction from the flavin in the BLUF domain to the active site in the AC domain is illustrated with colours. Upon blue light excitation, the chromophore binding pockets are altered, and a combination of PCET/CPET, glutamine rotation and tautomerisation create a modified hydrogen bond network corresponding to the lit state. The signal is then further transmitted from β -sheet 5 to the linker region via a $\text{Met}_{\text{out}}/\text{Trp}_{\text{in}}$ transition, where Trp will move from solvent exposed to buried near the flavin. Subsequently, in the presence of ATP, further rearrangements occur in the tongue region as well as several α -helices, and the AC domains open up to enable ATP conversion to cAMP. Eventually, the AC domain relaxes to the dark state, followed by the linker region and the BLUF domain in a second time. In the absence of ATP, the pathway is short-circuited and the BLUF domain relaxes faster, without rearrangement occurring in the AC domain.

Figure prepared by the PyMOL Molecular Graphics System, Version 2.5.4 Schrödinger, LLC (Schrödinger and DeLano, 2020).

References

- Adams, P.D., Afonine, P.V., Bunkóczi, G., Chen, V.B., Davis, I.W., Echols, N., Headd, J.J., Hung, L.-W., Kapral, G.J., Grosse-Kunstleve, R.W., McCoy, A.J., Moriarty, N.W., Oeffner, R., Read, R.J., Richardson, D.C., Richardson, J.S., Terwilliger, T.C. and Zwart, P.H. (2010). PHENIX: a comprehensive Python-based system for macromolecular structure solution. *Acta crystallographica. Section D, Biological crystallography* 66: 213–221.
- Agilent Technologies (Inc. 2010). *Manual : ArcticExpress Competent Cells and ArcticExpress (DE3) Competent Cells*.
- Agirre, J., Atanasova, M., Bagdonas, H., Ballard, C.B., Baslé, A., Beilsten-Edmands, J., Borges, R.J., Brown, D.G., Burgos-Mármol, J.J., Berrisford, J.M., Bond, P.S., Caballero, I., Catapano, L., Chojnowski, G., Cook, A.G., Cowtan, K.D., Croll, T.I., Debreczeni, J.É., Devenish, N.E., Dodson, E.J., Drevon, T.R., Emsley, P., Evans, G., Evans, P.R., Fando, M., Foadi, J., Fuentes-Montero, L., Garman, E.F., Gerstel, M., Gildea, R.J., Hatti, K., Hekkelman, M.L., Heuser, P., Hoh, S.W., Hough, M.A., Jenkins, H.T., Jiménez, E., Joosten, R.P., Keegan, R.M., Keep, N., Krissinel, E.B., Kolenko, P., Kovalevskiy, O., Lamzin, V.S., Lawson, D.M., Lebedev, A.A., Leslie, A.G.W., Lohkamp, B., Long, F., Malý, M., McCoy, A.J., McNicholas, S.J., Medina, A., Millán, C., Murray, J.W., Murshudov, G.N., Nicholls, R.A., Noble, M.E.M., Oeffner, R., Pannu, N.S., Parkhurst, J.M., Pearce, N., Pereira, J., Perrakis, A., Powell, H.R., Read, R.J., Rigden, D.J., Rochira, W., Sammito, M., Sánchez Rodríguez, F., Sheldrick, G.M., Shelley, K.L., Simkovic, F., Simpkin, A.J., Skubak, P., Sobolev, E., Steiner, R.A., Stevenson, K., Tews, I., Thomas, J.M.H., Thorn, A., Valls, J.T., Uski, V., Usón, I., Vagin, A., Velankar, S., Vollmar, M., Walden, H., Waterman, D., Wilson, K.S., Winn, M.D., Winter, G., Wojdyr, M. and Yamashita, K. (2023). The CCP4 suite: integrative software for macromolecular crystallography. *Acta crystallographica. Section D, Structural biology* 79: 449–461.
- Allahgholi, A., Becker, J., Delfs, A., Dinapoli, R., Goettlicher, P., Greiffenberg, D., Henrich, B., Hirsemann, H., Kuhn, M., Klanner, R., Klyuev, A., Krueger, H., Lange, S., Laurus, T., Marras, A., Mezza, D., Mozzanica, A., Niemann, M., Poehlsen, J., Schwandt, J., Sheviakov, I., Shi, X., Smoljanin, S., Steffen, L., Sztuk-Dambietz, J., Trunk, U., Xia, Q., Zeribi, M.,

- Zhang, J., Zimmer, M., Schmitt, B. and Graafsma, H. (2019). The Adaptive Gain Integrating Pixel Detector at the European XFEL. *Journal of synchrotron radiation* 26: 74–82.
- Anderson, S., Dragnea, V., Masuda, S., Ybe, J., Moffat, K. and Bauer, C. (2005). Structure of a novel photoreceptor, the BLUF domain of AppA from Rhodobacter sphaeroides. *Biochemistry* 44: 7998–8005.
- Aumonier, S., Santoni, G., Gotthard, G., von Stetten, D., Leonard, G.A. and Royant, A. (2020). Millisecond time-resolved serial oscillation crystallography of a blue-light photoreceptor at a synchrotron. *IUCrJ* 7: 728–736.
- Azher, O.A. (2018). *Spectroscopic Characterisation of Purine Nucleotides and their Interaction with Proteins*, University of Manchester, UK, 237pp.
- Barends, T.R.M., Gorel, A., Bhattacharyya, S., Schirò, G., Bacellar, C., Cirelli, C., Colletier, J.-P., Foucar, L., Grünbein, M.L., Hartmann, E., Hilpert, M., Holton, J.M., Johnson, P.J.M., Kloos, M., Knopp, G., Marekha, B., Nass, K., Nass Kovacs, G., Ozerov, D., Stricker, M., Weik, M., Doak, R.B., Shoeman, R.L., Milne, C.J., Huix-Rotllant, M., Cammarata, M. and Schlichting, I. (2024). Influence of pump laser fluence on ultrafast myoglobin structural dynamics. *Nature* 626: 905–911.
- Barends, T.R.M., Hartmann, E., Griese, J.J., Beitlich, T., Kirienko, N.V., Ryjenkov, D.A., Reinstein, J., Shoeman, R.L., Gomelsky, M. and Schlichting, I. (2009). Structure and mechanism of a bacterial light-regulated cyclic nucleotide phosphodiesterase. *Nature* 459: 1015–1018.
- Barth, A. and Mäntele, W. (1998). ATP-Induced phosphorylation of the sarcoplasmic reticulum Ca²⁺ ATPase: molecular interpretation of infrared difference spectra. *Biophysical journal* 75: 538–544.
- Barth, A. and Zscherp, C. (2002). What vibrations tell us about proteins. *Quarterly reviews of biophysics* 35: 369–430.
- Barty, A., Kirian, R.A., Maia, F.R.N.C., Hantke, M., Yoon, C.H., White, T.A. and Chapman, H. (2014). Cheetah: software for high-throughput reduction and analysis of serial femtosecond X-ray diffraction data. *J Appl Crystallogr* 47: 1118–1131.

- Belle, V., Rouger, S., Costanzo, S., Liquière, E., Strancar, J., Guigliarelli, B., Fournel, A. and Longhi, S. (2008). Mapping alpha-helical induced folding within the intrinsically disordered C-terminal domain of the measles virus nucleoprotein by site-directed spin-labeling EPR spectroscopy. *Proteins* 73: 973–988.
- Bharambe, N.G., Barathy, D.V., Syed, W., Visweswariah, S.S., Colaço, M., Misquith, S. and Suguna, K. (2016). Substrate specificity determinants of class III nucleotidyl cyclases. *The FEBS journal* 283: 3723–3738.
- Black, C.B., Huang, H.-W. and Cowan, J.A. (1994). Biological coordination chemistry of magnesium, sodium, and potassium ions. Protein and nucleotide binding sites. *Coordination Chemistry Reviews* 135-136: 165–202.
- Bonetti, C., Mathes, T., van Stokkum, I.H.M., Mullen, K.M., Groot, M.-L., van Grondelle, R., Hegemann, P. and Kennis, J.T.M. (2008). Hydrogen bond switching among flavin and amino acid side chains in the BLUF photoreceptor observed by ultrafast infrared spectroscopy. *Biophysical journal* 95: 4790–4802.
- Bonetti, C., Stierl, M., Mathes, T., van Stokkum, I.H.M., Mullen, K.M., Cohen-Stuart, T.A., van Grondelle, R., Hegemann, P. and Kennis, J.T.M. (2009). The role of key amino acids in the photoactivation pathway of the *Synechocystis* Slr1694 BLUF domain. *Biochemistry* 48: 11458–11469.
- Borgstahl, G.E., Williams, D.R. and Getzoff, E.D. (1995). 1.4 Å structure of photoactive yellow protein, a cytosolic photoreceptor: unusual fold, active site, and chromophore. *Biochemistry* 34: 6278–6287.
- Borshchevskiy, V., Kovalev, K., Volkov, O., Polovinkin, V., Marin, E., Balandin, T., Astashkin, R., Bamann, C., Bueldt, G., Willbold, D., Popov, A., Bamberg, E. and Gordeliy, V. (2017). *Crystal structure of wild-type Channelrhodopsin 2*.
- Bosman, R., Prester, A., Sung, S., Soosten, L. von, Dibenedetto, S., Bartels, K., Stetten, D. von, Mehrabi, P., Blatter, M., Lu, G., Suer, B., Wilmanns, M., Osbild, M. and Schulz, E.C. (2024). A systematic comparison of Kapton-based HARE chips for fixed-target serial crystallography. *Cell Reports Physical Science* 5: 101987.

- Bourhis, J.-M., Receveur-Bréchet, V., Oglesbee, M., Zhang, X., Buccellato, M., Darbon, H., Canard, B., Finet, S. and Longhi, S. (2005). The intrinsically disordered C-terminal domain of the measles virus nucleoprotein interacts with the C-terminal domain of the phosphoprotein via two distinct sites and remains predominantly unfolded. *Protein science : a publication of the Protein Society* 14: 1975–1992.
- Boutet, S., Fromme, P. and Hunter, M.S. (Eds.) (2018). *X-ray Free Electron Lasers*, Springer International Publishing, Cham.
- Braatsch, S., Gomelsky, M., Kuphal, S. and Klug, G. (2002). A single flavoprotein, AppA, integrates both redox and light signals in *Rhodobacter sphaeroides*. *Molecular microbiology* 45: 827–836.
- Brookner, D.E. and Hekstra, D.R. (2024). MatchMaps: non-isomorphous difference maps for X-ray crystallography. *J Appl Crystallogr* 57: 885–895.
- Brudler, R., Hitomi, K., Daiyasu, H., Toh, H., Kucho, K., Ishiura, M., Kanehisa, M., Roberts, V.A., Todo, T., Tainer, J.A. and Getzoff, E.D. (2003). Identification of a new cryptochrome class. Structure, function, and evolution. *Molecular cell* 11: 59–67.
- Brust, R., Lukacs, A., Haigney, A., Addison, K., Gil, A., Towrie, M., Clark, I.P., Greetham, G.M., Tonge, P.J. and Meech, S.R. (2013). Proteins in action: femtosecond to millisecond structural dynamics of a photoactive flavoprotein. *Journal of the American Chemical Society* 135: 16168–16174.
- Burkhardt, A., Pakendorf, T., Reime, B., Meyer, J., Fischer, P., Stübe, N., Panneerselvam, S., Lorbeer, O., Stachnik, K., Warmer, M., Rödig, P., Göries, D. and Meents, A. (2016). Status of the crystallography beamlines at PETRA III. *Eur. Phys. J. Plus* 131: 56.
- Caramello, N. and Royant, A. (2024). From femtoseconds to minutes: time-resolved macromolecular crystallography at XFELs and synchrotrons. *Acta Crystallogr D Struct Biol* 80: 60–79.
- Cheng, R. (2020). Towards an Optimal Sample Delivery Method for Serial Crystallography at XFEL. *Crystals* 10: 215.
- Chitrakar, I., Iuliano, J.N., He, Y., Woroniecka, H.A., Tolentino Collado, J., Wint, J.M., Walker, S.G., Tonge, P.J. and French, J.B. (2020). Structural Basis for the Regulation of Biofilm

Formation and Iron Uptake in *A. baumannii* by the Blue-Light-Using Photoreceptor, BlsA. *ACS infectious diseases* 6: 2592–2603.

Chretien, A., Nagel, M.F., Botha, S., Wijn, R. de, Brings, L., Dörner, K., Han, H., Koliyadu, J.C., Letrun, R., Round, A., Sato, T., Schmidt, C., Secareanu, R.-C., von Stetten, D., Vakili, M., Wrona, A., Bean, R., Mancuso, A., Schulz, J., Pearson, A.R., Kottke, T., Lorenzen, K. and Schubert, R. (2024). Light-induced Trpin/Metout switching during BLUF domain activation in ATP-bound photoactivatable adenylate cyclase OaPAC. *Journal of molecular biology* 168439.

Christie, J.M., Arvai, A.S., Baxter, K.J., Heilmann, M., Pratt, A.J., O'Hara, A., Kelly, S.M., Hothorn, M., Smith, B.O., Hitomi, K., Jenkins, G.I. and Getzoff, E.D. (2012a). Plant UVR8 photoreceptor senses UV-B by tryptophan-mediated disruption of cross-dimer salt bridges. *Science (New York, N.Y.)* 335: 1492–1496.

Christie, J.M., Gawthorne, J., Young, G., Fraser, N.J. and Roe, A.J. (2012b). LOV to BLUF: flavoprotein contributions to the optogenetic toolkit. *Molecular plant* 5: 533–544.

Christou, N.-E., Apostolopoulou, V., Melo, D.V.M., Ruppert, M., Fadini, A., Henkel, A., Sprenger, J., Oberthuer, D., Günther, S., Pateras, A., Rahmani Mashhour, A., Yefanov, O.M., Galchenkova, M., Reinke, P.Y.A., Kremling, V., Scheer, T.E.S., Lange, E.R., Middendorf, P., Schubert, R., de Zitter, E., Lumbao-Conradson, K., Herrmann, J., Rahighi, S., Kunavar, A., Beale, E.V., Beale, J.H., Cirelli, C., Johnson, P.J.M., Dworkowski, F., Ozerov, D., Bertrand, Q., Wranik, M., Bacellar, C., Bajt, S., Wakatsuki, S., Sellberg, J.A., Huse, N., Turk, D., Chapman, H.N. and Lane, T.J. (2023). Time-resolved crystallography captures light-driven DNA repair. *Science (New York, N.Y.)* 382: 1015–1020.

Collado, J.T., Iuliano, J.N., Pirisi, K., Jewlikar, S., Adamczyk, K., Greetham, G.M., Towrie, M., Tame, J.R.H., Meech, S.R., Tonge, P.J. and Lukacs, A. (2022). Unraveling the Photoactivation Mechanism of a Light-Activated Adenylate Cyclase Using Ultrafast Spectroscopy Coupled with Unnatural Amino Acid Mutagenesis. *ACS chemical biology* 17: 2643–2654.

Collette, F., Renger, T. and Am Schmidt Busch, M. (2014). Revealing the functional states in the active site of BLUF photoreceptors from electrochromic shift calculations. *The journal of physical chemistry. B* 118: 11109–11119.

- Conrad, K.S., Manahan, C.C. and Crane, B.R. (2014). Photochemistry of flavoprotein light sensors. *Nature chemical biology* 10: 801–809.
- Crosson, S. and Moffat, K. (2002). Photoexcited structure of a plant photoreceptor domain reveals a light-driven molecular switch. *The Plant cell* 14: 1067–1075.
- Czarna, A., Berndt, A., Singh, H.R., Grudziecki, A., Ladurner, A.G., Timinszky, G., Kramer, A. and Wolf, E. (2013). Structures of *Drosophila* cryptochrome and mouse cryptochrome1 provide insight into circadian function. *Cell* 153: 1394–1405.
- D’Hondt, E., Martín-Juárez, J., Bolado, S., Kasperoviciene, J., Koreiviene, J., Sulcius, S., Elst, K. and Bastiaens, L. (2017). In *Microalgae-Based Biofuels and Bioproducts*, Elsevier, pp. 133–154.
- Damough, S., Sabzalinezhad, M., Talebkhan, Y., Nematollahi, L., Bayat, E., Torkashvand, F., Adeli, A., Jahandar, H., Barkhordari, F. and Mahboudi, F. (2021). Optimization of culture conditions for high-level expression of soluble and active tumor necrosis factor- α in *E. coli*. *Protein expression and purification* 179: 105805.
- Davis, S.J., Vener, A.V. and Vierstra, R.D. (1999). Bacteriophytochromes: phytochrome-like photoreceptors from nonphotosynthetic eubacteria. *Science (New York, N.Y.)* 286: 2517–2520.
- de Zitter, E., Coquelle, N., Oeser, P., Barends, T.R.M. and Colletier, J.-P. (2022). Xtrapol8 enables automatic elucidation of low-occupancy intermediate-states in crystallographic studies. *Communications biology* 5: 640.
- Deisseroth, K. (2011). Optogenetics. *Nature methods* 8: 26–29.
- Deisseroth, K. (2015). Optogenetics: 10 years of microbial opsins in neuroscience. *Nature neuroscience* 18: 1213–1225.
- Diensthuber, R.P., Bommer, M., Gleichmann, T. and Möglich, A. (2013). Full-length structure of a sensor histidine kinase pinpoints coaxial coiled coils as signal transducers and modulators. *Structure* 21: 1127–1136.

- Do, T.N., Menendez, D., Bizhga, D., Stojković, E.A. and Kennis, J.T.M. (2024). Two-photon Absorption and Photoionization of a Bacterial Phytochrome. *Journal of molecular biology* 436: 168357.
- Domratcheva, T., Grigorenko, B.L., Schlichting, I. and Nemukhin, A.V. (2008). Molecular models predict light-induced glutamine tautomerization in BLUF photoreceptors. *Biophysical journal* 94: 3872–3879.
- Domratcheva, T., Hartmann, E., Schlichting, I. and Kottke, T. (2016). Evidence for Tautomerisation of Glutamine in BLUF Blue Light Receptors by Vibrational Spectroscopy and Computational Chemistry. *Scientific reports* 6: 22669.
- Dragnea, V., Arunkumar, A.I., Lee, C.W., Giedroc, D.P. and Bauer, C.E. (2010). A Q63E Rhodobacter sphaeroides AppA BLUF domain mutant is locked in a pseudo-light-excited signaling state. *Biochemistry* 49: 10682–10690.
- Dragnea, V., Waegele, M., Balascuta, S., Bauer, C. and Dragnea, B. (2005). Time-resolved spectroscopic studies of the AppA blue-light receptor BLUF domain from Rhodobacter sphaeroides. *Biochemistry* 44: 15978–15985.
- Dudás, E.F. and Bodor, A. (2019). Quantitative, Diffusion NMR Based Analytical Tool To Distinguish Folded, Disordered, and Denatured Biomolecules. *Analytical chemistry* 91: 4929–4933.
- Duisenberg, A.J.M. (1992). Indexing in single-crystal diffractometry with an obstinate list of reflections. *J Appl Crystallogr* 25: 92–96.
- Durbin, S.D. and Feher, G. (1996). Protein crystallization. *Annual review of physical chemistry* 47: 171–204.
- Dyson, H.J. and Wright, P.E. (2005). Intrinsically unstructured proteins and their functions. *Nature reviews. Molecular cell biology* 6: 197–208.
- Echelmeier, A., Cruz Villarreal, J., Messerschmidt, M., Kim, D., Coe, J.D., Thifault, D., Botha, S., Egatz-Gomez, A., Gandhi, S., Brehm, G., Conrad, C.E., Hansen, D.T., Madsen, C., Bajt, S., Meza-Aguilar, J.D., Oberthür, D., Wiedorn, M.O., Fleckenstein, H., Mendez, D., Knoška, J., Martin-Garcia, J.M., Hu, H., Lisova, S., Allahgholi, A., Gevorkov, Y., Ayyer, K., Aplin, S., Ginn, H.M., Graafsma, H., Morgan, A.J., Greiffenberg, D., Klujev, A., Laurus, T., Poehlsen,

J., Trunk, U., Mezza, D., Schmidt, B., Kuhn, M., Fromme, R., Sztuk-Dambietz, J., Raab, N., Hauf, S., Silenzi, A., Michelat, T., Xu, C., Danilevski, C., Parenti, A., Mekinda, L., Weinhausen, B., Mills, G., Vagovic, P., Kim, Y., Kirkwood, H., Bean, R., Bielecki, J., Stern, S., Giewekemeyer, K., Round, A.R., Schulz, J., Dörner, K., Grant, T.D., Mariani, V., Barty, A., Mancuso, A.P., Weierstall, U., Spence, J.C.H., Chapman, H.N., Zatsepin, N., Fromme, P., Kirian, R.A. and Ros, A. (2020). Segmented flow generator for serial crystallography at the European X-ray free electron laser. *Nature communications* 11: 4511.

Efetova, M., Petereit, L., Rosiewicz, K., Overend, G., Haußig, F., Hovemann, B.T., Cabrero, P., Dow, J.A.T. and Schwärzel, M. (2013). Separate roles of PKA and EPAC in renal function unraveled by the optogenetic control of cAMP levels in vivo. *Journal of cell science* 126: 778–788.

Emsley, P., Lohkamp, B., Scott, W.G. and Cowtan, K. (2010). Features and development of Coot. *Acta crystallographica. Section D, Biological crystallography* 66: 486–501.

Engilberge, S., Caramello, N., Bukhdruker, S., Byrdin, M., Giraud, T., Jacquet, P., Scortani, D., Biv, R., Gonzalez, H., Broquet, A., van der Linden, P., Rose, S.L., Flot, D., Balandin, T., Gordeliy, V., Lahey-Rudolph, J.M., Roessle, M., Sanctis, D. de, Leonard, G.A., Mueller-Dieckmann, C. and Royant, A. (2024). The TR-icOS setup at the ESRF: time-resolved microsecond UV-Vis absorption spectroscopy on protein crystals. *Acta Crystallogr D Struct Biol* 80: 16–25.

Essen, L.-O., Mailliet, J. and Hughes, J. (2008). The structure of a complete phytochrome sensory module in the Pr ground state. *Proceedings of the National Academy of Sciences of the United States of America* 105: 14709–14714.

Evans, P.R. and Murshudov, G.N. (2013). How good are my data and what is the resolution? *Acta crystallographica. Section D, Biological crystallography* 69: 1204–1214.

Fangohr, H., Aplin, S., Barty, A., Beg, M., Bondar, V., Boukhelef, D., Brockhauser, S., Danilevski, C., Ehsan, W., Esenov, S., Flucke, G., Giovanetti, G., Goeries, D., Hauf, S., Heisen, B., Hickin, D., Khakhulin, D., Klimovskaia, A., Kluyver, T., Kuhn, M., Kuster, M., Lang, P.-M., Maia, L., Mariani, V., Mekinda, L., Michelat, T., Parenti, A., Previtali, G., Santos, H., Silenzi, A., Sztuk-Dambietz, J., Szuba, J., Teichmann, M., Weger, K., Wiggins, J., Wrona, K. and Xu, C. (Eds.) (2018). *Data Analysis Support in Karabo at European XFEL*.

- Farahani, P.E., Reed, E.H., Underhill, E.J., Aoki, K. and Toettcher, J.E. (2021). Signaling, Deconstructed: Using Optogenetics to Dissect and Direct Information Flow in Biological Systems. *Annual review of biomedical engineering* 23: 61–87.
- Ferrari, D., Merli, A., Peracchi, A., Di Valentin, M., Carbonera, D. and Rossi, G.L. (2003). Catalysis and electron transfer in protein crystals: the binary and ternary complexes of methylamine dehydrogenase with electron acceptors. *Biochimica et biophysica acta* 1647: 337–342.
- Fischer, P., Schiewer, E., Broser, M., Busse, W., Spreen, A., Grosse, M., Hegemann, P. and Bartl, F. (2024). The Functionality of the DC Pair in a Rhodopsin Guanylyl Cyclase from *Catenaria anguillulae*. *Journal of molecular biology* 436: 168375.
- Flot, D., Mairs, T., Giraud, T., Guijarro, M., Lesourd, M., Rey, V., van Brussel, D., Morawe, C., Borel, C., Hignette, O., Chavanne, J., Nurizzo, D., McSweeney, S. and Mitchell, E. (2010). The ID23-2 structural biology microfocus beamline at the ESRF. *Journal of synchrotron radiation* 17: 107–118.
- Fraikin, G.Y. and Belenikina, N.S. (2023). Photochemistry and Signaling Activity of Plant Cryptochromes: A Review. *Biol Bull Russ Acad Sci* 50: 266–275.
- Francis, D.M. and Page, R. (2010). Strategies to optimize protein expression in *E. coli*. *Current protocols in protein science* Chapter 5: 5.24.1-5.24.29.
- Franke, D., Petoukhov, M.V., Konarev, P.V., Panjkovich, A., Tuukkanen, A., Mertens, H.D.T., Kikhney, A.G., Hajizadeh, N.R., Franklin, J.M., Jeffries, C.M. and Svergun, D.I. (2017). ATSAS 2.8: a comprehensive data analysis suite for small-angle scattering from macromolecular solutions. *J Appl Crystallogr* 50: 1212–1225.
- Franke, D. and Svergun, D.I. (2009). DAMMIF, a program for rapid ab-initio shape determination in small-angle scattering. *J Appl Crystallogr* 42: 342–346.
- Fulton, A.B. (1982). How crowded is the cytoplasm? *Cell* 30: 345–347.
- Galchenkova, M., Rahmani Mashhour, A., Reinke, P.Y.A., Günther, S., Meyer, J., Chapman, H.N. and Yefanov, O.M. (2023). An Optimized Approach for Serial Crystallography Using Chips. *Crystals* 13: 1225.

- Galea, C.A., Wang, Y., Sivakolundu, S.G. and Kriwacki, R.W. (2008). Regulation of cell division by intrinsically unstructured proteins: intrinsic flexibility, modularity, and signaling conduits. *Biochemistry* 47: 7598–7609.
- Garbers, D.L. and Johnson, R.A. (1975). Metal and metal-ATP interactions with brain and cardiac adenylate cyclases. *The Journal of biological chemistry* 250: 8449–8456.
- Gauden, M., Grinstead, J.S., Laan, W., van Stokkum, I.H.M., Avila-Perez, M., Toh, K.C., Boelens, R., Kaptein, R., van Grondelle, R., Hellingwerf, K.J. and Kennis, J.T.M. (2007). On the Role of Aromatic Side Chains in the Photoactivation of BLUF Domains. *Biochemistry* 45: 7405–7415.
- Gauden, M., van Stokkum, I.H.M., Key, J.M., Lührs, D.C., van Grondelle, R., Hegemann, P. and Kennis, J.T.M. (2006a). Hydrogen-bond switching through a radical pair mechanism in a flavin-binding photoreceptor. *Proceedings of the National Academy of Sciences of the United States of America* 103: 10895–10900.
- Gauden, M., van Stokkum, I.H.M., Key, J.M., Lührs, D.C., van Grondelle, R., Hegemann, P. and Kennis, J.T.M. (2006b). Hydrogen-bond switching through a radical pair mechanism in a flavin-binding photoreceptor. *Proceedings of the National Academy of Sciences of the United States of America* 103: 10895–10900.
- Gauden, M., Yeremenko, S., Laan, W., van Stokkum, Ivo H. M., Ihalainen, Janne A., van Grondelle, R., Hellingwerf, K.J. and Kennis, J.T.M. (2005). Photocycle of the Flavin-Binding Photoreceptor AppA, a Bacterial Transcriptional Antirepressor of Photosynthesis Genes. *Biochemistry* 44: 3653–3662.
- Getzoff, E.D., Gutwin, K.N. and Genick, U.K. (2003). Anticipatory active-site motions and chromophore distortion prime photoreceptor PYP for light activation. *Nature structural biology* 10: 663–668.
- Gevorkov, Y., Yefanov, O., Barty, A., White, T.A., Mariani, V., Brehm, W., Tolstikova, A., Grigat, R.R. and Chapman, H.N. (2019). XGANDALF - extended gradient descent algorithm for lattice finding. *Acta crystallographica. Section A, Foundations and advances* 75: 694–704.
- Gil, A., Haigney, A., Laptanok, S.P., Brust, R., Lukacs, A., Iuliano, J., Jeng, J., Melief, E., Zhao, R.-K., Yoon, E., Clark, I., Towrie, M., Greetham, G.M., Ng, A., Truglio, J., French, J.,

- Meech, S.R. and Tonge, P.J. (2016). Mechanism of the AppABLUF Photocycle Probed by Site-Specific Incorporation of Fluorotyrosine Residues: Effect of the Y21 pKa on the Forward and Reverse Ground-State Reactions. *Journal of the American Chemical Society* 138: 926–935.
- Gil, A.A., Laptanok, S.P., Iuliano, J.N., Lukacs, A., Verma, A., Hall, C.R., Yoon, G.E., Brust, R., Greetham, G.M., Towrie, M., French, J.B., Meech, S.R. and Tonge, P.J. (2017). Photoactivation of the BLUF Protein PixD Probed by the Site-Specific Incorporation of Fluorotyrosine Residues. *Journal of the American Chemical Society* 139: 14638–14648.
- Goings, J.J. and Hammes-Schiffer, S. (2019). Early Photocycle of Slr1694 Blue-Light Using Flavin Photoreceptor Unraveled through Adiabatic Excited-State Quantum Mechanical/Molecular Mechanical Dynamics. *Journal of the American Chemical Society* 141: 20470–20479.
- Goings, J.J., Li, P., Zhu, Q. and Hammes-Schiffer, S. (2020). Formation of an unusual glutamine tautomer in a blue light using flavin photocycle characterizes the light-adapted state. *Proceedings of the National Academy of Sciences of the United States of America* 117: 26626–26632.
- Gold, M.G., Gonen, T. and Scott, J.D. (2013). Local cAMP signaling in disease at a glance. *Journal of cell science* 126: 4537–4543.
- Golic, A.E., Valle, L., Jaime, P.C., Álvarez, C.E., Parodi, C., Borsarelli, C.D., Abatedaga, I. and Mussi, M.A. (2019). BlsA Is a Low to Moderate Temperature Blue Light Photoreceptor in the Human Pathogen *Acinetobacter baumannii*. *Front. Microbiol.* 10.
- Gomelsky, M. and Kaplan, S. (1995). appA, a novel gene encoding a trans-acting factor involved in the regulation of photosynthesis gene expression in *Rhodobacter sphaeroides* 2.4.1. *Journal of bacteriology* 177: 4609–4618.
- Gomelsky, M. and Kaplan, S. (1997). Molecular genetic analysis suggesting interactions between AppA and PpsR in regulation of photosynthesis gene expression in *Rhodobacter sphaeroides* 2.4.1. *Journal of bacteriology* 179: 128–134.

- Gomelsky, M. and Kaplan, S. (1998). AppA, a redox regulator of photosystem formation in *Rhodobacter sphaeroides* 2.4.1, is a flavoprotein. Identification of a novel fad binding domain. *The Journal of biological chemistry* 273: 35319–35325.
- Gomelsky, M. and Klug, G. (2002). BLUF: a novel FAD-binding domain involved in sensory transduction in microorganisms. *Trends in biochemical sciences* 27: 497–500.
- Goyal, P. and Hammes-Schiffer, S. (2017). Role of active site conformational changes in photocycle activation of the AppA BLUF photoreceptor. *Proceedings of the National Academy of Sciences of the United States of America* 114: 1480–1485.
- Grabski, A.C. (2009). Advances in preparation of biological extracts for protein purification. *Methods in enzymology* 463: 285–303.
- Grigorenko, B., Polyakov, I. and Nemukhin, A. (2020). Mechanisms of ATP to cAMP Conversion Catalyzed by the Mammalian Adenylyl Cyclase: A Role of Magnesium Coordination Shells and Proton Wires. *The journal of physical chemistry. B* 124: 451–460.
- Grinstead, J.S., Hsu, S.-T.D., Laan, W., Bonvin, A.M.J.J., Hellingwerf, K.J., Boelens, R. and Kaptein, R. (2006). The solution structure of the AppA BLUF domain: insight into the mechanism of light-induced signaling. *Chembiochem : a European journal of chemical biology* 7: 187–193.
- Grünbein, M.L. and Nass Kovacs, G. (2019). Sample delivery for serial crystallography at free-electron lasers and synchrotrons. *Acta Crystallogr D Struct Biol* 75: 178–191.
- Grünbein, M.L., Stricker, M., Nass Kovacs, G., Kloos, M., Doak, R.B., Shoeman, R.L., Reinstein, J., Lecler, S., Haacke, S. and Schlichting, I. (2020). Illumination guidelines for ultrafast pump-probe experiments by serial femtosecond crystallography. *Nature methods* 17: 681–684.
- Grusch, M., Schelch, K., Riedler, R., Reichhart, E., Differ, C., Berger, W., Inglés-Prieto, Á. and Janovjak, H. (2014). Spatio-temporally precise activation of engineered receptor tyrosine kinases by light. *The EMBO journal* 33: 1713–1726.
- Guinier, A. and Fournet, J. (1955). *Small-angle Scattering of X-rays*, John Wiley & Sons Inc., New York.

- Gutiérrez-González, M., Farías, C., Tello, S., Pérez-Etcheverry, D., Romero, A., Zúñiga, R., Ribeiro, C.H., Lorenzo-Ferreiro, C. and Molina, M.C. (2019). Optimization of culture conditions for the expression of three different insoluble proteins in *Escherichia coli*. *Scientific reports* 9: 16850.
- Hadden, J.M., Chapman, D. and Lee, D.C. (1995). A comparison of infrared spectra of proteins in solution and crystalline forms. *Biochimica et biophysica acta* 1248: 115–122.
- Hadjidemetriou, K., Coquelle, N., Barends, T.R.M., de Zitter, E., Schlichting, I., Colletier, J.P. and Weik, M. (2022). Time-resolved serial femtosecond crystallography on fatty-acid photodecarboxylase: lessons learned. *Acta crystallographica. Section D, Structural biology* 78: 1131–1142.
- Hahn, D.K., Tusell, J.R., Sprang, S.R. and Chu, X. (2015). Catalytic Mechanism of Mammalian Adenylyl Cyclase: A Computational Investigation. *Biochemistry* 54: 6252–6262.
- Hall, C.R., Tolentino Collado, J., Iuliano, J.N., Gil, A.A., Adamczyk, K., Lukacs, A., Greetham, G.M., Sazanovich, I., Tonge, P.J. and Meech, S.R. (2019). Site-Specific Protein Dynamics Probed by Ultrafast Infrared Spectroscopy of a Noncanonical Amino Acid. *The journal of physical chemistry. B* 123: 9592–9597.
- Han, H., Round, E., Schubert, R., Gül, Y., Makroczyová, J., Meza, D., Heuser, P., Aepfelbacher, M., Barák, I., Betzel, C., Fromme, P., Kursula, I., Nissen, P., Tereschenko, E., Schulz, J., Uetrecht, C., Ulicný, J., Wilmanns, M., Hajdu, J., Lamzin, V.S. and Lorenzen, K. (2021). The XBI BioLab for life science experiments at the European XFEL. *J Appl Crystallogr* 54: 7–21.
- Harper, S.M., Christie, J.M. and Gardner Kevin H. (2004). Disruption of the LOV-J α Helix Interaction Activates Phototropin Kinase Activity. *Biochemistry* 43: 16184–16192.
- Harper, S.M., Neil, L.C. and Gardner, K.H. (2003). Structural basis of a phototropin light switch. *Science* 301: 1541–1544.
- Hasegawa, K., Masuda, S. and Ono, T. (2005). Spectroscopic analysis of the dark relaxation process of a photocycle in a sensor of blue light using FAD (BLUF) protein Slr1694 of the cyanobacterium *Synechocystis* sp. PCC6803. *Plant & cell physiology* 46: 136–146.

- Hasegawa, K., Masuda, S. and Ono, T. (2006). Light induced structural changes of a full-length protein and its BLUF domain in YcgF(Blrp), a blue-light sensing protein that uses FAD (BLUF). *Biochemistry* 45: 3785–3793.
- He, M., Jin, L. and Austen, B. (1993). Specificity of factor Xa in the cleavage of fusion proteins. *Journal of protein chemistry* 12: 1–5.
- Hendriks, J., van der Horst, M.A., Chua, T.K., Pérez1, M.Á., van Wilderen, L.J., Alexandre, M.T., Groot, M.-L., Kennis, J.T.M. and Hellingwerf, K.J. (2009). *The Purple Phototrophic Bacteria – Photoreceptor Proteins from Purple Bacteria*, Springer Science, 811–837.
- Hirano, M., Takebe, M., Ishido, T., Ide, T. and Matsunaga, S. (2019). The C-terminal region affects the activity of photoactivated adenylyl cyclase from *Oscillatoria acuminata*. *Scientific reports* 9: 20262.
- Hontani, Y., Mehlhorn, J., Domratcheva, T., Beck, S., Kloz, M., Hegemann, P., Mathes, T. and Kennis, J.T.M. (2023). Spectroscopic and Computational Observation of Glutamine Tautomerization in the Blue Light Sensing Using Flavin Domain Photoreaction. *Journal of the American Chemical Society* 145: 1040–1052.
- Horrell, S., Agthe, M., von Stetten, D., Mehrabi, P., Schulz, E.-C., Bourenkov, G., Nikolova, M., Karpics, I., Fiedler, S., Tellkamp, F., Miller, R.D., Huse, N., Pearson, A.R. and Schneider, T.R. (2019). P14 T-REXX: first results from the Jurassic beamline. *Acta crystallographica. Section A, Foundations and advances* 75: e35-e35.
- Horrell, S., Axford, D., Devenish, N.E., Ebrahim, A., Hough, M.A., Sherrell, D.A., Storm, S.L.S., Tews, I., Worrall, J.A.R. and Owen, R.L. (2021). Fixed Target Serial Data Collection at Diamond Light Source. *Journal of visualized experiments : JoVE*.
- Hüll, K., Morstein, J. and Trauner, D. (2018). In Vivo Photopharmacology. *Chemical reviews* 118: 10710–10747.
- Iakoucheva, L.M., Brown, C.J., Lawson, J.D., Obradović, Z. and Dunker, A.K. (2002). Intrinsic disorder in cell-signaling and cancer-associated proteins. *Journal of molecular biology* 323: 573–584.

- Iseki, M., Matsunaga, S., Murakami, A., Ohno, K., Shiga, K., Yoshida, K., Sugai, M., Takahashi, T., Hori, T. and Watanabe, M. (2002). A blue-light-activated adenylyl cyclase mediates photoavoidance in *Euglena gracilis*. *Nature* 415: 1047–1051.
- Ito, S., Murakami, A., Iseki, M., Takahashi, T., Higashi, S. and Watanabe, M. (2010). Differentiation of photocycle characteristics of flavin-binding BLUF domains of α - and β -subunits of photoactivated adenylyl cyclase of *Euglena gracilis*. *Photochemical & photobiological sciences : Official journal of the European Photochemistry Association and the European Society for Photobiology* 9: 1327–1335.
- Ito, S., Murakami, A., Sato, K., Nishina, Y., Shiga, K., Takahashi, T., Higashi, S., Iseki, M. and Watanabe, M. (2005). Photocycle features of heterologously expressed and assembled eukaryotic flavin-binding BLUF domains of photoactivated adenylyl cyclase (PAC), a blue-light receptor in *Euglena gracilis*. *Photochemical & photobiological sciences : Official journal of the European Photochemistry Association and the European Society for Photobiology* 4: 762–769.
- Iuliano, J.N., Gil, A.A., Laptенок, S.P., Hall, C.R., Tolentino Collado, J., Lukacs, A., Hag Ahmed, S.A., Abyad, J., Daryae, T., Greetham, G.M., Sazanovich, I.V., Illarionov, B., Bacher, A., Fischer, M., Towrie, M., French, J.B., Meech, S.R. and Tonge, P.J. (2018). Variation in LOV Photoreceptor Activation Dynamics Probed by Time-Resolved Infrared Spectroscopy. *Biochemistry* 57: 620–630.
- Iwata, T., Watanabe, A., Iseki, M., Watanabe, M. and Kandori, H. (2011). Strong Donation of the Hydrogen Bond of Tyrosine during Photoactivation of the BLUF Domain. *J. Phys. Chem. Lett.* 2: 1015–1019.
- Jenkins, G.I. (2009). Signal transduction in responses to UV-B radiation. *Annual review of plant biology* 60: 407–431.
- Jung, A., Domratcheva, T., Tarutina, M., Wu, Q., Ko, W., Shoeman, R.L., Mark Gomelsky, Gardner, Kevin H. and Schlichting, I. (2005). Structure of a bacterial BLUF photoreceptor: Insights into blue light-mediated signal transduction. *Proceedings of the National Academy of Sciences of the United States of America* 102: 12350–12355.

- Jung, A., Reinstein, J., Domratcheva, T., Shoeman, R.L. and Schlichting, I. (2006). Crystal structures of the AppA BLUF domain photoreceptor provide insights into blue light-mediated signal transduction. *Journal of molecular biology* 362: 717–732.
- Kabsch, W. (2010). XDS. *Acta crystallographica. Section D, Biological crystallography* 66: 125–132.
- Kapetanaki, S.M., Coquelle, N., von Stetten, D., Byrdin, M., Rios-Santacruz, R., Bean, R., Bielecki, J., Boudjelida, M., Fekete, Z., Grime, G.W., Han, H., Hatton, C., Kantamneni, S., Kharitonov, K., Kim, C., Kloos, M., Koua, F.H., Diego Martinez, I. de, Melo, D., Rane, L., Round, A., Round, E., Sarma, A., Schubert, R., Schulz, J., Sikorski, M., Vakili, M., Valerio, J., Vitas, J., Wijn, R. de, Wrona, A., Zala, N., Pearson, A., Dorner, K., Schiro, G., Garman, E.F., Lukacs, A. and Weik, M. (2024). *Crystal structure of a bacterial photoactivated adenylate cyclase determined at room temperature by serial femtosecond crystallography*.
- Karadi, K., Kapetanaki, S.M., Raics, K., Pecs, I., Kapronczai, R., Fekete, Z., Iuliano, J.N., Collado, J.T., Gil, A.A., Orban, J., Nyitrai, M., Greetham, G.M., Vos, M.H., Tonge, P.J., Meech, S.R. and Lukacs, A. (2020). Functional dynamics of a single tryptophan residue in a BLUF protein revealed by fluorescence spectroscopy. *Scientific reports* 10: 2061.
- Kataoka, M., Shimizu, S. and Yamada, H. (1992). Purification and characterization of a novel FMN-dependent enzyme. Membrane-bound L-(+)-pantoyl lactone dehydrogenase from *Nocardia asteroides*. *European journal of biochemistry* 204: 799–806.
- Kattinig, D.R., Solov'yov, I.A. and Hore, P.J. (2016). Electron spin relaxation in cryptochrome-based magnetoreception. *Physical chemistry chemical physics : PCCP* 18: 12443–12456.
- Kaur, J., Kumar, A. and Kaur, J. (2018). Strategies for optimization of heterologous protein expression in *E. coli*: Roadblocks and reinforcements. *International journal of biological macromolecules* 106: 803–822.
- Kennis, J.T.M. and Groot, M.-L. (2007). Ultrafast spectroscopy of biological photoreceptors. *Current opinion in structural biology* 17: 623–630.
- Kennis, J.T.M. and Mathes, T. (2013). Molecular eyes: proteins that transform light into biological information. *Interface focus* 3: 20130005.

- Khrenova, M.G., Nemukhin, A.V. and Domratcheva, T. (2013). Photoinduced electron transfer facilitates tautomerization of the conserved signaling glutamine side chain in BLUF protein light sensors. *The journal of physical chemistry. B* 117: 2369–2377.
- Kim, Y., Babnigg, G., Jedrzejczak, R., Eschenfeldt, W.H., Li, H., Maltseva, N., Hatzos-Skintges, C., Gu, M., Makowska-Grzyska, M., Wu, R., An, H., Chhor, G. and Joachimiak, A. (2011). High-throughput protein purification and quality assessment for crystallization. *Methods (San Diego, Calif.)* 55: 12–28.
- Kimata, K., Takahashi, H., Inada, T., Postma, P. and Aiba, H. (1997). cAMP receptor protein-cAMP plays a crucial role in glucose-lactose diauxie by activating the major glucose transporter gene in *Escherichia coli*. *Proceedings of the National Academy of Sciences of the United States of America* 94: 12914–12919.
- Kita, A., Okajima, K., Morimoto, Y., Ikeuchi, M. and Miki, K. (2005). Structure of a cyanobacterial BLUF protein, Tll0078, containing a novel FAD-binding blue light sensor domain. *Journal of molecular biology* 349: 1–9.
- Kleinboelting, S., van den Heuvel, J. and Steegborn, C. (2014). Structural analysis of human soluble adenylyl cyclase and crystal structures of its nucleotide complexes-implications for cyclase catalysis and evolution. *The FEBS journal* 281: 4151–4164.
- Kneuttinger, A.C., Straub, K., Bittner, P., Simeth, N.A., Bruckmann, A., Busch, F., Rajendran, C., Hupfeld, E., Wysocki, V.H., Horinek, D., König, B., Merkl, R. and Sterner, R. (2019). Light Regulation of Enzyme Allostery through Photo-responsive Unnatural Amino Acids. *Cell chemical biology* 26: 1501-1514.e9.
- Koliyadu, J.C.P., Letrun, R., Kirkwood, H.J., Liu, J., Jiang, M., Emons, M., Bean, R., Bellucci, V., Bielecki, J., Birnsteinova, S., Wijn, R. de, Dietze, T., E, J., Grünert, J., Kane, D., Kim, C., Kim, Y., Lederer, M., Manning, B., Mills, G., Morillo, L.L., Reimers, N., Rompotis, D., Round, A., Sikorski, M., Takem, C.M.S., Vagovič, P., Venkatesan, S., Wang, J., Wegner, U., Mancuso, A.P. and Sato, T. (2022). Pump-probe capabilities at the SPB/SFX instrument of the European XFEL. *Journal of synchrotron radiation* 29: 1273–1283.

- Konold, P.E., Arik, E., Weißenborn, J., Arents, J.C., Hellingwerf, K.J., van Stokkum, I.H.M., Kennis, J.T.M. and Groot, M.L. (2020). Confinement in crystal lattice alters entire photocycle pathway of the Photoactive Yellow Protein. *Nature communications* 11: 4248.
- Konold, P.E., Mathes, T., Weißenborn, J., Groot, M.L., Hegemann, P. and Kennis, J.T.M. (2016). Unfolding of the C-Terminal J α Helix in the LOV2 Photoreceptor Domain Observed by Time-Resolved Vibrational Spectroscopy. *The journal of physical chemistry letters* 7: 3472–3476.
- Kort, R., Hoff, W.D., van West, M., Kroon, A.R., Hoffer, S.M., Vlieg, K.H., Crielaand, W., van Beeumen, J.J. and Hellingwerf, K.J. (1996). The xanthopsins: a new family of eubacterial blue-light photoreceptors. *The EMBO journal* 15: 3209–3218.
- Kubota, T., Tani, O., Yamaguchi, T., Namatame, I., Sakashita, H., Furukawa, K. and Yamasaki, K. (2018). Crystal structures of FMN-bound and FMN-free forms of dihydroorotate dehydrogenase from *Trypanosoma brucei*. *FEBS open bio* 8: 680–691.
- Kyriacou, C.P. and Rosato, E. (2022). Genetic analysis of cryptochrome in insect magnetosensitivity. *Frontiers in physiology* 13: 928416.
- Laan, W., Gauden, M., Yeremenko, S., van Grondelle, R., Kennis, J.T.M. and Hellingwerf, K.J. (2006). On the mechanism of activation of the BLUF domain of AppA. *Biochemistry* 45: 51–60.
- Laptenko, O., Tong, D.R., Manfredi, J. and Prives, C. (2016). The Tail That Wags the Dog: How the Disordered C-Terminal Domain Controls the Transcriptional Activities of the p53 Tumor-Suppressor Protein. *Trends in biochemical sciences* 41: 1022–1034.
- Laskowski, R.A. and Swindells, M.B. (2011). LigPlot+: multiple ligand-protein interaction diagrams for drug discovery. *Journal of chemical information and modeling* 51: 2778–2786.
- Linder, J., Hupfeld, E., Weyand, M., Steegborn, C. and Moniot, S. (2020). Crystal structure of a class III adenylyl cyclase-like ATP-binding protein from *Pseudomonas aeruginosa*. *Journal of structural biology* 211: 107534.
- Lindner, M., Gilhooley, M.J., Hughes, S. and Hankins, M.W. (2022). Optogenetics for visual restoration: From proof of principle to translational challenges. *Progress in retinal and eye research* 91: 101089.

- Lindner, R. (2018). *Blue-Light-Regulated Adenylyl Cyclases, optogenetic tools and model systems for inter-domain communication*, [Academic institution is missing!], University of Heidelberg, Germany, 190pp.
- Lindner, R., Hartmann, E., Tarnawski, M., Winkler, A., Frey, D., Reinstein, J., Meinhart, A. and Schlichting, I. (2017). Photoactivation Mechanism of a Bacterial Light-Regulated Adenylyl Cyclase. *Journal of molecular biology* 429: 1336–1351.
- Losi, A., Gardner, K.H. and Möglich, A. (2018). Blue-Light Receptors for Optogenetic. *Chem. Rev.* 118: 10659–10709.
- Lukacs, A., Brust, R., Haigney, A., Laptanok, S.P., Addison, K., Gil, A., Towrie, M., Greetham, G.M., Tonge, P.J. and Meech, S.R. (2014). BLUF domain function does not require a metastable radical intermediate state. *Journal of the American Chemical Society* 136: 4605–4615.
- Lukacs, A., Tonge, P.J. and Meech, S.R. (2022). Photophysics of the Blue Light Using Flavin Domain. *Accounts of chemical research* 55: 402–414.
- Macheroux, P. (1999). UV-visible spectroscopy as a tool to study flavoproteins. *Methods in molecular biology (Clifton, N.J.)* 131: 1–7.
- Majerus, T., Kottke, T., Laan, W., Hellingwerf, K. and Heberle, J. (2007). Time-resolved FT-IR spectroscopy traces signal relay within the blue-light receptor AppA. *Chemphyschem : a European journal of chemical physics and physical chemistry* 8: 1787–1789.
- Makinen, M.W. and Fink, A.L. (1977). Reactivity and cryoenzymology of enzymes in the crystalline state. *Ann Rev Biophys Bioeng* 6: 301–343.
- Manalastas-Cantos, K., Konarev, P.V., Hajizadeh, N.R., Kikhney, A.G., Petoukhov, M.V., Molodenskiy, D.S., Panjkovich, A., Mertens, H.D.T., Gruzinov, A., Borges, C., Jeffries, C.M., Svergun, D.I. and Franke, D. (2021). ATSAS 3.0: expanded functionality and new tools for small-angle scattering data analysis. *J Appl Crystallogr* 54: 343–355.
- Mancuso, A.P., Aquila, A., Batchelor, L., Bean, R.J., Bielecki, J., Borchers, G., Doerner, K., Giewekemeyer, K., Graceffa, R., Kelsey, O.D., Kim, Y., Kirkwood, H.J., Legrand, A., Letrun, R., Manning, B., Lopez Morillo, L., Messerschmidt, M., Mills, G., Raabe, S., Reimers, N., Round, A., Sato, T., Schulz, J., Signe Takem, C., Sikorski, M., Stern, S., Thute, P., Vagovič,

- P., Weinhausen, B. and Tschentscher, T. (2019). The Single Particles, Clusters and Biomolecules and Serial Femtosecond Crystallography instrument of the European XFEL: initial installation. *Journal of synchrotron radiation* 26: 660–676.
- Mariani, V., Morgan, A., Yoon, C.H., Lane, T.J., White, T.A., O'Grady, C., Kuhn, M., Aplin, S., Koglin, J., Barty, A. and Chapman, H.N. (2016). OnDA: online data analysis and feedback for serial X-ray imaging. *J Appl Crystallogr* 49: 1073–1080.
- Masuda, S. (2013). Light detection and signal transduction in the BLUF photoreceptors. *Plant & cell physiology* 54: 171–179.
- Masuda, S. and Bauer, C.E. (2002). AppA is a blue light photoreceptor that antirepresses photosynthesis gene expression in *Rhodobacter sphaeroides*. *Cell* 110: 613–623.
- Masuda, S., Hasegawa, K., Ohta, H. and Ono, T. (2008). Crucial role in light signal transduction for the conserved Met93 of the BLUF protein PixD/Slr1694. *Plant & cell physiology* 49: 1600–1606.
- Masuda, S., Hasegawa, K. and Ono, T. (2005a). Adenosine diphosphate moiety does not participate in structural changes for the signaling state in the sensor of blue-light using FAD domain of AppA. *FEBS letters* 579: 4329–4332.
- Masuda, S., Hasegawa, K. and Ono, T. (2005b). Light-induced structural changes of apoprotein and chromophore in the sensor of blue light using FAD (BLUF) domain of AppA for a signaling state. *Biochemistry* 44: 1215–1224.
- Masuda, S., Hasegawa, K. and Ono, T. (2005c). Tryptophan at position 104 is involved in transforming light signal into changes of beta-sheet structure for the signaling state in the BLUF domain of AppA. *Plant & cell physiology* 46: 1894–1901.
- Masuda, S., Tomida, Y., Ohta, H. and Takamiya, K.-I. (2007). The critical role of a hydrogen bond between Gln63 and Trp104 in the blue-light sensing BLUF domain that controls AppA activity. *Journal of molecular biology* 368: 1223–1230.
- Mathes, T. and Götze, J.P. (2015). A proposal for a dipole-generated BLUF domain mechanism. *Frontiers in molecular biosciences* 2: 62.

- Mathes, T., van Stokkum, I.H.M., Bonetti, C., Hegemann, P. and Kennis, J.T.M. (2011). The hydrogen-bond switch reaction of the Blrb Bluf domain of *Rhodobacter sphaeroides*. *The journal of physical chemistry. B* 115: 7963–7971.
- Mehrabi, P., Müller-Werkmeister, H.M., Leimkohl, J.P., Schikora, H., Ninkovic, J., Krivokuca, S., Andriček, L., Epp, S.W., Sherrell, D., Owen, R.L., Pearson, A.R., Tellkamp, F., Schulz, E.C. and Miller, R.J.D. (2020). The HARE chip for efficient time-resolved serial synchrotron crystallography. *Journal of synchrotron radiation* 27: 360–370.
- Mehrabi, P., Schulz, E.C., Dsouza, R., Müller-Werkmeister, H.M., Tellkamp, F., Miller, R.J.D. and Pai, E.F. (2019). Time-resolved crystallography reveals allosteric communication aligned with molecular breathing. *Science (New York, N.Y.)* 365: 1167–1170.
- Mehrabi, P., Sung, S., von Stetten, D., Prester, A., Hatton, C.E., Kleine-Döpke, S., Berkes, A., Gore, G., Leimkohl, J.-P., Schikora, H., Kollwe, M., Rohde, H., Wilmanns, M., Tellkamp, F. and Schulz, E.C. (2023). Millisecond cryo-trapping by the spitrobot crystal plunger simplifies time-resolved crystallography. *Nature communications* 14: 2365.
- Melnikov, I., Svensson, O., Bourenkov, G., Leonard, G. and Popov, A. (2018). The complex analysis of X-ray mesh scans for macromolecular crystallography. *Acta Crystallogr D Struct Biol* 74: 355–365.
- Moffat, K. (2001). Time-resolved biochemical crystallography: a mechanistic perspective. *Chemical reviews* 101: 1569–1581.
- Moffat, K. (2014). Time-resolved crystallography and protein design: signalling photoreceptors and optogenetics. *Philosophical transactions of the Royal Society of London. Series B, Biological sciences* 369: 20130568.
- Moffat, K., Szebenyi, D. and Bilderback, D. (1984). X-ray Laue Diffraction from Protein Crystals. *Science (New York, N.Y.)* 223: 1423–1425.
- Möglich, A., Ayers, R.A. and Moffat, K. (2009). Design and signaling mechanism of light-regulated histidine kinases. *Journal of molecular biology* 385: 1433–1444.
- Möglich, A. and Moffat, K. (2007). Structural basis for light-dependent signaling in the dimeric LOV domain of the photosensor YtvA. *Journal of molecular biology* 373: 112–126.

- Monteiro, D.C.F., Amoah, E., Rogers, C. and Pearson, A.R. (2021). Using photocaging for fast time-resolved structural biology studies. *Acta Crystallogr D Struct Biol* 77: 1218–1232.
- Mou, T.-C., Masada, N., Cooper, D.M.F. and Sprang, S.R. (2009). Structural basis for inhibition of mammalian adenylyl cyclase by calcium. *Biochemistry* 48: 3387–3397.
- Mous, S., Gotthard, G., Ehrenberg, D., Sen, S., Weinert, T., Johnson, P.J.M., James, D., Nass, K., Furrer, A., Kekilli, D., Ma, P., Brünle, S., Casadei, C.M., Martiel, I., Dworkowski, F., Gashi, D., Skopintsev, P., Wranik, M., Knopp, G., Panepucci, E., Panneels, V., Cirelli, C., Ozerov, D., Schertler, G.F.X., Wang, M., Milne, C., Standfuss, J., Schapiro, I., Heberle, J. and Nogly, P. (2022). Dynamics and mechanism of a light-driven chloride pump. *Science (New York, N.Y.)* 375: 845–851.
- Mueller, C., Marx, A., Epp, S.W., Zhong, Y., Kuo, A., Balo, A.R., Soman, J., Schotte, F., Lemke, H.T., Owen, R.L., Pai, E.F., Pearson, A.R., Olson, J.S., Anfinrud, P.A., Ernst, O.P. and Dwayne Miller, R.J. (2015). Fixed target matrix for femtosecond time-resolved and in situ serial micro-crystallography. *Structural dynamics (Melville, N.Y.)* 2: 54302.
- Nagahama, T., Suzuki, T., Yoshikawa, S. and Iseki, M. (2007). Functional transplant of photoactivated adenylyl cyclase (PAC) into Aplysia sensory neurons. *Neuroscience research* 59: 81–88.
- Nagata, T. and Inoue, K. (2021). Rhodopsins at a glance. *Journal of cell science* 134.
- Nagel, G., Szellas, T., Huhn, W., Kateriya, S., Adeishvili, N., Berthold, P., Ollig, D., Hegemann, P. and Bamberg, E. (2003). Channelrhodopsin-2, a directly light-gated cation-selective membrane channel. *Proceedings of the National Academy of Sciences of the United States of America* 100: 13940–13945.
- Nakasone, Y., Murakami, H., Tokonami, S., Oda, T. and Terazima, M. (2023). Time-resolved study on signaling pathway of photoactivated adenylate cyclase and its nonlinear optical response. *The Journal of biological chemistry* 299: 105285.
- New England Biolabs. *NEBuilder Assembly Tool*.
- Oberthuer, D., Knoška, J., Wiedorn, M.O., Beyerlein, K.R., Bushnell, D.A., Kovaleva, E.G., Heymann, M., Gumprecht, L., Kirian, R.A., Barty, A., Mariani, V., Tolstikova, A., Adriano, L., Awel, S., Barthelmess, M., Dörner, K., Xavier, P.L., Yefanov, O., James, D.R., Nelson, G.,

- Wang, D., Calvey, G., Chen, Y., Schmidt, A., Szczepek, M., Frielingsdorf, S., Lenz, O., Snell, E., Robinson, P.J., Šarler, B., Belšak, G., Maček, M., Wilde, F., Aquila, A., Boutet, S., Liang, M., Hunter, M.S., Scheerer, P., Lipscomb, J.D., Weierstall, U., Kornberg, R.D., Spence, J.C.H., Pollack, L., Chapman, H.N. and Bajt, S. (2017). Double-flow focused liquid injector for efficient serial femtosecond crystallography. *Scientific reports* 7: 44628.
- Ohki, M., Sato-Tomita, A., Matsunaga, S., Iseki, M., Tame, J.R.H., Shibayama, N. and Park, S.-Y. (2017). Molecular mechanism of photoactivation of a light-regulated adenylate cyclase. *Proceedings of the National Academy of Sciences of the United States of America* 114: 8562–8567.
- Ohki, M., Sugiyama, K., Kawai, F., Tanaka, H., Nihei, Y., Unzai, S., Takebe, M., Matsunaga, S., Adachi, S.-I., Shibayama, N., Zhou, Z., Koyama, R., Ikegaya, Y., Takahashi, T., Tame, J.R.H., Iseki, M. and Park, S.-Y. (2016). Structural insight into photoactivation of an adenylate cyclase from a photosynthetic cyanobacterium. *Proceedings of the National Academy of Sciences of the United States of America* 113: 6659–6664.
- Okajima, K., Fukushima, Y., Suzuki, H., Kita, A., Ochiai, Y., Katayama, M., Shibata, Y., Miki, K., Noguchi, T., Itoh, S. and Ikeuchi, M. (2006). Fate determination of the flavin photoreceptions in the cyanobacterial blue light receptor TePixD (Tll0078). *Journal of molecular biology* 363: 10–18.
- Oscarsson, M., Beteva, A., Flot, D., Gordon, E., Guijarro, M., Leonard, G., McSweeney, S., Monaco, S., Mueller-Dieckmann, C., Nanao, M., Nurizzo, D., Popov, A.N., von Stetten, D., Svensson, O., Rey-Bakaikoa, V., Chado, I., Chavas, L.M.G., Gadea, L., Gourhant, P., Isabet, T., Legrand, P., Savko, M., Sirigu, S., Shepard, W., Thompson, A., Mueller, U., Nan, J., Eguiraun, M., Bolmsten, F., Nardella, A., Milàn-Otero, A., Thunnissen, M., Hellmig, M., Kastner, A., Schmuckermaier, L., Gerlach, M., Feiler, C., Weiss, M.S., Bowler, M.W., Gobbo, A., Papp, G., Sinoir, J., McCarthy, A.A., Karpics, I., Nikolova, M., Bourenkov, G., Schneider, T., Andreu, J., Cuní, G., Juanhuix, J., Boer, R., Fogh, R., Keller, P., Flensburg, C., Paciorek, W., Vonrhein, C., Bricogne, G. and Sanctis, D. de (2019). MXCuBE2: the dawn of MXCuBE Collaboration. *Journal of synchrotron radiation* 26: 393–405.
- Owen, R.L., Sanctis, D. de, Pearson, A.R. and Beale, J.H. (2023). A standard descriptor for fixed-target serial crystallography. *Acta Crystallogr D Struct Biol* 79: 668–672.

- Pace, C.N., Vajdos, F., Fee, L., Grimsley, G. and Gray, T. (1995). How to measure and predict the molar absorption coefficient of a protein. *Protein science : a publication of the Protein Society* 4: 2411–2423.
- Pal, D. and Chakrabarti, P. (2001). Non-hydrogen bond interactions involving the methionine sulfur atom. *Journal of biomolecular structure & dynamics* 19: 115–128.
- Palczewski, K. (2006). G protein-coupled receptor rhodopsin. *Annual review of biochemistry* 75: 743–767.
- Palczewski, K., Kumasaka, T., Hori, T., Behnke, C.A., Motoshima, H., Fox, B.A., Le Trong, I., Teller, D.C., Okada, T., Stenkamp, R.E., Yamamoto, M. and Miyano, M. (2000). Crystal structure of rhodopsin: A G protein-coupled receptor. *Science (New York, N.Y.)* 289: 739–745.
- Palmer, G., Kellert, M., Wang, J., Emons, M., Wegner, U., Kane, D., Pallas, F., Jezynski, T., Venkatesan, S., Rompotis, D., Brambrink, E., Monoszlai, B., Jiang, M., Meier, J., Kruse, K., Pergament, M. and Lederer, M.J. (2019). Pump-probe laser system at the FXE and SPB/SFX instruments of the European X-ray Free-Electron Laser Facility. *Journal of synchrotron radiation* 26: 328–332.
- Pande, K., Hutchison, C.D.M., Groenhof, G., Aquila, A., Robinson, J.S., Tenboer, J., Basu, S., Boutet, S., DePonte, D.P., Liang, M., White, T.A., Zatsepin, N.A., Yefanov, O., Morozov, D., Oberthuer, D., Gati, C., Subramanian, G., James, D., Zhao, Y., Koralek, J., Brayshaw, J., Kupitz, C., Conrad, C., Roy-Chowdhury, S., Coe, J.D., Metz, M., Xavier, P.L., Grant, T.D., Koglin, J.E., Ketawala, G., Fromme, R., Šrajter, V., Henning, R., Spence, J.C.H., Ourmazd, A., Schwander, P., Weierstall, U., Frank, M., Fromme, P., Barty, A., Chapman, H.N., Moffat, K., van Thor, J.J. and Schmidt, M. (2016). Femtosecond structural dynamics drives the trans/cis isomerization in photoactive yellow protein. *Science (New York, N.Y.)* 352: 725–729.
- Pandey, S., Bean, R., Sato, T., Poudyal, I., Bielecki, J., Cruz Villarreal, J., Yefanov, O., Mariani, V., White, T.A., Kupitz, C., Hunter, M., Abdellatif, M.H., Bajt, S., Bondar, V., Echelmeier, A., Doppler, D., Emons, M., Frank, M., Fromme, R., Gevorkov, Y., Giovanetti, G., Jiang, M., Kim, D., Kim, Y., Kirkwood, H., Klimovskaia, A., Knoska, J., Koua, F.H.M., Letrun, R., Lisova, S., Maia, L., Mazalova, V., Meza, D., Michelat, T., Ourmazd, A., Palmer, G., Ramilli, M., Schubert, R., Schwander, P., Silenzi, A., Sztuk-Dambietz, J., Tolstikova, A., Chapman,

- H.N., Ros, A., Barty, A., Fromme, P., Mancuso, A.P. and Schmidt, M. (2020). Time-resolved serial femtosecond crystallography at the European XFEL. *Nature methods* 17: 73–78.
- Panneels, V., Wu, W., Tsai, C.-J., Nogly, P., Rheinberger, J., Jaeger, K., Cicchetti, G., Gati, C., Kick, L.M., Sala, L., Capitani, G., Milne, C., Padeste, C., Pedrini, B., Li, X.-D., Standfuss, J., Abela, R. and Schertler, G. (2015). Time-resolved structural studies with serial crystallography: A new light on retinal proteins. *Structural dynamics (Melville, N.Y.)* 2: 41718.
- Park, S.-Y. and Tame, J.R.H. (2017). Seeing the light with BLUF proteins. *Biophysical reviews* 9: 169–176.
- Pearson, A.R. and Mehrabi, P. (2020). Serial synchrotron crystallography for time-resolved structural biology. *Current opinion in structural biology* 65: 168–174.
- Penzkofer, A., Kateriya, S. and Hegemann, P. (2016). Photodynamics of the optogenetic BLUF coupled photoactivated adenylyl cyclases (PACs). *Dyes and Pigments* 135: 102–112.
- Penzkofer, A., Stierl, M., Hegemann, P. and Kateriya, S. (2011). Photo-dynamics of the BLUF domain containing soluble adenylylase (nPAC) from the amoeboflagellate *Naegleria gruberi* NEG-M strain. *Chemical Physics* 387: 25–38.
- Penzkofer, A., Tanwar, M., Veetil, S.K. and Kateriya, S. (2014). Photo-dynamics of photoactivated adenylyl cyclase LiPAC from the spirochete bacterium *Leptonema illini* strain 3055 T. *Trends in Applied Spectroscopy* 11.
- Penzkofer, A., Tanwar, M., Veetil, S.K. and Kateriya, S. (2015). Photo-dynamics of photoactivated adenylyl cyclase TpPAC from the spirochete bacterium *Turneriella parva* strain H(T). *Journal of photochemistry and photobiology. B, Biology* 153: 90–102.
- Pergament, M., Palmer, G., Kellert, M., Kruse, K., Wang, J., Wissmann, L., Wegner, U., Emons, M., Kane, D., Priebe, G., Venkatesan, S., Jezynski, T., Pallas, F. and Lederer, M.J. (2016). Versatile optical laser system for experiments at the European X-ray free-electron laser facility. *Optics express* 24: 29349–29359.
- Powell, H.R., Johnson, O. and Leslie, A.G.W. (2013). Autoindexing diffraction images with iMosflm. *Acta crystallographica. Section D, Biological crystallography* 69: 1195–1203.

- Pudasaini, A., El-Arab, K.K. and Zoltowski, B.D. (2015). LOV-based optogenetic devices: light-driven modules to impart photoregulated control of cellular signaling. *Frontiers in molecular biosciences* 2: 18.
- Putnam, C.D., Hammel, M., Hura, G.L. and Tainer, J.A. (2007). X-ray solution scattering (SAXS) combined with crystallography and computation: defining accurate macromolecular structures, conformations and assemblies in solution. *Quarterly reviews of biophysics* 40: 191–285.
- Qing, G., Ma, L.-C., Khorchid, A., Swapna, G.V.T., Mal, T.K., Takayama, M.M., Xia, B., Phadtare, S., Ke, H., Acton, T., Montelione, G.T., Ikura, M. and Inouye, M. (2004). Cold-shock induced high-yield protein production in *Escherichia coli*. *Nature biotechnology* 22: 877–882.
- Rockwell, N.C. and Lagarias, J.C. (2010). A brief history of phytochromes. *Chemphyschem : a European journal of chemical physics and physical chemistry* 11: 1172–1180.
- Rredhi, A., Petersen, J., Wagner, V., Vuong, T., Li, W., Li, W., Schrader, L. and Mittag, M. (2024). The UV-A Receptor CRY-DASH1 Up- and Downregulates Proteins Involved in Different Plastidial Pathways. *Journal of molecular biology* 436: 168271.
- Ryu, M.-H., Moskvina, O.V., Siltberg-Liberles, J. and Gomelsky, M. (2010). Natural and engineered photoactivated nucleotidyl cyclases for optogenetic applications. *The Journal of biological chemistry* 285: 41501–41508.
- Sadeghian, K., Bocola, M. and Schütz, M. (2008). A conclusive mechanism of the photoinduced reaction cascade in blue light using flavin photoreceptors. *Journal of the American Chemical Society* 130: 12501–12513.
- Salvadori, G., Mazzeo, P., Accomasso, D., Cupellini, L. and Mennucci, B. (2024). Deciphering Photoreceptors Through Atomistic Modeling from Light Absorption to Conformational Response. *Journal of molecular biology* 436: 168358.
- Savvides, S.N., Raghunathan, S., Fütterer, K., Kozlov, A.G., Lohman, T.M. and Waksman, G. (2004). The C-terminal domain of full-length *E. coli* SSB is disordered even when bound to DNA. *Protein science : a publication of the Protein Society* 13: 1942–1947.

- Schmidt, M. (2020). Reaction Initiation in Enzyme Crystals by Diffusion of Substrate. *Crystals* 10: 116.
- Schmidt, M. (2023). Practical considerations for the analysis of time-resolved x-ray data. *Structural dynamics (Melville, N.Y.)* 10: 44303.
- Schmidt, M., Graber, T., Henning, R. and Srajer, V. (2010). Five-dimensional crystallography. *Acta crystallographica. Section A, Foundations of crystallography* 66: 198–206.
- Schröder-Lang, S., Schwärzel, M., Seifert, R., Strünker, T., Kateriya, S., Looser, J., Watanabe, M., Kaupp, U.B., Hegemann, P. and Nagel, G. (2007). Fast manipulation of cellular cAMP level by light in vivo. *Nature methods* 4: 39–42.
- Schrödinger, L. and DeLano, W. (2020). *PyMOL*.
- Schroeder, C., Werner, K., Otten, H., Krätzig, S., Schwalbe, H. and Essen, L.-O. (2008). Influence of a joining helix on the BLUF domain of the YcgF photoreceptor from *Escherichia coli*. *Chembiochem : a European journal of chemical biology* 9: 2463–2473.
- Schulz, E.C., Mehrabi, P., Müller-Werkmeister, H.M., Tellkamp, F., Jha, A., Stuart, W., Persch, E., Gasparo, R. de, Diederich, F., Pai, E.F. and Miller, R.J.D. (2018). The hit-and-return system enables efficient time-resolved serial synchrotron crystallography. *Nature methods* 15: 901–904.
- Schulz, E.C., Yorke, B.A., Pearson, A.R. and Mehrabi, P. (2022). Best practices for time-resolved serial synchrotron crystallography. *Acta Crystallogr D Struct Biol* 78: 14–29.
- Sierra, R.G., Weierstall, U., Oberthuer, D., Sugahara, M., Nango, E., Iwata, S. and Meents, A. (2018). In *X-ray Free Electron Lasers*, Boutet, S., Fromme, P. and Hunter, M.S. (Eds.), Springer International Publishing, Cham, pp. 109–184.
- Steebhorn, C., Litvin, T.N., Levin, L.R., Buck, J. and Wu, H. (2005). Bicarbonate activation of adenylyl cyclase via promotion of catalytic active site closure and metal recruitment. *Nature structural & molecular biology* 12: 32–37.
- Stelling, A.L., Ronayne, K.L., Nappa, J., Tonge, P.J. and Meech, S.R. (2007). Ultrafast structural dynamics in BLUF domains: transient infrared spectroscopy of AppA and its mutants. *Journal of the American Chemical Society* 129: 15556–15564.

- Stierl, M., Penzkofer, A., Kennis, J.T.M., Hegemann, P. and Mathes, T. (2014). Key Residues for the Light Regulation of the Blue Light-Activated Adenylyl Cyclase from *Beggiatoa* sp. *Biochemistry* 53: 5121–5130.
- Stierl, M., Stumpf, P., Udvari, D., Gueta, R., Hagedorn, R., Losi, A., Gärtner, W., Petereit, L., Efetova, M., Schwarzel, M., Oertner, T.G., Nagel, G. and Hegemann, P. (2011). Light modulation of cellular cAMP by a small bacterial photoactivated adenylyl cyclase, bPAC, of the soil bacterium *Beggiatoa*. *The Journal of biological chemistry* 286: 1181–1188.
- Strickland, D., Yao, X., Gawlak, G., Rosen, M.K., Gardner, K.H. and Sosnick, T.R. (2010). Rationally improving LOV domain-based photoswitches. *Nature methods* 7: 623–626.
- Svergun, D.I. (1992). Determination of the regularization parameter in indirect-transform methods using perceptual criteria. *J Appl Crystallogr* 25: 495–503.
- Svergun, D.I. (1999). Restoring low resolution structure of biological macromolecules from solution scattering using simulated annealing. *Biophysical journal* 76: 2879–2886.
- Svergun, D.I., Feigin, L.A. and Taylor, G.W. (1987). *Structure analysis by small-angle x-ray and neutron scattering*, Springer Science+Business Media, LLC, New York.
- Tanwar, M., Sharma, K., Moar, P. and Kateriya, S. (2018). Biochemical Characterization of the Engineered Soluble Photoactivated Guanylate Cyclases from Microbes Expands Optogenetic Tools. *Applied biochemistry and biotechnology* 185: 1014–1028.
- Terwilliger, T.C. and Berendzen, J. (1995). Difference refinement: obtaining differences between two related structures. *Acta crystallographica. Section D, Biological crystallography* 51: 609–618.
- Tesmer, J.J.G., Sunahara, R.K., Johnson, R.A., Gosselin, G., Gilman, A.G. and Sprang, S.R. (1999). Two-Metal-Ion Catalysis in Adenylyl Cyclase. *Science* 285: 756–760.
- Toh, K.C., van Stokkum, I.H.M., Hendriks, J., Alexandre, M.T.A., Arents, J.C., Perez, M.A., van Grondelle, R., Hellingwerf, K.J. and Kennis, J.T.M. (2008). On the signaling mechanism and the absence of photoreversibility in the AppA BLUF domain. *Biophysical journal* 95: 312–321.

- Tokonami, S., Onose, M., Nakasone, Y. and Terazima, M. (2022). Slow Conformational Changes of Blue Light Sensor BLUF Proteins in Milliseconds. *Journal of the American Chemical Society* 144: 4080–4090.
- Tolentino Collado, J., Bodis, E., Pasitka, J., Szucs, M., Fekete, Z., Kis-Bicskei, N., Telek, E., Pozsonyi, K., Kapetanaki, S.M., Greetham, G., Tonge, P.J., Meech, S.R. and Lukacs, A. (2024). Single Amino Acid Mutation Decouples Photochemistry of the BLUF Domain from the Enzymatic Function of OaPAC and Drives the Enzyme to a Switched-on State. *Journal of molecular biology* 436: 168312.
- Tully, M.D., Kieffer, J., Brennich, M.E., Cohen Aberdam, R., Florial, J.B., Hutin, S., Oscarsson, M., Beteva, A., Popov, A., Moussaoui, D., Theveneau, P., Papp, G., Gigmès, J., Cipriani, F., McCarthy, A., Zubieta, C., Mueller-Dieckmann, C., Leonard, G. and Pernot, P. (2023). BioSAXS at European Synchrotron Radiation Facility - Extremely Brilliant Source: BM29 with an upgraded source, detector, robot, sample environment, data collection and analysis software. *Journal of synchrotron radiation* 30: 258–266.
- Turkot, O., Dall'Antonia, F., Bean, R.J., E, J., Fangohr, H., Ferreira de Lima, D.E., Kantamneni, S., Kirkwood, H., Koua, F., Mancuso, A.P., Melo, D., Round, A., Sobolev, E., Wijn, R. de, Wrigley, J.J. and Gelisio, L., p. 45.
- Udvarhelyi, A. and Domratcheva, T. (2011). Photoreaction in BLUF receptors: proton-coupled electron transfer in the flavin-Gln-Tyr system. *Photochemistry and photobiology* 87: 554–563.
- Udvarhelyi, A. and Domratcheva, T. (2013). Glutamine rotamers in BLUF photoreceptors: a mechanistic reappraisal. *The journal of physical chemistry. B* 117: 2888–2897.
- Ujfalusi-Pozsonyi, K., Bódis, E., Nyitrai, M., Kengyel, A., Telek, E., Pécsi, I., Fekete, Z., Varnyuné Kis-Bicskei, N., Mas, C., Moussaoui, D., Pernot, P., Tully, M.D., Weik, M., Schirò, G., Kapetanaki, S.M. and Lukács, A. (2024). ATP-dependent conformational dynamics in a photoactivated adenylate cyclase revealed by fluorescence spectroscopy and small-angle X-ray scattering. *Communications biology* 7: 147.

- Unno, M., Kikuchi, S. and Masuda, S. (2010). Structural refinement of a key tryptophan residue in the BLUF photoreceptor AppA by ultraviolet resonance Raman spectroscopy. *Biophysical journal* 98: 1949–1956.
- Unno, M., Masuda, S., Ono, T. and Yamauchi, S. (2006). Orientation of a key glutamine residue in the BLUF domain from AppA revealed by mutagenesis, spectroscopy, and quantum chemical calculations. *Journal of the American Chemical Society* 128: 5638–5639.
- Unno, M., Sano, R., Masuda, S., Ono, T. and Yamauchi, S. (2005). Light-induced structural changes in the active site of the BLUF domain in AppA by Raman spectroscopy. *The journal of physical chemistry. B* 109: 12620–12626.
- Ursby, T. and Bourgeois, D. (1997). Improved Estimation of Structure-Factor Difference Amplitudes from Poorly Accurate Data. *Acta Crystallogr A Found Crystallogr* 53: 564–575.
- Vakili, M., Bielecki, J., Knoška, J., Otte, F., Han, H., Kloos, M., Schubert, R., Delmas, E., Mills, G., Wijn, R. de, Letrun, R., Dold, S., Bean, R., Round, A., Kim, Y., Lima, F.A., Dörner, K., Valerio, J., Heymann, M., Mancuso, A.P. and Schulz, J. (2022). 3D printed devices and infrastructure for liquid sample delivery at the European XFEL. *Journal of synchrotron radiation* 29: 331–346.
- Valsecchi, I., Guittard-Crilat, E., Maldiney, R., Habricot, Y., Lignon, S., Lebrun, R., Miginiac, E., Ruelland, E., Jeannette, E. and Lebreton, S. (2013). The intrinsically disordered C-terminal region of Arabidopsis thaliana TCP8 transcription factor acts both as a transactivation and self-assembly domain. *Molecular bioSystems* 9: 2282–2295.
- van der Horst, M.A. and Hellingwerf, K.J. (2004). Photoreceptor proteins, "star actors of modern times": a review of the functional dynamics in the structure of representative members of six different photoreceptor families. *Accounts of chemical research* 37: 13–20.
- Vide, U., Kasapović, D., Fuchs, M., Heimböck, M.P., Totaro, M.G., Zenzmaier, E. and Winkler, A. (2023). Illuminating the inner workings of a natural protein switch: Blue-light sensing in LOV-activated diguanylate cyclases. *Science advances* 9: eadh4721.
- Volkov, V.V. and Svergun, D.I. (2003). Uniqueness of ab initio shape determination in small-angle scattering. *J Appl Crystallogr* 36: 860–864.

- von Stetten, D., Giraud, T., Carpentier, P., Sever, F., Terrien, M., Dobias, F., Juers, D.H., Flot, D., Mueller-Dieckmann, C., Leonard, G.A., Sanctis, D. de and Royant, A. (2015). In crystallo optical spectroscopy (icOS) as a complementary tool on the macromolecular crystallography beamlines of the ESRF. *Acta crystallographica. Section D, Biological crystallography* 71: 15–26.
- Weickert, M.J., Doherty, D.H., Best, E.A. and Olins, P.O. (1996). Optimization of heterologous protein production in Escherichia coli. *Current Opinion in Biotechnology* 7: 494–499.
- Weierstall, U. (2014). Liquid sample delivery techniques for serial femtosecond crystallography. *Philosophical transactions of the Royal Society of London. Series B, Biological sciences* 369: 20130337.
- Weinert, T., Skopintsev, P., James, D., Dworkowski, F., Panepucci, E., Kekilli, D., Furrer, A., Brünle, S., Mous, S., Ozerov, D., Nogly, P., Wang, M. and Standfuss, J. (2019). Proton uptake mechanism in bacteriorhodopsin captured by serial synchrotron crystallography. *Science (New York, N.Y.)* 365: 61–65.
- Weissenberger, S., Schultheis, C., Liewald, J.F., Erbguth, K., Nagel, G. and Gottschalk, A. (2011). PAC α -an optogenetic tool for in vivo manipulation of cellular cAMP levels, neurotransmitter release, and behavior in Caenorhabditis elegans. *Journal of neurochemistry* 116: 616–625.
- Whitby, L.G. (1953). A new method for preparing flavin-adenine dinucleotide. *The Biochemical journal* 54: 437–442.
- White, T.A. (2019). Processing serial crystallography data with CrystFEL: a step-by-step guide. *Acta Crystallogr D Struct Biol* 75: 219–233.
- White, T.A., Kirian, R.A., Martin, A.V., Aquila, A., Nass, K., Barty, A. and Chapman, H.N. (2012). CrystFEL : a software suite for snapshot serial crystallography. *J Appl Crystallogr* 45: 335–341.
- Wijn, R. de, Melo, D.V.M., Koua, F.H.M. and Mancuso, A.P. (2022). Potential of Time-Resolved Serial Femtosecond Crystallography Using High Repetition Rate XFEL Sources. *Applied Sciences* 12: 2551.

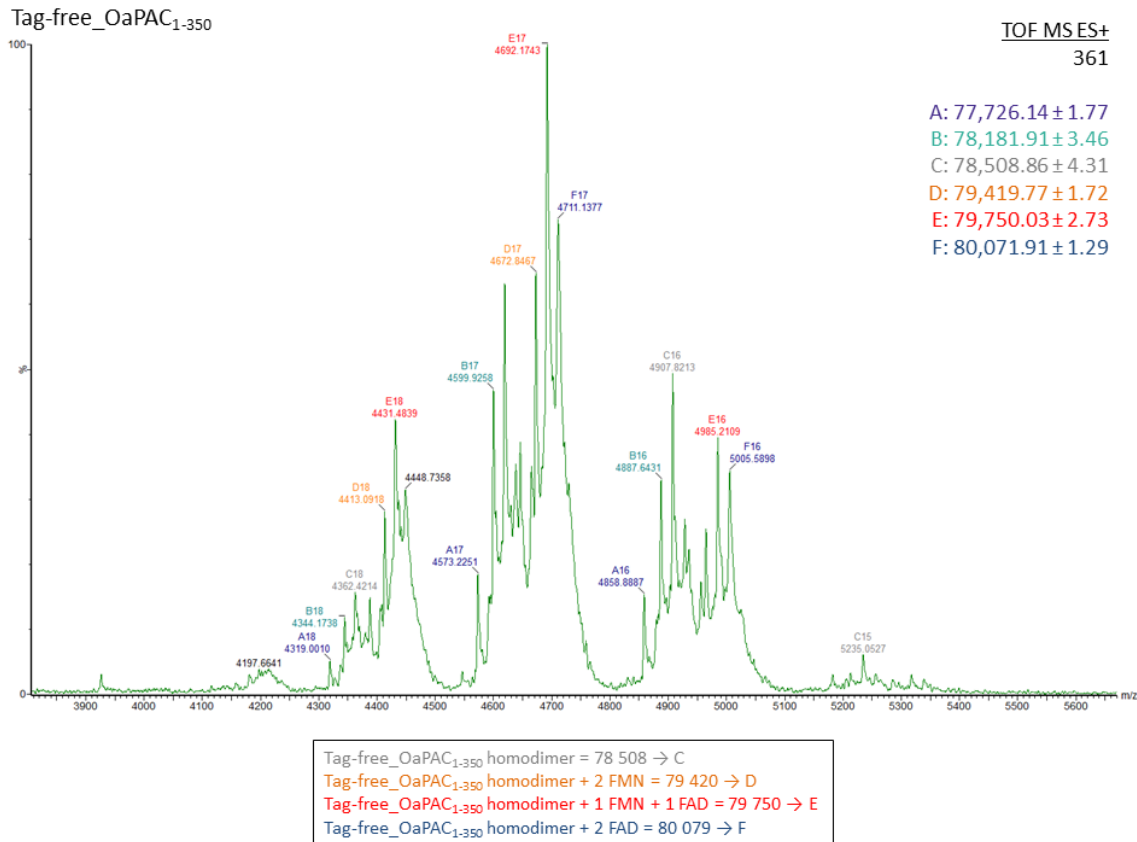
- Wilkins, M.R., Gasteiger, E., Bairoch, A., Sanchez, J.C., Williams, K.L., Appel, R.D. and Hochstrasser, D.F. (1999). Protein identification and analysis tools in the ExPASy server. *Methods in molecular biology (Clifton, N.J.)* 112: 531–552.
- Wilmot, C.M. (2003). Oxygen activation in a copper-containing amine oxidase. *Biochemical Society Transactions* 31: 493–496.
- Winkler, A., Heintz, U., Lindner, R., Reinstein, J., Shoeman, R.L. and Schlichting, I. (2013). A ternary AppA-PpsR-DNA complex mediates light regulation of photosynthesis-related gene expression. *Nature structural & molecular biology* 20: 859–867.
- Wranik, M., Weinert, T., Slavov, C., Masini, T., Furrer, A., Gaillard, N., Gioia, D., Ferrarotti, M., James, D., Glover, H., Carrillo, M., Kekilli, D., Stipp, R., Skopintsev, P., Brünle, S., Mühlethaler, T., Beale, J., Gashi, D., Nass, K., Ozerov, D., Johnson, P.J.M., Cirelli, C., Bacellar, C., Braun, M., Wang, M., Dworkowski, F., Milne, C., Cavalli, A., Wachtveitl, J., Steinmetz, M.O. and Standfuss, J. (2023). Watching the release of a photopharmacological drug from tubulin using time-resolved serial crystallography. *Nature communications* 14: 903.
- Wright, P.E. and Dyson, H.J. (1999). Intrinsically unstructured proteins: re-assessing the protein structure-function paradigm. *Journal of molecular biology* 293: 321–331.
- Wu, Q. and Gardner, K.H. (2009). Structure and insight into blue light-induced changes in the BlrP1 BLUF domain. *Biochemistry* 48: 2620–2629.
- Wu, Y.I., Frey, D., Lungu, O.I., Jaehrig, A., Schlichting, I., Kuhlman, B. and Hahn, K.M. (2009). A genetically encoded photoactivatable Rac controls the motility of living cells. *Nature* 461: 104–108.
- Xing, J., Gumerov, V.M. and Zhulin, I.B. (2022). Photoactive Yellow Protein Represents a Distinct, Evolutionarily Novel Family of PAS Domains. *Journal of bacteriology* 204: e0030022.
- Yamada, D. and Kandori, H. (2014). In *Flavins and Flavoproteins*, Vol. 1146, Weber, S. and Schleicher, E. (Eds.), Springer New York, New York, NY, pp. 361–376.

- Yang, J., Yun, S. and Park, W. (2023). Blue Light Sensing BlsA-Mediated Modulation of Meropenem Resistance and Biofilm Formation in *Acinetobacter baumannii*. *mSystems* 8: e0089722.
- Yasukawa, H., Sato, A., Kita, A., Kodaira, K.-I., Iseki, M., Takahashi, T., Shibusawa, M., Watanabe, M. and Yagita, K. (2013). Identification of photoactivated adenylyl cyclases in *Naegleria australiensis* and BLUF-containing protein in *Naegleria fowleri*. *The Journal of general and applied microbiology* 59: 361–369.
- Yuan, H., Anderson, S., Masuda, S., Dragnea, V., Moffat, K. and Bauer, C. (2006). Crystal structures of the *Synechocystis* photoreceptor Slr1694 reveal distinct structural states related to signaling. *Biochemistry* 45: 12687–12694.
- Yuan, H., Dragnea, V., Wu, Q., Gardner, K.H. and Bauer, C.E. (2011). Mutational and structural studies of the PixD BLUF output signal that affects light-regulated interactions with PixE. *Biochemistry* 50: 6365–6375.
- Zhang, H., Hu, X., Mao, X. and Wang, Y. (2009). Optimization of culture conditions for recombinant dextransucrase expression. *Sheng wu gong cheng xue bao = Chinese journal of biotechnology* 25: 2022–2028.
- Zhang, Z.-X., Nong, F.-T., Wang, Y.-Z., Yan, C.-X., Gu, Y., Song, P. and Sun, X.-M. (2022). Strategies for efficient production of recombinant proteins in *Escherichia coli*: alleviating the host burden and enhancing protein activity. *Microbial cell factories* 21: 191.
- Zhou, Z., Chen, Z., Kang, X.-W., Zhou, Y., Wang, B., Tang, S., Zou, S., Zhang, Y., Hu, Q., Bai, F., Ding, B. and Zhong, D. (2022). The nature of proton-coupled electron transfer in a blue light using flavin domain. *Proceedings of the National Academy of Sciences of the United States of America* 119: e2203996119.
- Zirak, P., Penzkofer, A., Schiereis, T., Hegemann, P., Jung, A. and Schlichting, I. (2005). Absorption and fluorescence spectroscopic characterization of BLUF domain of AppA from *Rhodobacter sphaeroides*. *Chemical Physics* 315: 142–154.
- Zirak, P., Penzkofer, A., Schiereis, T., Hegemann, P., Jung, A. and Schlichting, I. (2006). Photodynamics of the small BLUF protein BlrB from *Rhodobacter sphaeroides*. *Journal of photochemistry and photobiology. B, Biology* 83: 180–194.

Zoltowski, B.D. and Gardner, K.H. (2011). Tripping the light fantastic: blue-light photoreceptors as examples of environmentally modulated protein-protein interactions. *Biochemistry* 50: 4–16.

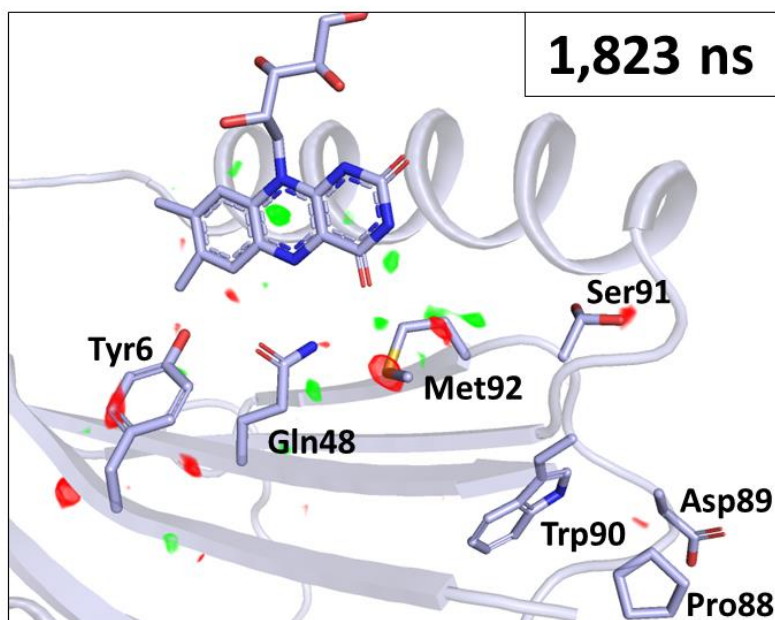
A. Appendices

A.1. Appendix Figures



Appendix Figure 1: Mass spectrometry analysis of Tag-free_OaPAC₁₋₃₅₀ in solution.

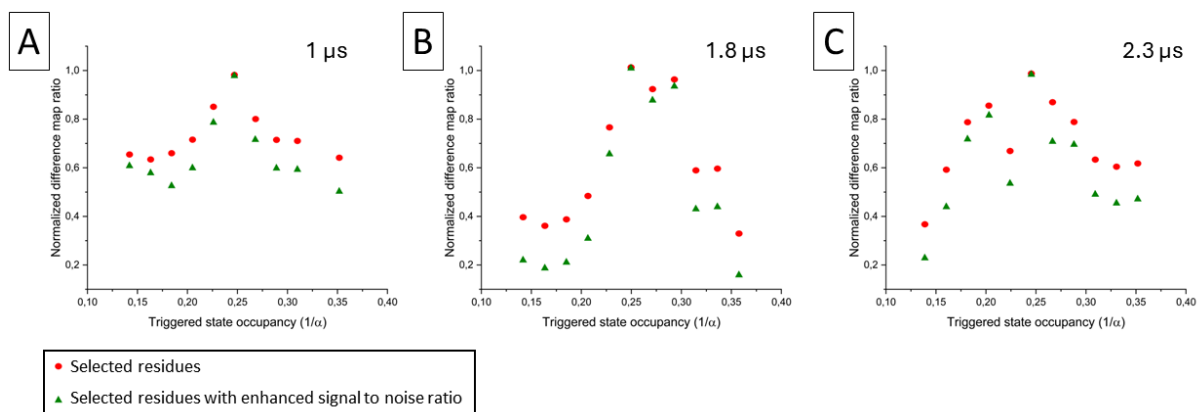
The three dominant populations correspond to OaPAC₁₋₃₅₀ bound to one FMN and one FAD (E), two FADs (F) and two FMNs (D). The remaining peaks correspond to apo OaPAC₁₋₃₅₀ (C) and potentially OaPAC₁₋₃₅₀ with few deleted residues (A-B).



Appendix Figure 2: BLUF photoexcitation after 1,823 ns delay revealed by TR-SFX.

$F_{o-light} - F_{o-dark}$ difference maps contoured at +3 rmsd (green) and -3 rmsd (red) reveal initial changes around the flavin chromophore after excitation. The dark model (light blue) is shown as cartoon and involved amino acids in stick representation.

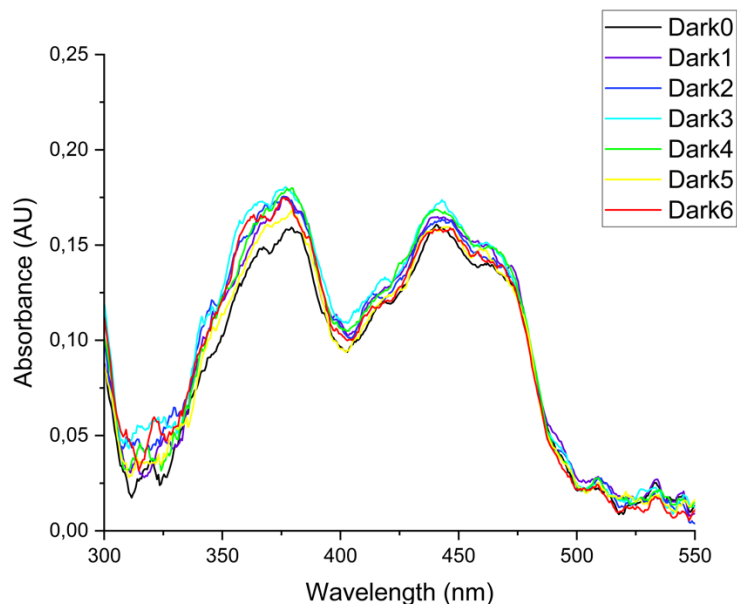
Figure prepared by the PyMOL Molecular Graphics System, Version 2.0 Schrödinger, LLC (Schrödinger and DeLano, 2020).



Appendix Figure 3: Occupancy determination of the light-activated states during TR-SFX experiment using the difference map method.

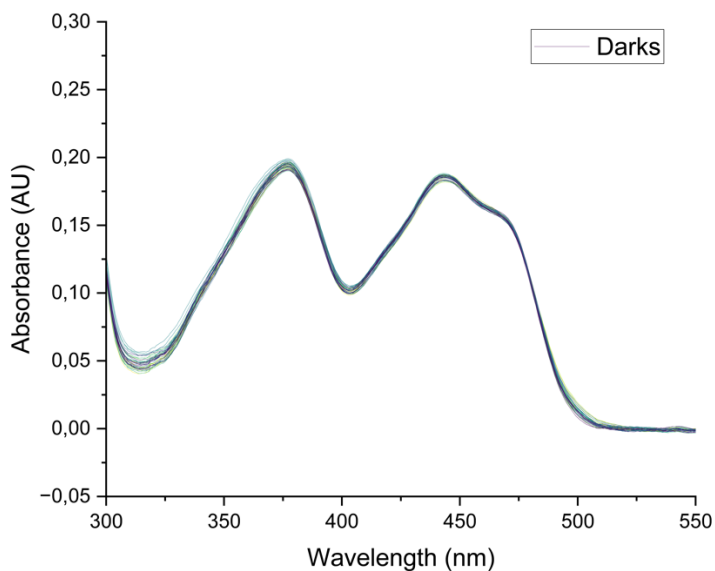
Light excited states estimated for the 1 μ s (A), 1.8 μ s (B) and 2.3 μ s (C) data sets using the difference map method of Xtrapol8 (de Zitter et al., 2022) with selected residues containing the most significant peaks in the difference maps (red circles) and the latter with increased signal to noise ratio (green triangles). The normalized difference map ratio was maximized around 25 % occupancy for each time point.

Figures were created with Origin software version 2024.



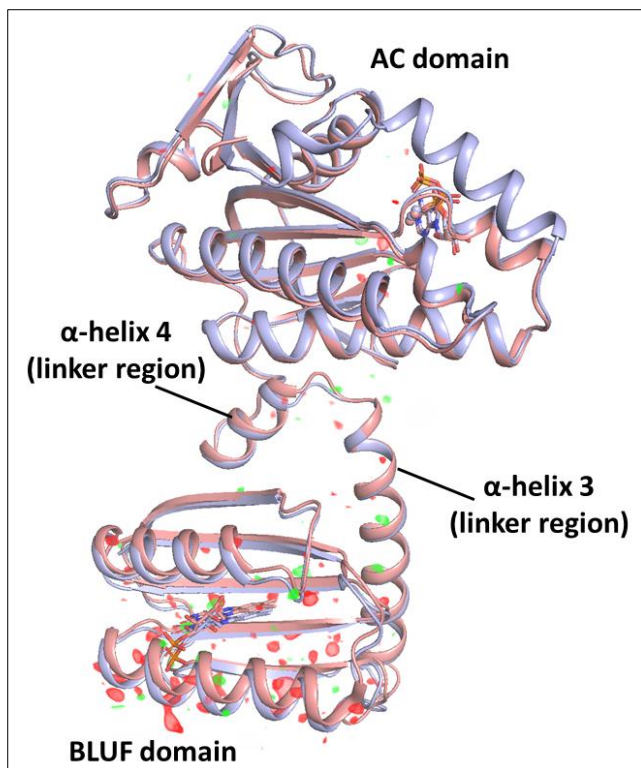
Appendix Figure 4: Bleaching analysis of C222₁ OaPAC₁₋₃₅₀ crystals.

In crystallo optical spectroscopy analysis of OaPAC₁₋₃₅₀ C222₁ crystals after excitation with several laser pulses of 280.3 mJ/cm² fluence. UV-Vis absorption measurements are performed after each photoexcitation and a 1 min delay to enable the decay to the dark state. Even after six independent photoexcitation at 280.3 mJ/cm² (Dark6), the UV-Vis spectrum is matching the initial dark (Dark0), indicating that no bleaching happened. Figures were created with Origin software version 2024.



Appendix Figure 5: Dark spectra of C222₁ OaPAC₁₋₃₅₀ crystals recorded before each subsequent photoexcitation during the time series analysis shown in Figure 28.

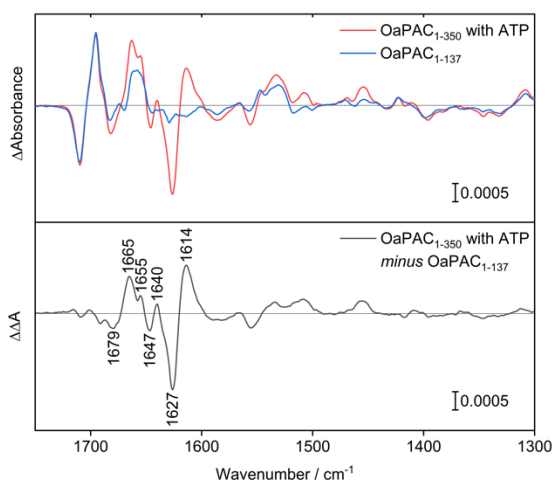
Figures were created with Origin software version 2024.



Appendix Figure 6: Difference electron density map between holo OaPAC dark state at cryogenic temperature and OaPAC 5 s light illuminated cryo-trapped state.

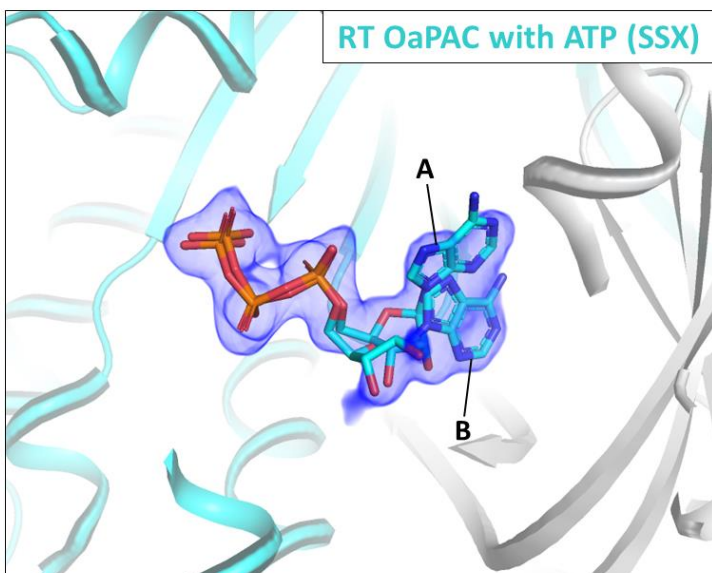
$F_{o-light} - F_{o-dark}$ difference map contoured at +3 rmsd (green) and -3 rmsd (red) was calculated in real space to overcome non-isomorphous data using MatchMaps (Brookner and Hekstra, 2024). The changes are localised in the BLUF domain, and few changes are still visible in the α -helix linker region (α -helices 3 and 4) between OaPAC dark state (light blue) and OaPAC cryo-trapped state (salmon).

Figure prepared by the PyMOL Molecular Graphics System, Version 2.5.4 Schrödinger, LLC (Schrödinger and DeLano, 2020).



Appendix Figure 7: Light-minus-dark FTIR difference spectra of OaPAC₁₋₃₅₀ and OaPAC₁₋₁₃₇ and their double difference spectrum isolating contributions of the AC domain.

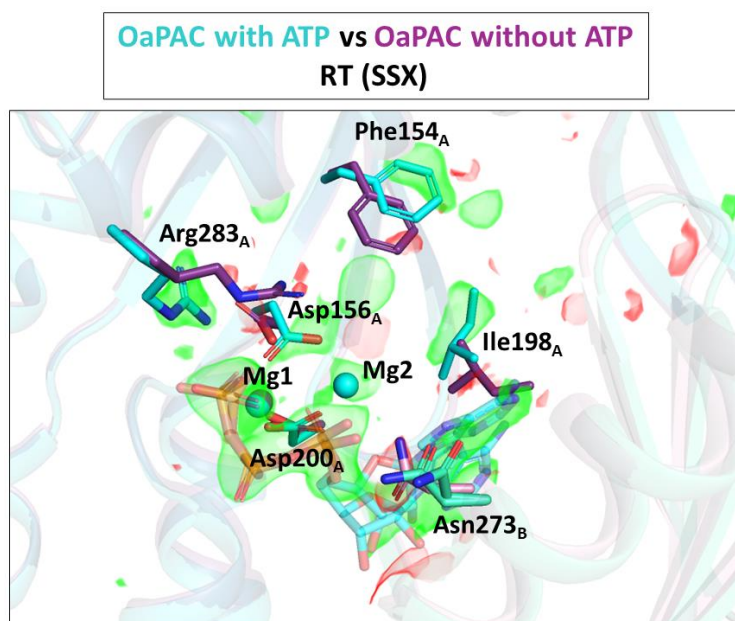
Figure modified from (Chretien et al., 2024).



Appendix Figure 8: ATP binding conformations in OaPAC active site at room-temperature.

Cartoon representation of the structural model of holo OaPAC at room-temperature with one protomer in cyan and the second protomer in grey. ATP binding in two distinct conformations at room-temperature according to the SSX structure is visible without bias, as shown by the F_o-F_c Polder map contoured at 3 rmsd.

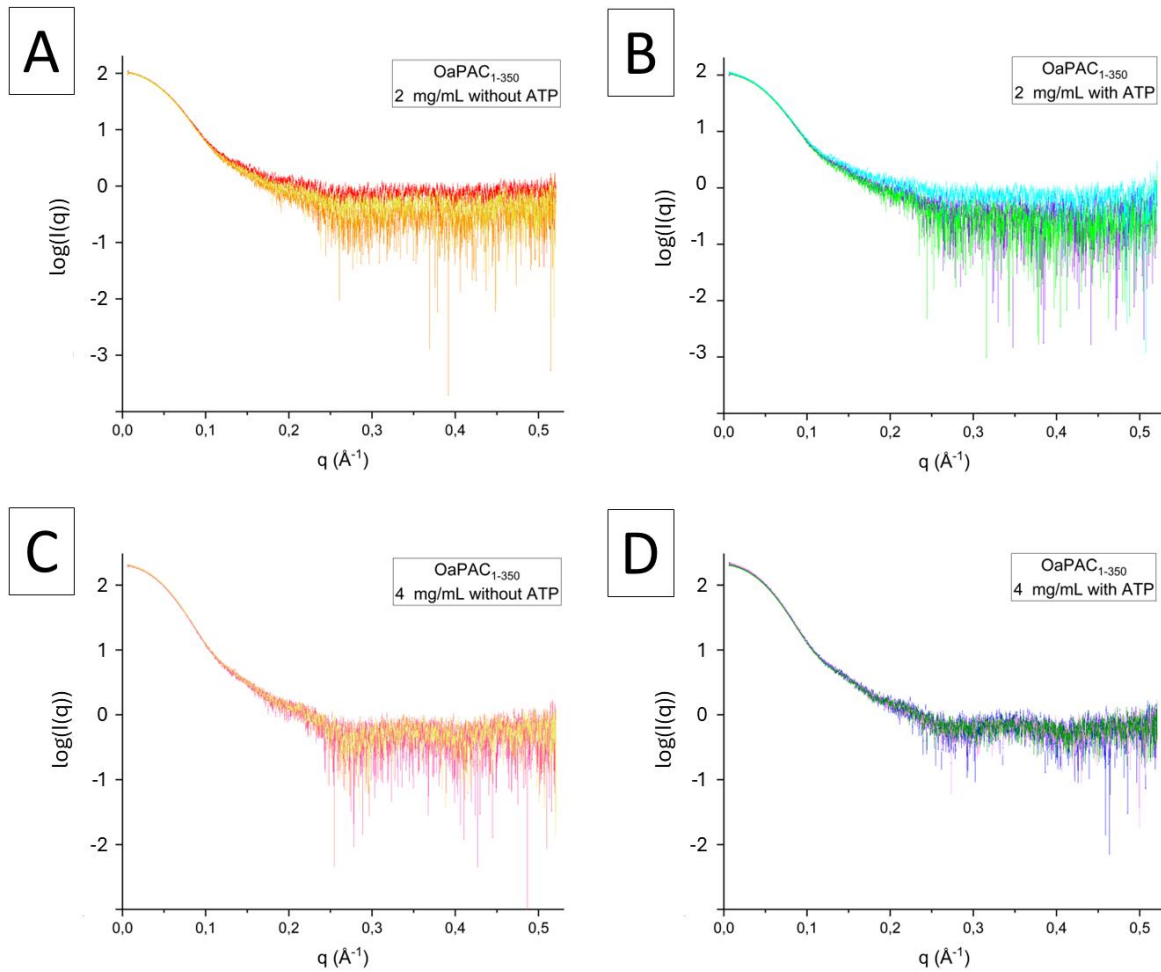
Figure prepared by the PyMOL Molecular Graphics System, Version 2.5.4 Schrödinger, LLC (Schrödinger and DeLano, 2020).



Appendix Figure 9: Difference electron density map revealing differences in the active site between holo and ATP-free OaPAC.

Non-isomorphous difference map between holo OaPAC (cyan) against ATP-free OaPAC (purple) data collected at room-temperature with SSX was calculated in real space to overcome poorly-isomorphous crystals using MatchMaps (Brookner and Hekstra, 2024). The differences contoured at +3 rmsd (green) and -3 rmsd (red) confirm the involvement of Phe154, Asp256, Asp200, Ile198, Asn273 and Arg283 in ATP binding coordination.

Figure prepared by the PyMOL Molecular Graphics System, Version 2.5.4 Schrödinger, LLC (Schrödinger and DeLano, 2020).

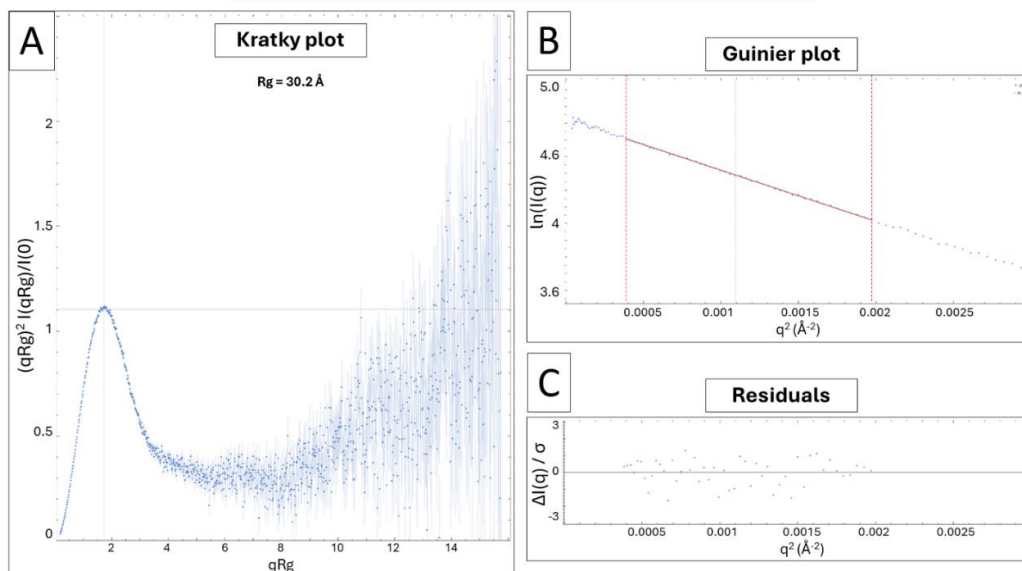


Appendix Figure 10: X-ray scattering pattern from OaPAC₁₋₃₅₀ SAXS data.

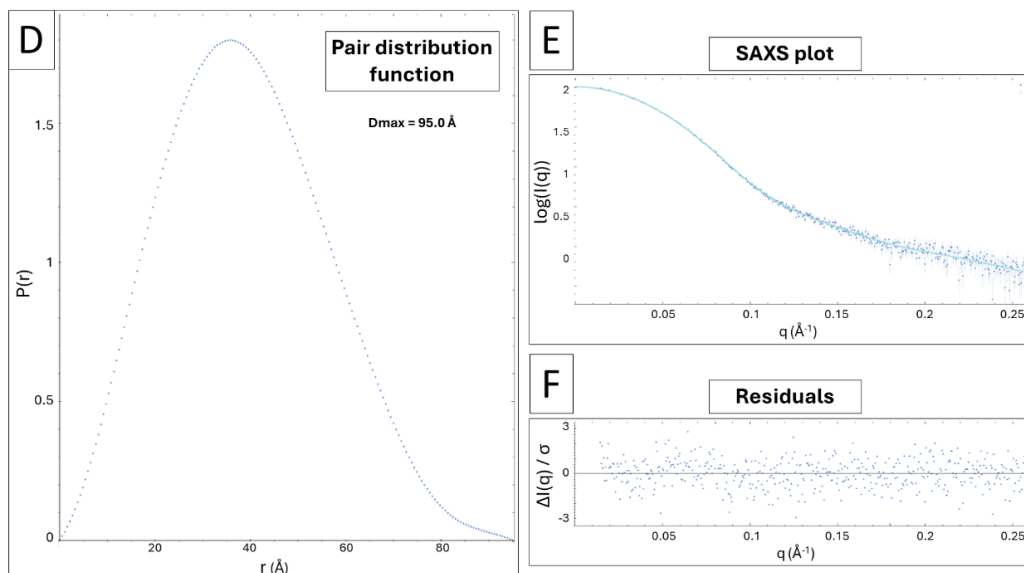
X-ray scattering patterns of OaPAC at 2 mg/mL without ATP (A) and with ATP (B), and at 4 mg/mL without ATP (C) and with ATP (D). Each condition was measured in triplicate.

Figures were created with Origin software version 2024.

**Guinier analysis of OaPAC₁₋₃₅₀ 2 mg/mL without ATP
Measurement 1**



Distance distribution analysis



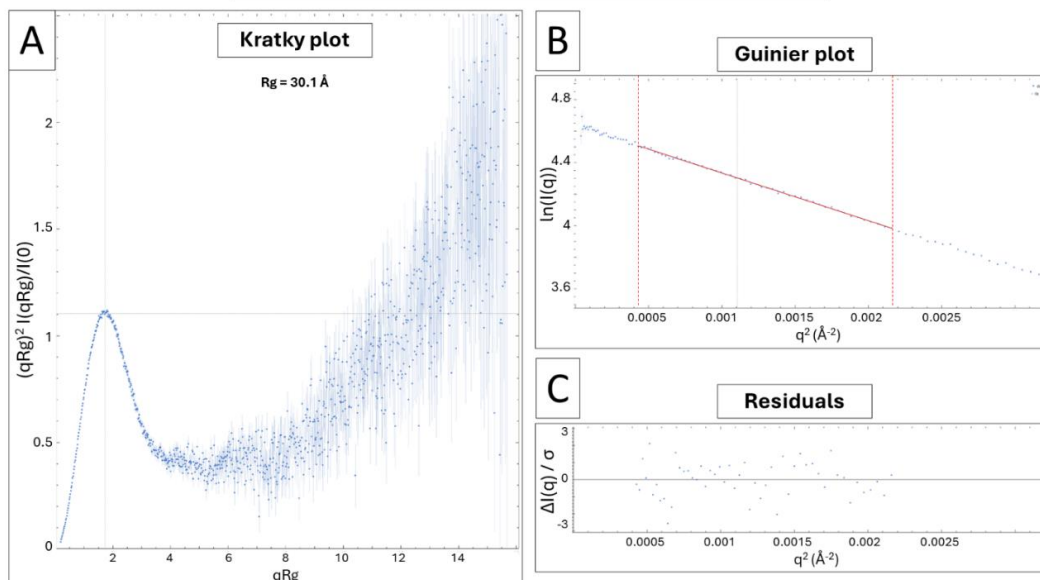
Appendix Figure 11: SAXS data analysis of the first measurement of OaPAC₁₋₃₅₀ at 2 mg/mL without ATP.

(A-C) Guinier analysis of OaPAC₁₋₃₅₀ at 2 mg/mL without ATP measurement 1 with dimensionless Kratky plot (A), Guinier plot and its linear fit (red) (B) and corresponding normalized residual plot of the Guinier plot fit (C). The analysis reveals a radius of gyration R_g of 30.2 Å and a compact and globular shape of OaPAC₁₋₃₅₀ without ATP in solution.

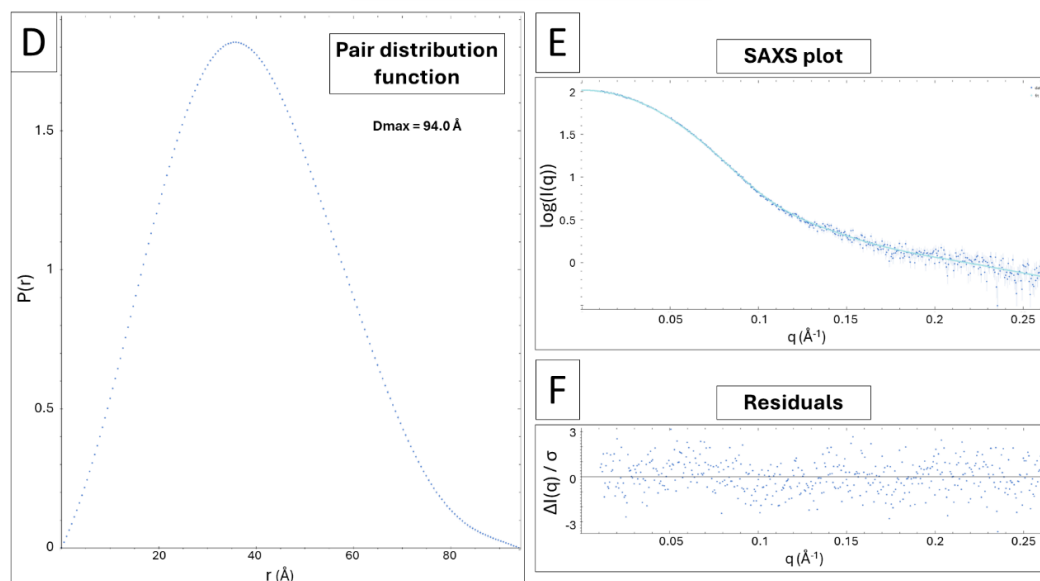
(D-F) Distance distribution analysis using GNOM version 5.0 (Svergun, 1992) with Pair distribution function $P(r)$ plot (A), fit of the X-ray scattering curve by Fourier transform of the $P(r)$ function (light blue) (B) and corresponding normalized residual plot of the SAXS plot fit (C). The analysis reveals a D_{max} of 95.0 Å and a compact and globular shape with a slight asymmetry of OaPAC₁₋₃₅₀ without ATP in solution.

Analysis and corresponding figures were produced with using PRIMUS graphical interface from the ATSAS software suite version 3.0 (Manalastas-Cantos et al., 2021).

**Guinier analysis of OaPAC₁₋₃₅₀ 2 mg/mL without ATP
Measurement 2**



Distance distribution analysis

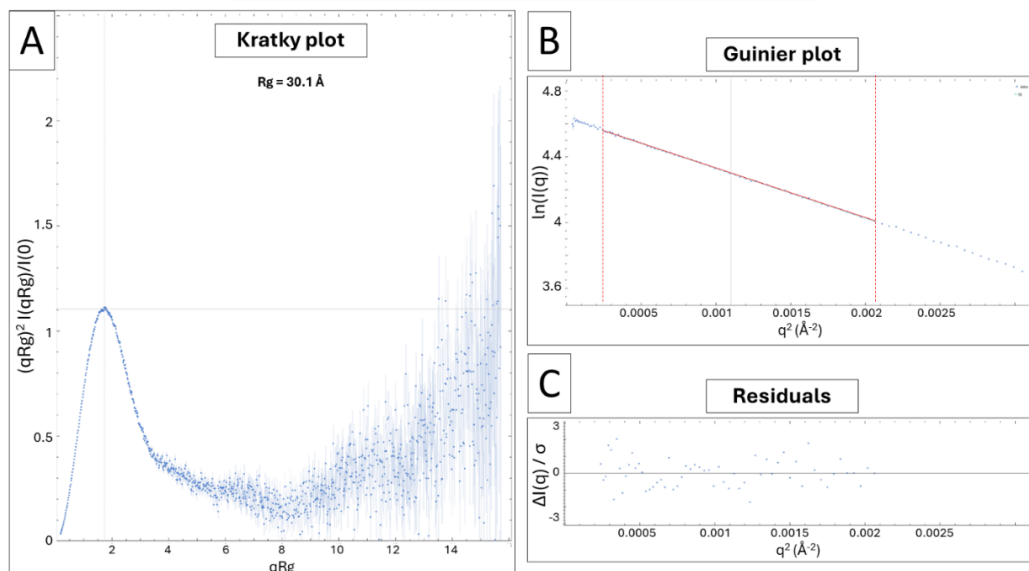


Appendix Figure 12: SAXS data analysis of the second measurement of OaPAC₁₋₃₅₀ at 2 mg/mL without ATP. (A-C) Guinier analysis of OaPAC₁₋₃₅₀ at 2 mg/mL without ATP measurement 2 with dimensionless Kratky plot (A), Guinier plot and its linear fit (red) (B) and corresponding normalized residual plot of the Guinier plot fit (C). The analysis reveals a radius of gyration R_g of 30.1 Å and a compact and globular shape of OaPAC₁₋₃₅₀ without ATP in solution.

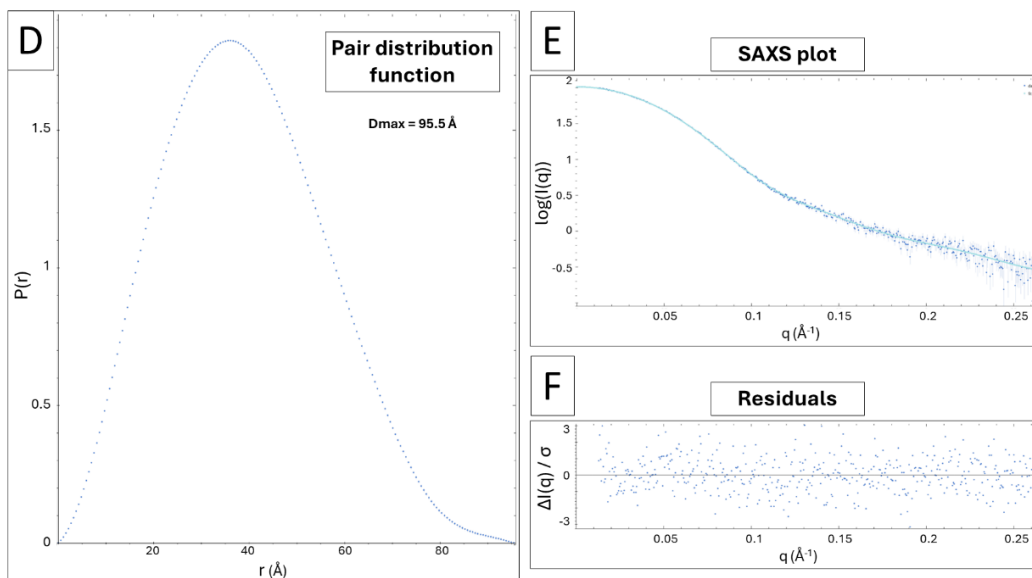
(D-F) Distance distribution analysis using GNOM version 5.0 (Svergun, 1992) with Pair distribution function $P(r)$ plot (A), fit of the X-ray scattering curve by Fourier transform of the $P(r)$ function (light blue) (B) and corresponding normalized residual plot of the SAXS plot fit (C). The analysis reveals a D_{max} of 94.0 Å and a compact and globular shape with a slight asymmetry of OaPAC₁₋₃₅₀ without ATP in solution.

Analysis and corresponding figures were produced with using PRIMUS graphical interface from the ATSAS software suite version 3.0 (Manalastas-Cantos et al., 2021).

**Guinier analysis of OaPAC₁₋₃₅₀ 2 mg/mL without ATP
Measurement 3**



Distance distribution analysis



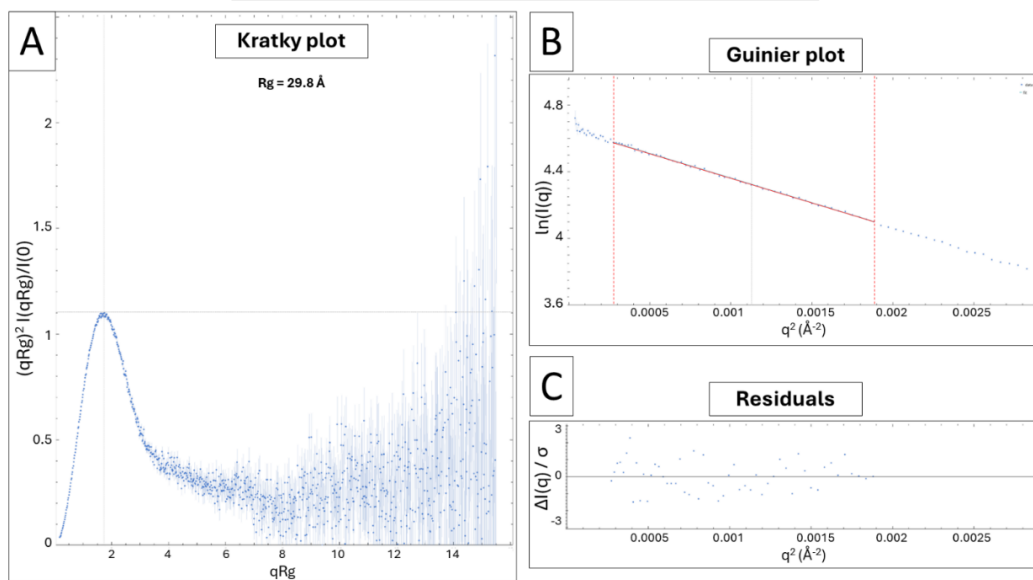
Appendix Figure 13: SAXS data analysis of the third measurement of OaPAC₁₋₃₅₀ at 2 mg/mL without ATP.

(A-C) Guinier analysis of OaPAC₁₋₃₅₀ at 2 mg/mL without ATP measurement 3 with dimensionless Kratky plot (A), Guinier plot and its linear fit (red) (B) and corresponding normalized residual plot of the Guinier plot fit (C). The analysis reveals a radius of gyration R_g of 30.1 Å and a compact and globular shape of OaPAC₁₋₃₅₀ without ATP in solution.

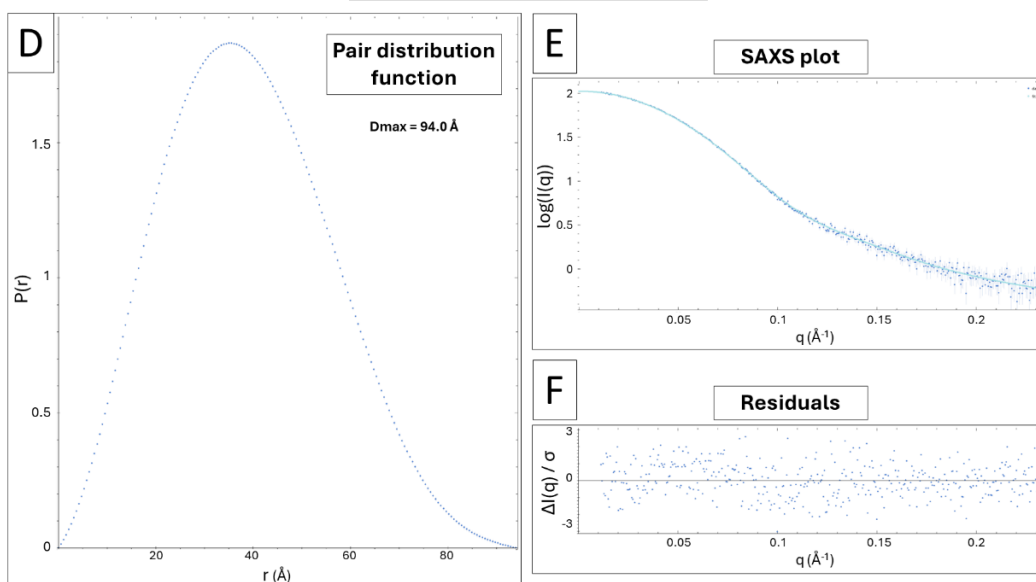
(D-F) Distance distribution analysis using GNOM version 5.0 (Svergun, 1992) with Pair distribution function $P(r)$ plot (A), fit of the X-ray scattering curve by Fourier transform of the $P(r)$ function (light blue) (B) and corresponding normalized residual plot of the SAXS plot fit (C). The analysis reveals a D_{max} of 95.5 Å and a compact and globular shape with a slight asymmetry of OaPAC₁₋₃₅₀ without ATP in solution.

Analysis and corresponding figures were produced with using PRIMUS graphical interface from the ATSAS software suite version 3.0 (Manalastas-Cantos et al., 2021).

**Guinier analysis of OaPAC₁₋₃₅₀ 2 mg/mL with ATP
Measurement 1**



Distance distribution analysis



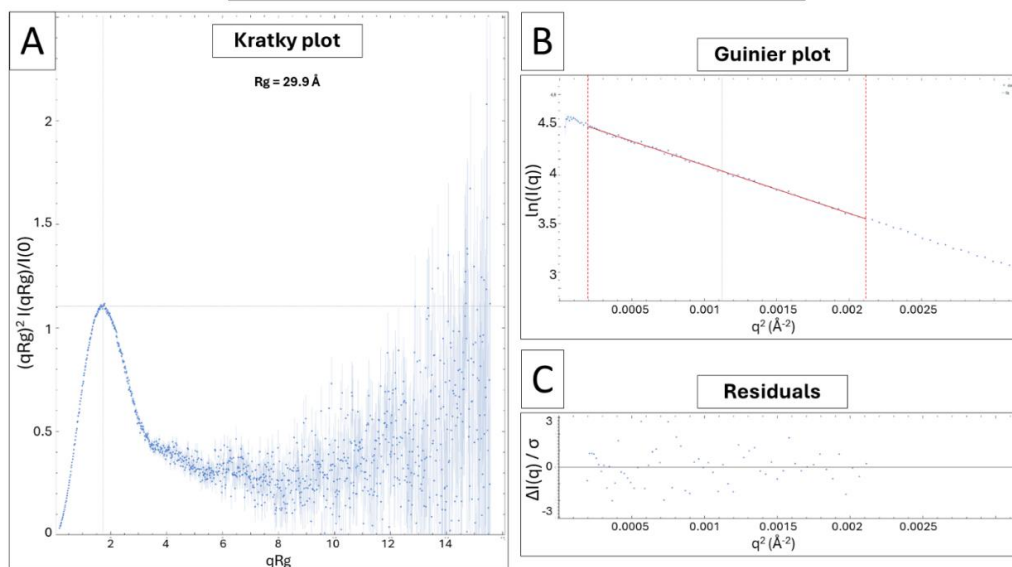
Appendix Figure 14: SAXS data analysis of the first measurement of OaPAC₁₋₃₅₀ at 2 mg/mL with ATP.

(A-C) Guinier analysis of OaPAC₁₋₃₅₀ at 2 mg/mL with ATP measurement 1 with dimensionless Kratky plot (A), Guinier plot and its linear fit (red) (B) and corresponding normalized residual plot of the Guinier plot fit (C). The analysis reveals a radius of gyration R_g of 29.8 Å and a compact and globular shape of OaPAC₁₋₃₅₀ with ATP in solution.

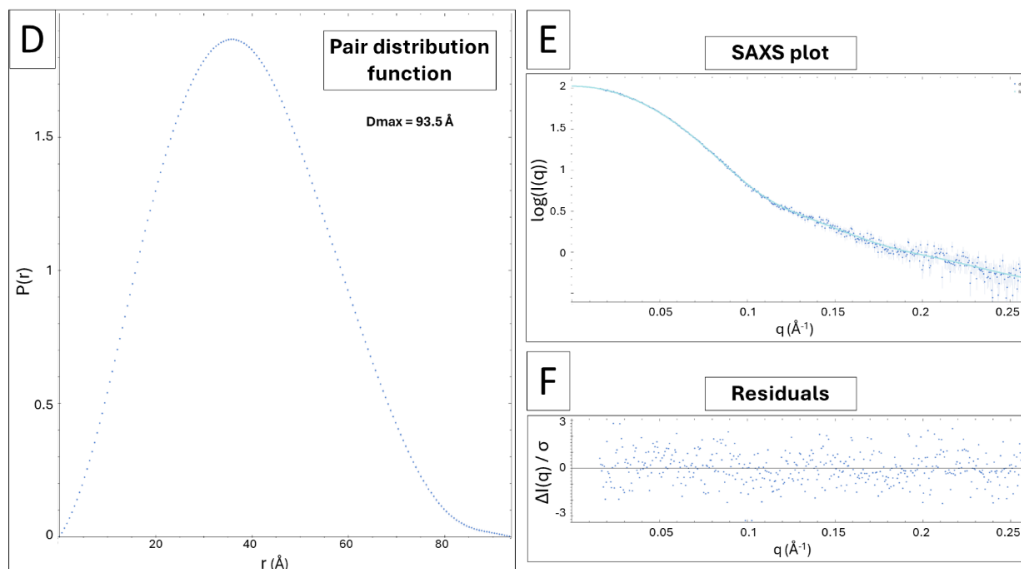
(D-F) Distance distribution analysis using GNOM version 5.0 (Svergun, 1992) with Pair distribution function $P(r)$ plot (A), fit of the X-ray scattering curve by Fourier transform of the $P(r)$ function (light blue) (B) and corresponding normalized residual plot of the SAXS plot fit (C). The analysis reveals a D_{max} of 94.0 Å and a compact and globular shape with a slight asymmetry of OaPAC₁₋₃₅₀ with ATP in solution.

Analysis and corresponding figures were produced with using PRIMUS graphical interface from the ATSAS software suite version 3.0 (Manalastas-Cantos et al., 2021).

Guinier analysis of OaPAC₁₋₃₅₀ 2 mg/mL with ATP
Measurement 2



Distance distribution analysis



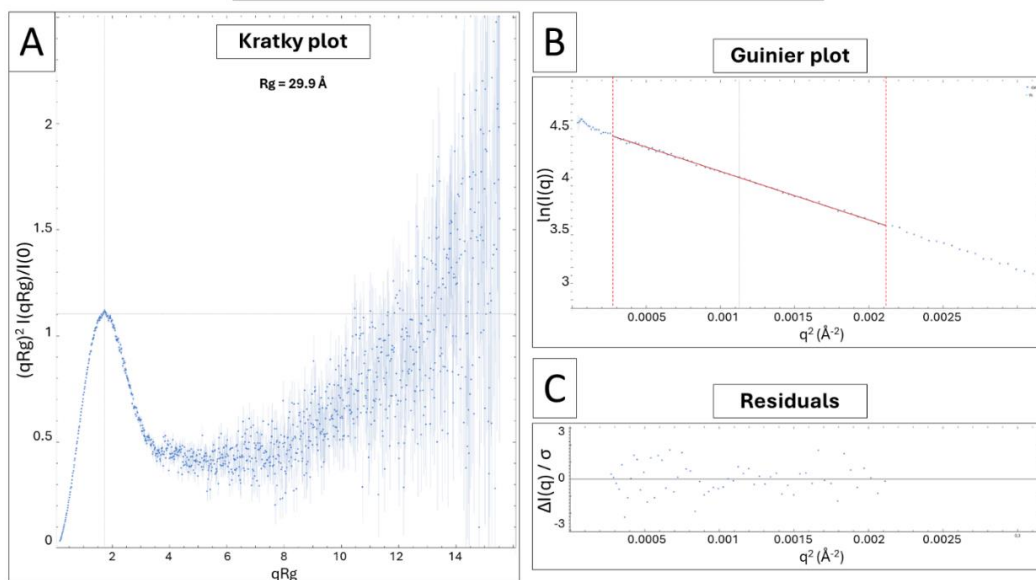
Appendix Figure 15: SAXS data analysis of the second measurement of OaPAC₁₋₃₅₀ at 2 mg/mL with ATP.

(A-C) Guinier analysis of OaPAC₁₋₃₅₀ at 2 mg/mL with ATP measurement 2 with dimensionless Kratky plot (A), Guinier plot and its linear fit (red) (B) and corresponding normalized residual plot of the Guinier plot fit (C). The analysis reveals a radius of gyration R_g of 29.9 Å and a compact and globular shape of OaPAC₁₋₃₅₀ with ATP in solution.

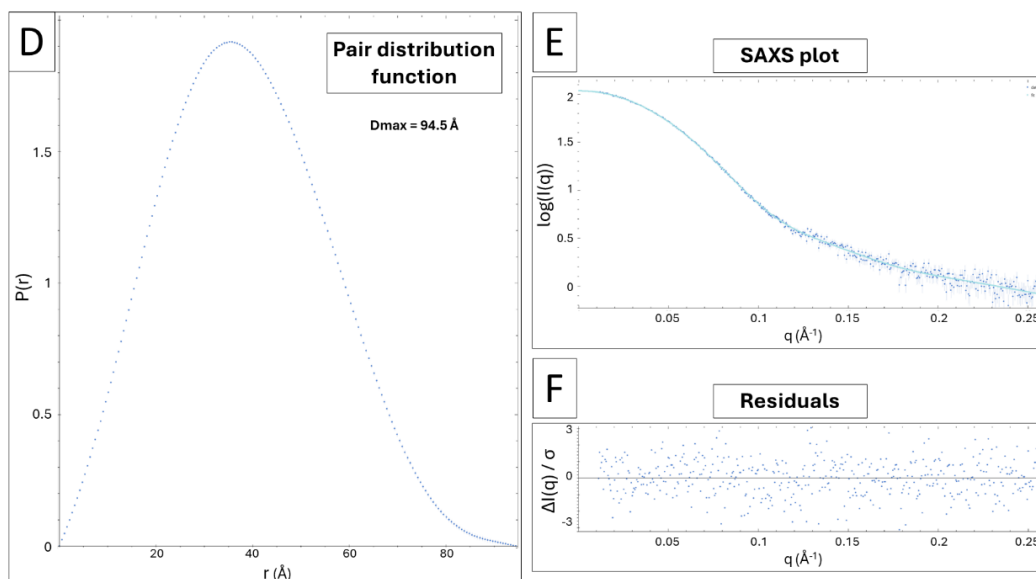
(D-F) Distance distribution analysis using GNOM version 5.0 (Svergun, 1992) with Pair distribution function $P(r)$ plot (A), fit of the X-ray scattering curve by Fourier transform of the $P(r)$ function (light blue) (B) and corresponding normalized residual plot of the SAXS plot fit (C). The analysis reveals a D_{max} of 93.5 Å and a compact and globular shape with a slight asymmetry of OaPAC₁₋₃₅₀ with ATP in solution.

Analysis and corresponding figures were produced with using PRIMUS graphical interface from the ATSAS software suite version 3.0 (Manalastas-Cantos et al., 2021).

**Guinier analysis of OaPAC₁₋₃₅₀ 2 mg/mL with ATP
Measurement 3**



Distance distribution analysis



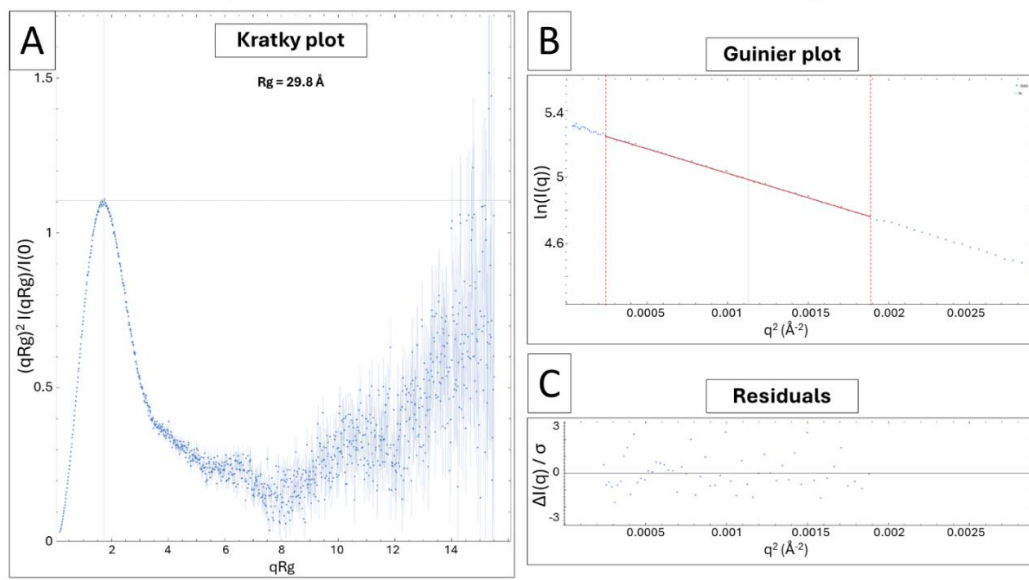
Appendix Figure 16: SAXS data analysis of the third measurement of OaPAC₁₋₃₅₀ at 2 mg/mL with ATP.

(A-C) Guinier analysis of OaPAC₁₋₃₅₀ at 2 mg/mL with ATP measurement 3 with dimensionless Kratky plot (A), Guinier plot and its linear fit (red) (B) and corresponding normalized residual plot of the Guinier plot fit (C). The analysis reveals a radius of gyration R_g of 29.9 Å and a compact and globular shape of OaPAC₁₋₃₅₀ with ATP in solution.

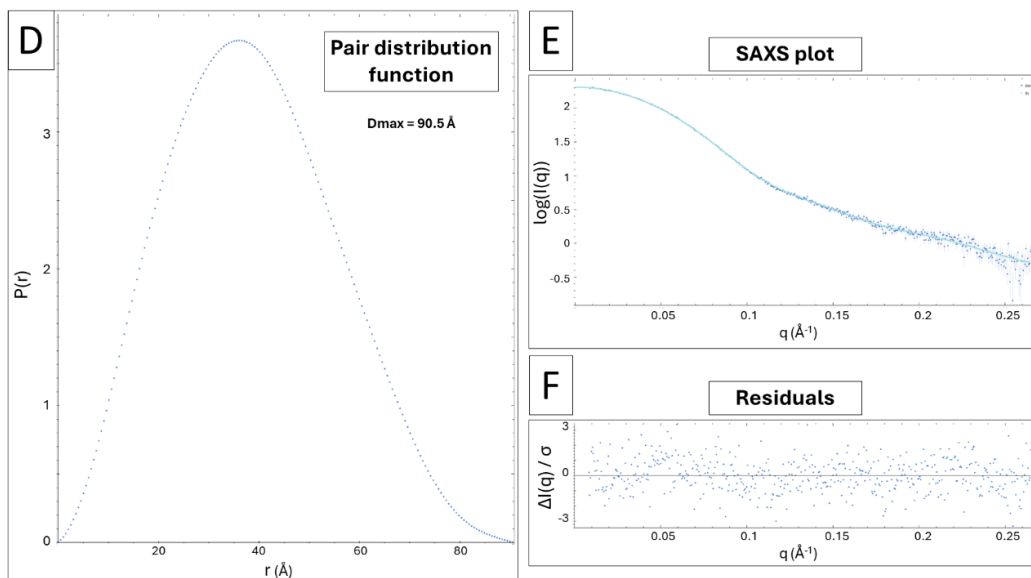
(D-F) Distance distribution analysis using GNOM version 5.0 (Svergun, 1992) with Pair distribution function $P(r)$ plot (A), fit of the X-ray scattering curve by Fourier transform of the $P(r)$ function (light blue) (B) and corresponding normalized residual plot of the SAXS plot fit (C). The analysis reveals a D_{max} of 94.5 Å and a compact and globular shape with a slight asymmetry of OaPAC₁₋₃₅₀ with ATP in solution.

Analysis and corresponding figures were produced with using PRIMUS graphical interface from the ATSAS software suite version 3.0 (Manalastas-Cantos et al., 2021).

**Guinier analysis of OaPAC₁₋₃₅₀ 4 mg/mL without ATP
Measurement 2**



Distance distribution analysis



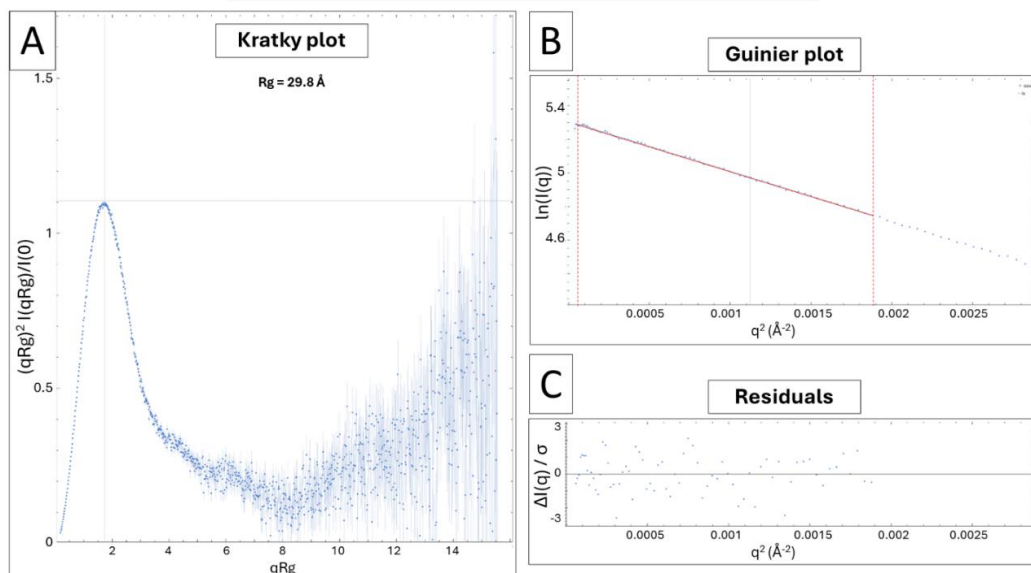
Appendix Figure 17: SAXS data analysis of the second measurement of OaPAC₁₋₃₅₀ at 4 mg/mL without ATP.

(A-C) Guinier analysis of OaPAC₁₋₃₅₀ at 4 mg/mL without ATP measurement 2 with dimensionless Kratky plot (A), Guinier plot and its linear fit (red) (B) and corresponding normalized residual plot of the Guinier plot fit (C). The analysis reveals a radius of gyration R_g of 29.8 Å and a compact and globular shape of OaPAC₁₋₃₅₀ without ATP in solution.

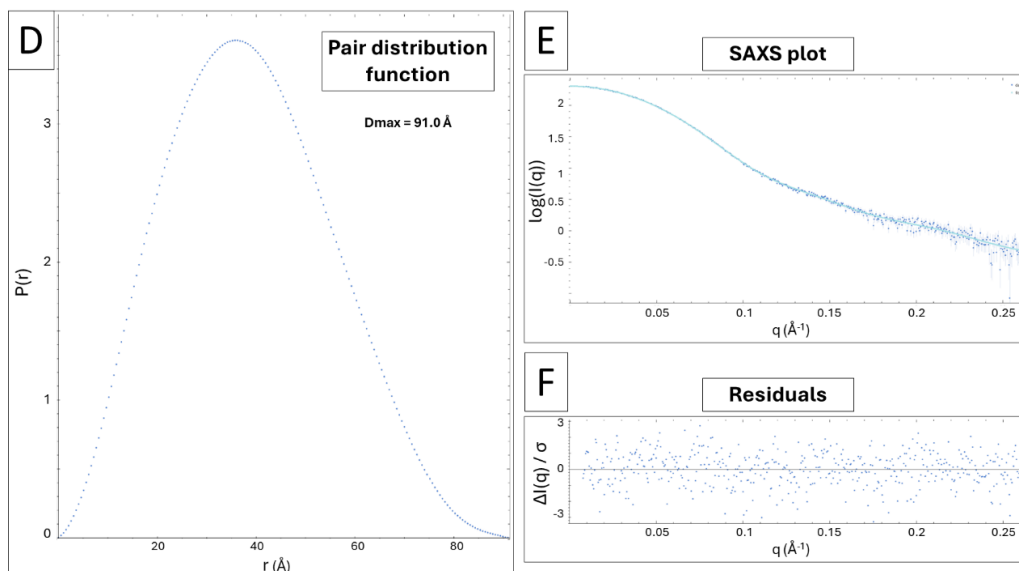
(D-F) Distance distribution analysis using GNOM version 5.0 (Svergun, 1992) with Pair distribution function $P(r)$ plot (A), fit of the X-ray scattering curve by Fourier transform of the $P(r)$ function (light blue) (B) and corresponding normalized residual plot of the SAXS plot fit (C). The analysis reveals a D_{max} of 90.5 Å and a compact and globular shape with a slight asymmetry of OaPAC₁₋₃₅₀ without ATP in solution.

Analysis and corresponding figures were produced with using PRIMUS graphical interface from the ATSAS software suite version 3.0 (Manalastas-Cantos et al., 2021).

**Guinier analysis of OaPAC₁₋₃₅₀ 4 mg/mL without ATP
Measurement 3**



Distance distribution analysis



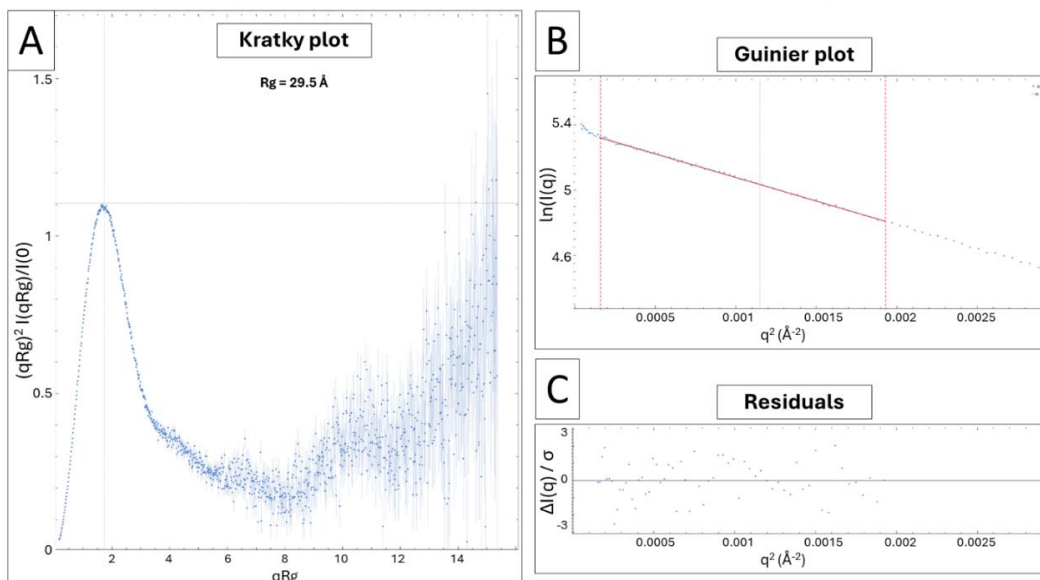
Appendix Figure 18: SAXS data analysis of the third measurement of OaPAC1-350 at 4 mg/mL without ATP.

(A-C) Guinier analysis of OaPAC1-350 at 4 mg/mL without ATP measurement 3 with dimensionless Kratky plot (A), Guinier plot and its linear fit (red) (B) and corresponding normalized residual plot of the Guinier plot fit (C). The analysis reveals a radius of gyration R_g of 29.8 Å and a compact and globular shape of OaPAC1-350 without ATP in solution.

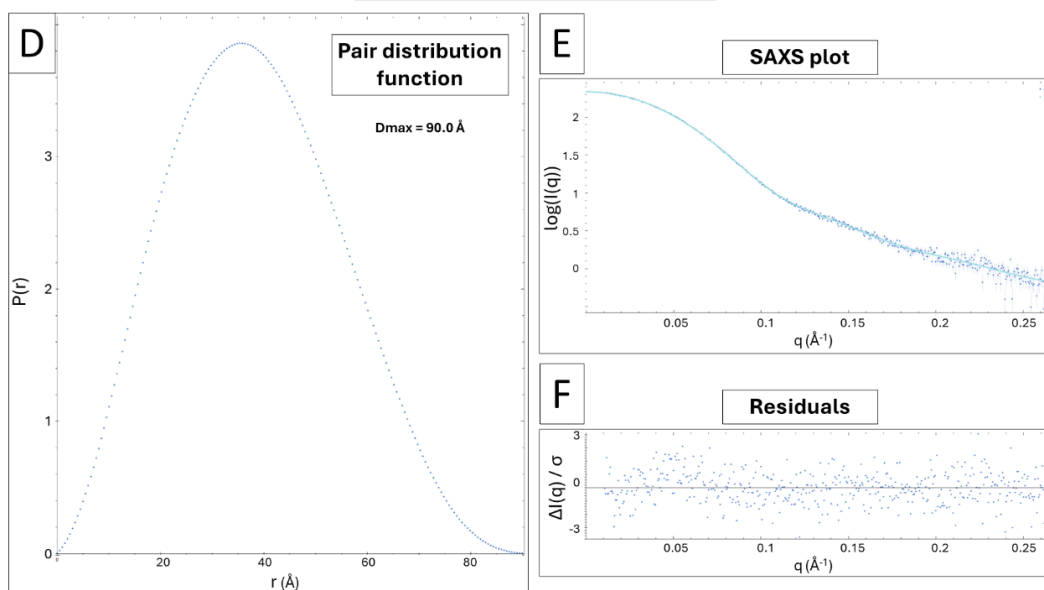
(D-F) Distance distribution analysis using GNOM version 5.0 (Svergun, 1992) with Pair distribution function $P(r)$ plot (A), fit of the X-ray scattering curve by Fourier transform of the $P(r)$ function (light blue) (B) and corresponding normalized residual plot of the SAXS plot fit (C). The analysis reveals a D_{max} of 91.0 Å and a compact and globular shape with a slight asymmetry of OaPAC1-350 without ATP in solution.

Analysis and corresponding figures were produced with using PRIMUS graphical interface from the ATSAS software suite version 3.0 (Manalastas-Cantos et al., 2021).

**Guinier analysis of OaPAC₁₋₃₅₀ 4 mg/mL with ATP
Measurement 2**

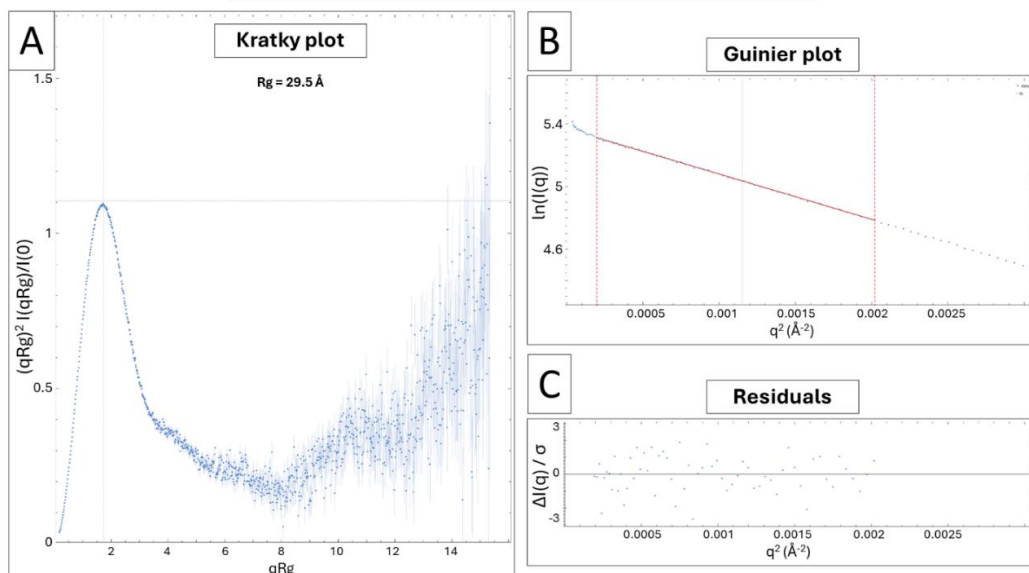


Distance distribution analysis

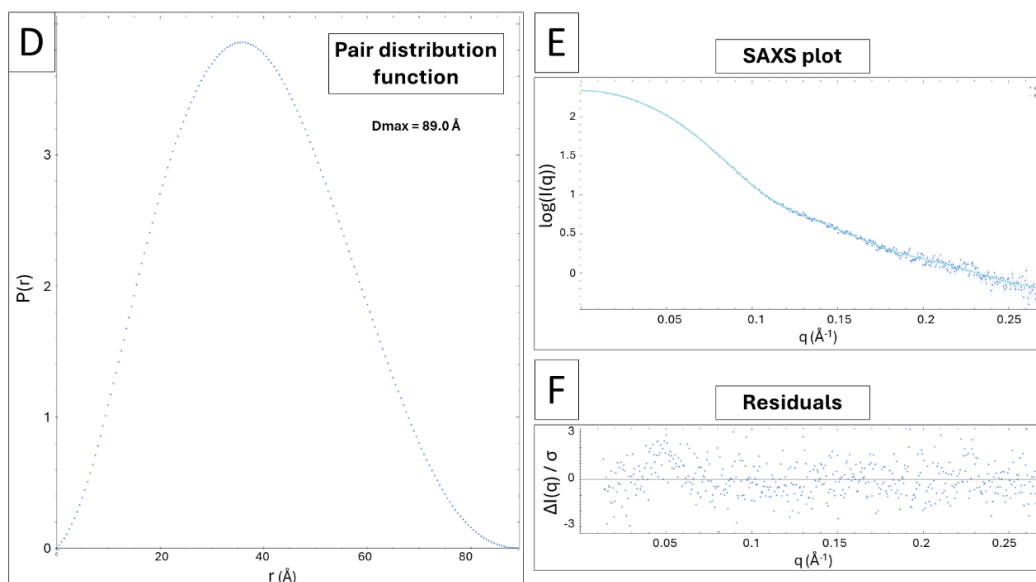


Appendix Figure 19: SAXS data analysis of the second measurement of OaPAC₁₋₃₅₀ at 4 mg/mL with ATP. (A-C) Guinier analysis of OaPAC₁₋₃₅₀ at 4 mg/mL with ATP measurement 2 with dimensionless Kratky plot (A), Guinier plot and its linear fit (red) (B) and corresponding normalized residual plot of the Guinier plot fit (C). The analysis reveals a radius of gyration R_g of 29.5 Å and a compact and globular shape of OaPAC₁₋₃₅₀ with ATP in solution. (D-F) Distance distribution analysis using GNOM version 5.0 (Svergun, 1992) with Pair distribution function $P(r)$ plot (A), fit of the X-ray scattering curve by Fourier transform of the $P(r)$ function (light blue) (B) and corresponding normalized residual plot of the SAXS plot fit (C). The analysis reveals a D_{max} of 90.0 Å and a compact and globular shape with a slight asymmetry of OaPAC₁₋₃₅₀ with ATP in solution. Analysis and corresponding figures were produced with using PRIMUS graphical interface from the ATSAS software suite version 3.0 (Manalastas-Cantos et al., 2021).

**Guinier analysis of OaPAC₁₋₃₅₀ 4 mg/mL with ATP
Measurement 3**



Distance distribution analysis

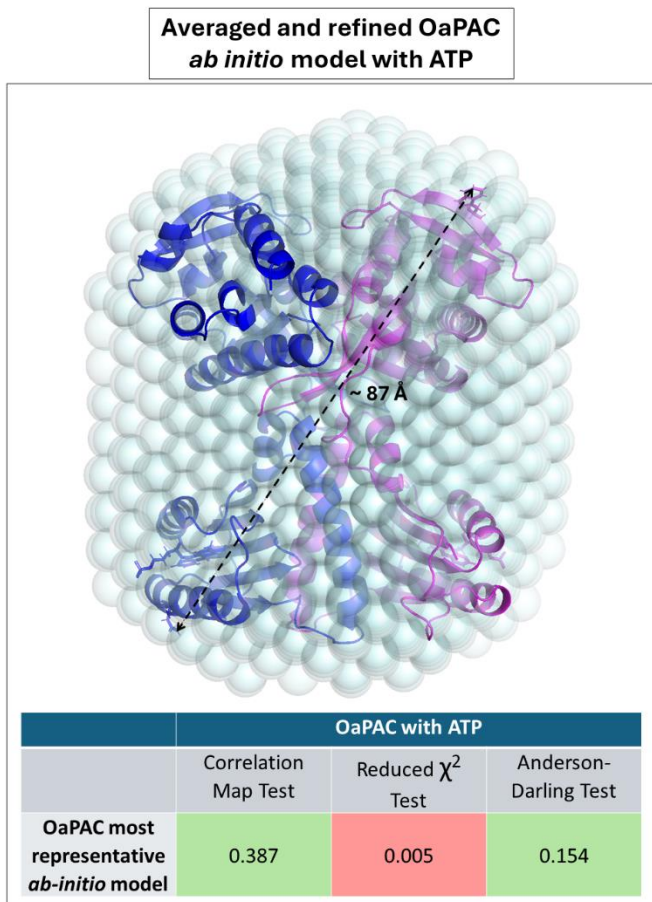


Appendix Figure 20: SAXS data analysis of the third measurement of OaPAC₁₋₃₅₀ at 4 mg/mL with ATP.

(A-C) Guinier analysis of OaPAC₁₋₃₅₀ at 4 mg/mL with ATP measurement 3 with dimensionless Kratky plot (A), Guinier plot and its linear fit (red) (B) and corresponding normalized residual plot of the Guinier plot fit (C). The analysis reveals a radius of gyration R_g of 29.5 Å and a compact and globular shape of OaPAC₁₋₃₅₀ with ATP in solution.

(D-F) Distance distribution analysis using GNOM version 5.0 (Svergun, 1992) with Pair distribution function $P(r)$ plot (A), fit of the X-ray scattering curve by Fourier transform of the $P(r)$ function (light blue) (B) and corresponding normalized residual plot of the SAXS plot fit (C). The analysis reveals a D_{max} of 89.0 Å and a compact and globular shape with a slight asymmetry of OaPAC₁₋₃₅₀ with ATP in solution.

Analysis and corresponding figures were produced with using PRIMUS graphical interface from the ATSAS software suite version 3.0 (Manalastas-Cantos et al., 2021).



Appendix Figure 21: *Ab initio* model from the SAXS data of OaPAC₁₋₃₅₀ in the presence of ATP.

Ab initio model of OaPAC obtained from 19 selected models out of 20 produced by DAMMIF version 1.1.2 (Franke and Svergun, 2009) averaged with DAMAVER version 5.0 (Volkov and Svergun, 2003) and refined with DAMMIN version 5.3 (Svergun, 1999). The molecular envelope is displayed in sphere representation. OaPAC crystallography structure in orthorhombic form with space group $C222_1$ is presented in carton representation and overlaid to the SAXS *ab initio* model. The maximum intramolecular distance of ~ 87 Å in the crystal structure is slightly reduced compared to the D_{max} obtained from the $P(r)$ function (~ 90 Å). Figure was prepared by the PyMOL Molecular Graphics System, Version 2.5.4 Schrödinger, LLC. (Schrödinger and DeLano, 2020).

The inserted table displays p -values from the pairwise similarity tests between OaPAC SAXS data in solution with ATP and OaPAC most representative *ab initio* model fit obtained with DAMMIF. Analysis was performed with using PRIMUS graphical interface from the ATSAS software suite version 3.0 (Manalastas-Cantos et al., 2021).

A.2. Appendix Tables

OaPAC	Cryo ATP-free	Cryo ATP bound	5 s illuminated cryo-trapped
PDB deposition code	8QFE	8QFF	8QFG
Data collection			
Source	ESRF (ID23-2)	ESRF (ID23-2)	PETRA III (P11)
Temperature (K)		100	
Wavelength (Å)	0.8731	0.8731	1.0332
Detector	DECTRIS PILATUS3 X 2M	DECTRIS PILATUS3 X 2M	DECTRIS EIGER2 X 16M
Space group	C222 ₁		
Cell dimensions			
<i>a</i> , <i>b</i> , <i>c</i> (Å)	52.9, 146.2, 103.6	54.5, 146.4, 104.9	52.5, 141.4, 104.7
<i>α</i> , <i>β</i> , <i>γ</i> (°)	90, 90, 90	90, 90, 90	90, 90, 90
Solvent Content (%)	51.6	53.7	50.2
Resolution (Å)	33.86-1.50 (1.53-1.50)	60.04-2.10 (2.16-2.10)	42.08-1.70 (1.73-1.70)
<i>R</i> _{meas} (%)	5.5 (131.2)	23.0 (211.5)	3.6 (94.4)
<i><I></i> / <i>sigI</i>	19.7 (1.1)	9.0 (1.2)	34.9 (2.7)
CC _{1/2}	1.000 (0.846)	0.997 (0.501)	1.000 (0.939)
No. unique reflections	64,596 (3,212)	24,956 (2,002)	42,861 (2,140)
Completeness (%)	100.0 (100.0)	100.0 (100.0)	99.2 (95.7)
Redundancy	13.0 (12.8)	10.9 (11.3)	13.3 (12.0)
Refinement			
Resolution (Å)	33.22-1.50 (1.52-1.50)	60.04-2.10 (2.20-2.10)	42.08-1.70 (1.74-1.70)
Completeness (%)	99.96 (99.96)	99.96 (100.00)	98.63 (95.33)
No. unique reflections	64,543 (2,636)	24,924 (2,935)	42,714 (2,559)
<i>R</i> _{work} / <i>R</i> _{free}	0.163 / 0.186	0.189 / 0.223	0.209 / 0.221
No. atoms			
Protein	3,097	2,979	2,608
Ligand/ion	50	93	93
Water	328	189	107
<i>B</i>-factors			
Protein (Å ²)	30.44	45.33	60.14
Ligand/ion (Å ²)	24.53	46.05	49.86
Water (Å ²)	40.150	47.55	49.88
r.m.s. deviations			
Bond lengths (Å)	0.013	0.010	0.014
Bond angles (°)	1.190	1.020	1.160
Ramachandran			
favoured (%)	96.55	97.70	93.88
allowed (%)	3.16	2.01	6.12
outliers (%)	0.29	0.29	0
Clashscore	3.34	2.12	7.13

Appendix Table 1: Synchrotron data collection and processing statistics.
Table from (Chretien et al., 2024).

OaPAC (SFX)	Dark-RT (all frames)	Dark (60k subset)	1 μ s delay	1.8 μ s delay	2.3 μ s delay
PDB deposition code	8QFH	-	-	8QFI	8QFJ
Data collection					
Source	EuXFEL (SPB/SFX instrument)				
Temperature (K)	293				
Wavelength (Å)	1.3332				
Detector	AGIPD				
Space group	C222 ₁				
Cell dimensions					
a, b, c (Å)	54.3, 145.8, 105.3				
α, β, γ (°)	90, 90, 90				
Solvent Content (%)	53.6				
Resolution (Å)	31.63-1.80 (1.86-1.80)	31.63-1.82 (1.88-1.82)	31.63-1.82 (1.88-1.82)	31.63-1.82 (1.88-1.82)	31.63-1.82 (1.88-1.82)
# patterns merged	299,140	59,892	50,054	50,786	68,993
R_{split} (%)	5.4 (41.6)	10.5 (74.1)	13.5 (179.5)	13.2 (171.1)	11.0 (157.0)
$\langle I \rangle / \text{sig}I$	11.6 (2.6)	6.2 (1.5)	1.2 (0.7)	1.2 (0.6)	1.3 (0.8)
CC _{1/2}	0.997 (0.876)	0.987 (0.645)	0.982 (0.384)	0.983 (0.391)	0.988 (0.448)
CC*	0.999 (0.996)	0.997 (0.886)	0.995 (0.745)	0.996 (0.750)	0.997 (0.787)
No. unique reflections	39,352 (3,858)	39,352 (3,858)	37,614 (3,263)	36,898 (3,192)	37,632 (3,250)
Completeness (%)	100.00 (100.00)	100.00 (100.00)	98.55 (86.71)	96.61 (84.92)	98.52 (86.37)
Redundancy	3,079 (1,836)	448 (267)	646 (388)	711 (428)	936 (563)
Refinement					
Resolution (Å)	31.63-1.80 (1.82-1.80)		31.63-1.90 (1.96-1.90)	31.63-1.90 (1.96-1.90)	31.63-1.90 (1.96-1.90)
Completeness (%)	99.80 (99.93)		99.86 (99.76)	99.92 (99.85)	99.89 (99.89)
No. unique reflections	39,103 (12,73)		33,346 (2,606)	33,355 (2,609)	33,344 (2,609)
$R_{\text{work}} / R_{\text{free}}$	0.165 / 0.194		0.316 / 0.355	0.307 / 0.340	0.294 / 0.354
No. atoms					
Protein	2,988		2,738	2,782	2,770
Ligand/ion	135		135	135	135
Water	81		130	129	127
B-factors					
Protein (Å ²)	59.02		45.54	41.89	46.12
Ligand/ion (Å ²)	44.47		34.38	34.19	43.73
Water (Å ²)	56.91		41.95	41.64	42.17
r.m.s. deviations					
Bond lengths (Å)	0.007		0.011	0.014	0.006
Bond angles (°)	0.93		1.21	0.95	0.81
Ramachandran					
favoured (%)	97.13		94.83	97.26	96.04
allowed (%)	2.59		4.89	2.74	3.96
outliers (%)	0.29		0.29	0	0
Clashscore	3.88		4.99	4.30	5.38

*Appendix Table 2: Data collection and refinement statistics of TR-SFX data.
Table modified from (Chretien et al., 2024).*

OaPAC (SSX)	Dark-RT With ATP	Dark Without ATP	50 ms delay 55.1 mJ/cm ²	50 ms delay 220.5 mJ/cm ²	50 ms delay 441 mJ/cm ²	480 ms delay 110.3mJ/cm ²	480 ms delay 220.5mJ/cm ²	960 ms delay 110.3mJ/cm ²	960 ms delay 220.5mJ/cm ²
Data collection									
Source	PETRA III (P14.EH2, T-REXX instrument)								
Temperature (K)	293								
Wavelength (Å)	0.976								
Detector	DECTRIS EIGER2 x 4M								
Space group	C222 ₁								
Cell dimensions									
a, b, c (Å)	54.3, 145.8, 105.5	53.7, 146.4, 103.5	54.3, 145.8, 105.5	54.3, 145.8, 105.5	54.3, 145.8, 105.5	53.7, 146.4, 103.5	53.7, 146.4, 103.5	53.7, 146.4, 103.5	53.7, 146.4, 103.5
α, β, γ (°)	90, 90, 90	90, 90, 90	90, 90, 90	90, 90, 90	90, 90, 90	90, 90, 90	90, 90, 90	90, 90, 90	90, 90, 90
Solvent Content (%)	53.6	52.4	53.6	53.6	53.6	52.4	52.4	52.4	52.4
Resolution (Å)	72.90 – 2.00 (2.04-2.00)	73.20 – 2.05 (2.09-2.05)	72.90 – 2.00 (2.04-2.00)	72.90 – 2.00 (2.04-2.00)	72.90 – 2.00 (2.04-2.00)	73.20 – 2.05 (2.09-2.05)	73.20 – 2.05 (2.09-2.05)	73.20 – 2.05 (2.09-2.05)	73.20 – 2.05 (2.09-2.05)
# patterns merged	12,181	7,530	17,524	9,960	22,645	16,010	11,966	11,375	14,387
R_{split} (%)	19.3 (76.4)	17.8 (89.9)	16.5 (60.1)	21.2 (93.5)	13.9 (58.9)	15.0 (85.8)	13.3 (101.3)	12.2 (77.2)	14.6 (110.9)
<I> / sigI	3.91 (1.34)	4,26 (1.23)	4.69 (1.72)	3.52 (1.12)	5.30 (1.71)	4.75 (1.15)	5.12 (1.11)	5.67 (1.38)	4.69 (1.02)
CC_{1/2}	0.957 (0.575)	0.964 (0.451)	0.964 (0.689)	0.949 (0.465)	0.978 (0.700)	0.976 (0.470)	0.982 (0.418)	0.984 (0.527)	0.981 (0.349)
CC*	0.989 (0.854)	0.991 (0.788)	0.991 (0.903)	0.987 (0.797)	0.994 (0.908)	0.994 (0.799)	0.996 (0.768)	0.996 (0.831)	0.995 (0.719)
No. unique reflections	28,769 (2,813)	26,077 (2,558)	28,769 (2,813)	28,768 (2,812)	28,769 (2813)	26,077 (2,558)	26,077 (2,558)	26,077 (2,558)	26,077 (2,558)
Completeness (%)	100.00 (100.00)	100.00 (100.00)	100.00 (100.00)	99.99 (99.96)	100.00 (100.00)	100.00 (100.00)	100.00 (100.00)	100.00 (100.00)	100.00 (100.00)
Redundancy	64.2 (43.8)	79.7 (55.0)	88.9 (60.3)	53.9 (36.8)	127.3 (86.5)	110.1 (75.8)	138.2 (95.2)	158.8 (109.1)	112.0 (77.2)

Appendix Table 3: Data collection and refinement statistics of TR-SSX data

Refinement									
Resolution (Å)	72.90 – 2.00 (2.07-2.00)	73.20 – 2.05 (2.13-2.05)							
Completeness (%)	99.92 (99.86)	99.86 (99.84)							
No. unique reflections	28,722 (2,808)	26,017 (2,553)							
$R_{\text{work}} / R_{\text{free}}$	0.188 / 0.221	0.183 / 0.229							
No. atoms									
Protein	2,687	2,800							
Ligand/ion	135	50							
Water	113	118							
B-factors									
Protein (Å²)	41.65	44.51							
Ligand/ion (Å²)	31.77	41.83							
Water (Å²)	43.88	42.72							
r.m.s. deviations									
Bond lengths (Å)	0.008	0.007							
Bond angles (°)	0.73	0.63							
Ramachandran									
favoured (%)	97.85	97.97							
allowed (%)	2.15	2.03							
outliers (%)	0	0							
Clashscore	0.90	0.18							

Appendix Table 3: Data collection and refinement statistics of TR-SSX data (continuation)

A.3. List of Hazardous Substances According to GHS

Ampicillin sodium salt

Section	Hazard class	Category	Hazard class and category	Hazard statement
3.4R	Respiratory sensitisation	1	Resp. Sens. 1	H334
3.4S	Skin sensitisation	1	Skin Sens. 1	H317

Signal word: Danger

Hazard statements: H317-H334

Precautionary statements: P261 P280 P302+P352 P342+P311

Pictogram: GHS08



Guanidine hydrochloride

Section	Hazard class	Category	Hazard class and category	Hazard statement
3.1O	Acute toxicity (oral)	4	Acute Tox. 4	H302
3.1I	Acute toxicity (inhal.)	4	Acute Tox. 4	H332
3.2	Skin corrosion/irritation	2	Skin Irrit. 2	H315
3.3	Serious eye damage/eye irritation	2	Eye Dam. 2	H319

Signal word: Warning

Hazard statements: H302+H332-H315-H319

Precautionary statements: P260 P280 P302+P352 P305+P351+P338

Pictogram: GHS07



Hydrochloric acid solution (37%)

Section	Hazard class	Category	Hazard class and category	Hazard statement
2.16	Substance or mixture corrosive to metals	1	Met. Corr. 1	H290
3.2	Skin corrosion/irritation	1	Skin Corr. 1	H314
3.3	Serious eye damage/eye irritation	1	Eye Dam. 1	H318
3.8R	Specific target organ toxicity - single exposure (respiratory tract irritation)	3	STOT SE 3	H335

Signal word: Danger

Hazard statements: H290-H314-H335

Precautionary statements: P280 P303+P361+P353 P304+P340 P305+P351+P338 P310

Pictograms: GHS05, GHS07



Imidazole

Section	Hazard class	Category	Hazard class and category	Hazard statement
3.10	Acute toxicity (oral)	4	Acute Tox. 4	H302
3.2	Skin corrosion/irritation	1C	Skin Irrit. 1	H314
3.3	Serious eye damage/eye irritation	1	Eye Dam. 1	H318
3.7	Reproductive toxicity	1B	Repr. 1B	H360D

Signal word: Danger

Hazard statements: H302-H314-H360D

Precautionary statements: P202 P270 P280 P305+P351+P338 P310

Pictograms: GHS05, GHS07, GHS08



Sodium dodecyl sulphate

Section	Hazard class	Category	Hazard class and category	Hazard statement
2.7	Flammable solid	2	Flam. Sol. 2	H328
3.1O	Acute toxicity (oral)	4	Acute Tox. 4	H302
3.1I	Acute toxicity (inhal.)	4	Acute Tox. 4	H332
3.2	Skin corrosion/irritation	2	Skin Irrit. 2	H315
3.3	Serious eye damage/eye irritation	1	Eye Dam. 1	H318
3.8R	Specific target organ toxicity - single exposure (respiratory tract irritation)	3	STOT SE 3	H335

Signal word: Danger

Hazard statements: H228-H302+H332-H315-H318-H335-H412

Precautionary statements: P210 P261 P280 P302+P352 P305+P351+P338 P312

Pictograms: GHS02, GHS05, GHS07



Sodium hydroxide solution (20%)

Section	Hazard class	Category	Hazard class and category	Hazard statement
2.16	Substance or mixture corrosive to metals	1	Met. Corr. 1	H290

Signal word: Warning

Hazard statements: H290

Precautionary statements: P234 P390

Pictogram: GHS05



2-mercaptoethanol

Section	Hazard class	Category	Hazard class and category	Hazard statement
2.6	Flammable liquid	4	Flam. Liq. 4	H227
3.1O	Acute toxicity (oral)	3	Acute Tox. 3	H301
3.1D	Acute toxicity (dermal)	2	Acute Tox. 2	H310
3.1I	Acute toxicity (inhal.)	3	Acute Tox. 3	H331
3.2	Skin corrosion/irritation	2	Skin Irrit. 2	H315
3.3	Serious eye damage/eye irritation	1	Eye Dam. 1	H318
3.4S	Skin sensitisation	1	Skin Sens. 1	H317
3.9	Specific target organ toxicity - repeated exposure	2	STOT RE 2	H373

Signal word: Danger

Hazard statements: H301+H331-H310-H315-H317-H318-H373-H410

Precautionary statements: P273 P280 P302+P352 P304+P340 P305+P351+P338 P310

Pictograms: GHS05, GHS06, GHS08



Acknowledgements

The completion of this doctoral thesis has been an arduous yet immensely rewarding journey, and it would not have been possible without the support, guidance, and encouragement of many individuals. I would like to express my deepest gratitude to those who have contributed to this work in various ways.

First and foremost, I would like to extend my sincere thanks to my supervisor, Robin Schubert, for his unwavering support, insightful guidance, patience, and constant encouragement throughout this research. His expertise and mentorship have been invaluable in shaping this thesis.

I am profoundly grateful to my advisors, Arwen Pearson and Kristina Lorenzen, for their thoughtful feedback, constructive criticism, and invaluable suggestions, which have significantly enhanced the quality of this work.

Special thanks go to my colleagues in the Sample Environment and Characterization group, the SPB-SFX group and fellow graduate students at European XFEL, whose camaraderie and collaborative spirit have made the research process enjoyable and stimulating. I am particularly indebted to Christina Schmidt, Ekaterina Round, Huijong Han, Iñaki de Diego and Lea Brings for their insightful discussions and technical assistance.

I am also grateful to Sabine Botha from Arizona State University, for her tremendous help in data processing, and for teaching me how to handle serial crystallography data.

I am deeply appreciative of my collaborators Marius Nagel and Tilman Kottke at Bielefeld University for being great co-authors and for scientific discussions.

My sincere thanks go to the T-REXX team at DESY and to the icOS and ID29 teams at ESRF, for their great support during data collection. Especially I would like to thank Nicolas Caramello, for his support during our long days (and nights) collecting spectroscopy data and for great discussions at conferences.

I would also like to acknowledge the financial support provided by the European XFEL R&D program, without which this research would not have been possible.

On a personal note, I am deeply thankful to my partner David, for his unwavering support and patience during the challenging times. His love and encouragement have been a constant source of strength and motivation.

To my parents, who have always believed in me and supported my academic endeavours, and to my sister, for her constant encouragement, I am eternally thankful.

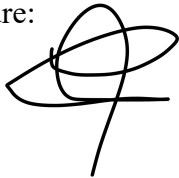
Thank you all for being a part of this journey.

Declaration on Oath

I hereby declare and affirm that this doctoral dissertation is my own work and that I have not used any aids and sources other than those indicated. If electronic resources based on generative artificial intelligence (gAI) were used in the course of writing this dissertation, I confirm that my own work was the main and value-adding contribution and that complete documentation of all resources used is available in accordance with good scientific practice. I am responsible for any erroneous or distorted content, incorrect references, violations of data protection and copyright law or plagiarism that may have been generated by the gAI.

Date: July 28th 2024

Signature:

A handwritten signature consisting of several overlapping loops and a long vertical stroke extending downwards.